

Crystal Growth on Complex Framework Structures

A thesis submitted to The University of Manchester for the degree of
Doctor of Philosophy
in the Faculty of Science and Engineering

2019

Nani Farida

School of Chemistry

List of Contents

List of Contents.....	2
List of Tables.....	7
List of Figures	8
List of Equations	20
List of Abbreviations	21
Abstract.....	22
Declaration.....	23
Copyright Statement.....	24
Acknowledgements	25
1. Introduction to Nanoporous Materials, Crystal Growth and <i>CrystalGrower</i> Simulation	27
1.1. Nanoporous materials.....	27
1.1.1. Zeolites.....	27
1.1.2. Applications of zeolites.....	30
1.1.3. Synthesis of zeolites.....	33
1.2. Crystal Growth	37
1.3. Crystal Simulation	43
1.4. Aims of the study	45
1.5. References.....	49
2. Experimental Techniques	57
2.1. Powder X-ray Diffraction	57
2.2. Scanning Electron Microscopy	59
2.3. Atomic Force Microscopy	61

2.4.	References	62
3.	IM-17 Crystal Dissolution Studied by AFM	65
3.1.	Introduction.....	65
3.2.	Experimental	68
3.2.1.	Synthesis of the IM-17 crystal.....	68
3.2.2.	Material characterizations.....	68
3.2.3.	Dissolution of IM-17 crystal studied with in-situ AFM	69
3.3.	Results and Discussions	70
3.3.1.	Synthesis and characterization of IM-17 crystal.....	70
3.3.2.	Ex-situ AFM of IM-17 crystal.....	73
3.3.3.	UOV crystal simulation	77
3.3.4.	In-situ AFM of IM-17 crystal	81
3.3.4.1.	Dissolution of (100) facet of the IM-17 crystal	82
3.3.4.2.	Simulation of IM-17 crystal dissolution on (100) facet.....	89
3.3.4.3.	Dissolution of screw dislocation on (100) facet of the IM-17 crystal	94
3.3.4.4.	Dissolution of (013) facet of the IM-17 crystal	103
3.3.4.5.	Simulation of IM-17 crystal dissolution on (013) facet.....	111
3.3.5.	IM-17 crystal growth studied using X-ray diffraction data.....	115
3.4.	Conclusions.....	119
3.5.	References.....	120
4.	DAF-1 Crystal Dissolution Studied by AFM	123
4.1.	Introduction.....	123
4.2.	Experimental and Analytical Techniques	126
4.2.1.	Synthesis of the DAF-1 crystal	126
4.2.2.	Material characterizations.....	127
4.2.2.1.	Powder X-Ray Diffraction (PXRD).....	127
4.2.2.2.	Scanning Electron Microscopy (SEM)	127

4.2.2.3.	Ex-situ Atomic Force Microscopy (AFM)	127
4.2.3.	Dissolution of DAF-1 crystal studied with in-situ AFM	127
4.3.	Results and Discussions	128
4.3.1.	Synthesis and characterization of the DAF-1 crystal	128
4.3.2.	Ex-situ AFM of DAF-1 crystal.....	130
4.3.2.1.	Crystal surface topography	130
4.3.2.2.	Structure analysis based on AFM result.....	133
4.3.2.3.	Crystal surface impurities	137
4.3.3.	DFO crystal simulation	141
4.3.4.	In-situ AFM of DAF-1 crystal dissolution.....	144
4.3.4.1.	Dissolution of DAF-1 crystal in solution 1	144
4.3.4.2.	Dissolution of DAF-1 crystal in solution 2	146
4.3.4.3.	Dissolution of DAF-1 crystal in solution 3	148
4.3.4.4.	Dissolution of DAF-1 crystal in solution 4	158
4.3.4.5.	Dissolution of DAF-1 crystal in solution 5	168
4.3.4.6.	Pits formation on the DAF-1 crystal surface	174
4.3.4.7.	Dissolution mechanism of DAF-1 crystal	177
4.3.4.8.	Suggested DAF-1 crystal growth	179
4.3.5.	Simulations of DAF-1 crystal dissolution	180
4.3.5.1.	Simulation of DAF-1 crystal dissolution on (010) facet.....	180
4.3.5.2.	Simulation of DAF-1 crystal dissolution on (001) facet.....	184
4.4.	Conclusions.....	188
4.5.	References.....	189
5.	Zeolite Rho Crystal Dissolution Studied by AFM	192
5.1.	Introduction.....	192
5.2.	Experimental and Analytical Techniques	194
5.2.1.	Synthesis of the zeolite Rho crystal	194
5.2.2.	Material characterizations.....	194

5.2.3.	Dissolution of zeolite Rho crystal studied with in-situ AFM.....	195
5.3.	Results and Discussions.....	195
5.3.1.	Characterization of the zeolite Rho crystal.....	195
5.3.2.	Ex-situ AFM of zeolite Rho crystal	197
5.3.3.	RHO crystal simulation.....	199
5.3.4.	In-situ AFM of zeolite Rho crystal dissolution	200
5.4.	Conclusions.....	205
5.5.	References.....	205
6.	NU-87 Crystal Dissolution Studied by AFM.....	208
6.1.	Introduction.....	208
6.2.	Experimental and Analytical Techniques	211
6.2.1.	Synthesis of the NU-87 crystal.....	211
6.2.2.	Material characterizations.....	212
6.2.3.	Dissolution of NU-87 crystal studied with in-situ AFM.....	213
6.3.	Results and Discussions	214
6.3.1.	Synthesis and characterization of the NU-87 crystal.....	214
6.3.2.	Ex-situ AFM of NU-87 crystal	215
6.3.3.	NES crystal simulation.....	217
6.3.4.	In-situ AFM of NU-87 crystal dissolution	218
6.4.	Conclusions.....	221
6.5.	References.....	222
7.	Conclusions and Future Work	225
7.1.	Conclusions.....	225
7.2.	Future Work	227
7.3.	References.....	228
	Appendices.....	230

Appendix 1.....	230
Appendix 2.....	232

Word count: 49,095

List of Tables

Table 1.1. Applications of zeolites.....	30
Table 1.2. Seven crystal systems [85]	39
Table 1.3 Comparisons of the materials used in this project and why they are selected in this study	48
Table 4.1. Cell parameters of DAF-1 crystal	129
Table 4.2. Solutions used in in-situ AFM experiment to dissolve the DAF-1 crystal	144
Table 5.1. A comparison of RHO, PAU and MWF structures [2]	192
Table 6.1. A summary of the NU-87 crystal dissolutions performed using solutions other than NaOH solution.	220

List of Figures

Figure 1.1. FAU framework structure with its cages and cation positions. D6R: double 6-membered ring, 12R: 12-membered ring (Adapted from Y. Nozue et al., “Insulating state and metallic phase transition of heavily sodium-doped low-silica X (LSX) zeolites,” J. Phys. Chem. Solids, vol. 73, no. 12, pp. 1538–1541, 2012 [23].	28
Figure 1.2. Atomic representations of zeolite’s inorganic framework. a) One negative charge is balanced by one Na^+ . b) Two negative charges are balanced by one Ca^{2+} .	29
Figure 1.3. Bravais lattices (taken from C. Hammond, The Basics of Crystallography and Diffraction, 3rd ed. New York: Oxford University Press Inc., 2009 [85]).	38
Figure 1.4. Crystal surface structure model by Kossel [84].	40
Figure 1.5. Illustration of layer growth mechanism [84].	41
Figure 1.6. A diagram showing the spiral growth mechanism [84].	42
Figure 1.7. Supersaturation and growth mechanism relationship [84].	42
Figure 1.8. Energy ladder for each cage type in zeolite A model. The thick ladder represents the energy level for the cage type in different surface configurations [95].	44
Figure 2.1. Shaded planes in a rectangular system.	57
Figure 2.2. Bragg’s Law (Taken from https://serc.carleton.edu/research_education/geochemsheets/BraggsLaw.htm [2]).	58
Figure 2.3. A chart of the main elements of a scanning electron microscope (Adapted from R. F. Egerton, <i>Physical Principles of Electron Microscopy: An Introduction to TEM, SEM, and AEM</i> . New York: Springer Science+Business Media, Inc., 2005. [4]).	59
Figure 2.4. SEM images derived from a) secondary electrons and b) backscattered electrons [4].	61

Figure 2.5. Diagram of the main components of AFM (Taken from https://undergrad.research.ucsb.edu/2014/03/atomic-force-microscope-tiny-record-player/ , accessed on May 26, 2015 [7].	62
Figure 3.1. SEM images of the IM-17 crystal from literature [6].	65
Figure 3.2. The a) (100) facet, b) (001) facet and c) (010) facet of the UOV structure. Red dashed line shows one unit cell.	66
Figure 3.3. Sixteen tiles constructing UOV structure [11].	67
Figure 3.4. PXRD patterns of the calcined IM-17 sample compared to UOV (Ref. [11]).	70
Figure 3.5. PXRD patterns comparison between calcined IM-17 sample (red), calculated MFI (blue, Ref. [11]) and UOV (black, Ref. [11]).	71
Figure 3.6. SEM image of as-prepared IM-17 crystal. Inset shows scanning on a larger area.	72
Figure 3.7. A diagram of the IM-17 crystal with its three different facets.	73
Figure 3.8. a) A vertical deflection AFM image of IM-17 crystals showing (100) facet. The scanned area in this image is $2.5\ \mu\text{m} \times 2.4\ \mu\text{m}$. b) A diagram showing the orientation of the IM-17 intergrowth crystals in the image (a). c) Cross-sectional height measurement along the blue line in the image (a).	74
Figure 3.9. A lateral deflection AFM image of IM-17 showing (100) facet with screw dislocation (indicated with blue arrows) and height measurements on some terraces marked with yellow lines. AFM scanned area is $1.9\ \mu\text{m} \times 1.9\ \mu\text{m}$.	74
Figure 3.10. i) Cross-sectional height measurements of terraces grew from spiral growth on (100) facet along the blue lines. The AFM image is $0.7\ \mu\text{m} \times 1.0\ \mu\text{m}$ in size. ii) An outline of the newly formed spiral in (i) with the heights on some lines across it.	75
Figure 3.11. A vertical deflection AFM image ($1.0\ \mu\text{m} \times 1.2\ \mu\text{m}$ in size) of IM-17 crystal showing (013) facet and its height measurements on some terraces. Inset illustrates a schematic diagram of the crystal with its intergrowth.	76

Figure 3.12. Simulation of UOV crystal using CrystalGrower viewed with a) VMD and b) CG Visualiser showing (100) facet on top rows and (013) facet on the bottom row. The simulation was performed with $\Delta U_s = 2 \text{ kcal mol}^{-1}$. The simulated crystal is approximately $0.07 \mu\text{m} \times 0.23 \mu\text{m} \times 0.44 \mu\text{m}$ in size.....	78
Figure 3.13. Simulated UOV crystal in Figure 3.12 viewed closely at a – b) (100) facet and c – d) (013) facet with (1) denotes single nucleation, (2) denotes defect and (3) marks newly grown layer. Cyan arrows on images (b) and (d) show clearly one layer height of (100) and (013) facets, respectively.....	79
Figure 3.14. UOV structure on (100) facet presented to clarify the tilings arrangement.....	80
Figure 3.15. UOV structure depicted (001) facet (the left image shows its tiles and the right image shows its framework). Red square on the right image shows one unit cell. Black dashed lines display the most possible surface termination.	80
Figure 3.16. UOV tiling and structure showing the corresponding d_{013} 's height. Black dashed line depicts the most possible surface termination.	81
Figure 3.17. Consecutive AFM vertical deflection images of IM-17 crystal dissolution in 4 M NaOH solution. Scanned area: $0.8 \mu\text{m} \times 0.5 \mu\text{m}$ (to be continued on the next page).	83
Figure 3.18. Subsequent vertical deflection AFM images of IM-17 crystal dissolution in 4 M NaOH solution with height measurement on the same spot. AFM image's size: $0.9 \mu\text{m} \times 0.5 \mu\text{m}$	86
Figure 3.19. A vertical deflection AFM image of IM-17 crystal dissolution in 4 M NaOH solution at $t = 115 \text{ min}$ with one segment's height measurement.	87
Figure 3.20. UOV structure viewed at (001) and its height breakdown.	87
Figure 3.21. Schematic illustration of step by step IM-17 crystal dissolution on (100) facet drawn as tiling.	88
Figure 3.22. Comparison of AFM images of IM-17 crystal surface on (100) facet comparison before dissolution and after being dissolved for 275 minutes. Image width: $0.8 \mu\text{m}$	89

Figure 3.23. Subsequent images of IM-17 crystal dissolution simulation on (100) facet with $\Delta\mu_{eq} = 9.7$ and $\Delta\mu$ for dissolution = 5. The simulation was set with $\Delta U_s = 2 \text{ kcal mol}^{-1}$. The simulated crystal is c.a. $0.04 \mu\text{m} \times 0.23 \mu\text{m} \times 0.12 \mu\text{m}$. The first image is the crystal before the dissolution started (to be continued on the next page).	90
Figure 3.24. i–v) A closer look at (100) facet of the simulation of UOV crystal dissolution. Image number 1 shows the surface before dissolution begins, the rests are the consecutive images of the dissolution event.	93
Figure 3.25. Dissolution process of IM-17 crystal with screw dislocation in 4 M NaOH solution. Scanned area: $1.9 \mu\text{m} \times 1.9 \mu\text{m}$ (to be continued on the next page).	95
Figure 3.26. A closer look at some images in Figure 3.25 ($t = 97 - 114 \text{ min}$) revealing how IM-17 particles on (100) surface next to the screw dislocation dissolved in patches. Yellow arrows indicate pits created by the solution attack on the crystal surface, whilst cyan arrows show the crystal particles left on the surface during the dissolution process. AFM image's size: $0.5 \mu\text{m} \times 0.7 \mu\text{m}$	100
Figure 3.27. Vertical deflection AFM images (sized $0.6 \mu\text{m} \times 1.1 \mu\text{m}$) revealing starting events of dissolution of the spiral's end.	101
Figure 3.28. Height measurements on small segments of sequential AFM images of IM-17 crystal's (100) facet dissolution.	102
Figure 3.29. Subsequent vertical deflection AFM images showing (013) facet of IM-17 crystal with faults dissolved in 3 M NaOH solution. Scanned area: $0.9 \mu\text{m} \times 1.2 \mu\text{m}$ (to be continued on the next page).	104
Figure 3.30. Height measurements performed on the same spot of consecutive AFM images of (013) facet of IM-17 crystal.	109
Figure 3.31. a) UOV breakdown for (013) facet viewed along 100 direction. b) Schematic illustration of the stepwise dissolution of IM-17 crystal on (013) facet.	110
Figure 3.32. Subsequent images of IM-17 crystal dissolution simulation on (013) facet with $\Delta\mu_{eq} = 9.7$ and $\Delta\mu$ for dissolution = 5. The simulation was set with $\Delta U_s = 2 \text{ kcal mol}^{-1}$. The (013) facet of the simulated crystal above is c.a. 0.04	

$\mu\text{m} \times 0.14 \mu\text{m}$. The first image is the crystal before the dissolution started (to be continued on the next page).	112
Figure 3.33. Images of IM-17 crystal dissolution simulation on (013) facet with $\Delta\mu_{\text{eq}} = 9.7$ and $\Delta\mu$ for dissolution = 7. Images are viewed from a point right between [013] and 013 directions. The simulation was set with $\Delta U_s = 2 \text{ kcal mol}^{-1}$. The simulated crystal has approximately $0.23 \mu\text{m}$ longest diagonal and about $0.04 \mu\text{m}$ thickness. The first image is the crystal before the dissolution started.	114
Figure 3.34. PXRD patterns of as-synthesized IM-17 prepared in different crystallization times (in days). UOV and MFI references are XRD patterns for both structures taken from literature [11].....	116
Figure 3.35. SEM images of IM-17 crystals prepared in a) 4 days, b) 7 days, c) 11 days, d) 11 days (showing MFI phase), e) 12 days, f) 13 days, g) 14 days and h) 14 days (showing MFI phase).	117
Figure 3.36. Crystallinity curve of the IM-17 crystal.	118
Figure 4.1. DFO framework structure showing a) (001) and b) (010) facets. Blue dashed-lined shapes illustrate one unit cell. The structure is drawn in ball and stick mode. The blue dots represent the Al, P or Mg atoms, whilst the black sticks illustrate the oxygen bridging in between those Al, P or Mg atoms. Oxygen atoms are omitted for clarity.....	124
Figure 4.2. Eleven tiles constructing the DFO structure [5].	125
Figure 4.3. PXRD patterns of the as-prepared DAF-1 sample (red line) and DFO reference (black line) [5].....	129
Figure 4.4. Scanning electron micrographs of as-synthesized DAF-1 crystal showing a) (001) and b) (010) facets.	130
Figure 4.5. AFM vertical deflection images of DAF-1 crystal surface and its orientation under AFM microscope on a) (010) facet sized $6 \times 6 \mu\text{m}^2$, b) (010) facet sized $10 \times 6.62 \mu\text{m}^2$ and c) (001) facet sized $10 \times 10 \mu\text{m}^2$. White irregular dots on the surface are the impurity particles. Yellow double arrows and cyan dashed lines show the matching orientations of the crystal and its layers.	131

- Figure 4.6. AFM vertical deflection images of DAF-1 crystal showing defects on a) (001) facet sized $3 \times 3 \mu\text{m}^2$ and b) (010) facet sized $10 \times 10 \mu\text{m}^2$. Insets depict the crystal orientation. 132
- Figure 4.7. a) AFM vertical deflection image of DAF-1 crystal on (001) facet. b) and c) Histogram and cross-sectional terrace height measurements of the yellow rectangle and line, respectively, in the image (a). d) DFO framework structure showing its unit cell (black dashed rectangle) and two possible growth steps illustrated in red and green colours. The blue dots in the structure represent the Al, P or Mg atoms, whilst the black sticks illustrate the oxygen bridging in between those Al, P or Mg atoms. Oxygen atoms are omitted for clarity. 133
- Figure 4.8. a) AFM vertical deflection image of DAF-1 crystal on (010) facet. b) and c) Histogram and cross-sectional terrace height measurements of the yellow rectangle and line, respectively, in the image (a). d) DFO framework structure showing its unit cell (black dashed parallelogram) and three prospective growth steps. The blue dots in the structure represent the Al, P or Mg atoms, whilst the black sticks illustrate the oxygen bridging in between those Al, P or Mg atoms. Oxygen atoms are omitted for clarity. 134
- Figure 4.9. a) and b) AFM vertical images of DAF-1 showing (001) and (010) facets, respectively. c) and d) Cross-sectional measurement of surface texture along the yellow lines on (001) and (010) crystal facets, respectively. 136
- Figure 4.10. AFM vertical deflection (a – c) and its corresponding lateral deflection (d – f) images showing white particles of impurities scattered all over the (001) facet of DAF-1 crystal and random particles' heights. 138
- Figure 4.11. AFM images of stacked hexagonal sheets grew on (001) facet (a – d) and (010) facet (e – f) of the DAF-1 crystal surface. The inset shows the face's orientation scanned under the AFM. All images are vertical deflection images, except (b) and (d), which are height images of the corresponding (a) and (c) images, respectively. The dimension of image (a – b) $3.2 \mu\text{m} \times 3.2 \mu\text{m}$, (c – d) $1.7 \mu\text{m} \times 1.7 \mu\text{m}$, (e) $2.8 \mu\text{m} \times 2.4 \mu\text{m}$ and (f) $7.4 \mu\text{m} \times 7.4 \mu\text{m}$ 140
- Figure 4.12. Simulation of DFO crystal using CrystalGrower with $\Delta U_s = 0.875 \text{ kcal mol}^{-1}$ and viewed with CG Visualiser. The simulated crystal has approximately

0.13 μm long of the (001) facet's diameter and 0.10 μm of the hexagonal thickness.	141
Figure 4.13. a) Cross-sectional of the (001) facet of simulated DFO crystal. Yellow double arrows show one growth layer. b) and c) DFO structure tilings drawn with Gavrog 3dt having the same orientation as the crystal model in (a), although the orientation of the image (b) is a little tilted to show the tiles on (001) surface termination. d) Simulated (001) surface of the DFO crystal model.	142
Figure 4.14. a) Cross-sectional of the (010) facet of simulated DFO crystal. b) and c) DFO structure tilings drawn using Gavrog 3dt having the same orientation as the crystal model in (a), although the orientation of the image (b) is a little tilted to show the tiles on (010) surface termination. d) Simulated (010) surface of the DFO crystal model. Cyan double arrows show one growth layer.	143
Figure 4.15. Sequential AFM vertical deflection images sized $3.0\ \mu\text{m} \times 2.8\ \mu\text{m}$ of DAF-1 crystal dissolution in $\text{Dec}(\text{OH})_2$ with $\text{pH} \approx 11$ on (010) facet. Pit formation is shown, indicated by cyan arrows.	145
Figure 4.16. DAF-1 crystal showing (010) facet under the optical microscope during in-situ AFM scanning in $\text{Dec}(\text{OH})_2$ solution ($\text{pH} \approx 11$).	146
Figure 4.17. AFM vertical deflection images of DAF-1 crystal on (010) facet sized $1.0\ \mu\text{m} \times 0.6\ \mu\text{m}$ dissolved in an H_3PO_4 solution having $\text{pH} \approx 3$. White arrows point to pit formation sequence.	147
Figure 4.18. AFM vertical deflection images of DAF-1 crystal on (001) facet sized $1.4\ \mu\text{m} \times 0.9\ \mu\text{m}$ dissolved in H_3PO_4 having $\text{pH} \approx 3$. White arrows point to pit formation sequence.	148
Figure 4.19. DAF-1 crystal orientation during in-situ AFM experiment in solution 3.	149
Figure 4.20. AFM vertical deflection images of DAF-1 crystal dissolution in solution 3 displaying $1.7\ \mu\text{m} \times 1.0\ \mu\text{m}$ area of (010) facet and height measurements along the cyan lines drawn on several images (to be continued on the next page).	150

Figure 4.21. A series of height measurements performed on the same nano-dot (very small DAF-1 particle) on (010) DAF-1 crystal surface at three consecutive dissolution times.	153
Figure 4.22. a) Possibility 1 and b) possibility 2 of the DFO structure breakdown viewed along the [001] direction. The blue dots in the structure represent the Al, P or Mg atoms, whilst the black sticks illustrate the oxygen bridging in between those Al, P or Mg atoms. Oxygen atoms are omitted for clarity.	154
Figure 4.23. Successive AFM vertical deflection images on (001) facet of DAF-1 crystal dissolution in solution 3, with cross-sectional height measurements performed on cyan lines. Scanned area: $1.7\ \mu\text{m} \times 1.0\ \mu\text{m}$ ($t = 0 - 100\ \text{min}$) and $5.2\ \mu\text{m} \times 3.0\ \mu\text{m}$ ($t = 142\ \text{min}$). White rectangle in the image at $t = 142\ \text{minutes}$ is the area scanned previously (to be continued on the next page).	156
Figure 4.24. AFM vertical deflection images of DAF-1 crystal on (001) facet during dissolution in solution 3 showing a closer look (the scanned area is $0.7\ \mu\text{m} \times 0.4\ \mu\text{m}$) of the scanned area in Figure 4.23.	158
Figure 4.25. Subsequent AFM vertical deflection images displaying the dissolution of (010) facet of DAF-1 crystal in solution 4. Scanned areas are $5.5\ \mu\text{m} \times 3.0\ \mu\text{m}$ ($t = 0 - 5\ \text{min}$), $3.0\ \mu\text{m} \times 1.3\ \mu\text{m}$ ($t = 13 - 119\ \text{min}$), $1.3\ \mu\text{m} \times 1.3\ \mu\text{m}$ ($t = 141 - 168\ \text{min}$) and $5.0\ \mu\text{m} \times 5.0\ \mu\text{m}$ ($t = 324\ \text{min}$). Blue squares in images at $t = 119$ and $324\ \text{mins}$ show the scanning areas for $t = 141 - 168\ \text{min}$, whilst white rectangle in image at $t = 324\ \text{min}$ is the scanning region for $t = 13 - 119\ \text{min}$ (to be continued on the next page).	160
Figure 4.26. Cross-sectional height measurements of random dots on (010) facet of DAF-1 crystal dissolution in solution 4.	163
Figure 4.27. Two possibilities of DFO structure break-down corresponding to the height measurements of nano-dots on (010) DAF-1 facet in Figure 4.26. The blue dots in the structure represent the Al, P or Mg atoms, whilst the black sticks illustrate the oxygen bridging in between those Al, P or Mg atoms. Oxygen atoms are omitted for clarity.	164
Figure 4.28. Consecutive AFM vertical deflection images of (001) facet of DAF-1 crystal dissolution in solution 4. Each area's width is $2.8\ \mu\text{m} \times 3.0\ \mu\text{m}$. Cyan rectangle represents the zoomed area scanned in Figure 4.29.	166

- Figure 4.29. A closer look at the cyan rectangle in Figure 4.28 of consecutive AFM vertical deflection images of (001) surface of DAF-1 crystal dissolution in solution 4 with each area's width is $1.7\ \mu\text{m} \times 1.0\ \mu\text{m}$ 167
- Figure 4.30. Corresponding AFM vertical deflection (left) and lateral deflection (right) images of (001) surface of DAF-1 crystal in solution 4. 168
- Figure 4.31. Subsequent AFM vertical deflection images of (010) facet of DAF-1 crystal dissolution in solution 5. Each image width is $3.0\ \mu\text{m} \times 1.8\ \mu\text{m}$. Cyan arrows point at step by step pit formation (to be continued on the next page). 169
- Figure 4.32. Consecutive AFM vertical deflection images of (001) facet of DAF-1 crystal dissolution in solution 5. Each image width is $1.7\ \mu\text{m} \times 1.0\ \mu\text{m}$, except the last image which is $20\ \mu\text{m} \times 20\ \mu\text{m}$. Cyan rectangle in the last image shows the area scanned prior to it (to be continued on the next page). 172
- Figure 4.33. AFM vertical deflection images sized $1.3\ \mu\text{m} \times 0.7\ \mu\text{m}$ of (010) facet of DAF-1 crystal exhibiting a pit formation in solution 5 and cross-sectional height measurements on the extrinsic impurity particle. The last image at $t = 228\ \text{min}$ (on the right) is a lateral deflection image corresponding to the image on its left (to be continued on the next page). 175
- Figure 4.34. Schematic illustration of the DFO crystal structure showing cross section for (010) crystal surface. The blue dots in the structure represent the Al, P or Mg atoms, whilst the black sticks illustrate the oxygen bridging in between those Al, P or Mg atoms. Oxygen atoms are omitted for clarity. 178
- Figure 4.35. Subsequent images of DAF-1 crystal dissolution simulation on (010) facet using CrystalGrower with $\Delta\mu_{\text{eq}} = 7.2$ and $\Delta\mu$ for dissolution = 5. The simulation was set with $\Delta U_s = 0.875\ \text{kcal mol}^{-1}$. The simulated hexagonal crystal's diameter is about 110 nm and its thickness is up to 85 nm. The first image is the crystal before the dissolution is started. The number on the top right-hand corner of each image is the frame's number, in which the frame was taken in every 200,000 iterations. 181
- Figure 4.36. DAF-1 crystal dissolution simulation on (010) facet using CrystalGrower with $\Delta\mu_{\text{eq}} = 7.2$ and $\Delta\mu$ for dissolution = 5. The simulation was set with $\Delta U_s = 0.875\ \text{kcal mol}^{-1}$. The first image is the crystal before the dissolution is started. The number on the bottom right-hand corner of each

image is the frame's number, in which the frame was taken in every 200,000 iterations. The left images are viewed closely in the right images along the [001] direction.....	183
Figure 4.37. Diagrams of DFO structure tiling drawn using Gavrog 3dt. a) The dissolution on (010) facet seen along [001] direction. b) Tilted image 1 in (a) to clearly display the (010) facet's tiles. c) The arrangement of t-ftt tile in the DFO structure with its two closest tiles above and below it parallel to [010] axis...	184
Figure 4.38. The left image shows nucleation on the (001) facet of DFO crystal simulated using CrystalGrower with $\Delta U_s = 0.875 \text{ kcal mol}^{-1}$. The modelled hexagonal crystal's diameter is about 110 nm and its thickness is up to 85 nm. The right image is the DFO structure tiling drawn with Gavrog 3dt and arrangement of some tiles constructing it.	185
Figure 4.39. A series of DAF-1 crystal dissolution simulation images on (001) facet with $\Delta\mu_{eq} = 7.2$ and $\Delta\mu$ for dissolution = 5. The simulation was performed using CrystalGrower with ΔU_s set to $0.875 \text{ kcal mol}^{-1}$. The simulated hexagonal crystal's diameter is about 110 nm and its thickness is up to 85 nm. The first image is the crystal before the dissolution is started. The number on the top right-hand corner of each image is the frame's number, in which the frame was taken in every 200,000 iterations.	186
Figure 4.40. DAF-1 crystal dissolution simulation on (001) facet using CrystalGrower with $\Delta\mu_{eq} = 7.2$ and $\Delta\mu$ for dissolution = 5. The simulation was set with $\Delta U_s = 0.875 \text{ kcal mol}^{-1}$. The first image is the crystal before the dissolution is started. The number on the bottom right-hand corner of each image is the frame's number, in which the frame was taken in every 200,000 iterations.....	187
Figure 5.1. PXRD patterns of the as-prepared zeolite Rho sample (red line) compared to the reference (black line) [2].	196
Figure 5.2. SEM image of the as-synthesized zeolite Rho crystals.	197
Figure 5.3. a–b) Vertical deflection AFM images of zeolite Rho crystals with the image (b) shows the (110) facet. c–d) Cross-sectional height measurements along the top and bottom horizontal black lines, respectively, in the image (b).	198

Figure 5.4. RHO structure framework viewed along c direction illustrated in ball and stick mode (left) and tiling drawn using Gavrog 3dt (right). The blue balls represent the Si or Al atoms, while the black sticks are the oxygen bridging in between the Si and Al. The oxygen atoms are omitted for clarity. The pink tiles on the right are the α -cages and the green ones are the double 8-rings. The growth step height is based on the calculation.....	198
Figure 5.5. Simulation of RHO crystal using CrystalGrower with $\Delta U_s = 2 \text{ kcal mol}^{-1}$ and viewed with CG Visualiser. a–b) Full look of the simulated crystals sized approximately $0.16 \mu\text{m}$. c–d) Closer looks at the $\{110\}$ surface of the simulated RHO crystal.....	199
Figure 5.6. Successive AFM vertical deflection images on the (110) facet of zeolite Rho crystal dissolution in 0.2 M KOH solution. The scanned area is $1.0 \mu\text{m} \times 1.0 \mu\text{m}$. Cyan and white arrows point at the dissolution of two different small terraces and their heights during the process. All heights given here have $\pm 0.1 \text{ nm}$ measurement error (to be continued on the next page).....	201
Figure 5.7. a) RHO structure breakdown of the (110) facet expressed in tiling (left) and ball and stick mode (right). The blue balls represent the Si or Al atoms, while the black sticks are the oxygen bridging in between the Si and Al. The oxygen atoms are omitted for clarity. b) Illustration of step by step RHO tiling breakdown.....	204
Figure 6.1. Decamethonium dications structure.	208
Figure 6.2. a) Framework structure of NU-87 crystal viewed at (201) facet drawn in ball and stick mode. The blue balls represent the Si or Al atoms, while the black sticks are the oxygen bridging in between the Si and Al. The oxygen atoms in this framework are omitted for clarity. One unit cell is displayed by the blue dashed lines. b) NU-87 tiling drawn using Gavrog 3dt (large blue tiles: t-nes, yellow tiles: t-non, pink tiles: t-pes and green tiles: t-euo).....	209
Figure 6.3. SEM images of NU-87 synthesized using decamethonium bromide as SDA reported by (a) Glaser et al. (1998) [8] and (b–c) Zhang et al. (2013) [10].	210
Figure 6.4. PXRD patterns of the as-prepared NU-87 sample (red line) compared to the reference (black line) [3].	214

Figure 6.5. SEM images of the as-synthesized NU-87 crystals.....	215
Figure 6.6. a–b) Vertical deflection AFM images of NU-87 crystals showing the surface having the largest area. c) Cross-sectional height measurement along the cyan line in the image (a). d–e) Vertical deflection AFM images of NU-87 crystals showing the side facet.	216
Figure 6.7. a) NU-87 structure framework illustrated in ball and stick mode. The blue balls represent the Si or Al atoms, while the black sticks are the oxygen bridging in between the Si and Al. The oxygen atoms in this framework are omitted for clarity. b) NU-87 tiling drawn using Gavrog 3dt (large blue tiles: t-nes, yellow tiles: t-non, pink tiles: t-pes and green tiles: t-euo). The growth step height of the framework in the image (a) and its corresponding tiling in the image (b) is shown with the red arrow. c) (001) surface of the simulated NU-87 crystal resulted from CrystalGrower calculation and viewed with CG Visualiser in ‘tyle type’ colouring. The colours of the tiles correspond to that of the tiling in the image (b). d) Tilted NU-87 tiling in the image (b) to show the (001) facet.	217
Figure 6.8. AFM vertical deflection images on the (001) facet of NU-87 crystal dissolution in 0.2 M NaOH solution. The scanned area is $2.0\ \mu\text{m} \times 1.2\ \mu\text{m}$...	219
Figure 6.9. A series of AFM vertical deflection images on the (001) facet of NU-87 crystal dissolution in 0.1 M Dec(OH) ₂ solution. The scanned area is $2.2\ \mu\text{m} \times 1.3\ \mu\text{m}$	221

List of Equations

Equation 1.1	45
Equation 3.1 Relative crystallinity (%) = $H_s H_r \times 100\%$	118

List of Abbreviations

Abbreviation	Definition
12R	12-membered ring
AFM	Atomic Force Microscopy
D4R	Double 4-membered rings
D6R	Double 6-membered rings
Dec(OH) ₂	Decamethonium hydroxide
FE-SEM	Field Emission Scanning Electron Microscopy
HR-SEM	High-Resolution Scanning Electron Microscopy
IUPAC	International Union of Pure and Applied Chemistry
IZA	International Zeolite Association
IZA-SC	Structure Commission of the International Zeolite Association
MOF	Metal Organic Framework
PXRD	Powder X-Ray Diffraction
SDA	Structure Directing Agent
SEM	Scanning Electron Microscopy
STM	Scanning Tunnelling Microscopy
TEA	Tetraethylammonium

Abstract

Crystal Growth on Complex Framework Structures

Nani Farida, The University of Manchester, January 2019

Newly discovered zeolite, IM-17 (UOV), with a complex structure directed by decamethonium dications, is fascinating owing to its very large unit cell ($12.68 \text{ \AA} \times 22.22 \text{ \AA} \times 39.06 \text{ \AA}$). This poses some interesting questions in crystal growth as to how the crystal memory is propagated over such a large distance. To investigate how such a large unit cell forms and allows stacking layers is the aim of this research. The investigation demands a powerful tool to study nanoscopic details, which can be reached employing Atomic Force Microscopy (AFM). Here we report results of our work on four crystals having complex structures: IM-17, DAF-1 (DFO), zeolite Rho (RHO) and NU-87 (NES).

The outcomes are also compared to the crystal models simulated using *CrystalGrower* program. The PXRD technique was used to confirm the as-prepared crystal structures. From the SEM micrographs, the crystal morphologies were revealed. The AFM exhibits the presence of terraces on all of the crystal surfaces. Cross-section and histogram height measurements of the terraces correspond to the growth steps of the materials.

The IM-17 crystal showed two mechanisms of growth: layer-by-layer on both (100) and (013) facets and spiral growth on the (100) facet. Layer-by-layer terraces dissolved in patches in alkaline solution while the spiral layer retreated during the dissolution. Meanwhile, the terraces on DAF-1 crystal surfaces demonstrated patches dissolution in solution combination of decamethonium hydroxide and phosphoric acid. Interestingly, these layers maintained their terrace positions throughout the dissolution time. Such phenomenon is called ‘surface thinning’.

Zeolite Rho possesses the simplest structure among the Rho-family zeolites. It has twelve {110} facets, on which the terraces grow with the same shape and orientation as the facet. The height of the small terraces did not decrease during the terrace retreat in alkaline solution until the critical surface area to maintain the structure together were achieved, after which the terrace height started to decrease. The NU-87 crystal was very resilient to the alkaline and acidic solution attack. In addition, the very thin crystal morphology of the NU-87 disadvantaged the crystal etching in basic solution.

All crystals under study and several dissolution processes were also simulated using *CrystalGrower* software based on the natural tiles. The simulated crystals were in a good agreement with the experimental results. The crystal models also proved very important to understand the crystal habit and their structure which cannot be solved in the laboratory.

Declaration

The work described in this thesis was conducted between August 2014 and August 2017 under the supervision of Professor Michael W. Anderson and Dr Martin P. Attfield in the School of Chemistry, The University of Manchester.

No portion of the work referred to in the dissertation has been submitted in support of an application for another degree or qualification of this or any other university or other institute of learning.

All the materials, figures and data presented in this work are my own original work, except where specifically stated and acknowledged.

Nani Farida

Manchester, 2018

Copyright Statement

- i. The author of this thesis (including any appendices and/or schedules to this thesis) owns certain copyright or related rights in it (the “Copyright”) and s/he has given The University of Manchester certain rights to use such Copyright, including for administrative purposes.
- ii. Copies of this thesis, either in full or in extracts and whether in hard or electronic copy, may be made **only** in accordance with the Copyright, Designs and Patents Act 1988 (as amended) and regulations issued under it or, where appropriate, in accordance with licensing agreements which the University has from time to time. This page must form part of any such copies made.
- iii. The ownership of certain Copyright, patents, designs, trademarks and other intellectual property (the “Intellectual Property”) and any reproductions of copyright works in the thesis, for example graphs and tables (“Reproductions”), which may be described in this thesis, may not be owned by the author and may be owned by third parties. Such Intellectual Property and Reproductions cannot and must not be made available for use without the prior written permission of the owner(s) of the relevant Intellectual Property and/or Reproductions.
- iv. Further information on the conditions under which disclosure, publication and commercialisation of this thesis, the Copyright and any Intellectual Property and/or Reproductions described in it may take place is available in the University IP Policy (see <http://documents.manchester.ac.uk/DocuInfo.aspx?DocID=24420>), in any relevant Thesis restriction declarations deposited in the University Library, The University Library’s regulations (see <http://www.library.manchester.ac.uk/about/regulations/>) and in The University’s policy on Presentation of Theses.

Acknowledgements

I would like to express my most sincere gratitude to my supervisors, Professor Michael W. Anderson and Dr Martin P. Attfield, for granting me an opportunity to conduct my PhD research under their supervisions as well as for their great support and encouragement throughout the journey, and also for all valuable knowledge they shared with me.

My special thanks are due to Dr Adam R. Hill for patiently training me on the *CrystalGrower* simulation as well as for the discussions and all help I cannot mention one by one. Also, my sincere gratitude to Dr Pablo Cubillas for the useful discussions and help. I am very grateful to Dr Inigo Vitorica-yrezabal for the PXRD training, Dr Patrick Hill and Dr Matthew Smith for the SEM and TEM training and Dr Rachel L. Smith and Dr Christopher A. Muryn for the AFM training. I want to extend my gratitude to Professor Suk Bong Hong and his research group at POSTECH, South Korea for providing me with some zeolite samples for this study.

I would like to thank all research group members of the Centre for Nanoporous Materials and all people in the office 2.57 for their help, discussions, friendship and support all the way through.

My gratitude to the Directorate General for Higher Education Republic of Indonesia for the research funding and scholarship, without whom it would have not been possible to complete the work, and the Chemistry Department, Universitas Negeri Malang, Indonesia for allowing me to pursue higher education and gain more experience.

I would like to especially thank my family and friends for their love and full support throughout the journey.

Manchester, 2018

The Author

Chapter 1

Introduction to Nanoporous Materials, Crystal Growth and *CrystalGrower* Simulation

1. Introduction to Nanoporous Materials, Crystal Growth and *CrystalGrower* Simulation

1.1. Nanoporous materials

Nowadays, nanoporous materials have obtained a great interest in worldwide research. This is due to the wide range of their applications, for instance their use as adsorbents [1]–[4], in ion exchange [5]–[7], as catalysts [8]–[13], in drug delivery and health [14], [15] and many more. These materials are also employed extensively in the oil industry [16], [17], water purification [18], as well as in nuclear waste remediation [5], [19]. The reason behind these numerous uses is governed mainly by the nanoporous materials' pores possessing size and shape, which specifically match most of the organic molecules to enter them.

Crystalline nanoporous materials can be defined as crystalline solids having pores sized between one nanometre and a few tens of nanometres [20]. These solid materials are further classified by IUPAC into three groups: macroporous, mesoporous and microporous solids. The pore dimension of the first group is more than 50 nm, while the second group has a pore dimension between *c.a.* 2 and 50 nm. The last category possesses less than 2 nm of pore diameters [21].

Examples of crystalline nanoporous materials are abundant. Zeolites, which will be described in more detail in this chapter, compose a part of these nanoporous materials. Other examples include metallophosphates and metal-organic frameworks (MOFs).

1.1.1. Zeolites

Zeolites were discovered in 1756 by Cronstedt, an expert in mineralogy from Sweden [22]. Naturally, zeolites are very stable crystalline aluminosilicate minerals having three-dimensional structures, which consists of $[\text{SiO}_4]^{4-}$ and $[\text{AlO}_4]^{5-}$ tetrahedra linked by their corners, so that oxygen bridges connect the ions. This structure forms an open framework with channels and cavities inside, which make the zeolite structure porous. Figure 1.1 illustrates a faujasite framework, a type of zeolite structure, with its channels which join the cavities or cages.

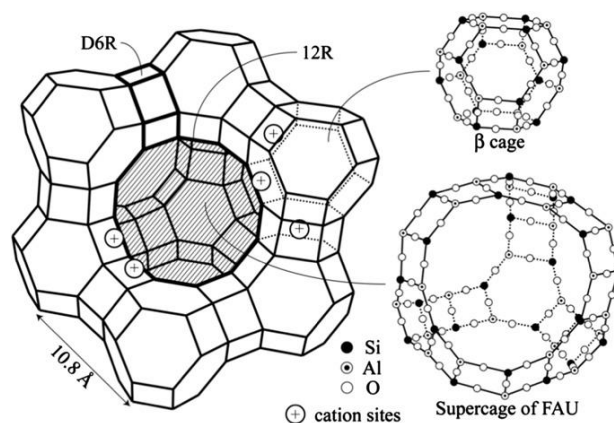


Figure 1.1. FAU framework structure with its cages and cation positions. D6R: double 6-membered ring, 12R: 12-membered ring (Adapted from Y. Nozue *et al.*, “Insulating state and metallic phase transition of heavily sodium-doped low-silica X (LSX) zeolites,” *J. Phys. Chem. Solids*, vol. 73, no. 12, pp. 1538–1541, 2012 [23]).

Voids in the zeolite are filled by cations and water molecules. The function of the cations sitting inside the voids is to balance negative charges formed by substitution of silicon with the aluminium atoms (see Figure 1.2). The more aluminium incorporated in a zeolite framework, the greater the negative charge of the framework is. Thus, more cations are needed to balance this charge. In addition to the cations, there also are water molecules, which move freely, in zeolite’s channels and cavities. This arrangement makes zeolites to be a good desiccant, adsorbent and ion exchanger [24]. Natural zeolites effortlessly lose water during heating. This fact gave rise to where the name of ‘zeolite’, which is derived from Greek words ‘zein’ (to boil) and ‘lithos’ (stone), came from [24].

The voids within the zeolite structures have specific dimensions (0.3 – 0.8 nm), which are comparable to small molecules [20]. This allows exact molecules to come into the voids and rejecting bigger molecules. Because of this nature as a ‘molecular sieve’, zeolites are broadly used in the world as listed in section 1.1.2.

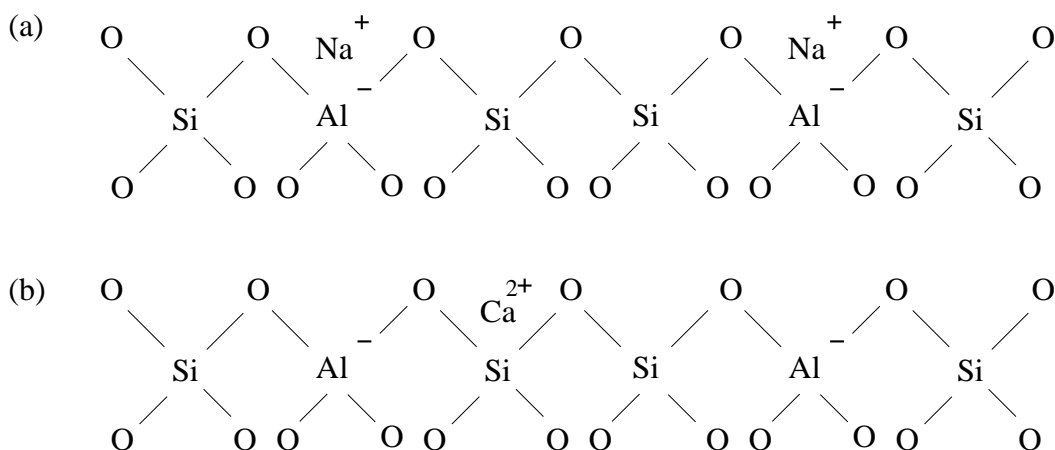


Figure 1.2. Atomic representations of zeolite's inorganic framework. a) One negative charge is balanced by one Na⁺. b) Two negative charges are balanced by one Ca²⁺.

Large-scale commercial use of zeolites leads to the need to produce the materials synthetically rather than just to depend on exploiting natural ones. Deville is claimed as the first person who made zeolite in the laboratory [24]. This success was then followed by rapid progress in zeolite synthesis. Not only synthesizing known natural zeolites, but researchers also created zeolites having new structures. They modified them to get optimum properties too. This can be done by changing the synthesis condition or incorporating elements other than aluminium in the framework. The massive exploration of zeolites leads to not only deeper understanding of these materials, but also to the discovery of new framework structures.

Progress in the investigation on zeolite led to the discovery of new families of the materials, metallophosphate and metal-organic frameworks (MOFs). In terms of metallophosphates, these are non-silica crystalline porous materials, in which other elements substitute the silicon atoms. Some metallophosphates crystallize in zeolitic structure frameworks and demonstrate zeolite properties (*i.e.* adsorbents, molecular-scale pore dimensions). Examples of these materials are aluminophosphate, zincophosphate and gallophosphate. Meanwhile, MOFs comprise metal ions connected by organic linkers and have large pores, cavities and surface area [25].

Those fast-growing development in finding zeolite and zeolite-like materials result in the term ‘zeolite’ no longer stick to the aluminosilicate minerals. The meaning became very broad and confusing. However, it is now limited for defining crystalline porous materials with silica framework combined with elements having three or four valences like Al, Fe, B, Ga, Ti, Ge, and so on [20].

The Structure Commission of the International Zeolite Association (IZA), on its website [26], lists more than 200 confirmed zeolite frameworks. Each framework has three-letter code written in capital letters. Taken as examples are MFI framework for ZSM-5, MOR framework for mordenite, MWW for MCM-22, SOD for sodalite and so on. Prefix ‘zeolite’ to name the materials is given to artificial zeolites without known naturally occurred ones, such as zeolite A, zeolite L, zeolite beta. The website also gives information on the framework parameters, three-dimensional images, powder patterns, type of materials formed and tilings.

1.1.2. Applications of zeolites

It has been mentioned in the previous section that the applications of zeolites have grown extensively since their discovery. Many of those zeolites’ applications are summarized in Table 1.1. As previously explained, the ability of zeolite materials to be used in many areas is provided by their unique characters.

Table 1.1. Applications of zeolites

Application fields	Names of the Zeolite		References
Desiccant	ETS-10	Used in CFC-free air conditioner	[27]
	Chabazite	Corn grain drying	[28]
	Zeolites 3A and 4A	Alcohols and acetic acid esters’ desiccant	[29]
	Zeolite A, X, and Y	Air dehumidifier	[30]

Application fields	Names of the Zeolite		References
Adsorbent (in separation and purification)	Zeolite Rho	CO ₂ and N ₂ adsorption	[31]
	Zeolite X, Y, A	CO ₂ adsorption	[32]–[34]
	Layered SAPO-34		[35]
	TNU-9, IM-5, SSZ-74, ferrierite, ZSM-5, ZSM-11		[36]
	AlPO-14	CO ₂ and methane adsorption	[37]
Adsorbent	Faujasite	Benzene and water vapours adsorption	[1]
	Zeolite A	Detergent	[2], [3]
	Sn-Beta	Biomass adsorption	[4]
Ion exchanger	Faujasite	Ion Cs ⁺ and NH ₄ ⁺ replacement	[5]
	Zeolite 4A	Ion Co ²⁺ , Cr ³⁺ , Cu ²⁺ , Zn ²⁺ and Ni ²⁺ replacement	[6]
	Na-P1, K-F, K-Phillipsite, K-Chabazite	Ion NH ₄ ⁺ replacement	[7]
Catalyst	Zeolite Beta, H-MCM-22, H-NU-87, and H-EU-1	Cumene production	[8], [11]
	Co-ZSM-5, Co-Beta, and Co-NU-87	Ethane ammoxidation to acetonitrile	[9]
	MCM-22, NU-87	Toluene disproportionation to xylene and tetramethylbenzene	[10]
	H-TNU-10, H-ZSM-57, H-ZSM-5	<i>m</i> -xylene isomerization and disproportionation	[38]
	H-NU-87	Methylnaphthalene conversion	[39]
	ZSM-5	Methanol to olefins reaction	[12], [13]
	ZSM-34		[40]

Application fields	Names of the Zeolite		References
	SSZ-13		[41], [42]
	SSZ-16, SSZ-17		[41]
	Cu-SSZ-13	Selective catalytic reduction of NO _x	[43]
	Sn-Beta	Biomass conversion	[44]–[48]
	H-Beta	Benzoylation of toluene with benzoyl chloride	[49]
Medical and Pharmaceuticals	Clinoptilolite	Heavy metals removal from urinary excretion	[15]
Water purification	MCM-41 combined with iron oxide	Magnetic adsorbent for As(V) and Cr(VI)	[18]
Oil industry	NU-87, MCM-22, ZSM-5	<i>n</i> -heptane cracking	[16]
	ITQ-2	Oil refining	[17]
	HZSM-5	Selective cracking of linear olefin	[17]
	Zeolite Y	Fluid catalytic cracking, hydrocracking	[50], [51]
	ZSM-20, ITQ-21	Bottom cracking	[50]
Wastewater treatment	Faujasite	Ion NH ₄ ⁺ elimination	[5]
	MCM-41	Metals removal	[3]
	Zeolite A	Methane abatement	[3]
	Zeolite 4A	Co ²⁺ , Cr ³⁺ , Cu ²⁺ , Zn ²⁺ and Ni ²⁺ removal	[6]
	Mullite, calcite, NaP1 zeolite, hydroxysodalite	Cr ³⁺ removal	[52]
Nuclear waste	Faujasite	Ion Cs ⁺ exchange	[5]

Application fields	Names of the Zeolite	References
treatment	Highly porous natural zeolites	²²² Rn adsorption [19]

1.1.3. Synthesis of zeolites

St. Claire Deville (1862) is said the first to successfully synthesize zeolite, levynite, from potassium silicate and sodium aluminate [24], [53]. This triumph triggered other scientists to conduct research to synthesize zeolite materials. Common chemicals required for zeolite syntheses are silicon source, aluminium source, base, organic cation and water. Some researchers claim that they had produced targeted zeolites by adding a small amount of seeds [54], [55]. These precursors required for producing zeolites, along with the factors that influence the action, are described in this section.

Silicon sources usually employed for synthesizing the aluminosilicates are soluble colloidal silica, sodium silicate, fumed silica, and amorphous silica. Others reported the use of dissimilar silicon sources, taken as examples are water glass, silicic acid, silica gel, although their numbers are insignificant [56]. Recently, many scholars investigated how to reuse industrial and agricultural wastes to produce zeolites, which was believed to help reduce environmental pollution problems. Examples of these wastes under investigation were coal fly ash, bottom ash, rice husk ash and kaolinite waste.

Jayaranjan and co-workers (2014) summarized that SiO₂ contained in coal fly ash and bottom ash reached up to 60% [57]. Even more, fly ash from one of the power plants in China consisted of 65% of silica [52]. Many articles reported the conversion of these wastes into commercial zeolite materials. Fly ash has been successfully used to synthesize faujasite and zeolite P [1], [5], pure crystalline zeolite 4A and MCM-41 [2], [3], Na-P1, K-F, K-Phillipsite and K-Chabazite [7], and so on. Meanwhile, the coal bottom ash has been altered to be useful kinds of zeolite, namely tobermorite [58]–[60], Na-P1, hydroxyl sodalite [58], MCM-41, SBA-15 and SBA-16 [61].

Fly ash and bottom ash conversion to zeolitic materials becomes more favourable not only because of its environmentally friendly purpose, but also owing to its up to around 40% of Al_2O_3 content [57], another main component in synthesizing aluminosilicate materials. This fact provides an even lower zeolite production cost since the addition of aluminium source can be neglected if those municipal wastes are used. Wu *et al.* (2008) have published an effective crystallization of mullite, calcite, Na-P1 zeolite and hydroxy sodalite by only adding NaOH solution into fly ash [52]. Both SiO_2 and Al_2O_3 were supplied by the ash.

However, there is one drawback of the use of coal ash as SiO_2 source to this purpose, which is that the ash contains many elements other than silicon and aluminium, then the zeolite materials obtained after its hydrothermal reaction have a high probability to be impure [52].

The utilization of agricultural waste, *i.e.* the ash obtained from rice husk calcination in air, gives a more promising future for this green aluminosilicate synthesis. Interestingly, rice husk contains very high silica, up to 85–98% [62]. Naskar *et al.* (2011) reported the use of rice husk ash to synthesize pure hydroxy sodalite [63]. Furthermore, this agricultural waste has also been easily used for synthesizing ZSM-5 with [64] and without [62] organic template molecules.

Nevertheless, the burning process of converting rice husk to silica results in another air pollution problem. The smoke produced from the process may risk health [65]. Although many researchers are interested in studying this particular promising alternative in zeolite synthesis in the laboratory, the cost disadvantage on burning the husk to some degree hinders the application in industrial scale.

Cheap kaolin mineral, which is abundant as clay constituent, is mainly made of kaolinite. Kaolinite itself, having empirical formula $\text{Si}_2\text{Al}_2\text{O}_5(\text{OH})_4$, contains silica and alumina [66]. Since a while ago, the triumph in synthesizing zeolitic materials from kaolinite substance has been reported for zeolite A [67]–[70], P [69], [71], X [67], [70]–[73], Y [67], [74] and hydroxy sodalite [69]. Recently, Hildebrando *et al.* (2014) employing kaolin waste from the Amazon region to prepare pure zeolite Na-P [75].

Metal aluminates, particularly sodium aluminate, are widely blended in the zeolite synthesis mixture. This chemical is mostly used as aluminium source for nanoporous material syntheses compared to other sources. Some preparations were reported using aluminium source that came from $\text{Al}(\text{OH})_3$, Al_2O_3 or $\text{AlO}(\text{OH})$. However, these must be made freshly before being mixed with the other components.

It is necessary for the production of zeolites to set the synthesis gel's pH high, mainly 11 – 13. This ensures that all silicates and aluminates are de-polymerized in the synthesis gel so that they can start the nucleation. Thus, the optimum pH in the mixture promotes the crystallization time [76]. The most common basic solution used is the hydroxide of alkaline and alkaline earth metals, especially NaOH and KOH. The two hydroxides produce Na^+ and K^+ , two cations largely found in natural zeolite's voids.

In regards to the organic cations, about which a long observation has been done, it is now well-known that the addition of organic cations in zeolite production plays a very important role. Organic cations serve as a template to shape the zeolite framework. They occupy the zeolite's channels and cages. Tetramethylammonium is an organic cation largely employed in zeolite crystallization.

Seeds have been believed to help increase the yield of targeted zeolite structure. Seeds usually used are the same crystals as the aimed materials. The seeds can be either in the form of powder or membrane [54], [55]. The successful routes of template-less seed-assisted zeolite synthesis have also been reported. Yang and co-workers (2012) synthesized pure crystalline ZSM-34 with seeds addition, but without organic template as the structure directing agent [40].

Nevertheless, some publications claimed that they made the zeolites using different seed crystals to the targeted structures. Yu *et al.* (2013) crystallized ZSM-5 (MFI-structured) using ZSM-11 crystal seeds with MEL framework [13]. This can be done successfully because ZSM-11 structure is related to ZSM-5 structure. They are similar in framework density and pore size, although their channel structure twists are different [77]. Another report stated that NU-87 synthesis was achieved using EU-1 seeds due to the structural similarity between those two types of zeolite.

Despite the success, that research also found that the use of hetero-structural seed caused a decline in crystal size [76].

One of the advantages of seed incorporation in the zeolite crystallization is that it is not necessary to add an organic template so that this provides a green synthesis route. Nonetheless, the seed production itself is still assisted by organic compounds as the template.

Beside those component sources to be paid attention to, it must be considered that other factors also influence the framework structure of zeolite obtained during its preparation. The synthesis aspects to also think about are concentration, temperature, pressure and time.

Concentration in synthesis mixture, particularly Si/Al ratio, is very crucial. One can acquire different kinds of zeolite by changing this ratio while maintaining the other conditions. Davis and Lobo (1992) have proved that tetraethylammonium (TEA) cation formed three distinctive phases with three variations of Si/Al ratio. ZSM-12 was obtained when a high Si/Al ratio was used, while zeolite beta and faujasite were formed at intermediate and low Si/Al ratios, respectively [78]. In addition to this, an experiment by Dutta and Bronic (1994) suggested that zeolite P was crystallized in high Si/Al ratio and zeolite Y was the main phase in low Si/Al ratio [79]. A similar finding was also observed by Shih and Chang in 1996. They found that at the same synthesis condition, an addition of $\text{Al}(\text{OH})_3$ into the synthesis mixture containing silica and NaOH led to zeolite A formation rather than faujasite, which was produced without the aluminium addition [5].

Apart from the framework structure formed, the Si/Al ratio also controls the hydrothermal stability of the zeolite. Increasing the Si/Al ratio of a zeolite material strengthens the zeolite to stay secure up to 900 °C. The benefit provided by the thermally stable materials derives it to be used in a large-scale as a catalyst for high-temperature reaction [80].

Another consideration in the zeolite synthesis is temperature. Work on conversion of faujasite into zeolite P performed by Shih and Chang (1996) suggested that heating zeolite synthesis gel at 80 °C tended to produce zeolite P while curing this gel at 38 °C formed faujasite [5]. This result seems to agree with LaRosa's observation (1992)

[81]. Such phenomenon happens due to the less stability of the faujasite, owing to its larger pore size and molar volume compared to zeolite P. Zhang *et al.* (2012) in their patent (EP 2 441 733 A1) claimed that variation in synthesis temperature had a great influence in NU-85 synthesis [82]. They mentioned that, although other synthesis conditions were set the same, converting the temperature from 160 °C to 180 °C and 200 °C changed the crystalline phase obtained from NU-85 to NU-85 intergrowth by EU-1 and pure EU-1, respectively.

Pressure becomes significant in zeolite preparation due to adapting the natural process of zeolite formation deep in the ground, which of course is in a high-pressure environment. A tightly sealed reactor used in the material's synthesis automatically generates high-pressure environment for the process. This high pressure enables the starting molecules in the synthesis mixture to break down into elements, which then self-orders to form a particular porous array.

Water content also plays an important role in zeolite synthesis. Varying the H₂O concentration in the synthesis gel surely affects the end product, especially the material's crystal morphology and phase. Finally, the last thing to take into account in producing zeolite is the synthesis time. Usually, when the reaction temperature is high, the time required to complete the crystallization is less and vice versa.

1.2. Crystal Growth

Before coming to the description of the crystal growth, it is important to know about the definitions of crystal and nucleation. Understanding these terms helps us to learn about crystal growth.

A crystalline solid is one having a regular and infinite arrangement of a pattern. Smallest part of the repeating pattern is called a unit cell if it is in three dimensions. In crystallography, there are fourteen different kinds of lattices known as Bravais lattices, as can be seen in Figure 1.3. The Bravais lattices create three-dimensional motifs by the work of symmetry elements, which then derive point and space groups. These all make up the seven different crystal systems listed in Table 1.2.

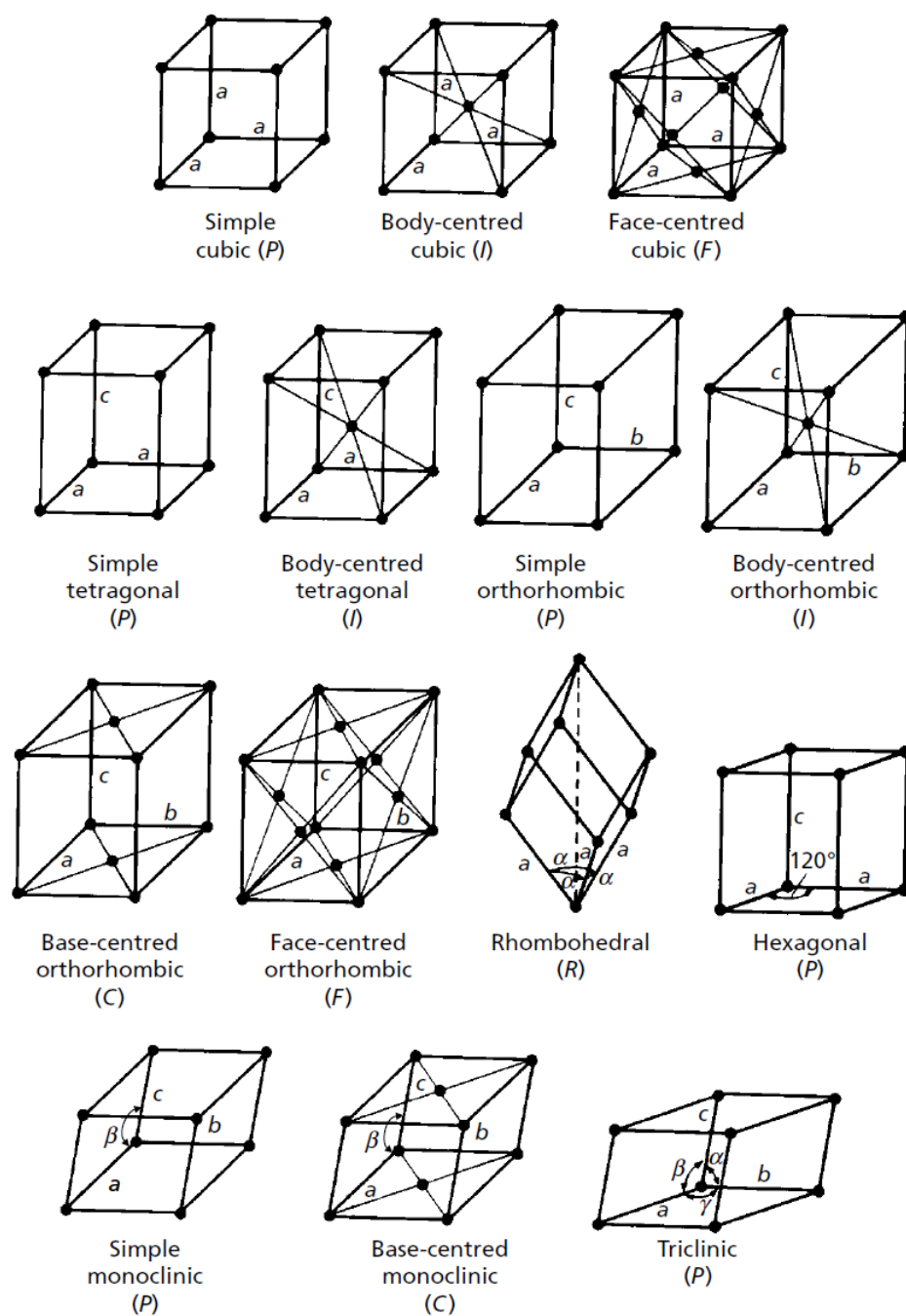


Figure 1.3. Bravais lattices (taken from C. Hammond, *The Basics of Crystallography and Diffraction*, 3rd ed. New York: Oxford University Press Inc., 2009 [85]).

Table 1.2. Seven crystal systems [85]

Crystal systems	Bravais lattices	Axial length and angles
Cubic	<i>PIF</i>	$a = b = c$ $\alpha = \beta = \gamma = 90^\circ$
Tetragonal	<i>PI</i>	$a = b \neq c$ $\alpha = \beta = \gamma = 90^\circ$
Orthorhombic	<i>PICF</i>	$a \neq b \neq c$ $\alpha = \beta = \gamma = 90^\circ$
Trigonal	<i>PR</i>	$a = b \neq c$ $\alpha = \beta = \gamma = 120^\circ$
Hexagonal	<i>P</i>	$a = b \neq c$ $\alpha = \beta = 120^\circ, \gamma = 90^\circ$
Monoclinic	<i>PC</i>	$a \neq b \neq c$ $\alpha = \gamma = 90^\circ \neq \beta$
Triclinic	<i>P</i>	$a \neq b \neq c$ $\alpha \neq \beta \neq \gamma$

A crystal is the product of nucleus growth initiated by nucleation. The nucleation stage allows the formation of a new phase of solid from a supersaturated solution, which is referred as the crystallization process [83].

There are two types of nucleation: primary and secondary nucleations. ‘Primary nucleation’ takes place in a homogeneous solution with or without other distinctive particles, such as dust. If the nucleation happens in a solution containing distinctive particles, it is defined as *heterogeneous nucleation*. Meanwhile, it is termed as *homogeneous nucleation* if no other particle presents in the solution. When a small amount of uniform crystal seeds are added into the supersaturated solution, by which the nucleation process is launched, the process is labelled as the ‘secondary nucleation’ [83], [84].

After the nucleus formation, it grows in size by the incorporation of atoms, molecules or growth units in a process called ‘crystal growth’. Transporting atoms or

molecules in the solution towards the nucleus surface, or named *transport process*, is the first step that instigates the crystal growth. The next step of the crystal growth is the *surface process*, which can be divided into three actions: atoms-surface contact, atoms motion on a crystal surface, attachment of the atoms to edges and kinks. The slowest of both processes determines the crystal growth [84].

A famous prototype proposed by Kossel [84] (see Figure 1.4) describes the crystal surface structure very well. This model makes it easy to understand the crystal growth mechanism. The model illustrates areas on the crystal surface called *terraces*, which is bordered by *steps*. Incoming growth unit incorporated into this step forms two bonds, one with the terrace beneath and one with the step. This bonding is stronger than the bond formed if the growth unit comes into contact only with the terrace. Due to the incorporation of growth unit into the step, a *kink* is created. The kink provides three sides to establish bonding with the incoming growth units. Thus, energetically, it is more likely that the crystal growth is carried on the kinks than any other sites.

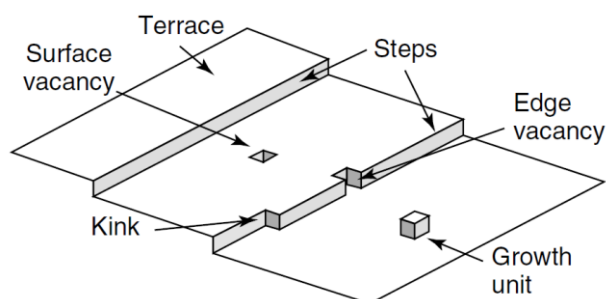


Figure 1.4. Crystal surface structure model by Kossel [84].

There are different kinds of crystal growth mechanism. The first and simplest one is *layer growth*. This type of mechanism usually becomes the path of crystal growth in a high supersaturation solution. Incoming growth unit is attached to a kink site, as illustrated in Figure 1.5 (a), making the kink moves along the step until the edge of it. Owing to this process, the terrace area expands. When the kink reaches the edge of a surface area, the growth unit is then attached to the step to build a new kink site, and so the process continues until the whole terrace is grown (see Figure 1.5 (b)). As

the whole terrace has grown, the incoming unit is bound on the surface to start new nucleation, and thus a new terrace is formed (see Figure 1.5 (c)). Because of its way of growing, layer growth mechanism is also called *single nucleation growth*.

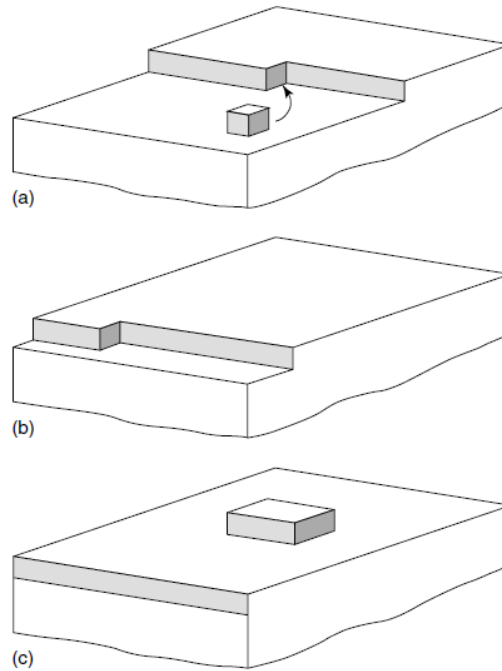


Figure 1.5. Illustration of layer growth mechanism [84].

However, another type of growth mechanism termed as *multinucleation multilayer growth* or *birth and spread* arises whenever the nucleation rate exceeds the speed for covering the crystal face. The excessive nuclei are spread on the surface and also located on other nuclei to form many layers.

The next type of crystal growth mechanism is *spiral growth*, which occurs in a low supersaturation solution and in the presence of dislocations in the crystal surface (see Figure 1.6 (a)). The dislocations are more favourable for growth units to be bounded. Compared to a smooth terrace surface, the presence of dislocations on the crystal surface provides lower energy for those growth units to be attached on. For this reason, the spiral growth mechanism seems to be mostly adapted by nanoporous materials having a very complex growth unit stacking owing to their internal porosity. The growth unit is incorporated in this dislocation to shape a second step

with a dimension equals to $2r_{2D}^*$, where r_{2D}^* is a critical radius of the two-dimensional nucleus (see Figure 1.6 (b)). Then, the third step, fourth step, and so on will be formed orderly producing a spiral (see Figure 1.6 (d)).

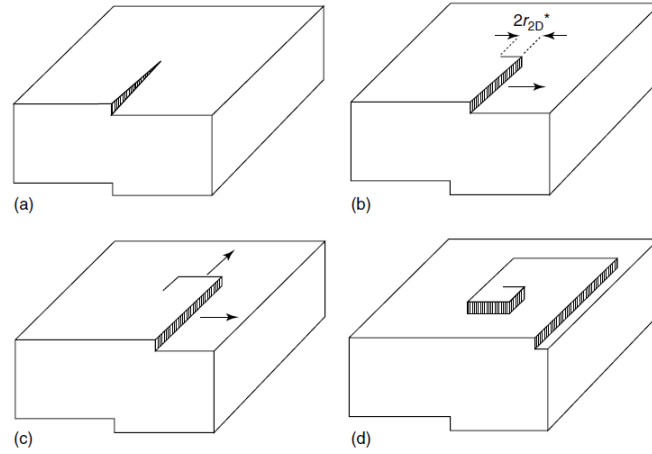


Figure 1.6. A diagram showing the spiral growth mechanism [84].

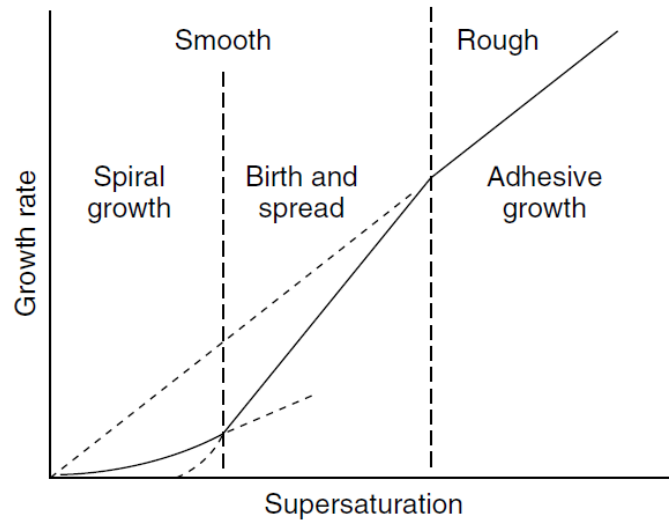


Figure 1.7. Supersaturation and growth mechanism relationship [84].

To understand the driving force of the chosen growth mechanism, Figure 1.7 reveals the relationship between the mechanism and the supersaturation of the mother solution. The spiral growth favours happening in a low supersaturation when the

surface of the crystal is smooth. Higher supersaturation provides a good condition for the birth and spread growth mechanism to take place, of which reason is explained previously. However, as the supersaturation is enhanced, steep rate of birth and spread method makes the crystal surface rough, which causes the *adhesive* type of crystal growth mechanism to come about. Here, in adhesive growth, the growth units can be attached in any locations and direction, leading to the formation of spheres, fractals, or dendritic shapes [84].

1.3. Crystal Simulation

Research development in order to study the habit and character of crystals is growing rapidly owing to the invention of modern microscopes to scan the crystal surface with good resolution. The Atomic Force Microscope (AFM) allows tracing the surface texture with its cantilever's tip. Since then, a large number of experiments on crystal growth and dissolution mechanism, particularly those of nanoporous materials, observed with AFM has been reported [86]–[92]. Based on these data, Anderson *et al.* (2017) [93] formulated a generic algorithm that works to explain the crystal growth parameters for all crystal systems in the *CrystalGrower* program.

In *CrystalGrower*, the units of growth are seen as natural tilings as described in the literature [94]. Atoms in natural tiles are tetrahedrally coordinated as Q^3 or Q^2 if they are connected to three or two other atoms, respectively. A tile having all Q^3 tetrahedrally coordinated atoms, thus forms a closed cage, is a low energy structure to build a crystal. Meanwhile, a tile possesses both Q^3 and Q^2 tetrahedrally coordinated atoms (which constructs an open cage) has higher stabilization energy. Natural tiles will try to have as many Q^3 and as little Q^2 as possible. However, only a few of the zeolite frameworks are built only in closed cages. Most of them have both open and closed cages.

Figure 1.8 illustrates the energy ladder for zeolite A model, which has three types of cages, namely double 4-rings (D4R), β cage and α cage. The three closed cages are all constructed from Q^3 atoms. The top ladders indicate the energy levels of the cage frameworks when all T-sites are Q^3 . D4R has eight Q^3 vertices (T-sites), when each of which connected to another T-site on a crystal surface forming a Q^4 , the

destabilization energy (ΔU_s) of the configuration will decrease one level. Therefore, D4R has 8 energy levels plus one level (zero level) when the cage is in bulk crystal. For the same reason, β cage and α cage have 25 and 49 energy levels, respectively. In another case, the energy level of a cage in a surface configuration also declines one level if Q^2 becomes Q^3 . The driving force to allow the crystal growth or dissolution proceeds is the solution's supersaturation ($\Delta\mu$) [95].

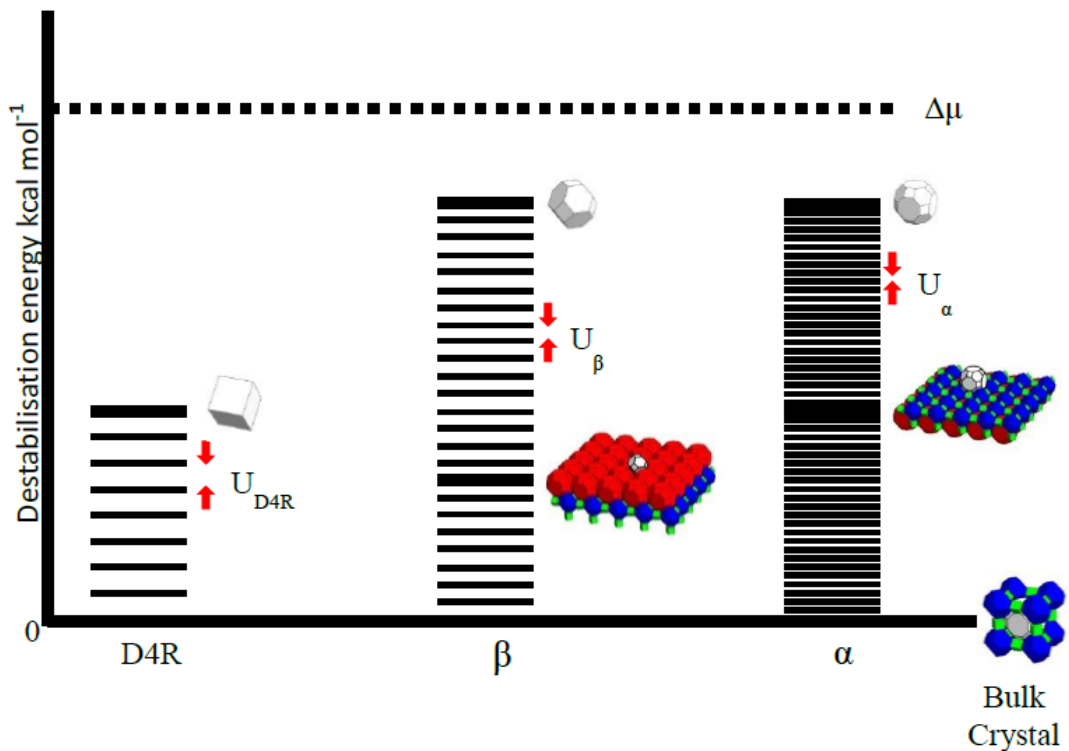


Figure 1.8. Energy ladder for each cage type in zeolite A model. The thick ladder represents the energy level for the cage type in different surface configurations [95].

At first, the *CrystalGrower* program seeds the crystal to grow to a particular extent at high supersaturation (decided by the user), after which the supersaturation drops to mimic the growing solution. The units of growth may be attached or dissolved on the crystal surface. Its probability to grow or dissolve is ruled by Boerrigter *et al.* (2004) [96] in Equation 1.1. The program's user can set the values of the solution's supersaturation ($\Delta\mu$) and ΔU_s of each tile in the system to control the growth.

Equation 1.1

$$P_s^{\text{growth}} = \exp \left[-0.5 \left(\frac{\Delta U_s}{kT} \right) + 0.5 \left(\frac{\Delta \mu}{kT} \right) \right]$$
$$P_s^{\text{dissolution}} = \exp \left[0.5 \left(\frac{\Delta U_s}{kT} \right) - 0.5 \left(\frac{\Delta \mu}{kT} \right) \right]$$

The crystal simulation resulted from the *CrystalGrower* was claimed to agree with the experimental observation [93]. A number of nanoporous crystal systems, namely LTA, FAU, UOV, NES, MFI, ETS-10, CHA, AEI, HKUST-1 and MOF-5, were reported to be simulated well with this approach. Other than those crystalline nanoporous materials, the *CrystalGrower* also resulted in a simulated crystal of L-cystine, which matches very well with the lab result. Crystal defects could also be accommodated in the program, although so far only screw dislocation is added to it. Despite the success and the easiness in predicting the crystal habit and surface structure, much deliberation of the crystal's system under study is needed before running the program.

1.4. Aims of the study

As it is explained in the previous sections, nanoporous materials are in the vanguard of being utilized in many sectors. This fascinating phenomenon is due to the material's properties of which one of the most important is its molecular-sized pores. The pore can accommodate certain desired molecules, organic species particularly, and discriminate other molecules bigger than the size of the pore.

Large scale of nanoporous materials production is required to supply the high demand with specific natures that this material must possess. However, there are still difficulties in synthesizing these materials caused by the covered nanoscopic details during their crystal growth. This often leads to the formation of unwanted phases or crystalline defect, which is troublesome especially if the high degree of perfection is needed, *e.g.* materials for drug transport. For that reason, understanding the nanoscopic information on crystal growth during its real-time hydrothermal

synthesis is very crucial since once it is revealed, controlling the growth becomes facile.

To achieve such nanoscopic details, a very powerful tool is needed. This requirement is well provided by the Atomic Force Microscopy (AFM), which can readily access Ångstrom vertical resolution. This makes the AFM better to be used for this purpose than other microscopy instruments, such as Scanning Electron Microscopy (SEM), Field Emission Scanning Electron Microscopy (FE-SEM), High-Resolution Scanning Electron Microscopy (HR-SEM) and Scanning Tunnelling Microscopy (STM) [84]. Satisfying work using AFM to explore the crystal surface topography, as well as to study the growth of some materials, for examples silicon [97], zeolite L [98], STA-7 and zeolite A [99], have been reported. Other than that, the AFM also offers the advantage to scan the crystal in solution, which is the key for real-time *in situ* crystal growth and dissolution observation. In situ AFM experiments have been done successfully to observe the growth of sodium oxalate [100] and the dissolution of barite [101], zeolite A [88], HKUST-1 [102].

Recently, Lorgouilloux *et al.* (2014) published the discovery of a novel nanoporous material, named IM-17, synthesized using decamethonium dications as the structure directing agent [103]. Fascinatingly, this new zeolitic material has a large unit cell sized $12.71 \times 21.99 \times 38.76$ Å. Other than that, the UOV structured crystal framework is also comprised of the largest number of tiles to build it, 16 tiles. The curiosity on how such large unit cell and complex structure grows becomes the fundamental aim of this research. This is important because the knowledge that we have so far in inorganic nanoporous crystal growth is limited to those having relatively small unit cell, *i.e.* SOD framework crystal with less than 10 Å of its unit cell length [91], zeolite L [90] and STA-7 [89], which both have less than 20 Å unit cell length.

Other inorganic nanoporous frameworks with large unit cells and complex structures that are studied here are the DAF-1, zeolite Rho and NU-87. The DAF-1 crystal (DFO framework) is a magnesium phosphate which has 43.386 Å long hexagonal unit cell [104], [105]. Both IM-17 and DAF-1 crystals are synthesized using decamethonium dications, which have a long carbon chain between trimethylammonium cations, as the structure directing agent. Another zeolite

successfully prepared with decamethonium dications as the SDA is NU-87 crystal with NES structure framework [106]. Although having a smaller unit cell, the NES tiling is constructed by a very large t-nes tile. Thus, a study on its growth will also add important knowledge into the crystal growth understanding.

Meanwhile, the background of zeolite Rho as one of the crystals to study in this project is because of the interesting PAU and MWF framework structures, which are Rho-family members [107]. PAU and MWF's large cubic unit cells have around 35 Å and 45 Å side lengths, respectively. However, owing to their very small and roundish crystal size and shape, the AFM does not give clear surface images of both synthesized crystals. Therefore, the investigation is performed on zeolite Rho crystal, which provides a flat surface area for the AFM tip to easily scan. The zeolite Rho having RHO framework is the simplest structure among the Rho-family zeolites.

Table 1.3 summarises the four nanoporous materials aimed to study in this project, which are IM-17, DAF-1, zeolite Rho and NU-87. It also gives reasons of the material's selection. IM-17 and DAF-1 are two materials with complex structures and large unit cells, which both are synthesized using the same structure directing agent. Although NU-87's unit cell is not as large as IM-17 and DAF-1, the material, which uses the same SDA as the former two in its synthesis, has interesting very large t-nes tile building its tiling. Zeolite Rho, on the other hand, is a zeolite with small unit cell and synthesized with different SDA as the other three materials mentioned above. However, its structure framework is the simplification of the other Rho-family zeolites (PAU and MWF) which have very large unit cell, 35.09 Å and 45.07 Å, respectively. It means that studying the growth of the zeolite Rho will also give insight into the growth of the large unit cell PAU and MWF.

The four nanoporous materials mentioned above, which are IM-17, DAF-1, zeolite Rho and NU-87, are all synthesized at high temperature, which is beyond the working temperature limit of the AFM. This makes us unable to perform in-situ AFM observation on their crystal growth. Nevertheless, it is believed that the dissolution of crystals may be related to their growth as they may be reverse processes. For that reason, instead of working on their growth, this project focuses on investigating the dissolution of the IM-17, DAF-1, zeolite Rho and NU-87 crystals using the AFM, which can be done in ambient temperature. The

experimental results are then compared with model crystals and their dissolutions simulated using the *CrystalGrower* program.

Table 1.3 Comparisons of the materials used in this project and why they are selected in this study

	IM-17	DAF-1	Zeolite Rho	NU-87
Type of material	Germano-silicate	Mg-containing alumino-phosphate	Alumino-silicate	Alumino-silicate
Unit cell	orthorhombic	hexagonal	cubic	monoclinic
Unit cell's size (Å)	$12.68 \times 22.22 \times 39.06$	$22.35 \times 22.35 \times 43.39$	$15.03 \times 15.03 \times 15.03$	$14.32 \times 22.38 \times 25.09$
Number of tiles constructing the tiling	16	11	2	4, including one very large t-nes tile
Crystal size (µm)	1 – 2	7 – 70	~ 2	2 – 3 (crystal's length)
SDA used in synthesis	Decamethonium dications	Decamethonium dications	18-crown-6 ether	Decamethonium dications
Rationale of the selection in this project	Large unit cell, having complex structure	Large unit cell, having complex structure	Member of Rho-family zeolites with effective surface to scan with AFM tip. Other Rho-family members with large unit cells up to 45 Å (PAU and MWF) have very small and roundish crystal surface, thus they give unclear AFM images to study.	Complex structure, the tiling is constructed by large t-nes tile

To reach the aim of the study explained above, several objectives are set as follows: to synthesize four materials (IM-17, DAF-1, zeolite Rho and NU-87); to characterize the four materials using PXRD, SEM and ex-situ AFM; to study the dissolution of the materials in different solutions using AFM; to simulate the growth/dissolution of

the four materials using *CrystalGrower* program and compare the results with the laboratory data obtained.

1.5. References

- [1] F. Mondragon, F. Rincon, L. Sierra, J. Escobar, J. Ramirez, and J. Fernandez, "New perspectives for coal ash utilization: synthesis of zeolitic materials," *Fuel*, vol. 69, no. 2, pp. 263–266, 1990.
- [2] K. S. Hui and C. Y. H. Chao, "Pure, single phase, high crystalline, chamfered-edge zeolite 4A synthesized from coal fly ash for use as a builder in detergents," *J. Hazard. Mater. B*, vol. 137, no. 1, pp. 401–409, 2006.
- [3] K. S. Hui, K. N. Hui, and S. K. Lee, "A Novel and Green Approach to Produce Nanoporous Materials Zeolite A and MCM-41 from Coal Fly Ash and their Applications in Environmental Protection," *World Acad. Sci. Eng. Technol.*, vol. 3, no. 5, pp. 162–172, 2009.
- [4] S. Roy, K. Bakhmutsky, E. Mahmoud, R. F. Lobo, and R. J. Gorte, "Probing Lewis Acid Sites in Sn-Beta Zeolite," *ACS Catal.*, vol. 3, no. 4, p. 573–580, 2013.
- [5] W.-H. Shih and H.-L. Chang, "Conversion of fly ash into zeolites for ion-exchange applications," *Mater. Lett.*, vol. 28, no. 4–6, pp. 263–268, 1996.
- [6] K. S. Hui, C. Y. H. Chao, and S. C. Kot, "Removal of mixed heavy metal ions in wastewater by zeolite 4A and residual products from recycled coal fly ash," *J. Hazard. Mater. B*, vol. 127, no. 1–3, pp. 89–101, 2005.
- [7] R. Juan, S. Hernandez, J. M. Andres, and C. Ruiz, "Synthesis of granular zeolitic materials with high cation exchange capacity from agglomerated coal fly ash," *Fuel*, vol. 86, no. 12–13, pp. 1811–1821, 2007.
- [8] K. S. N. Reddy, B. S. Rao, and V. P. Shiralkar, "Alkylation of benzene with isopropanol over zeolite beta," *Appl. Catal. A Gen.*, vol. 95, no. 1, pp. 53–63, 1993.
- [9] Y. Li and J. N. Armor, "Ammoxidation of Ethane to Acetonitrile over Metal-Zeolite Catalysts," *J. Catal.*, vol. 173, no. 2, pp. 511–518, 1998.
- [10] S.-H. Park and H.-K. Rhee, "Catalytic properties of zeolites MCM-22 and NU-87 in disproportionation of toluene," *React. Kinet. Catal. Lett.*, vol. 78, no. 1, pp. 81–89, 2003.
- [11] R. Glaser, S. Gomm, and J. Weitkamp, "In situ investigation of cumene synthesis over dealuminated zeolite catalysts by means of a tapered element oscillating microbalance," *Stud. Surf. Sci. Catal.*, vol. 154, pp. 2125–2132, 2004.
- [12] S. Mitchell, N.-L. Michels, K. Kunze, and J. Pérez-Ramírez, "Visualization of hierarchically structured zeolite bodies from macro to nano length scales," *Nat. Chem.*, vol. 4, no. 10, pp. 825–831, 2012.
- [13] Q. Yu, X. Meng, J. Liu, C. Li, and Q. Cui, "A fast organic template-free, ZSM-11 seed-assisted synthesis of ZSM-5 with good performance in methanol-to-olefin," *Microporous Mesoporous Mater.*, vol. 181, pp. 192–200, 2013.
- [14] B. Chen, Z. Yang, Y. Zhu, and Y. Xia, "Zeolitic imidazolate framework materials: recent progress in synthesis and applications," *J. Mater. Chem. A*, vol. 2, no. 40, pp. 16811–16831, 2014.

- [15] J. L. Flowers, S. A. Lonky, and E. J. Deitsch, "Clinical evidence supporting the use of an activated clinoptilolite suspension as an agent to increase urinary excretion of toxic heavy metals," *Nutr. Diet. Suppl.*, vol. 1, pp. 11–18, 2009.
- [16] A. Corma, V. González-Alfaro, and A. V. Orchillés, "The role of pore topology on the behaviour of FCC zeolite additives," *Appl. Catal. A Gen.*, vol. 187, no. 2, pp. 245–254, 1999.
- [17] A. Primo and H. Garcia, "Zeolites as catalysts in oil refining," *Chem. Soc. Rev.*, vol. 43, no. 22, pp. 7548–7561, 2014.
- [18] X. Chen, K. F. Lam, Q. Zhang, B. Pan, M. Arruebo, and K. L. Yeung, "Synthesis of Highly Selective Magnetic Mesoporous Adsorbent," *J. Phys. Chem. C*, vol. 113, no. 22, pp. 9804–9813, 2009.
- [19] I. Bikit *et al.*, "Radon adsorption by zeolite," *Radiat. Meas.*, vol. 72, pp. 70–74, 2015.
- [20] J. Patarin, O. Spalla, and F. Di Renzo, "Inverse Systems – Nanoporous Solids," in *Nanomaterials and Nanochemistry*, C. Brechignac, P. Houdy, and M. Lahmani, Eds. Berlin: Springer-Verlag, 2007, pp. 305–314.
- [21] K. S. W. Sing *et al.*, "Reporting Physisorption Data for Gas/Solid Systems with Special Reference to the Determination of Surface Area and Porosity," *Pure Appl. Chem.*, vol. 57, no. 4, pp. 603–619, 1985.
- [22] A. F. Cronstedt, J. L. Schlenker, and G. H. Kühl, "Observations and Descriptions: On an Unknown Mineral-Species Called Zeolites," in *Proceedings from the Ninth International Zeolite Conference*, 1993, pp. 3–9.
- [23] Y. Nozue, Y. Amako, R. Kawano, T. Mizukane, and T. Nakano, "Insulating state and metallic phase transition of heavily sodium-doped low-silica X (LSX) zeolites," *J. Phys. Chem. Solids*, vol. 73, no. 12, pp. 1538–1541, 2012.
- [24] A. Dyer, *An Introduction to Zeolite Molecular Sieves*. Avon: John Wiley & Sons Ltd., 1988.
- [25] J. L. C. Rowsell and O. M. Yaghi, "Metal-organic frameworks: A new class of porous materials," *Microporous Mesoporous Mater.*, vol. 73, no. 1–2, pp. 3–14, 2004.
- [26] "Database of Zeolite Structures." [Online]. Available: <http://www.iza-structure.org/databases/>. [Accessed: 17-Nov-2017].
- [27] X. Yang and R. E. Truitt, "129Xe NMR investigation of ETS-10 titanasilicate molecular sieves," *J. Phys. Chem.*, vol. 100, no. 9, pp. 3713–3718, 1996.
- [28] Z. Alikhan, G. S. V. Raghavan, and A. S. Mujumdar, "Adsorption drying of corn in zeolite granules using a rotary drum," *Dry. Technol.*, vol. 10, no. 3, pp. 783–797, 1992.
- [29] C. Pahl, C. Pasel, M. Luckas, and D. Bathen, "Adsorptive water removal from primary alcohols and acetic acid esters in the ppm-region," *J. Chem. Eng. Data*, vol. 57, no. 9, pp. 2465–2471, 2012.
- [30] W. Wang, L. Wu, Z. Li, Y. Fang, J. Ding, and J. Xiao, "An Overview of Adsorbents in the Rotary Desiccant Dehumidifier for Air Dehumidification," *Dry. Technol.*, vol. 31, no. 12, pp. 1334–1345, 2013.
- [31] S. Araki, Y. Kiyohara, S. Tanaka, and Y. Miyake, "Adsorption of carbon dioxide and nitrogen on zeolite rho prepared by hydrothermal synthesis using 18-crown-6 ether," *J. Colloid Interface Sci.*, vol. 388, no. 1, pp. 185–190, 2012.

- [32] S. Choi, J. H. Drese, and C. W. Jones, "Adsorbent materials for carbon dioxide capture from large anthropogenic point sources," *ChemSusChem*, vol. 2, no. 9, pp. 796–854, 2009.
- [33] D. Ko, R. Siriwardane, and L. T. Biegler, "Optimization of a Pressure-Swing Adsorption Process Using Zeolite 13X for CO₂ Sequestration," *Ind. Eng. Chem. Res.*, vol. 42, no. 2, pp. 339–348, 2003.
- [34] D. P. Bezerra, R. S. Oliveira, R. S. Vieira, C. L. Cavalcante Jr., and D. C. S. Azevedo, "Adsorption of CO₂ on nitrogen-enriched activated carbon and zeolite 13X," *Adsorption*, vol. 17, no. 1, pp. 235–246, 2011.
- [35] S. S. A. Talesh, S. Fatemi, M. Davoodpour, and S. J. Hashemi, "Preparation of core-shell SAPO-34 adsorbent on ceramic particles; Improvement of CO₂ separation from natural gas," *Sep. Sci. Technol.*, vol. 46, no. 7, pp. 1138–1143, 2011.
- [36] A. Zukal, J. Mayerová, and M. Kubů, "Adsorption of carbon dioxide on high-silica zeolites with different framework topology," *Top. Catal.*, vol. 53, no. 19–20, pp. 1361–1366, 2010.
- [37] X.-X. Zhao, X.-L. Xu, L.-B. Sun, L.-L. Zhang, and X.-Q. Liu, "Adsorption behavior of carbon dioxide and methane on AlPO₄-14: A neutral molecular sieve," *Energy and Fuels*, vol. 23, no. 3, pp. 1534–1538, 2009.
- [38] H.-K. Min, S. H. Cha, and S. B. Hong, "Mechanistic insights into the zeolite-catalyzed isomerization and disproportionation of m-xylene," *ACS Catal.*, vol. 2, no. 6, pp. 971–981, 2012.
- [39] R. Glaser, R. Li, M. Hunger, S. Ernst, and J. Weitkamp, "Zeolite HNU-87: synthesis, characterization and catalytic properties in the shape-selective conversion of methyl naphthalenes," *Catal. Letters*, vol. 50, no. 3–4, pp. 141–148, 1998.
- [40] C. Yang *et al.*, "Organotemplate-free and seed-directed synthesis of ZSM-34 zeolite with good performance in methanol-to-olefins," *J. Mater. Chem.*, vol. 22, no. 24, pp. 12238–12245, 2012.
- [41] Y. Bhawe, M. Moliner-Marin, J. D. Lunn, Y. Liu, A. Malek, and M. Davis, "Effect of cage size on the selective conversion of methanol to light olefins," *ACS Catal.*, vol. 2, no. 12, pp. 2490–2495, 2012.
- [42] L. Wu, V. Degirmenci, P. C. M. M. Magusin, B. M. Szyja, and E. J. M. Hensen, "Dual template synthesis of a highly mesoporous SSZ-13 zeolite with improved stability in the methanol-to-olefins reaction," *Chem. Commun.*, vol. 48, no. 76, pp. 9492–9494, 2012.
- [43] J. H. Kwak, R. G. Tonkyn, D. H. Kim, J. Szanyi, and C. H. F. Peden, "Excellent activity and selectivity of Cu-SSZ-13 in the selective catalytic reduction of NO_x with NH₃," *J. Catal.*, vol. 275, no. 2, pp. 187–190, 2010.
- [44] A. Corma, L. T. Nemeth, M. Renz, and S. Valencia, "Sn-zeolite beta as a heterogeneous chemoselective catalyst for Baeyer-Villiger oxidations," *Nature*, vol. 412, no. 6845, pp. 423–425, 2001.
- [45] A. Corma, M. E. Domine, and S. Valencia, "Water-resistant solid Lewis acid catalysts: Meerwein-Ponndorf-Verley and Oppenauer reactions catalyzed by tin-beta zeolite," *J. Catal.*, vol. 215, no. 2, pp. 294–304, 2003.
- [46] M. Moliner, Y. Roman-Leshkov, and M. E. Davis, "Tin-containing zeolites are highly active catalysts for the isomerization of glucose in water," *Proc. Natl. Acad. Sci.*, vol. 107, no. 14, pp. 6164–6168, 2010.

- [47] M. S. Holm, Y. J. Pagán-Torres, S. Saravanamurugan, A. Riisager, J. A. Dumesic, and E. Taarning, "Sn-Beta catalysed conversion of hemicellulosic sugars," *Green Chem.*, vol. 14, pp. 702–706, 2012.
- [48] C. M. Osmundsen, M. S. Holm, S. Dahl, and E. Taarning, "Tin-containing silicates: Structure-activity relations," *Proc. R. Soc. A Math. Phys. Eng. Sci.*, vol. 468, no. 2143, pp. 2000–2016, 2012.
- [49] A. P. Singh, D. Bhattacharya, and S. Sharma, "Benzoylation of toluene with benzoyl chloride over zeolite catalysts," *J. Mol. Catal. A Chem.*, vol. 102, no. 3, pp. 139–145, 1995.
- [50] C. Martínez and A. Corma, "Inorganic molecular sieves: Preparation, modification and industrial application in catalytic processes," *Coord. Chem. Rev.*, vol. 255, no. 13–14, pp. 1558–1580, 2011.
- [51] T. Li *et al.*, "Synthesis of zeolite Y from natural aluminosilicate minerals for fluid catalytic cracking application," *Green Chem.*, vol. 14, no. 12, pp. 3255–3259, 2012.
- [52] D. Wu, Y. Sui, S. He, X. Wang, C. Li, and H. Kong, "Removal of trivalent chromium from aqueous solution by zeolite synthesized from coal fly ash," *J. Hazard. Mater.*, vol. 155, no. 3, pp. 415–423, 2008.
- [53] E. M. Flanigen, R. W. Broach, and S. T. Wilson, "Introduction," in *Zeolites in Industrial Separation and Catalysis*, S. Kulprathipanja, Ed. Weinheim: WILEY-VCH Verlag GmbH & Co. KGaA, 2010, pp. 1–26.
- [54] Y. Kamimura, K. Itabashi, and T. Okubo, "Seed-assisted, OSDA-free synthesis of MTW-type zeolite and 'Green MTW' from sodium aluminosilicate gel systems," *Microporous Mesoporous Mater.*, vol. 147, no. 1, pp. 149–156, 2012.
- [55] T. Poerio, T. F. Mastropietro, E. Drioli, and C. Algieri, "Organic-template-free synthesis of nanosized NaY crystals induced by a FAU membrane," *RSC Adv.*, vol. 3, no. 46, pp. 24038–24040, 2013.
- [56] L. Zhang, S. Liu, S. Xie, and L. Xu, "Organic template-free synthesis of ZSM-5/ZSM-11 co-crystalline zeolite," *Microporous Mesoporous Mater.*, vol. 147, no. 1, pp. 117–126, 2012.
- [57] M. L. D. Jayaranjan, E. D. van Hullebusch, and A. P. Annachhatre, "Reuse options for coal fired power plant bottom ash and fly ash," *Rev. Environ. Sci. Biotechnol.*, vol. 13, no. 4, pp. 467–486, 2014.
- [58] J.-W. Ahn, G.-C. Han, K.-S. You, N.-I. Um, and H.-C. Cho, "Zeolite Synthesis from Coal Bottom Ash for Recycling as an Absorbent of Heavy Metals," *Mater. Sci. Forum*, vol. 510–511, pp. 626–629, 2006.
- [59] Z. Jing, F. Jin, N. Yamasaki, and E. H. Ishida, "Hydrothermal synthesis of a novel tobermorite-based porous material from municipal incineration bottom ash," *Ind. Eng. Chem. Res.*, vol. 46, no. 8, pp. 2657–2660, 2007.
- [60] Y. W. Chiang, K. Ghyselbrecht, R. M. Santos, B. Meesschaert, and J. A. Martens, "Synthesis of zeolitic-type adsorbent material from municipal solid waste incinerator bottom ash and its application in heavy metal adsorption," *Catal. Today*, vol. 190, no. 1, pp. 23–30, 2012.
- [61] G. Chandrasekar, K.-S. You, J.-W. Ahn, and W.-S. Ahn, "Synthesis of hexagonal and cubic mesoporous silica using power plant bottom ash," *Microporous Mesoporous Mater.*, vol. 111, no. 1–3, pp. 455–462, 2008.
- [62] K. P. Dey, S. Ghosh, and M. K. Naskar, "Organic template-free synthesis of ZSM-5 zeolite particles using rice husk ash as silica source," *Ceram. Int.*, vol. 39, no. 2, pp. 2153–2157, 2013.

- [63] M. K. Naskar, D. Kundu, and M. Chatterjee, "Coral-like hydroxy sodalite particles from rice husk ash as silica source," *Mater. Lett.*, vol. 65, no. 23–24, pp. 3408–3410, 2011.
- [64] M. K. Naskar, D. Kundu, and M. Chatterjee, "A facile hydrothermal conversion of rice husk ash to ZSM-5 zeolite powders," *J. Am. Ceram. Soc.*, vol. 95, no. 3, pp. 925–930, 2012.
- [65] S. Chandrasekhar, K. G. Satyanarayana, P. N. Pramada, P. Raghavan, and T. N. Gupta, "Processing, properties and applications of reactive silica from rice husk - An overview," *J. Mater. Sci.*, vol. 38, no. 15, pp. 3159–3168, 2003.
- [66] E. B. G. Johnson and S. E. Arshad, "Hydrothermally synthesized zeolites based on kaolinite: A review," *Appl. Clay Sci.*, vol. 97–98, pp. 215–221, 2014.
- [67] P. Bosch, L. Ortiz, and I. Schiffter, "Synthesis of Faujasite Type Zeolites from Calcined Kaolins," *Ind. Eng. Chem. Prod. Res. Dev.*, vol. 22, no. 3, pp. 401–406, 1983.
- [68] E. Costa, A. de Lucas, M. A. Uguina, and J. C. Ruiz, "Synthesis of 4A Zeolite from Calcined Kaolins for Use in Detergents," *Ind. Eng. Chem. Res.*, vol. 27, no. 7, pp. 1291–1296, 1988.
- [69] A. Madani, A. Aznar, J. Sanz, and J. M. Serratosa, "Silicon-29 and aluminum-27 NMR study of zeolite formation from alkali-leached kaolinites: influence of thermal preactivation," *J. Phys. Chem.*, vol. 94, no. 2, pp. 760–765, 1990.
- [70] S. Chandrasekhar and P. N. Pramada, "Sintering behaviour of calcium exchanged low silica zeolites synthesized from kaolin," *Ceram. Int.*, vol. 27, no. 1, pp. 105–114, 2001.
- [71] L. V. C. Rees and S. Chandrasekhar, "Hydrothermal reaction of kaolinite in presence of fluoride ions at pH < 10," *Zeolites*, vol. 13, no. 7, pp. 534–541, 1993.
- [72] A. de Lucas, M. A. Uguina, I. Covián, and L. Rodríguez, "Use of Spanish Natural Clays as Additional Silica Sources To Synthesize 13X Zeolite from Kaolin," *Ind. Eng. Chem. Res.*, vol. 32, no. 8, pp. 1645–1650, 1993.
- [73] S. Chandrasekhar and P. N. Pramada, "Investigation on the synthesis of zeolite NaX from Kerala kaolin," *J. Porous Mater.*, vol. 6, no. 4, pp. 283–297, 1999.
- [74] E. I. Basaldella, R. Bonetto, and J. C. Tara, "Synthesis of NaY Zeolite on Preformed Kaolinite Spheres. Evolution of Zeolite Content and Textural Properties with the Reaction Time," *Ind. Eng. Chem. Res.*, vol. 32, no. 4, pp. 751–752, 1993.
- [75] E. A. Hildebrando, C. G. B. Andrade, C. A. F. da Rocha Junior, R. S. Angélica, F. R. Valenzuela-Diaz, and R. de F. Neves, "Synthesis and characterization of zeolite NaP using kaolin waste as a source of silicon and aluminum," *Mater. Res.*, vol. 17, no. 1, pp. 174–179, 2014.
- [76] Z. Zhang, B. Qin, X. Zhang, F. Ling, W. Sun, and X. Fang, "The seeds effect on zeolite NU-87: Synthesis parameters and structural properties," *J. Porous Mater.*, vol. 20, no. 3, pp. 515–521, Jun. 2013.
- [77] G. T. Kokotailo, P. Chu, S. L. Lawton, and W. M. Meier, "Synthesis and structure of synthetic zeolite ZSM-11," *Nature*, vol. 275, pp. 119–120, 1978.
- [78] M. E. Davis and R. F. Lobo, "Zeolite and Molecular Sieve Synthesis," *Chem. Mater.*, vol. 4, no. 4, pp. 756–768, 1992.
- [79] P. K. Dutta and J. Bronic, "Mechanism of zeolite formation: Seed-gel interaction," *Zeolites*, vol. 14, no. 4, pp. 250–255, 1994.

- [80] J. Kumar, R. Jha, and B. K. Modhera, "Applications of Zeolite with Additives in Petroleum Refinery," *Int. J. Chem. Chem. Eng.*, vol. 3, no. 2, pp. 75–80, 2013.
- [81] J. L. LaRosa, S. Kwan, and M. W. Grutzeck, "Zeolite Formation in Class F Fly Ash Blended Cement Pastes," *J. Am. Ceram. Soc.*, vol. 75, no. 6, pp. 1574–1580, 1992.
- [82] Z. Zhang, X. Zhang, and B. Qin, "A NU-85 molecular sieve having a large pore volume and processes for preparing the same," EP 2 441 733 A1, 2012.
- [83] R. Davey and J. Garside, *From Molecules to Crystallizers: An Introduction to Crystallization*. New York: Oxford University Press Inc., 2000.
- [84] P. Cubillas and M. W. Anderson, "Synthesis Mechanism: Crystal Growth and Nucleation," in *Zeolites and Catalysis, Synthesis, Reactions and Applications*, Vol. 1., Weinheim, Germany: Wiley-VCH Verlag GmbH & Co. KGaA, 2010.
- [85] C. Hammond, *The Basics of Crystallography and Diffraction*, 3rd ed. New York: Oxford University Press Inc., 2009.
- [86] J. R. Agger, N. Hanif, and M. W. Anderson, "Fundamental zeolite crystal growth rates from simulation of atomic force micrographs," *Angew. Chemie - Int. Ed.*, vol. 40, no. 21, pp. 4065–4067, 2001.
- [87] J. R. Agger *et al.*, "Silicalite crystal growth investigated by atomic force microscopy," *J. Am. Chem. Soc.*, vol. 125, no. 3, pp. 830–839, 2003.
- [88] L. I. Meza, M. W. Anderson, B. Slater, and J. R. Agger, "In situ atomic force microscopy of zeolite A dissolution," *Phys. Chem. Chem. Phys.*, vol. 10, pp. 5066–5076, 2008.
- [89] P. Cubillas *et al.*, "Spiral Growth on Nanoporous Silicoaluminophosphate STA-7 as Observed by Atomic Force Microscopy," *Cryst. Growth Des.*, vol. 9, no. 9, pp. 4041–4050, 2009.
- [90] R. Brent *et al.*, "Unstitching the Nanoscopic Mystery of Zeolite Crystal Formation," *J. Am. Chem. Soc.*, vol. 132, no. 9, pp. 13858–13868, 2010.
- [91] M. A. Holden, P. Cubillas, M. P. Attfield, J. T. Gebbie, and M. W. Anderson, "Growth Mechanism of Microporous Zincophosphate Sodalite Revealed by In Situ Atomic Force Microscopy," *J. Am. Chem. Soc.*, vol. 134, no. 31, pp. 13066–13073, 2012.
- [92] R. Wagia, I. Strashnov, M. W. Anderson, and M. P. Attfield, "Determination of the Preassembled Nucleating Units That Are Critical for the Crystal Growth of the Metal–Organic Framework CdIF-4," *Angew. Chemie - Int. Ed.*, vol. 128, no. 31, pp. 9221–9225, 2016.
- [93] M. W. Anderson *et al.*, "Predicting crystal growth via a unified kinetic three-dimensional partition model," *Nature*, vol. 544, no. 7651, pp. 456–459, 2017.
- [94] V. A. Blatov, O. Delgado-Friedrichs, M. O’Keeffe, and D. M. Proserpio, "Three-periodic nets and tilings: natural tilings for nets," *Acta Crystallogr. A*, vol. 63, pp. 418–425, 2007.
- [95] J. T. Gebbie, "A theoretical study of crystal growth in nanoporous materials using the Monte Carlo method," The University of Manchester, 2014.
- [96] S. X. M. Boerrigter *et al.*, "MONTY: Monte Carlo Crystal Growth on Any Crystal Structure in Any Crystallographic Orientation; Application to Fats," *J. Phys. Chem. A*, vol. 108, pp. 5894–5902, 2004.
- [97] F. J. Giessibl, S. Hembacher, H. Bielefeldt, and J. Mannhart, "Subatomic Features on the Silicon (111)-(7*7) Surface Observed by Atomic Force Microscopy," *Science* (80-.), vol. 289, no. 5478, pp. 422–426, 2000.

- [98] R. Brent and M. W. Anderson, "Fundamental crystal growth mechanism in zeolite L revealed by atomic force microscopy," *Angew. Chemie - Int. Ed.*, vol. 47, no. 29, pp. 5327–5330, 2008.
- [99] S. M. Stevens *et al.*, "Nanometre resolution using high-resolution scanning electron microscopy corroborated by atomic force microscopy," *Chem. Commun.*, vol. 0, no. 33, pp. 3894–3896, 2008.
- [100] W. Fu, J. Vaughan, and A. Gillespie, "In situ AFM investigation of heterogeneous nucleation and growth of sodium oxalate on industrial gibbsite surfaces in concentrated alkaline solution," *Chem. Eng. Sci.*, vol. 126, pp. 399–405, 2015.
- [101] Y. Kuwahara and M. Makio, "In situ AFM study on barite (001) surface dissolution in NaCl solutions at 30 °C," *Appl. Geochemistry*, vol. 51, pp. 246–254, 2014.
- [102] N. S. John, C. Scherb, M. Shoaee, M. W. Anderson, M. P. Attfield, and T. Bein, "Single layer growth of sub-micron metal–organic framework crystals observed by in situ atomic force microscopy," *Chem. Commun.*, vol. 0, no. 41, pp. 6294–6296, 2009.
- [103] Y. Lorgouilloux *et al.*, "IM-17: a new zeolitic material, synthesis and structure elucidation from electron diffraction ADT data and Rietveld analysis," *RSC Adv.*, vol. 4, no. 37, pp. 19440–19449, 2014.
- [104] P. A. Wright *et al.*, "Synthesis and structure of a novel large-pore microporous magnesium-containing aluminophosphate (DAF-1)," *J. Chem. Soc. Chem. Commun.*, vol. 104, no. 7, pp. 633–635, 1993.
- [105] P. A. Wright *et al.*, "Synthesis, characterisation and catalytic performance of the solid acid DAF-1," *J. Chem. Soc. Faraday Trans.*, vol. 91, no. 19, pp. 3537–3547, 1995.
- [106] M. D. Shannon, J. L. Casci, P. A. Cox, and S. J. Andrews, "Structure of the two-dimensional medium-pore high-silica zeolite NU-87," *Nature*, vol. 353, pp. 417–420, 1991.
- [107] J. G. Min, H. J. Choi, J. Shin, and S. B. Hong, "Crystallization Mechanism of a Family of Embedded Isorecticular Zeolites," *J. Phys. Chem. C*, vol. 121, no. 30, pp. 16342–16350, 2017.

Chapter 2

Experimental Techniques

2. Experimental Techniques

2.1. Powder X-ray Diffraction

As it has been fore-mentioned in the previous chapter, a crystal has a regular and infinite arrangement of unit cells, providing the crystal with specific shapes and faces which can be indexed in some manner. The index represents the position of a plane in the crystal. The most well-known crystallographic indexing is *Miller index*, three numbers referring to the reciprocals of x , y , and z coordinates written in parentheses without any separation [1].

$$\left(\frac{1}{x} \frac{1}{y} \frac{1}{z}\right) \quad \text{Eq. 1.1}$$

Figure 2.1 is given as an example of crystal planes in a rectangular system. The pink, blue and yellow shaded planes have Miller index (100), (200) and (001), respectively. These are the results of reciprocal work on the coordinates where the shaded planes cut the rectangle: $\left(\frac{1}{1} \frac{1}{\infty} \frac{1}{\infty}\right)$ for the pink, $\left(\frac{1}{\frac{1}{2}} \frac{1}{\infty} \frac{1}{\infty}\right)$ for the blue and $\left(\frac{1}{\infty} \frac{1}{\infty} \frac{1}{1}\right)$ for the yellow ones.

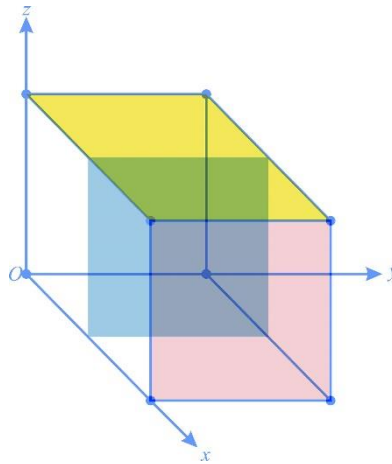


Figure 2.1. Shaded planes in a rectangular system.

Every plane or facet in a crystal is able to reflect the X-ray coming on them with different angles and emerging different peak positions, which are characteristic for each crystal system. That is why every crystal system has a distinctive XRD pattern. This is the principle used in Powder X-ray Diffraction (PXRD), a non-destructive method to get information about structure, composition and polycrystalline condition of a solid.

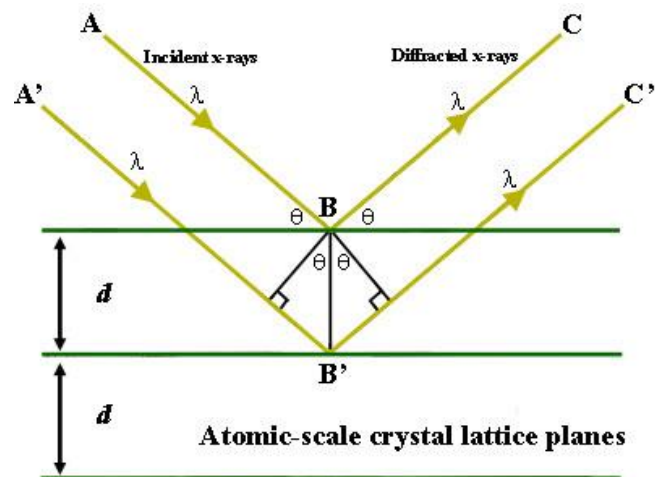


Figure 2.2. Bragg's Law (Taken from https://serc.carleton.edu/research_education/geochemsheets/BraggsLaw.htm [2]).

The relationship between the angle of incident X-rays (θ) and the space between the lattice planes (d) in Figure 2.2 is explained well by Bragg's Law:

$$n\lambda = 2d \sin \theta \quad \text{Eq. 1.2}$$

where n is the diffraction order.

In contrast to the crystalline solid, non-crystalline or amorphous solid has no or very low peaks due to the presence of many different faces or planes with the absence of the same planes. Therefore, no constructive X-ray reflection is detected by the detector, resulting in no peak in the PXRD pattern.

X-ray itself is part of the electromagnetic spectrum having a wavelength between 0.1 and 45 Å. It is generated by bombarding of high-speed electrons toward atoms of an

element. When bombarding electrons collide with an electron in the atomic shells, the targeted electron is dislodged from the shell, producing a vacancy in that shell. Another electron from outer shells having higher energy levels then falls into the vacancy. The movement of the electron from higher to a lower energy level releases some energy known as X-ray, which is characteristic for each element and each electron movement [3].

2.2. Scanning Electron Microscopy

Scanning Electron Microscopy (SEM) is a sufficient technique to get images of a solid's surface up to micron resolution. The basic principle of this technique is to focus a beam of electrons on to the surface of a specimen. Figure 2.3 depicts a diagram of the main components of the SEM machine.

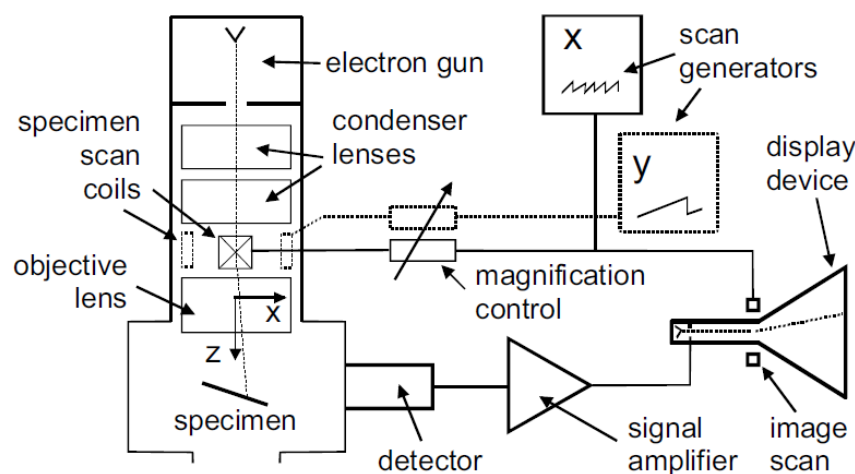


Figure 2.3. A chart of the main elements of a scanning electron microscope (Adapted from R. F. Egerton, *Physical Principles of Electron Microscopy: An Introduction to TEM, SEM, and AEM*. New York: Springer Science+Business Media, Inc., 2005. [4]).

The electron beam is produced by an electron gun, commonly made of the tungsten filament. The electron gun also speeds the beam up to create 2 – 40 keV energy. The electron beam then passes through condenser lenses, which function to demagnify

the beam, so that it will be just 2 – 10 nm in diameter when striking the specimen. The scan coils help the beam to scan the specimen.

After hitting the surface of the specimen, the incident electrons may experience inelastic or elastic scattering. When these probe electrons have low energy, inelastic scattering is more probable to occur. Some of the ‘primary electrons’ are absorbed or penetrated into the solid specimen to collide many times with the specimen’s electrons. As a result, other electrons from the specimen are forced to escape in lower energy due to energy loss during collisions. These escaping electrons are called ‘secondary electrons’. The depth from which the secondary electrons escape is only approximately 1 nm from the surface of the solid (depending on the specimen material).

Nevertheless, if primary electrons possess higher energy to escape from the solid specimen, they are backscattered in high angle (more than 90°) by the solid surface. This kind of electron is named ‘backscattered electron’, whose energy is slightly lower than the incident electron. Having high energy also means that the primary electrons are able to penetrate deeper into the solid, as well as to get away from it. Thus, the escape depth of backscattered electrons is more than that of the secondary ones. It is estimated to be some tens or hundreds of nanometers from the solid surface for higher than 3 keV of primary electrons. However, again, it depends also on to the type of specimen.

The backscattered and secondary electrons produced are then received by a detector. Afterwards, the signal is processed into the computer part of the machine to produce contrast colours, which is effortless to see by our eyes [\[4\]](#), [\[5\]](#).

Both signals from secondary and backscattered electrons produce different images. Since secondary electrons are only shallowly penetrated from the material surface, the images obtained represent the surface structure (topographical contrast) of the sample. Anyhow, backscattered electrons enter the solid deeper, allowing them to interact with varied atomic nuclei of the specimen. Consequently, the images yielded can indicate contrast and shadows. Figure 2.4 illustrates the difference.

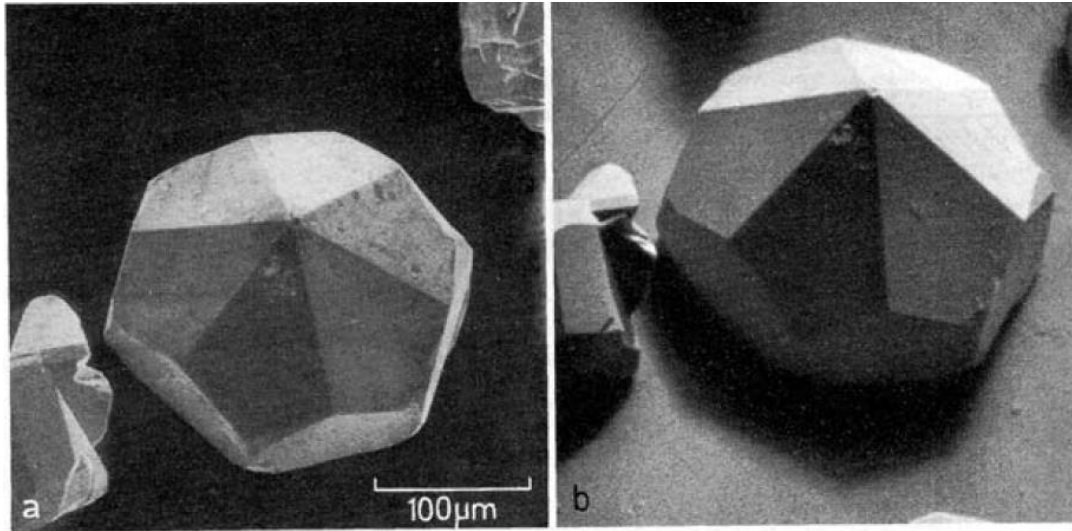


Figure 2.4. SEM images derived from a) secondary electrons and b) backscattered electrons [4].

2.3. Atomic Force Microscopy

Similarly to SEM, Atomic Force Microscopy (AFM) is a tool to provide surface images. Rather than using an electron beam to scan the surface of the specimen, AFM employs a sharp and very tiny tip, of which width is only a few nanometers. The AFM is very clever for exploring solid surface in Angstrom vertical resolution. Therefore, this instrument can be used to study the steps on a crystal surface or nuclei in crystal growth.

Main parts of the AFM is illustrated in Figure 2.5. Before scanning, a sample is brought up to be in contact with the AFM tip, which scans the sample's surface in x - y and z directions. As the tip moves along the sample's surface, the cantilever, to where the tip is attached, bends following the changes of force between the tip and the sample. A laser is shone onto the back of the cantilever to monitor its deflection and reflected toward a detector. The detector then transmits this signal to a computer. By this process, the topography of the surface is observed [6].

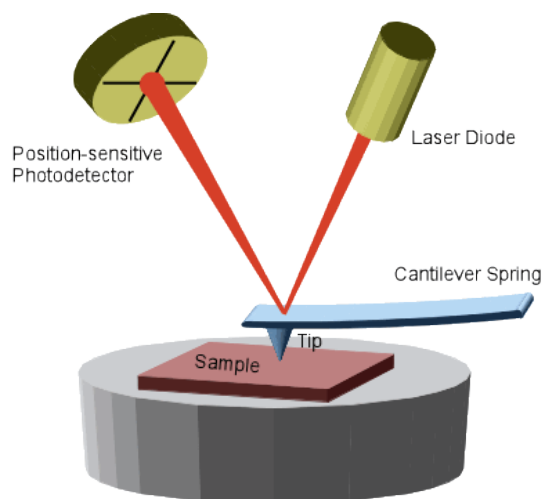


Figure 2.5. Diagram of the main components of AFM (Taken from <https://undergrad.research.ucsb.edu/2014/03/atomic-force-microscope-tiny-record-player/>, accessed on May 26, 2015 [7]).

There are three types of imaging modes in AFM. The ‘contact mode’ is an imaging mode where the cantilever deflection is kept constant by feedback control. In contrast, if the cantilever deflection is changing to keep the force between the tip and the sample minimized, then an ‘intermittent contact mode’ is used. This intermittent contact mode is favourable for soft specimens, such as biological samples. The last mode is the ‘non-contact mode’, in which the tip actually never touches the sample, but oscillates few nanometers in amplitude. The van der Waals forces are the one that is measured in this mode [6].

By using the AFM for surface imaging, there are several benefits that can be obtained. The AFM is a tool to get three-dimensional images with high vertical resolution exceeding the other microscopy techniques. Other than that, this instrument is superior since it allows scanning in liquid, which is advantageous for studying in situ crystal dissolution and growth.

2.4. References

- [1] C. Hammond, *The Basics of Crystallography and Diffraction*, 3rd ed. New York: Oxford University Press Inc., 2009.

- [2] D. Henry, N. Eby, J. Goodge, and D. Mogk, "X-ray reflection in accordance with Bragg's Law." [Online]. Available: https://serc.carleton.edu/research_education/geochemsheets/BraggsLaw.html. [Accessed: 06-Dec-2018].
- [3] E. W. Nuffield, *X-Ray diffraction Methods*. New York: John Wiley & Sons, Inc., 1966.
- [4] R. F. Egerton, *Physical Principles of Electron Microscopy: An Introduction to TEM, SEM, and AEM*. New York: Springer Science+Business Media, Inc., 2005.
- [5] P. J. Goodhew, J. Humphreys, and R. Beanland, *Electron Microscopy and Analysis*, 3rd ed. London: Taylor & Francis, 2001.
- [6] P. Cubillas and M. W. Anderson, "Synthesis Mechanism: Crystal Growth and Nucleation," in *Zeolites and Catalysis, Synthesis, Reactions and Applications*, Vol. 1., Weinheim, Germany: Wiley-VCH Verlag GmbH & Co. KGaA, 2010.
- [7] "https://undergrad.research.ucsb.edu/2014/03/atomic-force-microscope-tiny-record-player/, accessed on May 26, 2015." [Online]. Available: <https://undergrad.research.ucsb.edu/2014/03/atomic-force-microscope-tiny-record-player/>, accessed on May 26, 2015.

Chapter 3

IM-17 Crystal Dissolution Studied by AFM

3. IM-17 Crystal Dissolution Studied by AFM

3.1. Introduction

There is a growing interest in the investigation to understand nanoporous materials' crystal growth. However, these studies have reported the growth and dissolution of nanoporous materials with relatively small unit cells keeping the growth of crystals with large unit cells less understood. Such published works include the successful in-situ growth observation on crystals with the SOD framework with $8.956 \text{ \AA} \times 8.956 \text{ \AA} \times 8.956 \text{ \AA}$ unit cell dimension [1], the dissolution process of zeolite L (LTL structure) with $18.126 \text{ \AA} \times 18.126 \text{ \AA} \times 7.567 \text{ \AA}$ hexagonal unit cell [2], and the spiral growth revealed on STA-7 with tetragonal unit cell having comparable size with zeolite L [3]. Slightly larger than those, a cubic unit cell of zeolite A (LTA structure) with 24.610 \AA side length has also been studied to reveal its surface structure and dissolution [4], [5].

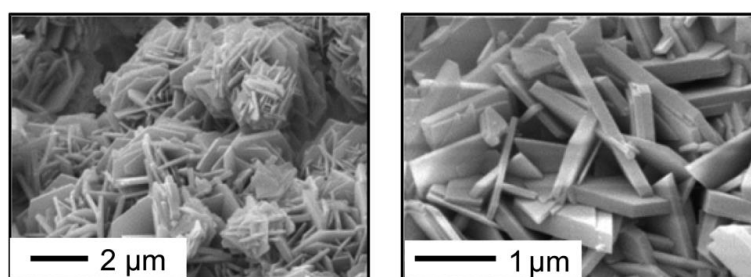


Figure 3.1. SEM images of the IM-17 crystal from literature [6].

Researchers continue to search for new crystalline nanoporous materials having certain properties for certain purposes. Recently, a novel zeolite named IM-17 having the UOV framework structure was invented in 2014 by Lorgouilloux *et al.* [6]. They reported that the crystal is plate-like with a rhombus shape as can be seen in Figure 3.1. The material is very interesting as this germanosilicate has a complex structure crystallised in an orthorhombic system with 16 tiles constructing it. Other than that, it possesses a relatively large unit cell, sized $12.679 \text{ \AA} \times 22.217 \text{ \AA} \times 39.058 \text{ \AA}$. Crystalline IM-17 was synthesized using decamethonium dihydroxide ($\text{Dec}(\text{OH})_2$) as the structure directing agent [6]. These long chain decamethonium

dications have also been studied before to form other nanoporous structures with a relatively large unit cell, such as NES [7], [8], MWF [9] and DFO [10].

The large unit cell of UOV structure has two types of channel seen from [100] direction, large 12-membered rings and small 8-membered rings (see Figure 3.2 (a)). Viewed along [001] direction, it shows one type of pore system, which is 10-membered rings (see Figure 3.2 (b)). However, there is no indication of any pore system seen along [010] direction (see Figure 3.2 (c)).

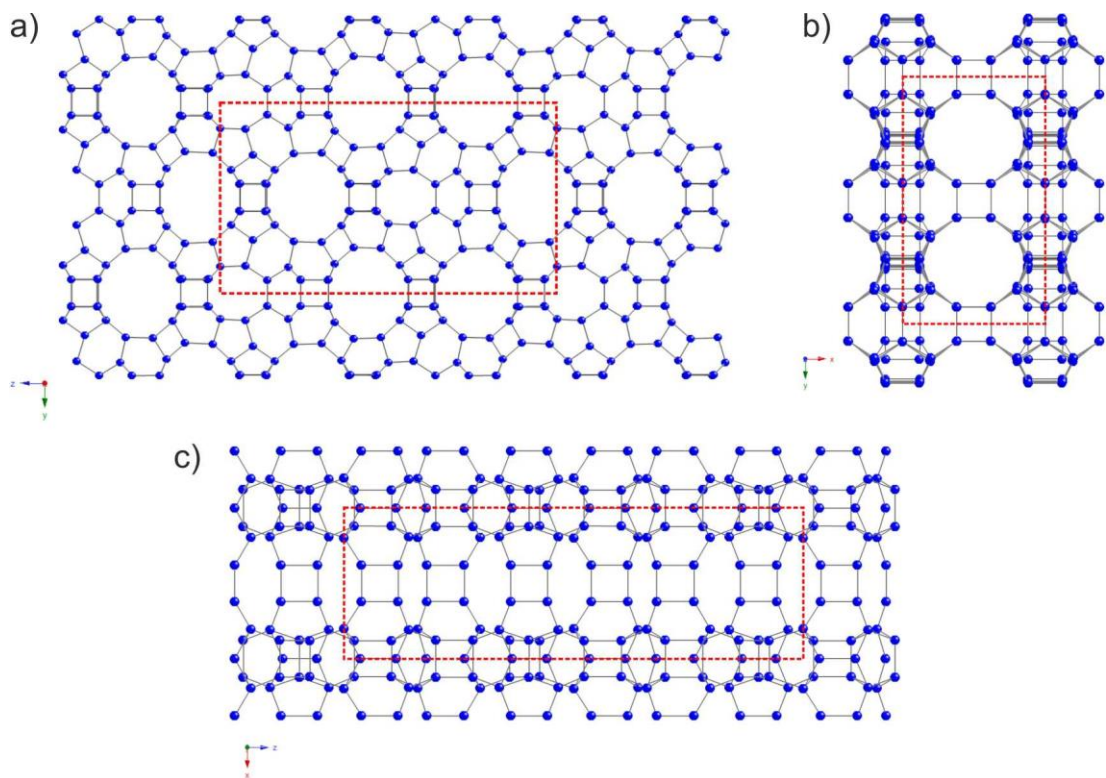


Figure 3.2. The a) (100) facet, b) (001) facet and c) (010) facet of the UOV structure. Red dashed line shows one unit cell.

UOV structure is built from 16 natural tilings listed in Figure 3.3, according to the Structure Commission of the International Zeolite Association (IZA-SC) [11]. This number of tiles is the largest according to IZA-SC so far. Among 235 zeolite framework types indexed by IZA-SC, there are only three frameworks possessing as large as 16 natural tilings, one of which is the UOV. The other two are IMF and ITG which, although both have such a large number of tiles, their unit cells are smaller compared to the UOV framework.

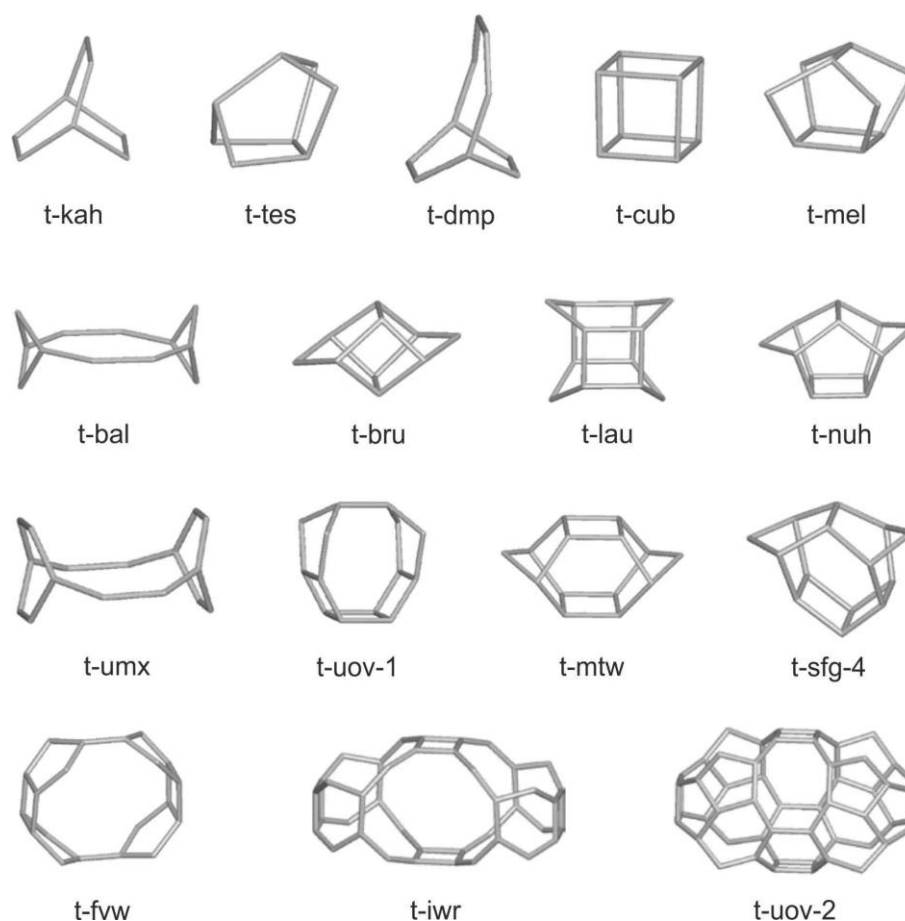


Figure 3.3. Sixteen tiles constructing UOV structure [11].

These two facts about IM-17 crystal mentioned above, *i.e.* large unit cell and complexity of the structure, have posed an important question in crystal growth study, which is how such large unit cell is repeated. Answering this question is the aim of the chapter. The study will, therefore, add valuable insights into the study to understand nanoporous materials' crystal growth. In order to answer this question, we used AFM to investigate the in-situ process. However, since the growth of IM-17 crystal occurs at a very high temperature [6], which is not suitable for the AFM, we then conducted the in-situ observation of its dissolution in basic solution at room temperature, considering that in some cases the dissolution may be related to the reverse process of the growth. In this work, we also compared the experimental results with the simulation employing the *CrystalGrower* program [12].

3.2. Experimental

3.2.1. Synthesis of the IM-17 crystal

IM-17 crystal was synthesized according to EP 2 219 997 A1 [13] using decamethonium hydroxide ($\text{Dec}(\text{OH})_2$) as the structure directing agent. The template was made by exchanging the anions in decamethonium bromide (DecBr_2) with hydroxides.

First of all, DecBr_2 (Sigma-Aldrich, 98%) was dissolved in deionized water. Anion resin (OH form) was added to the solution and stirred for 16 hours to exchange the bromides with hydroxides. The solution resulted was analyzed with acid-base titration to check the percentage of the exchange and with ^1H liquid NMR to make sure that the organic substances are not degraded. The $\text{Dec}(\text{OH})_2$ solution concentration was then adjusted to be 0.67 M by rotary evaporation.

The $\text{Dec}(\text{OH})_2$ solution was introduced into a 20 mL Teflon liner followed by addition of germanium oxide (GeO_2 , Aldrich, $\geq 99.99\%$) while being stirred for 15 minutes using a magnetic stirrer. After that, fumed silica (Cab-O-sil M-5, Sigma-Aldrich) was added to the solution and the stirring was continued for about 14 hours at room temperature. This was aimed to evaporate surplus water until the gel's molar ratio was $0.6 \text{ SiO}_2 : 0.4 \text{ GeO}_2 : 0.25 \text{ decamethonium} : 10 \text{ H}_2\text{O}$ with $\text{pH} = 14$. The liner containing the synthesis gel was then introduced into an autoclave and put inside an oven at 170°C for 14 days in a static condition.

After the hydrothermal reaction was completed, the solid was extracted from the mixture by filtration. Following this procedure, the solid was then washed with deionized water several times and dried at 70°C for 24 hours.

3.2.2. Material characterizations

The prepared IM-17 crystal underwent PXRD and SEM for characterization. PAN Analytical X'Pert Pro Diffractometer was used to analyze the phase obtained with $\text{CuK}\alpha$ as the source of X-rays. The tension was set 40 kV while the current is 30 mA. After being crushed, the sample (previously has been calcined at 550°C for 8 hours

under air) was placed on a sample holder and scanned with 2θ ranging from $4^\circ - 50^\circ$. The data were analyzed using X'Pert HighScore Plus software.

The crystal morphology analysis was conducted using a FEI Quanta 200 SEM. The solid was scattered on sticky carbon attached to the sample holder. Then, the sample was coated with platinum to avoid sample charging. The scanning was done in a vacuum with the high voltage set at 20.0 kV.

The crystal's surface study was performed under AFM from JPK Instruments. A small piece of thermoplastic was heated at 50°C on a glass slide until it was warm and can be pressed flat and clear. A very small amount of sample was then scattered on the flat thermoplastic and reheated so that the crystals stuck on it. The clear crystals were chosen to be scanned with set point 0.5 V using a non-conductive silicon nitride tip from Bruker. Terrace height on the crystal surface was measured employing JPK-SPM Data Processing software.

3.2.3. Dissolution of IM-17 crystal studied with in-situ AFM

An in-situ AFM experiment to observe IM-17 crystal dissolution was performed using a JPK instrument and a BioCell to hold the sample slide. To prepare the sample, a small amount of resin was placed on a glass slide. The slide was then heated to 60°C for about four hours. Subsequently, a very small amount of the powdery sample was scattered on top of it and was heated again at 60°C overnight.

The next step was putting the slide on the BioCell to which a tube was connected. This BioCell was set under the AFM head with a tip, having the same parameters as the one used in ex-situ experiment, on top of the chosen crystal. Selected area was first scanned ex-situ to get the surface image before the solution was injected. As soon as 0.25 mL solution was injected slowly through the tubing at $t = 0$ minute, the same area was scanned continuously to acquire surface images during the dissolution process. The scanning was conducted in contact mode at room temperature with set point of 0.3 V and scan rate of 4 Hz using the same tip as in the ex-situ experiment. The solution used to dissolve the IM-17 crystal in this experiment is sodium hydroxide 3 and 4 M. Again, JPKSPM Data Processing software was used for height measurement.

3.3. Results and Discussions

3.3.1. Synthesis and characterization of IM-17 crystal

Highly crystalline IM-17 solid has been successfully synthesized as confirmed by the PXRD pattern in Figure 3.4, in which the peaks in reference's diffractogram match the peaks in calcined IM-17 sample's diffractogram. *CelRef* analysis on the PXRD pattern of the IM-17 sample agrees with the references [6], [11]. The lattice parameters of the IM-17 sample are comparable (although with a slight difference) with those of the reference's (IM-17 sample's lattice parameters: $a = 12.6926 \text{ \AA}$, $b = 22.2393 \text{ \AA}$, $c = 39.0763 \text{ \AA}$; reference's lattice parameter: $a = 12.6790 \text{ \AA}$, $b = 22.2170 \text{ \AA}$, $c = 39.0580 \text{ \AA}$).

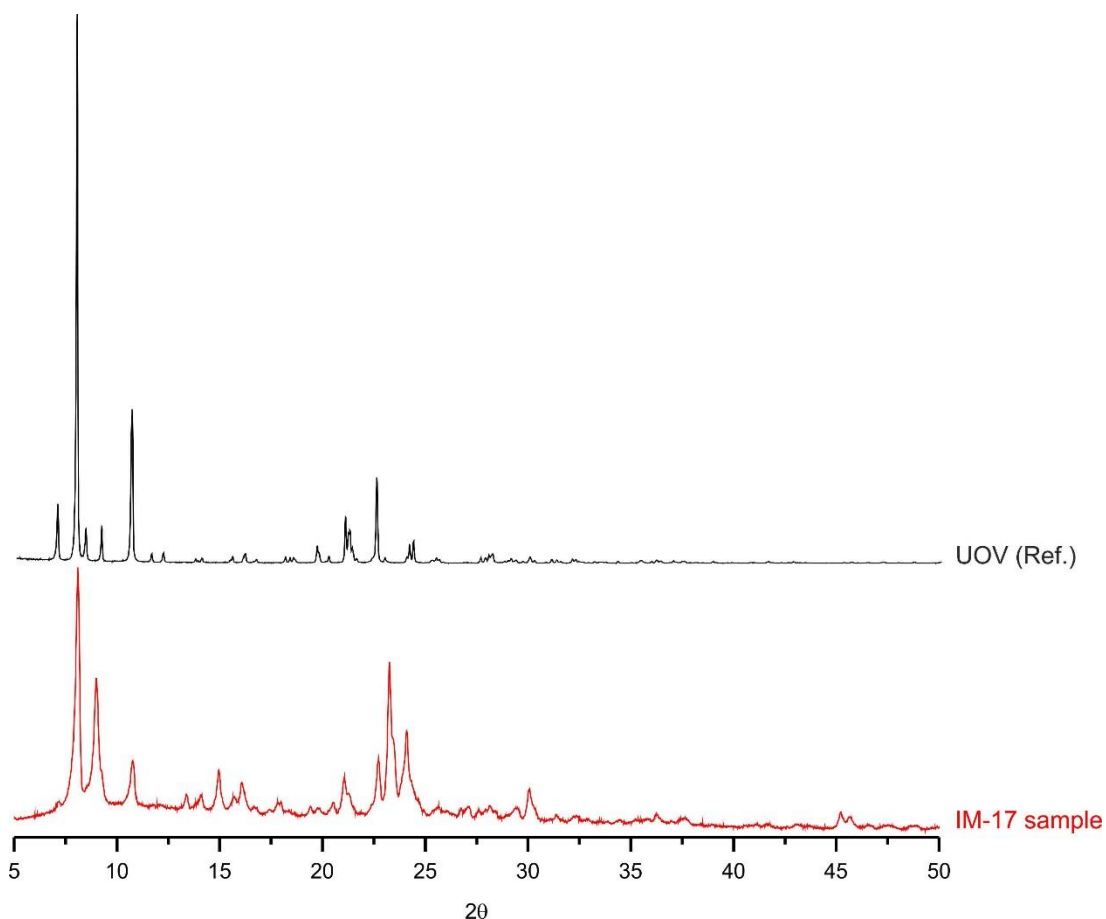


Figure 3.4. PXRD patterns of the calcined IM-17 sample compared to UOV (Ref. [11]).

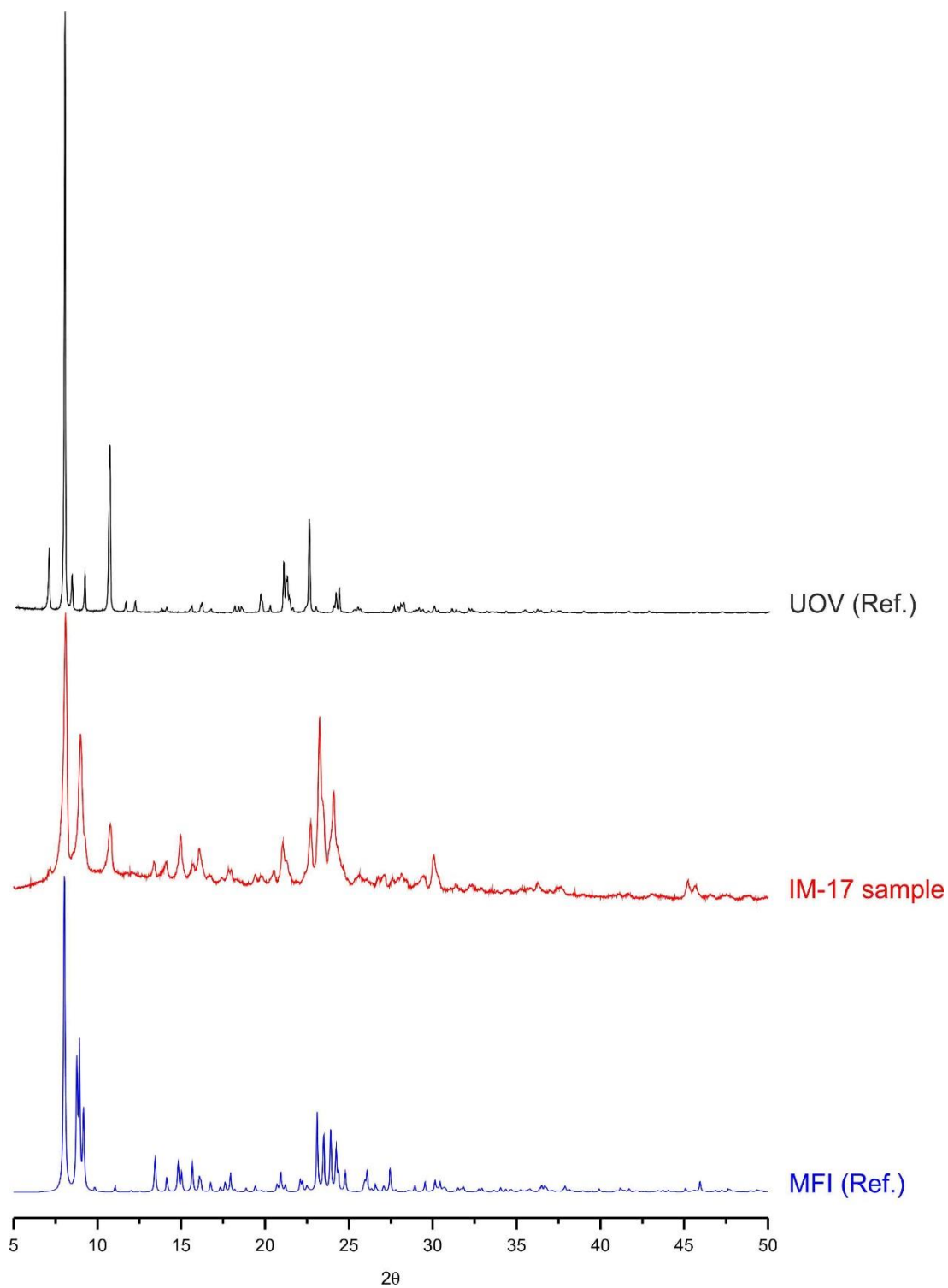


Figure 3.5. PXRD patterns comparison between calcined IM-17 sample (red), calculated MFI (blue, Ref. [11]) and UOV (black, Ref. [11]).

However, additional peaks are present in the sample's diffractogram (*i.e.* at $2\theta = 13^\circ, 14.6^\circ, 15.4^\circ, 19^\circ$) suggesting the existence of impurities in the IM-17 sample. This

deduction is strengthened by the high intensity of the peaks between $2\theta = 23^\circ - 25^\circ$, which is not the case for UOV crystal structure. Further analysis proved that those impurity peaks most probably come from MFI structure (see Figure 3.5). It matches the literature [6] that mentioned the formation of MFI-structured germanosilicate zeolite which corresponded with the amount of GeO_2 in synthesis gel.

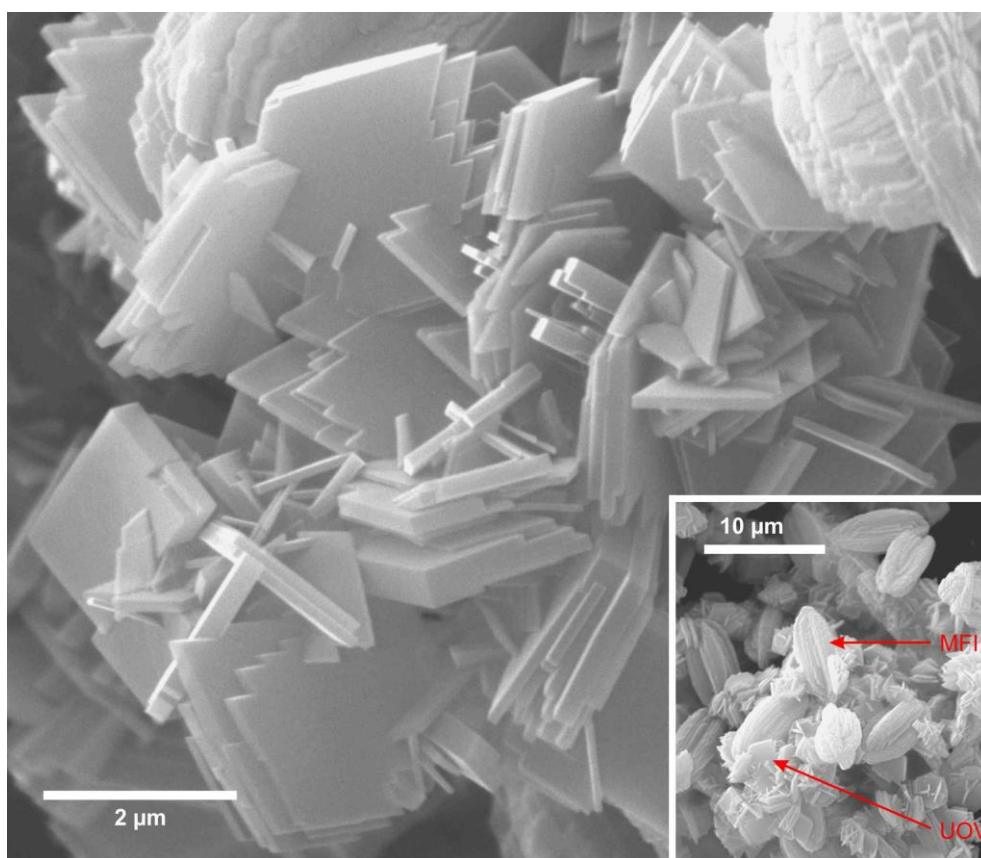


Figure 3.6. SEM image of as-prepared IM-17 crystal. Inset shows scanning on a larger area.

SEM image of the IM-17 sample agrees with the PXRD findings as it reveals the existence of two different phases in the sample (see Figure 3.6). Comparing this SEM image of the as-prepared IM-17 crystal (see Figure 3.6) with the one reported by Lorgouilloux *et al.* in 2014 [6] presented in Figure 3.1 assuring us that IM-17 phase in our sample is the very thin intergrowth plate-like rhombus-shaped crystals. The crystal size is very small and thin, around $1 - 2 \mu\text{m}$ in size and less than 500 nm thick. The other phase, which is a large chunk shown in the inset of Figure 3.6, is the

MFI phase as confirmed by the PXRD patterns. With these two phases in the sample having completely different shapes, there is no problem in working with the AFM instrument since we can easily pick the targeted crystal to scan under the optical microscope.

Being in a plate-like rhombus shape, IM-17 crystal possesses six faces (see Figure 3.7). As the literature defined that the shortest growth direction of the IM-17 crystal is related to its crystallographic direction a [6], it confirms that the large diamond-shaped facet is the (100) facet. In addition to this, Anderson *et al.* (2017) reported that the side faces are (013) and (01 $\bar{3}$) facets based on their *CrystalGrower* simulation [12].

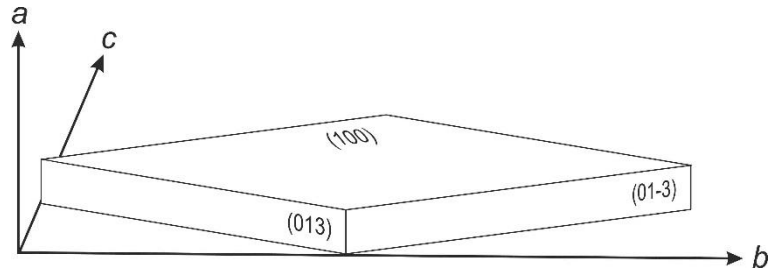


Figure 3.7. A diagram of the IM-17 crystal with its three different facets.

3.3.2. Ex-situ AFM of IM-17 crystal

In agreement with the SEM result, ex-situ AFM image (see Figure 3.8) reveals the inter-growth IM-17 crystals. We can also see in detail that the crystals inter-grow along $\langle 001 \rangle$ direction. More detailed observation provided by AFM scanning is the terraces on the crystal surface that evidence layer by layer growth mechanism adopted by the IM-17 crystal during its growth. The elliptical-shaped terraces grow faster toward $\langle 010 \rangle$ direction and slower toward $\langle 001 \rangle$ direction.

Cross-sectional height measurement in Figure 3.8 (c) shows that the terraces on the (100) facet are each 1.25 ± 0.1 nm high. This step height matches the height of a unit cell of the IM-17 sample analysed using *CelRef* as mentioned in the previous section, which is 1.27 nm (d_{100}).

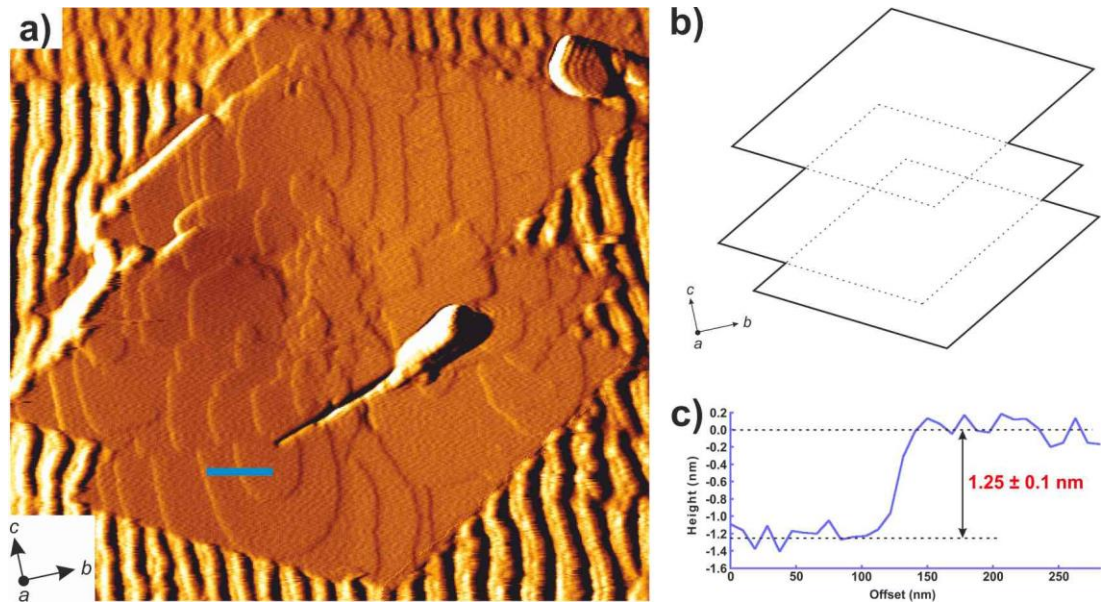


Figure 3.8. a) A vertical deflection AFM image of IM-17 crystals showing (100) facet. The scanned area in this image is $2.5 \mu\text{m} \times 2.4 \mu\text{m}$. b) A diagram showing the orientation of the IM-17 intergrowth crystals in the image (a). c) Cross-sectional height measurement along the blue line in the image (a).

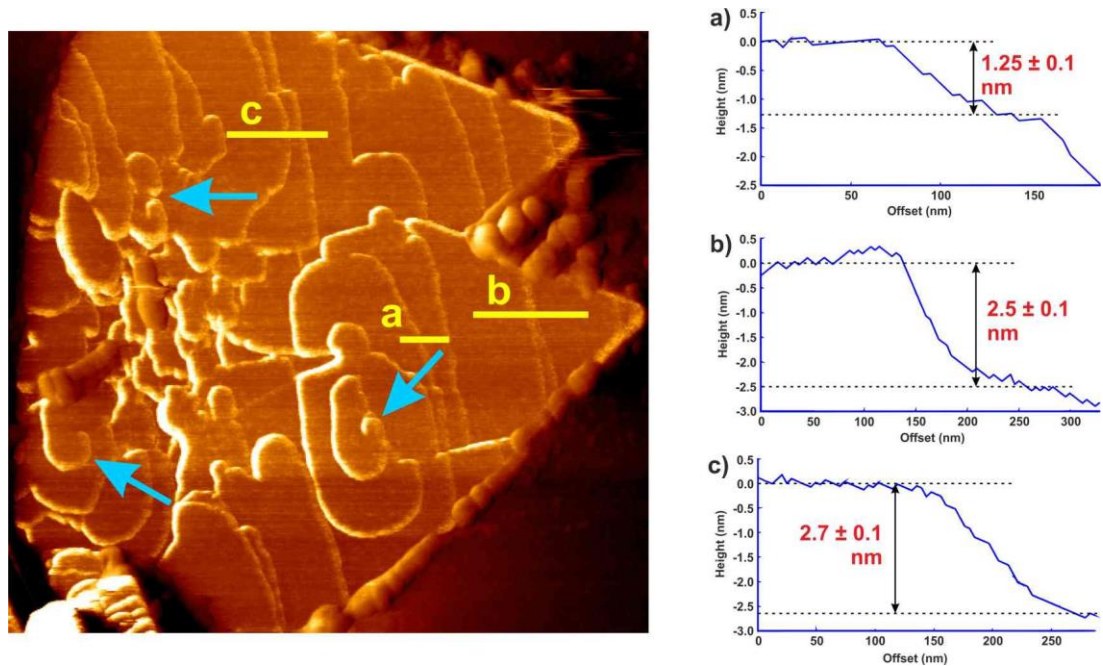


Figure 3.9. A lateral deflection AFM image of IM-17 showing (100) facet with screw dislocation (indicated with blue arrows) and height measurements on some terraces marked with yellow lines. AFM scanned area is $1.9 \mu\text{m} \times 1.9 \mu\text{m}$.

AFM scanning on IM-17 crystal surface also disclosed the existence of screw dislocations on (100) facet as depicted in Figure 3.9. There are three obvious fully grown screw dislocations in this particular image (denoted with blue arrows). The spiral seems to grow elongated terraces because the terrace grows faster toward $\langle 010 \rangle$ direction as the other terraces without screw dislocations. Each terrace on the crystal surface has the same 1.25 ± 0.1 nm height as the one grows via layer by layer mechanism. Height measurements of some points on the crystal surface are presented as well in Figure 3.9.

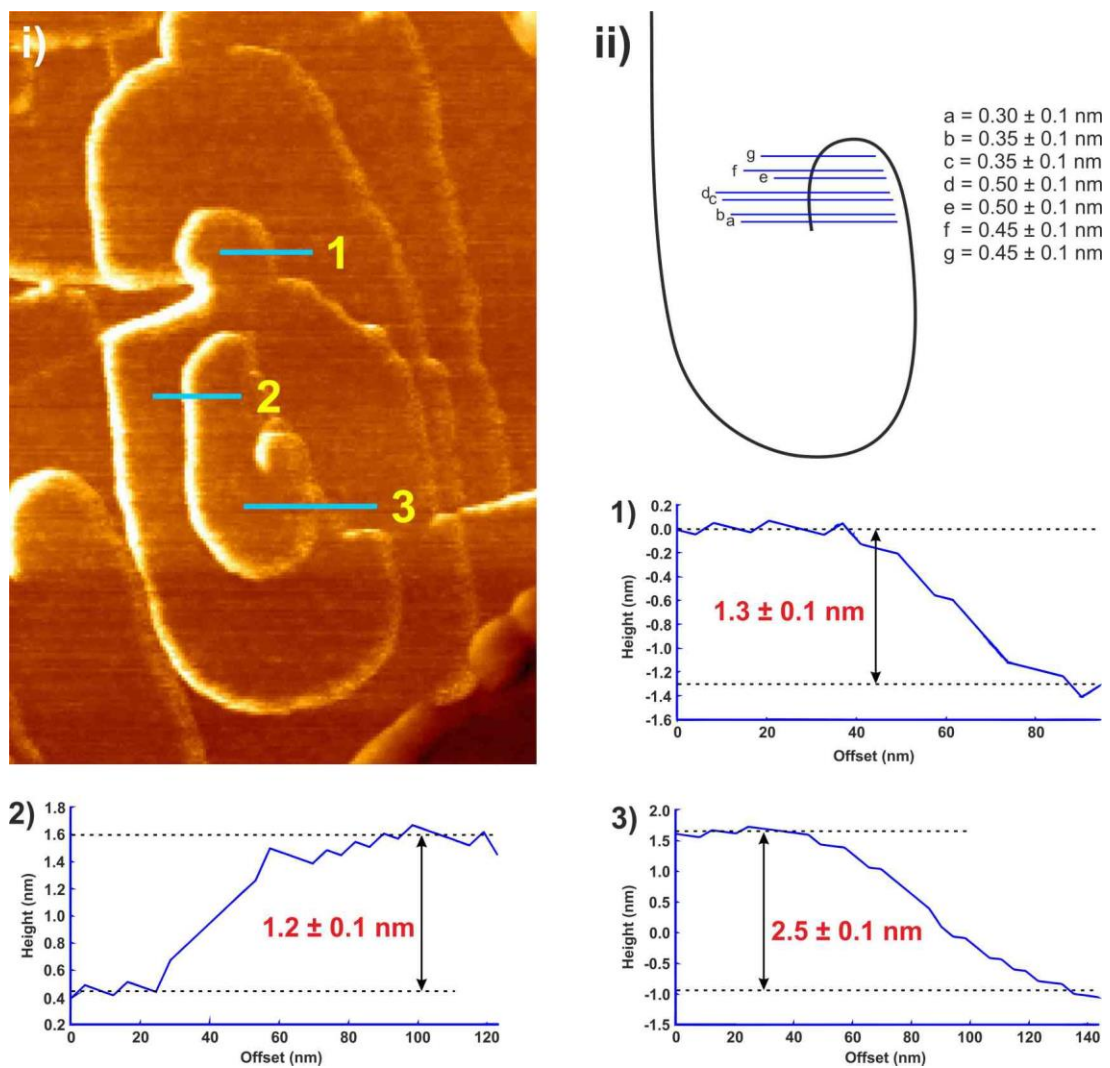


Figure 3.10. i) Cross-sectional height measurements of terraces grew from spiral growth on (100) facet along the blue lines. The AFM image is $0.7 \mu\text{m} \times 1.0 \mu\text{m}$ in size. ii) An outline of the newly formed spiral in (i) with the heights on some lines across it.

The spiral fully grew terraces with the same 1.25 ± 0.1 nm height as proved in Figure 3.10 (i). However, almost at the centre of the spiral, the terrace's height is lower. Figure 3.10 (ii) presents the heights on some points on the newly formed spiral terrace giving 0.30 ± 0.1 nm just next to the screw dislocation (along the blue line labelled as “a” in the image), which then levels up to 0.50 ± 0.1 nm in the middle of the curvature (“d” and “e”). This lower step height at the heart of the spiral is typical for one growing from a screw dislocation. Growth units were then attached to the low step created by the spiral and formed a full step, which is 1.25 nm high.

Meanwhile, AFM image of (013) facet of the IM-17 crystal is depicted in Figure 3.11. It reveals evidence of layer by layer growth mechanism on this surface as it is on the (100) facet. The terraces grew fast toward $\langle 100 \rangle$ direction and slow toward $\langle 013 \rangle$ direction. Height measurements on these steps gave *c.a.* 1.0 ± 0.1 nm high, which corresponds to d_{013} of the IM-17 sample ($d_{013} = 1.018$ nm) analysed with *CelRef*.

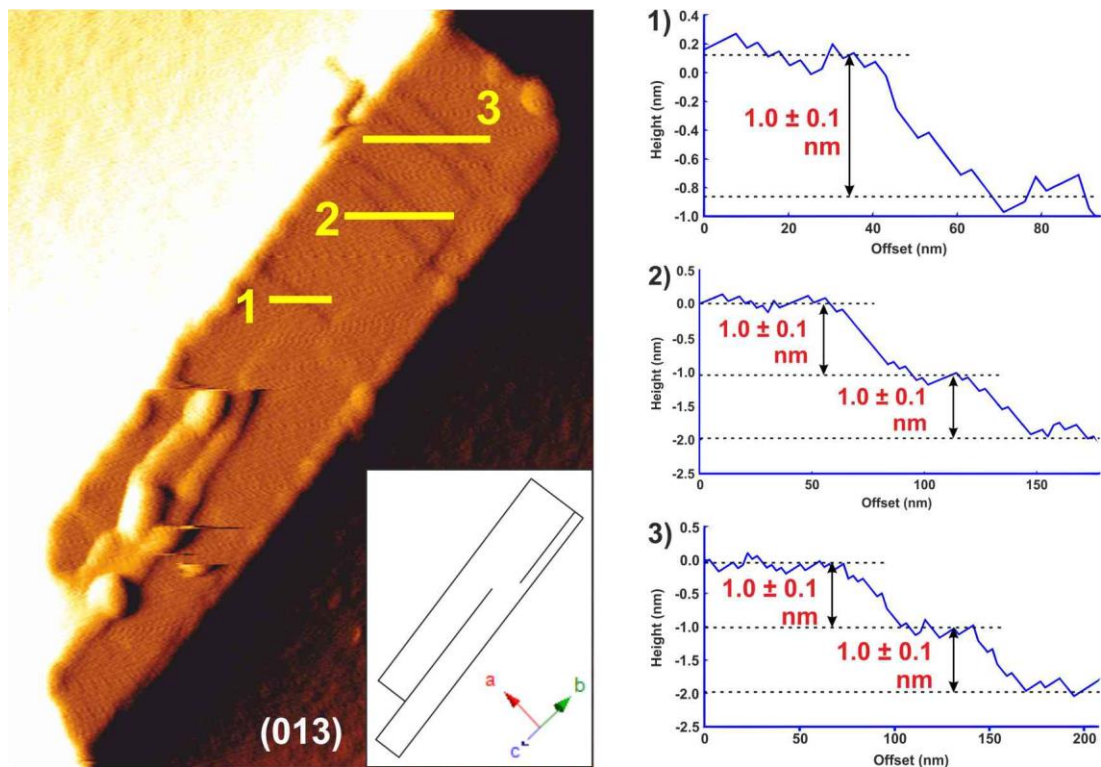


Figure 3.11. A vertical deflection AFM image ($1.0 \mu\text{m} \times 1.2 \mu\text{m}$ in size) of IM-17 crystal showing (013) facet and its height measurements on some terraces. Inset illustrates a schematic diagram of the crystal with its intergrowth.

In agreement with the SEM image of the IM-17 crystal presented in the previous section, which reveals intergrowth in the crystal, the AFM image in Figure 3.11 enables us to take a closer look at it. The inset in the image traces the crystal's twinning to clearly show the intergrowth's direction. This is an evidence that the IM-17 crystal does not intergrow only along $\langle 001 \rangle$ direction, but also along $\langle 100 \rangle$ direction. It seems that the intergrowth in (013) facet is a result of fault when the crystal repeated its unit cell toward $\langle 100 \rangle$ direction.

3.3.3. UOV crystal simulation

CrystalGrower was successfully used to simulate the UOV-structured crystal. The result was then pictured using VMD and *CG Visualiser* programs for a more detailed investigation on the crystal surface. The *CrystalGrower* modelled UOV single crystal as thin rhombus-shaped platelet, shown in Figure 3.12. This model agrees with the result from the laboratory experiment on IM-17 crystal and with our previous publication [12].

The simulation produced layer by layer terraces on both (100) and (013) facets of UOV crystal with the same features as those we observed experimentally under AFM. Some small nucleations are also seen on the simulated crystal surface.

Looking closely into the (100) crystal surface in the simulation, the tiling structure of the surface is revealed (see Figure 3.13 (a)). The surface of (100) facet is terminated with double-4-rings (the tile labelled in IZA Zeolite as t-cub [11]) directly supported by one of either t-lau or t-mtw (clarified in Figure 3.14 that double 4-rings sit on two distinctive tilings, t-lau and t-mtw, which are located alternately). Therefore, we can deduce that the terrace surface on (100) facet cuts through the 10-membered channel just above the double 4-rings as illustrated in Figure 3.15. This is also the most possible position for surface termination since it has the least bonds per unit cell to break.

The simulation in Figure 3.13 (a) also discloses the presence of nucleation sites (indicated by arrow 1) and defect (marked by arrow 2), which is a vacancy in this case. It suggests that, mostly, when the units of growth are attached on the surface double 4-rings constructing a structure as if t-lau or t-mtw are on top of those double

4-rings, new nucleation on (100) crystal surface starts. Then, the new nucleation leads to the formation of a new layer. Cyan arrow 3 in this image points at a small island on the crystal surface as a good example of a new rising layer. Single nucleation arises on crystal surface because the supersaturation of the mother solution is high enough for the growth units to bind to the surface but not too high to cause adhesive growth, which causes roughness on the surface.

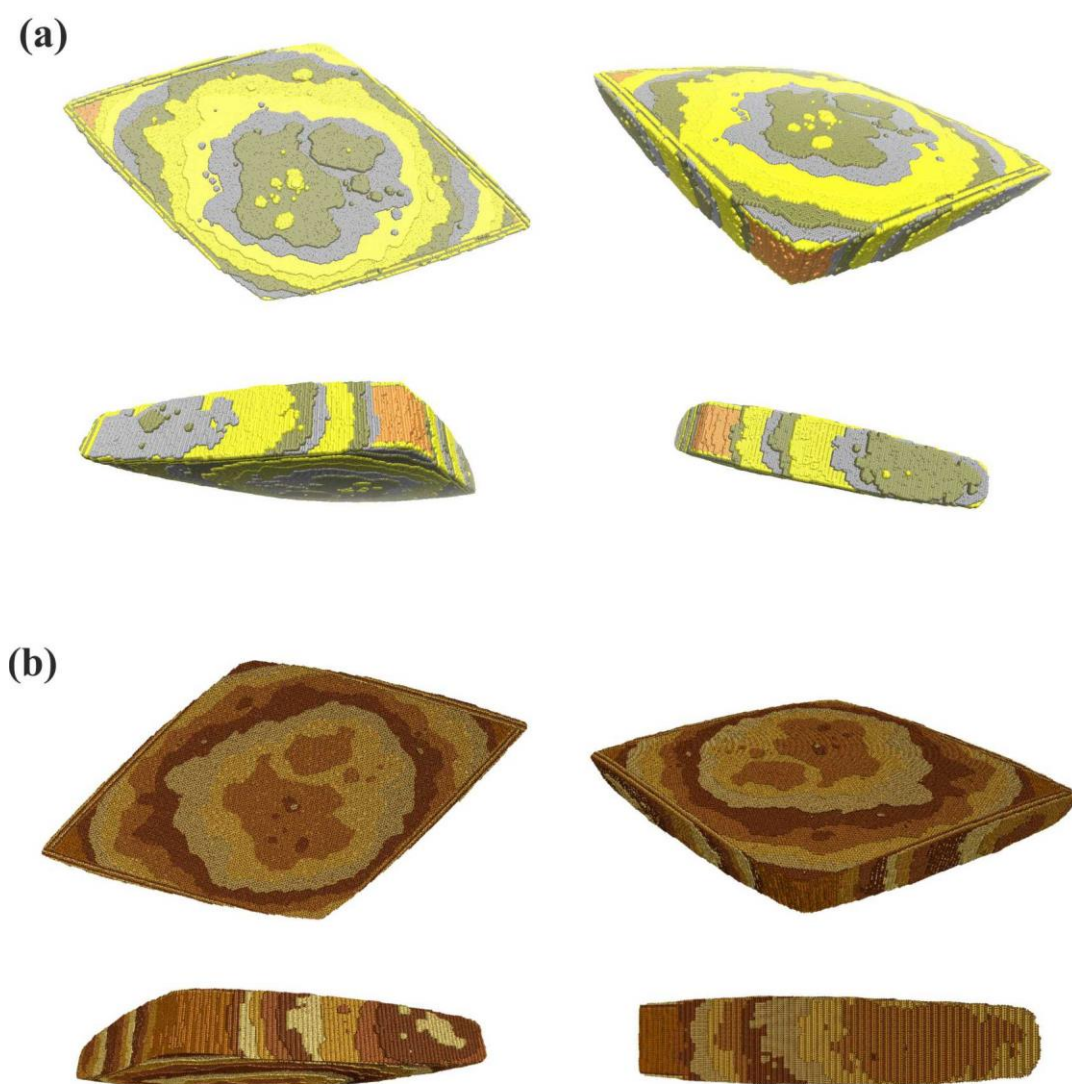


Figure 3.12. Simulation of UOV crystal using *CrystalGrower* viewed with a) VMD and b) *CG Visualiser* showing (100) facet on top rows and (013) facet on the bottom row. The simulation was performed with $\Delta U_s = 2 \text{ kcal mol}^{-1}$. The simulated crystal is approximately $0.07 \mu\text{m} \times 0.23 \mu\text{m} \times 0.44 \mu\text{m}$ in size.

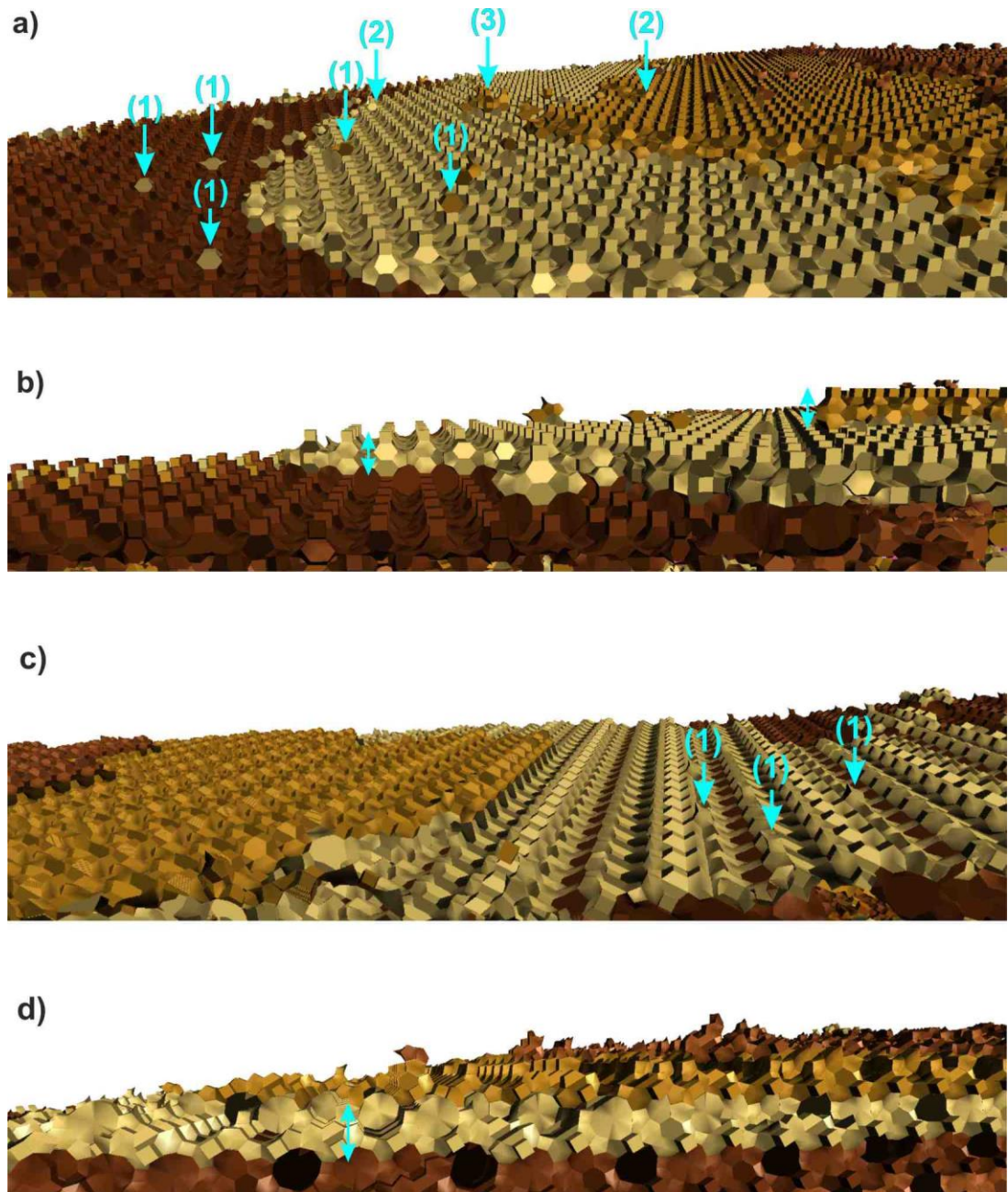


Figure 3.13. Simulated UOV crystal in Figure 3.12 viewed closely at a – b) (100) facet and c – d) (013) facet with (1) denotes single nucleation, (2) denotes defect and (3) marks newly grown layer. Cyan arrows on images (b) and (d) show clearly one layer height of (100) and (013) facets, respectively.

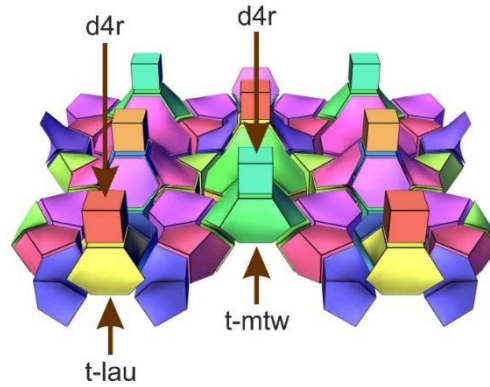


Figure 3.14. UOV structure on (100) facet presented to clarify the tilings arrangement.

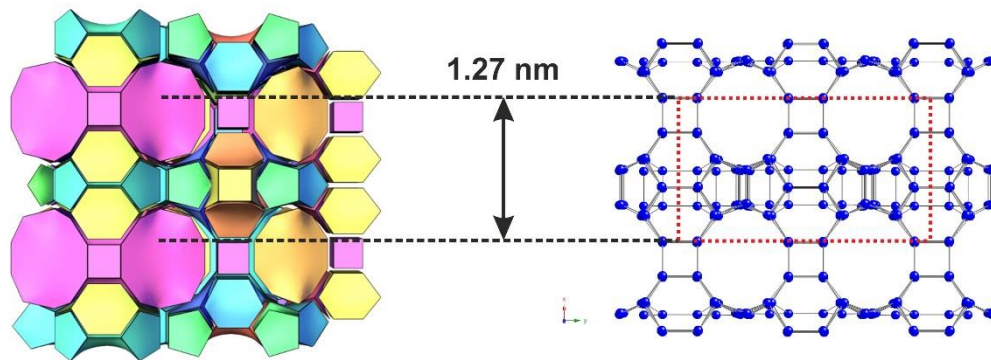


Figure 3.15. UOV structure depicted (001) facet (the left image shows its tiles and the right image shows its framework). Red square on the right image shows one unit cell. Black dashed lines display the most possible surface termination.

In Figure 3.13 (b), each cyan arrow displays height of the layer growing on (100) surface. Comparing this with our analysis based on ex-situ AFM result summarized in Figure 3.15 gives us a match layer height determination for (100) facet.

In terms of the (013) facet, this side face seen in the simulation (see Figure 3.13 (c)) is terminated just across the 12-membered channel. The reason is, again, there is the fewest number of bonds to cut when this plane is the surface termination. In accord with that, the program also calculated it as the most stable surface termination. Figure 3.16 illustrates this possible surface termination on (013) crystal face. The step height on (013) facet is the height from the middle of the 12-membered channel on the (013) plane to another 12-membered channel on the next (013) plane.

On the (013) surface, single nucleation site (labelled as (1)) can be started when units of growth are connected on the established layer creating a surface structure as though either t-bal, t-bru, t-nuh or t-sfg-4 are on the particular sites. The single nucleation formed on this crystal surface is a result of medium supersaturation in the synthesis condition. Furthermore, layer height simulation for (013) facet of the IM-17 crystal, marked by the cyan arrow in Figure 3.13 (d), fits perfectly with our illustration in Figure 3.16.

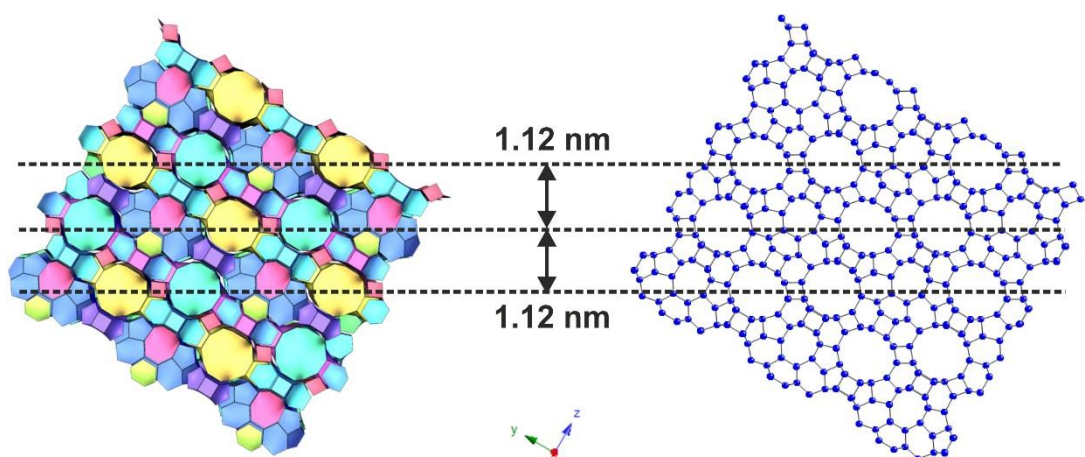


Figure 3.16. UOV tiling and structure showing the corresponding d_{013} 's height. Black dashed line depicts the most possible surface termination.

How the experimental result and the simulation for IM-17 crystal in this work structurally match in details is very fascinating. These findings, of course, convince us more that the *CrystalGrower* program gives a correct prediction on the nanoporous crystal growth.

3.3.4. In-situ AFM of IM-17 crystal

In-situ AFM was used to observe real-time dissolution of IM-17 crystal. We have tried to dissolve the IM-17 crystal in several acid and basic solutions (in various concentrations), namely sulfuric acid (H_2SO_4), hydrochloric acid (HCl), nitric acid (HNO_3), acetic acid (CH_3COOH), decamethonium hydroxide ($\text{Dec}(\text{OH})_2$), potassium hydroxide (KOH), sodium hydroxide (NaOH) and the mother liquor. However,

because of the experimental conditions and the materials used to attach IM-17 crystals on to glass slide, those experiments did not work except the dissolution of the crystal in 3 M and 4 M NaOH solution.

Here we present the results on IM-17 crystal dissolution carried out in the mentioned working system only, which are the dissolution in 4 M NaOH solution for (100) facet and dissolution in 3 M NaOH solution for (013) facet.

3.3.4.1. Dissolution of (100) facet of the IM-17 crystal

In this part, we discover the result on the dissolution of (100) facet of IM-17 crystal in 4 M NaOH solution observed using AFM. Subsequent AFM images scanned during the dissolution process are shown in Figure 3.17 and Movie 3-1 in Appendix 1.

Overall, we can observe from Figure 3.17 that after 4 M NaOH solution was in contact with the IM-17 crystal surface for a period of time, the exposed layers dissolved completely leading to the exposure of the layers below them. These newly exposed layers then soon dissolved in the solution as well.

The NaOH solution took about 50 minutes before it started to dissolve the IM-17 crystal. The long induction period before the dissolution process started proves how resilient the crystal was in a relatively high concentration of this basic solution. Despite the fact that IM-17 crystal used in this experiment is uncalcined, which is a factor reported to prolong the induction period in the alkaline dissolution process [14], [15], it could also happen because the ratio of silicon to germanium atoms in the IM-17 framework structure is very high, which is 17.06 : 4.94. It is well known that the more substitution atoms for silicon present in a zeolite framework, the zeolite structure will be getting weaker, and vice versa, with regard to zeolite stability during dissolution [16].

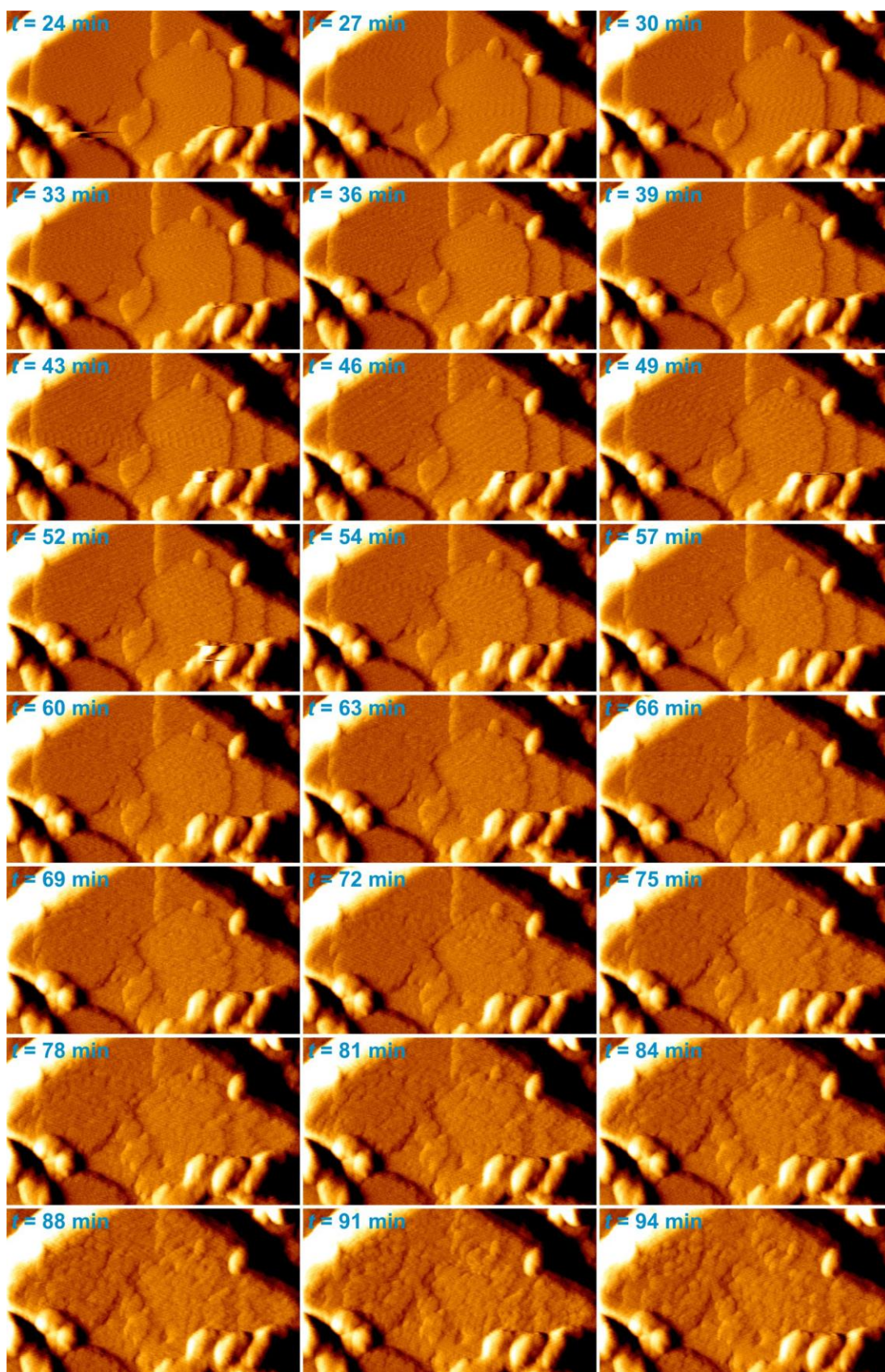


Figure 3.17. Consecutive AFM vertical deflection images of IM-17 crystal dissolution in 4 M NaOH solution. Scanned area: $0.8\ \mu\text{m} \times 0.5\ \mu\text{m}$ (to be continued on the next page).

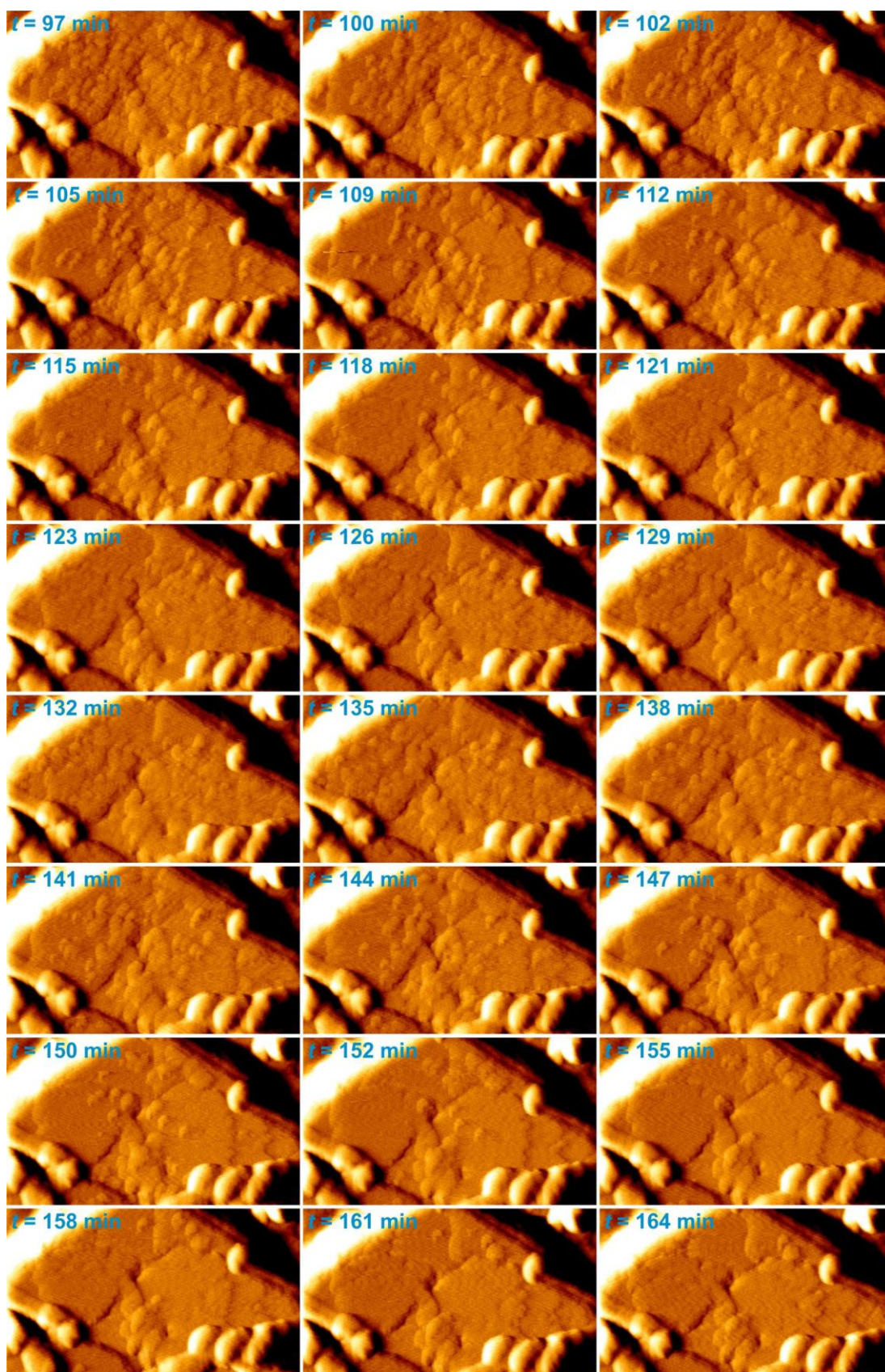


Figure 3.17 (continued). Consecutive AFM vertical deflection images of IM-17 crystal dissolution in 4 M NaOH solution. Scanned area: $0.8\ \mu\text{m} \times 0.5\ \mu\text{m}$.

The solution started to affect the crystal surface at $t = 52$ minutes as the particles on the step edges were beginning to retreat. Meza *et al.* (2008) [5] reported the stability of particles at straight terrace edges over the curvature hole edges. Thus, since the terrace edges in the IM-17 crystal are not straight, the solution is able to affect the layer edges to retreat first. The phenomenon is as expected because the bonding energy of the particles on the terrace edge is weaker than that on the bulk surface, as Kossel theory explains [18], resulting in the crystal particles on the terrace edges to be easily removed by the solution.

The top exposed layers dissolved completely over about 74 minutes (between $t = 52 - 126$ minutes in Figure 3.17) followed at once by the newly exposed layers. Hence, this dissolution is called layer by layer dissolution mechanism. There was a moment when layers were exposed to a solution but not started to dissolve yet. During this induction period, the particles maintained their existence on the surface regardless of the solution attack. The induction period was reported to depend on supersaturation [19] and the solution used [5].

Another important feature to note from the dissolution of IM-17 crystal in NaOH solution is how the layer dissolved. From Figure 3.17, it is clear that the solution attack on (100) facet of IM-17 crystal leads to layer break down into small segments as clearly seen from the images at $t = 102$ minutes. The same proceeding was also experienced in zeolite A dissolution in alkali solution as reported by Meza *et al.* [5], [20]. It happened because the surface terminating particles on this facet are disconnected from the adjacent particles. This correlates very well with unlinked double 4-rings as the (100) surface termination of IM-17 crystal we suggested earlier as displayed in Figure 3.15 and Figure 3.13 (a).

Height measurements on some patches left during the dissolution process (see Figure 3.18) prove that IM-17 crystal's growth step (approximately 1.25 nm) did not dissolve at once but sub-layer by sub-layer as we found it broke down from 1.25 to 1.00, 0.70, and then 0.27 ± 0.1 nm. These heights exactly match the heights of the UOV structure break down as illustrated in Figure 3.20. Gradual retreat phenomenon is common during the zeolite dissolution process. Zeolite A and zeolite L have also been reported in detail to experience stepwise dissolution process in NaOH solution [2], [5], [20].

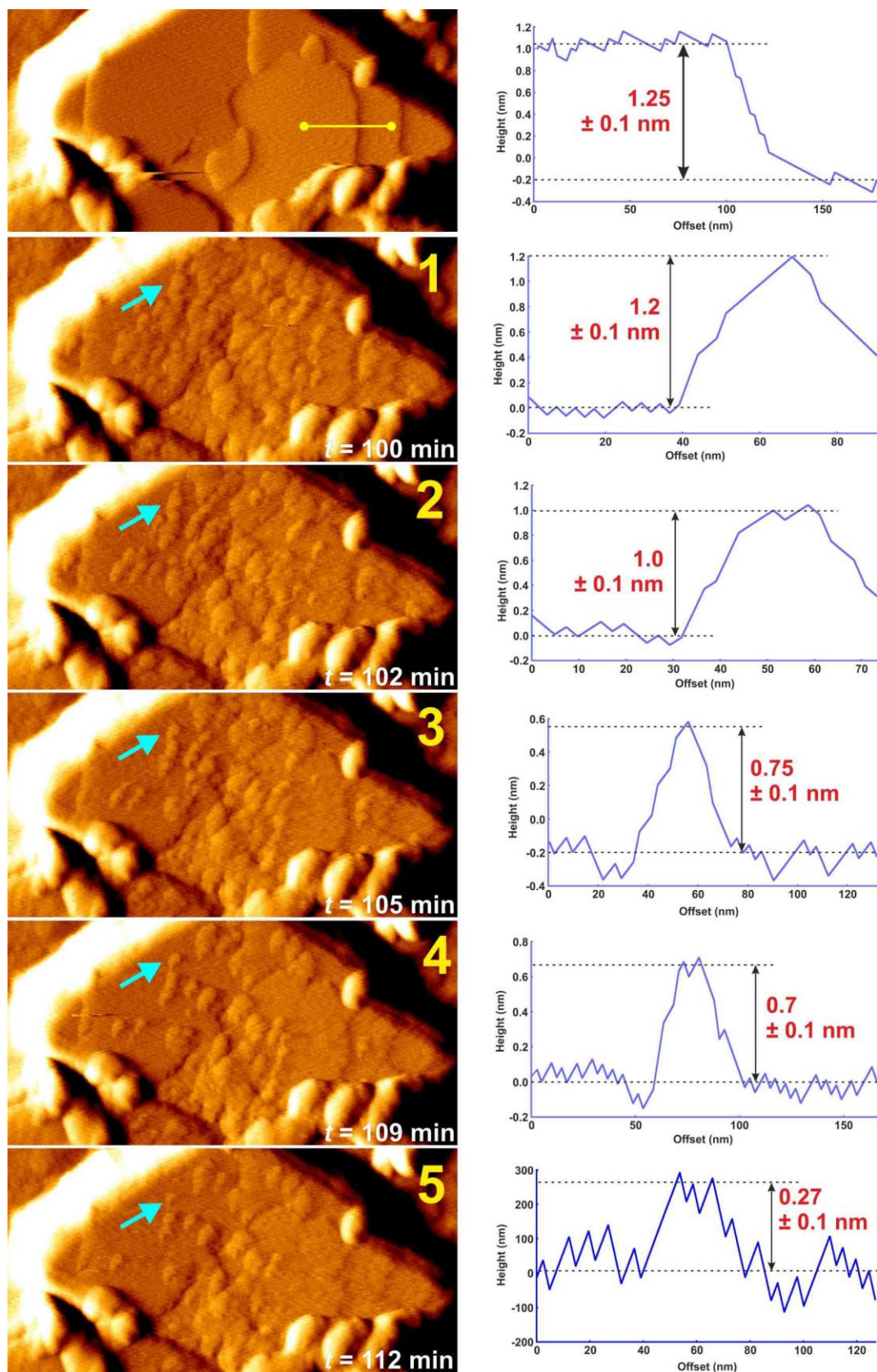


Figure 3.18. Subsequent vertical deflection AFM images of IM-17 crystal dissolution in 4 M NaOH solution with height measurement on the same spot. AFM image's size: $0.9 \mu\text{m} \times 0.5 \mu\text{m}$.

However, apart from those four levelled heights observed for the same spot in consecutive images, we also found a distinctive height from a different patch at a later time ($t = 115$ minutes), depicted in Figure 3.19. The segment height is 0.5 ± 0.1 nm, which also correlates with the 0.48 nm high of UOV structure break-down for this layer as illustrated in Figure 3.20.

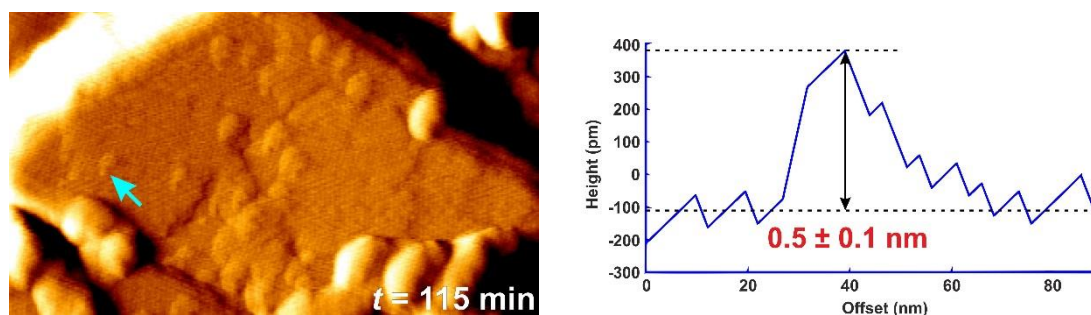


Figure 3.19. A vertical deflection AFM image of IM-17 crystal dissolution in 4 M NaOH solution at $t = 115$ min with one segment's height measurement.

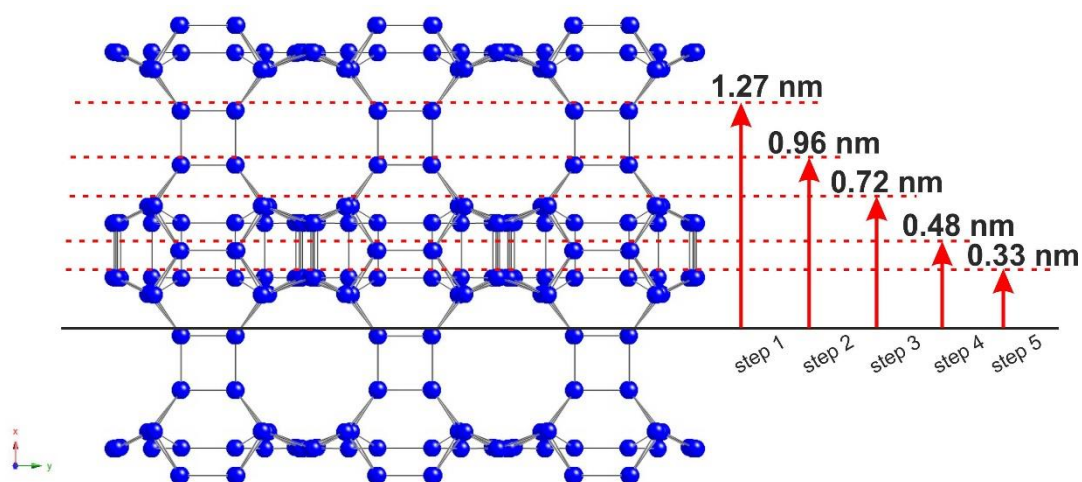


Figure 3.20. UOV structure viewed at (001) and its height breakdown.

To make it clearer, we illustrated the dissolution of this IM-17 crystal using tiling in Figure 3.21 to understand step by step crystal dissolution. However, it is crucial to note that the same tiles in the tiling illustration for this report can be distinctively coloured. As we can see in the diagram, the first units of the crystal dissolved in NaOH solution is the double 4-rings (t-cub) as the surface terminating particle. This

results in terrace break-down from 1.25 to 1.00 ± 0.1 nm (**step 1**). It is soon followed by the removal of t-kah, t-dmp, t-lau, t-umx, and t-mtw (**step 2**), making the height decreases to 0.70 ± 0.1 nm. Furthermore, the next growth units of the crystal dissolved in the solution are t-tes, t-mel, t-bru, t-nuh, t-uov-1, t-sfg-4, t-fvw (**step 3**), lowering the layer to 0.5 ± 0.1 nm high. After that, t-kah, t-dmp, t-lau, t-umx, and t-mtw are dissolved (**step 4**), which reduces the height even further down to 0.27 ± 0.1 nm. Finally, t-bal, t-iwr, and t-uov-2 are the last units collapsing in the solution (**step 5**).

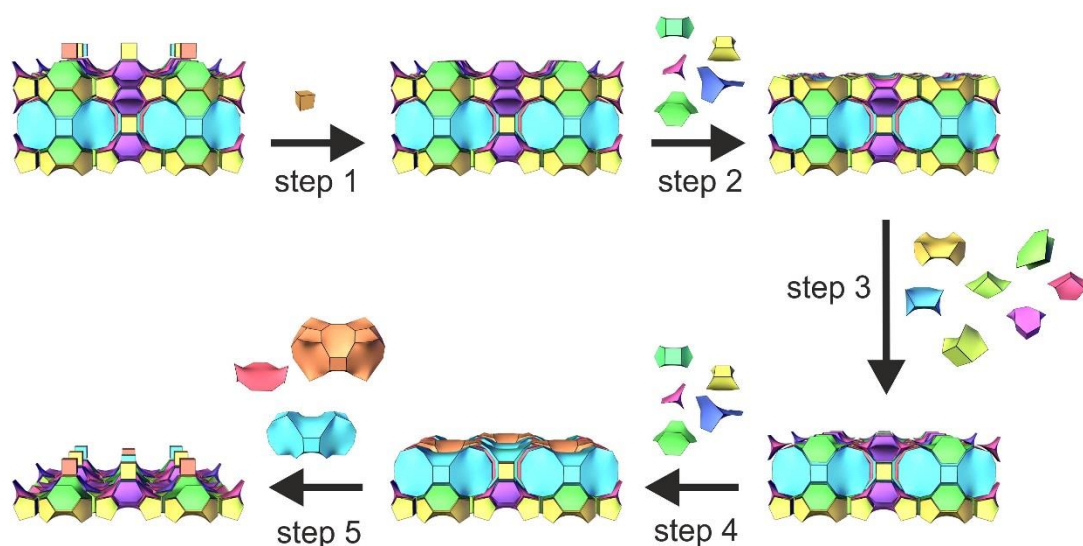


Figure 3.21. Schematic illustration of step by step IM-17 crystal dissolution on (100) facet drawn as tiling.

When dissolution took place for a long time, it was then able to break up the intergrowth crystals as observed in Figure 3.22 after immersion in a solution for 275 minutes. The small crystal (sized about $0.83 \mu\text{m}$ long) broke down into four even smaller rhombus-shaped single-crystals scaled around $0.3 - 0.4 \mu\text{m}$ long. This is also to prove that the IM-17 crystal synthesized in this experiment is very minute.

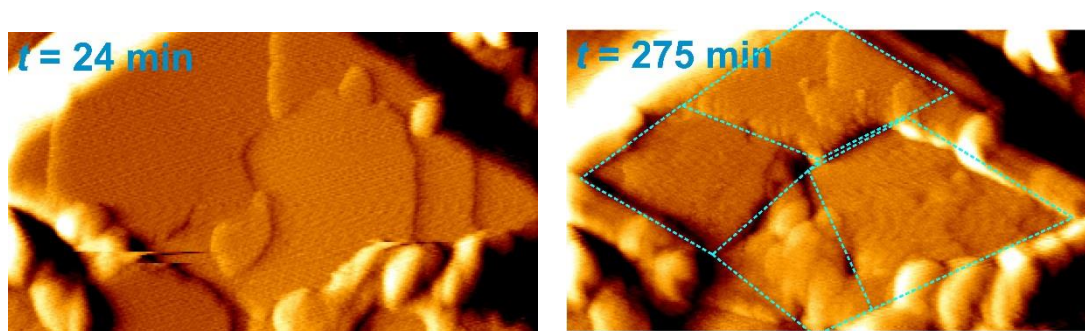


Figure 3.22. Comparison of AFM images of IM-17 crystal surface on (100) facet comparison before dissolution and after being dissolved for 275 minutes. Image width: 0.8 μm .

3.3.4.2. Simulation of IM-17 crystal dissolution on (100) facet

We managed to well simulate the dissolution process of IM-17 crystal using *CrystalGrower* program and viewed the result with *CG Visualiser*. Mimicking the lab experiment condition, in which the crystal was dissolved in an under-saturated solution, this simulation was also set to have much lower supersaturation than that in the equilibrium during the dissolution process of a fully grown crystal. The supersaturation in crystal simulation acts as a driving force to grow or dissolve the crystal.

Figure 3.23 displays the sequential images of simulation of the UOV crystal dissolution on (100) facet. This result is also presented in Movie 3-2 in Appendix 1. Small nuclei on the crystal surface are observed in the first image when the crystal has not yet been dissolved. These are then quickly dissolved as we no longer see them in image 12. Larger terraces are as expected to retreat slower than the small terraces or nuclei because of the large surface area that has to be dissolved. As observed experimentally, because of the unconnected double 4-rings as the surface terminal, the middle of the layer is able to be attacked creating holes which grow larger whilst the particles around them are being dissolved. This event can be clearly seen in image 14. Overall, the dissolution of UOV crystal simulated here is in a good agreement with the result from the laboratory experiment.

Nevertheless, in this simulation, $\Delta\mu$ was set to be 4.7 lower than $\Delta\mu_{\text{eq}}$ with the images taken every 50,000 iterations. Enlarging and reducing the gap between the $\Delta\mu$ in the dissolution system and $\Delta\mu_{\text{eq}}$ will increase and decrease, respectively, the dissolution rate.

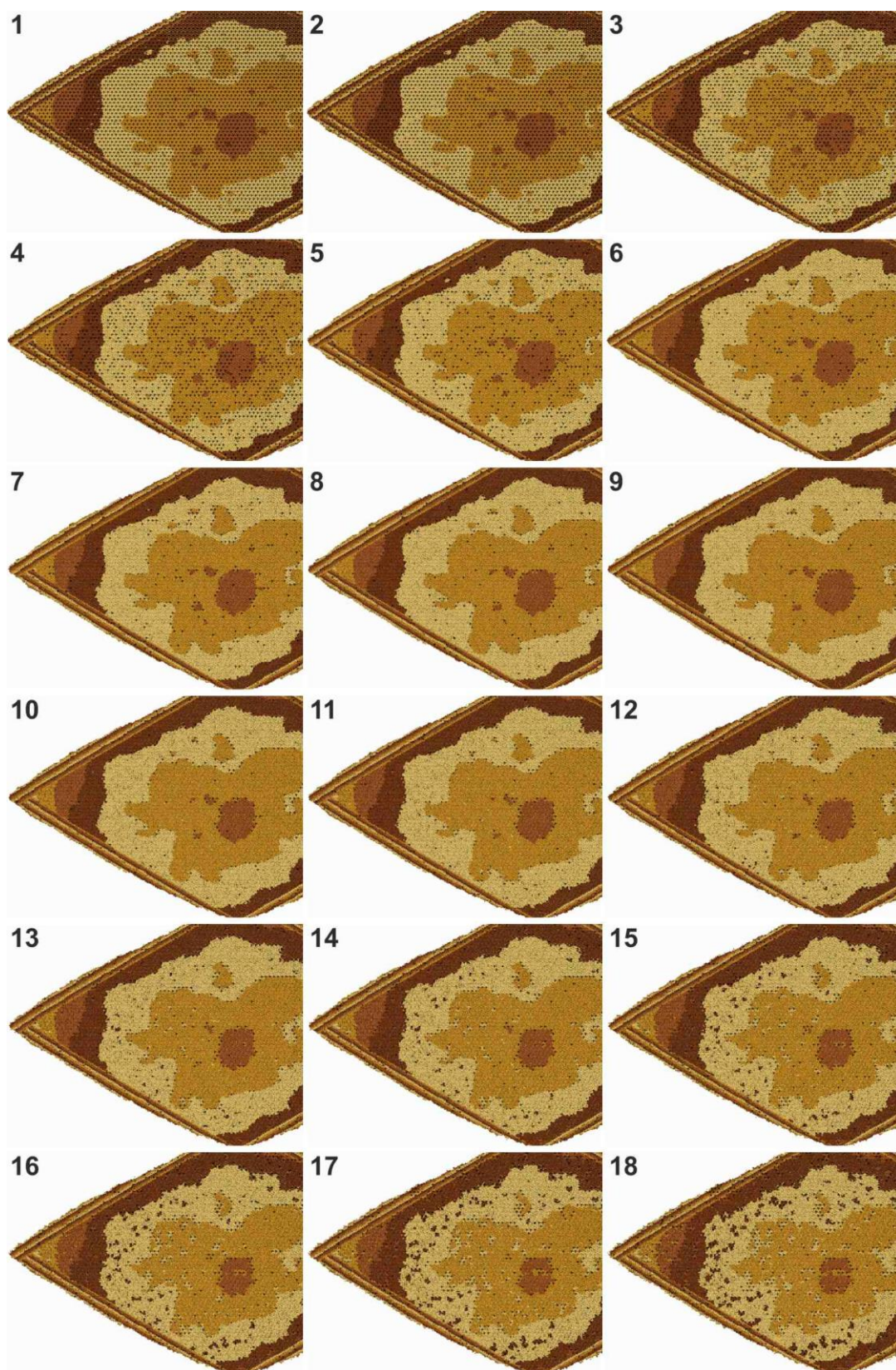


Figure 3.23. Subsequent images of IM-17 crystal dissolution simulation on (100) facet with $\Delta\mu_{eq} = 9.7$ and $\Delta\mu$ for dissolution = 5. The simulation was set with $\Delta U_s = 2 \text{ kcal mol}^{-1}$. The simulated crystal is *c.a.* $0.04 \text{ }\mu\text{m} \times 0.23 \text{ }\mu\text{m} \times 0.12 \text{ }\mu\text{m}$. The first image is the crystal before the dissolution started (*to be continued on the next page*).

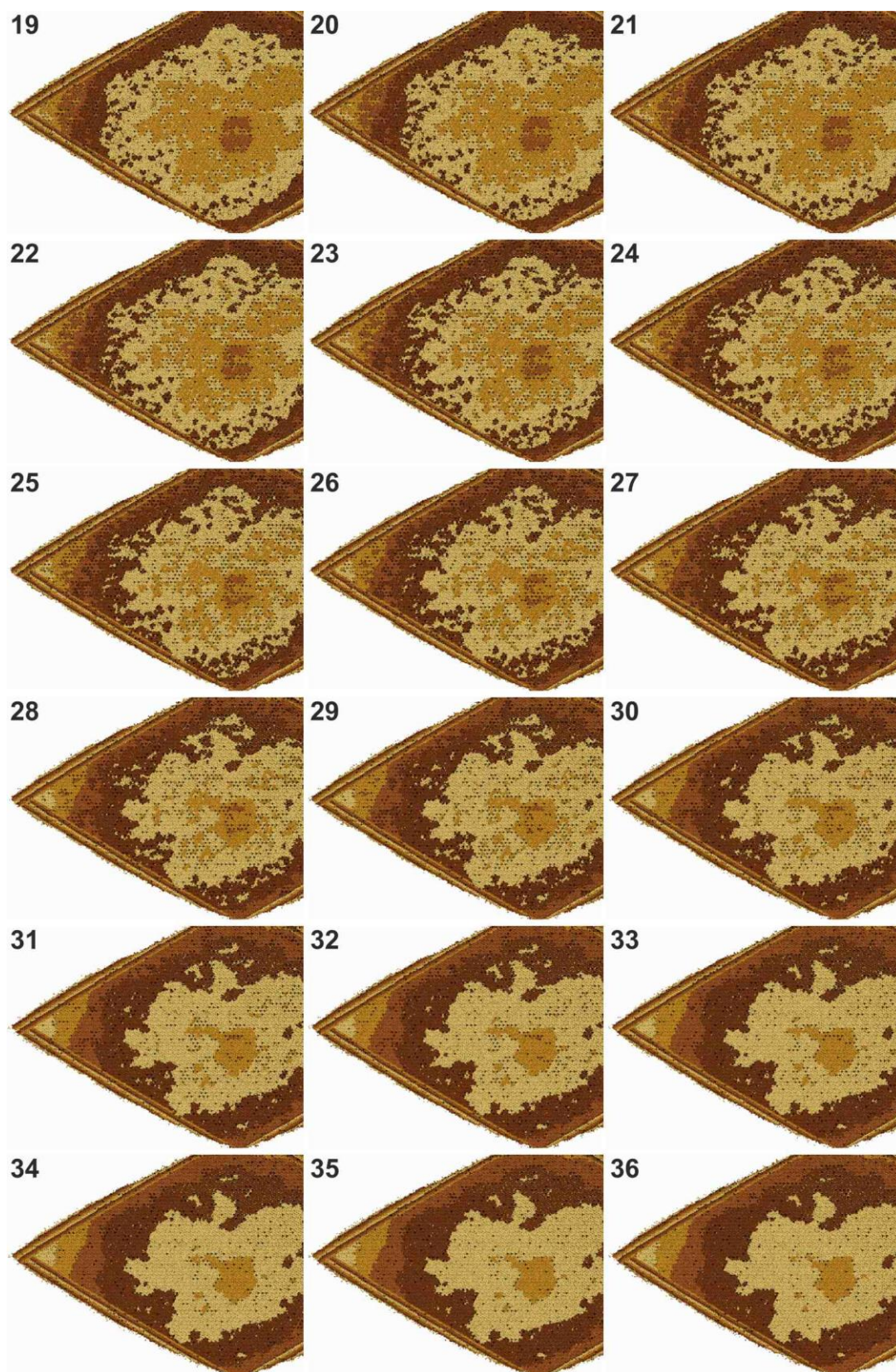


Figure 3.23 (continued). Subsequent images of IM-17 crystal dissolution simulation on (100) facet with $\Delta\mu_{\text{eq}} = 9.7$ and $\Delta\mu$ for dissolution = 5. The simulation was set with $\Delta U_s = 2 \text{ kcal mol}^{-1}$. The simulated crystal is *c.a.* $0.04 \mu\text{m} \times 0.23 \mu\text{m} \times 0.12 \mu\text{m}$. The first image is the crystal before the dissolution started (*to be continued on the next page*).

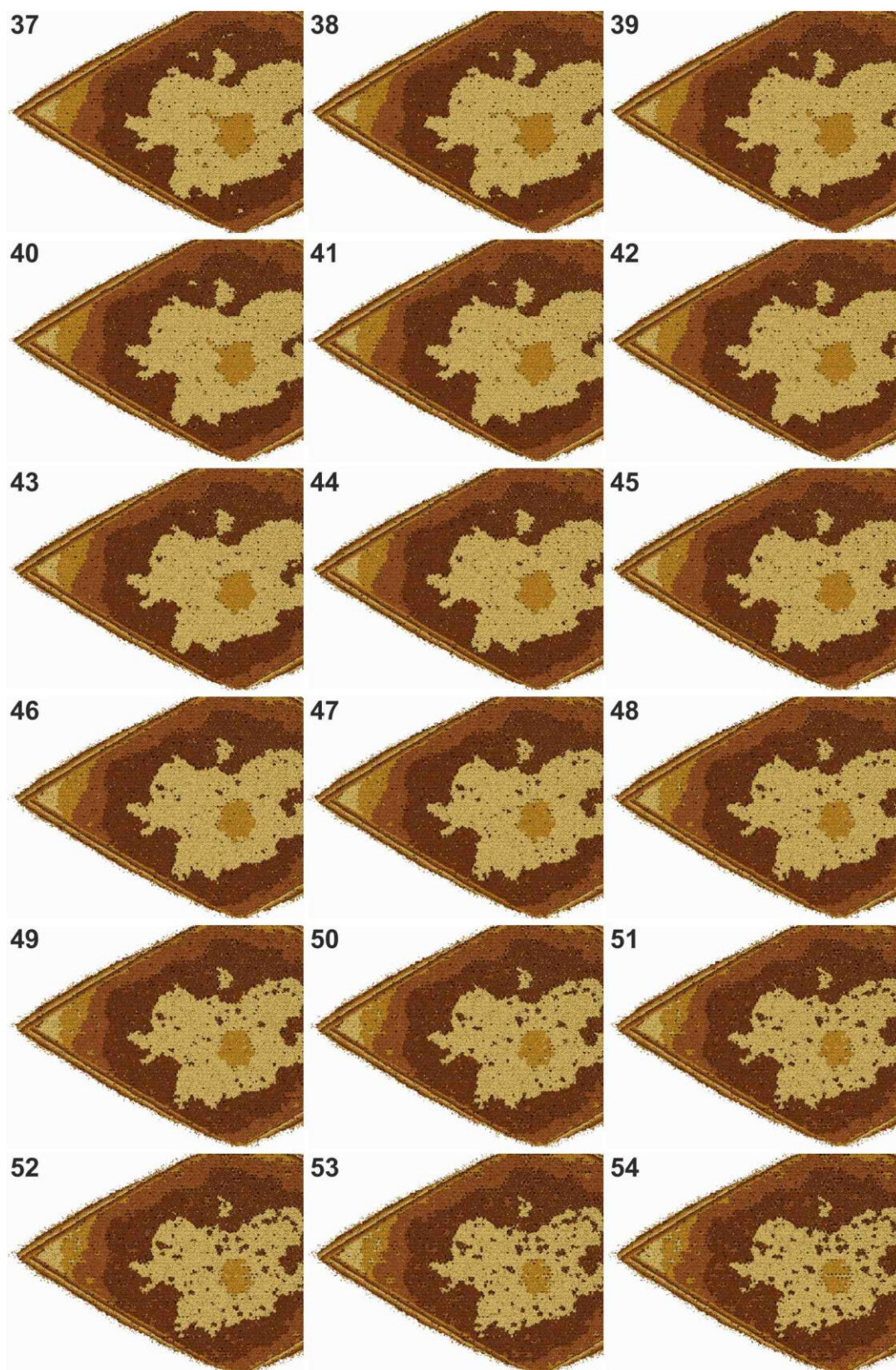


Figure 3.23 (continued). Subsequent images of IM-17 crystal dissolution simulation on (100) facet with $\Delta\mu_{\text{eq}} = 9.7$ and $\Delta\mu$ for dissolution = 5. The simulation was set with $\Delta U_s = 2 \text{ kcal mol}^{-1}$. The simulated crystal is *c.a.* $0.04 \mu\text{m} \times 0.23 \mu\text{m} \times 0.12 \mu\text{m}$. The first image is the crystal before the dissolution started.

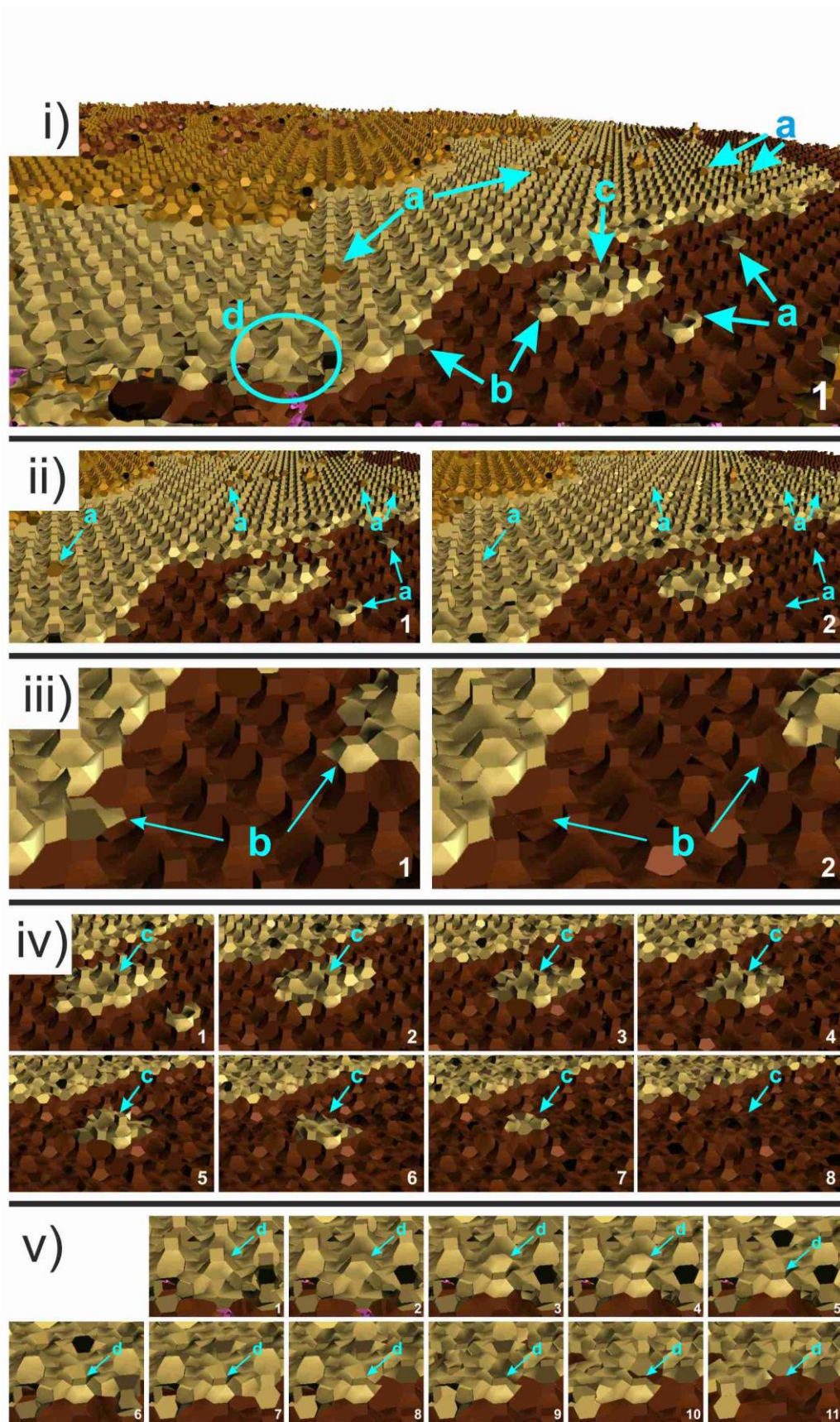


Figure 3.24. i–v) A closer look at (100) facet of the simulation of UOV crystal dissolution. Image number 1 shows the surface before dissolution begins, the rests are the consecutive images of the dissolution event.

To investigate the dissolution process in more detail, it is necessary to take a closer look at the crystal surface during the process in this simulation. Here we can observe that dissolution of one layer is going step by step. This meets very well with our findings from the lab work.

Figure 3.24 (i) zooms in the (100) facet of simulated UOV crystal before dissolution process with some features labelled to be explained here. In section (ii), “a” in image 1 denotes the single nucleations existed on crystal surface. These single nucleations are dissolved at once when the dissolution started in image 2. Similar to this single nucleation on the crystal surface, in section (iii) we can see that particles attached on steps (marked with “b” in image 1), which are not fully grown yet to be the same height as the layer, also easily disappear once the dissolution process begins in image 2. On the other hand, a small island (labelled “c” in section (iv)) formed from early grown nucleation on crystal surface retreats a little bit longer than the single nucleation as we can see in this simulation that it completely vanished in image 8.

Moreover, in section (v), we can observe how the layer gradually dissolved and this very much in agreement with the lab result and analysis we presented in section 3.3.4.1. Starting with the removal of double 4-rings from the layer topmost, the dissolution continues step by step to the crystal parts below the double 4-ring until all parts as high as the layer’s height is dissolved in image 11.

3.3.4.3. Dissolution of screw dislocation on (100) facet of the IM-17 crystal

A laboratory experiment on dissolving IM-17 crystal also successfully revealed screw dislocation and its dissolution on (100) crystal facet as depicted in Figure 3.25 and Movie 3-3 in Appendix 1. Overall, similarly to (100) facet without screw dislocation, the dissolution of (100) facet of IM-17 crystal with the presence of screw dislocation also happened following layer by layer dissolution mechanism because the solution dissolved each layer laid open to it before dissolving the newly revealed layers.

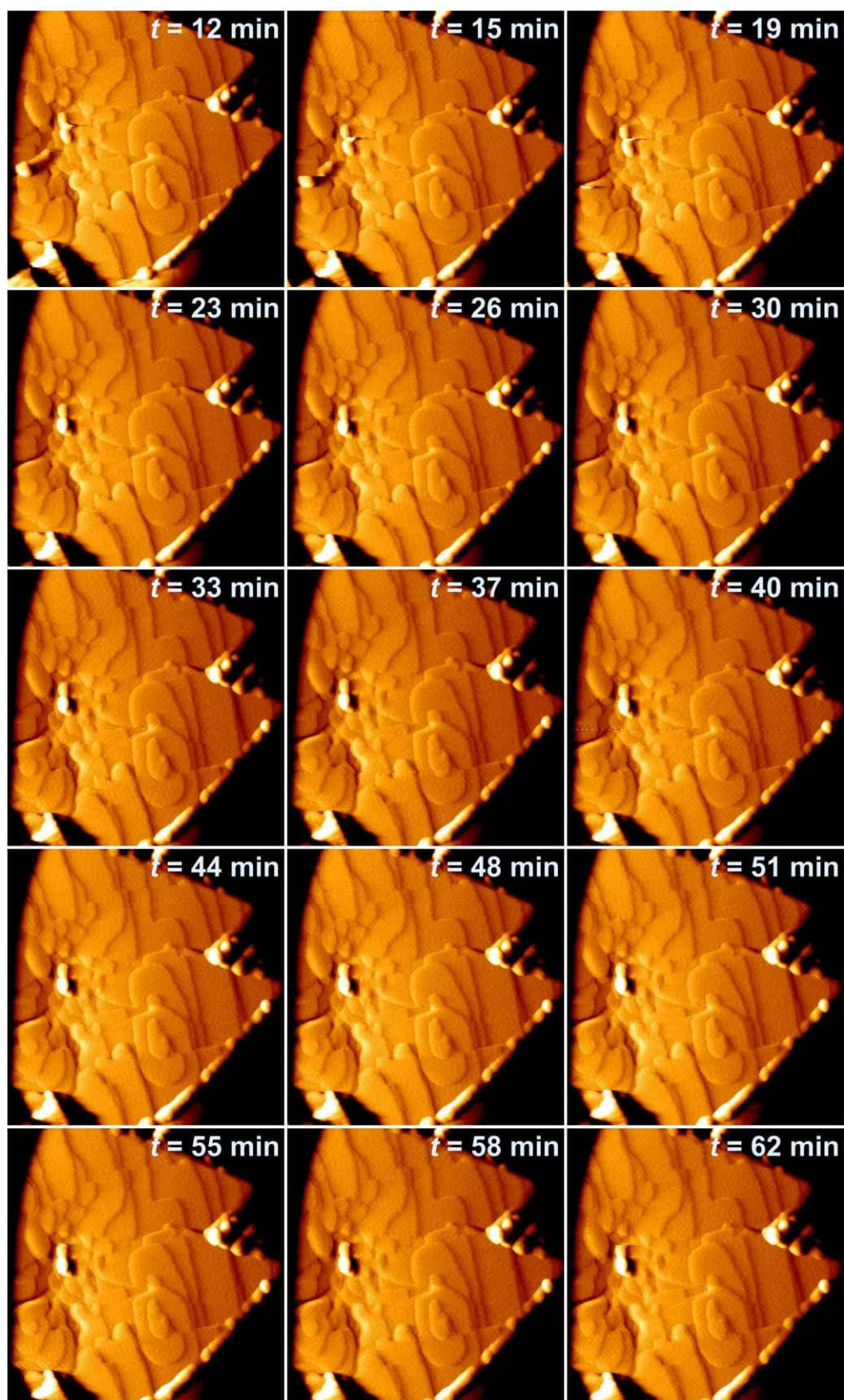


Figure 3.25. Dissolution process of IM-17 crystal with screw dislocation in 4 M NaOH solution. Scanned area: $1.9\ \mu\text{m} \times 1.9\ \mu\text{m}$ (to be continued on the next page).

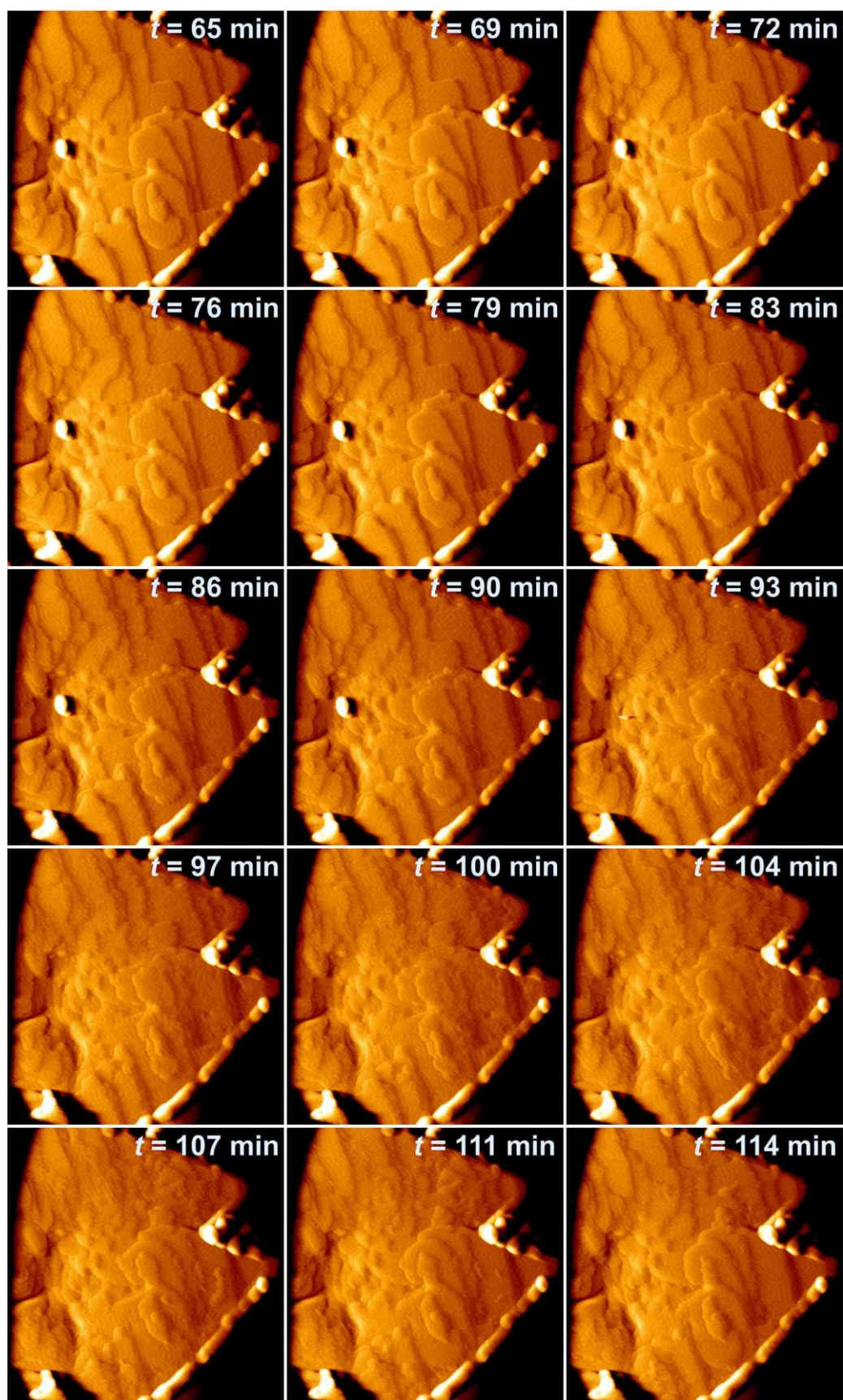


Figure 3.25 (continued). Dissolution process of IM-17 crystal with screw dislocation in 4 M NaOH solution. Scanned area: $1.9\ \mu\text{m} \times 1.9\ \mu\text{m}$ (*to be continued on the next page*).

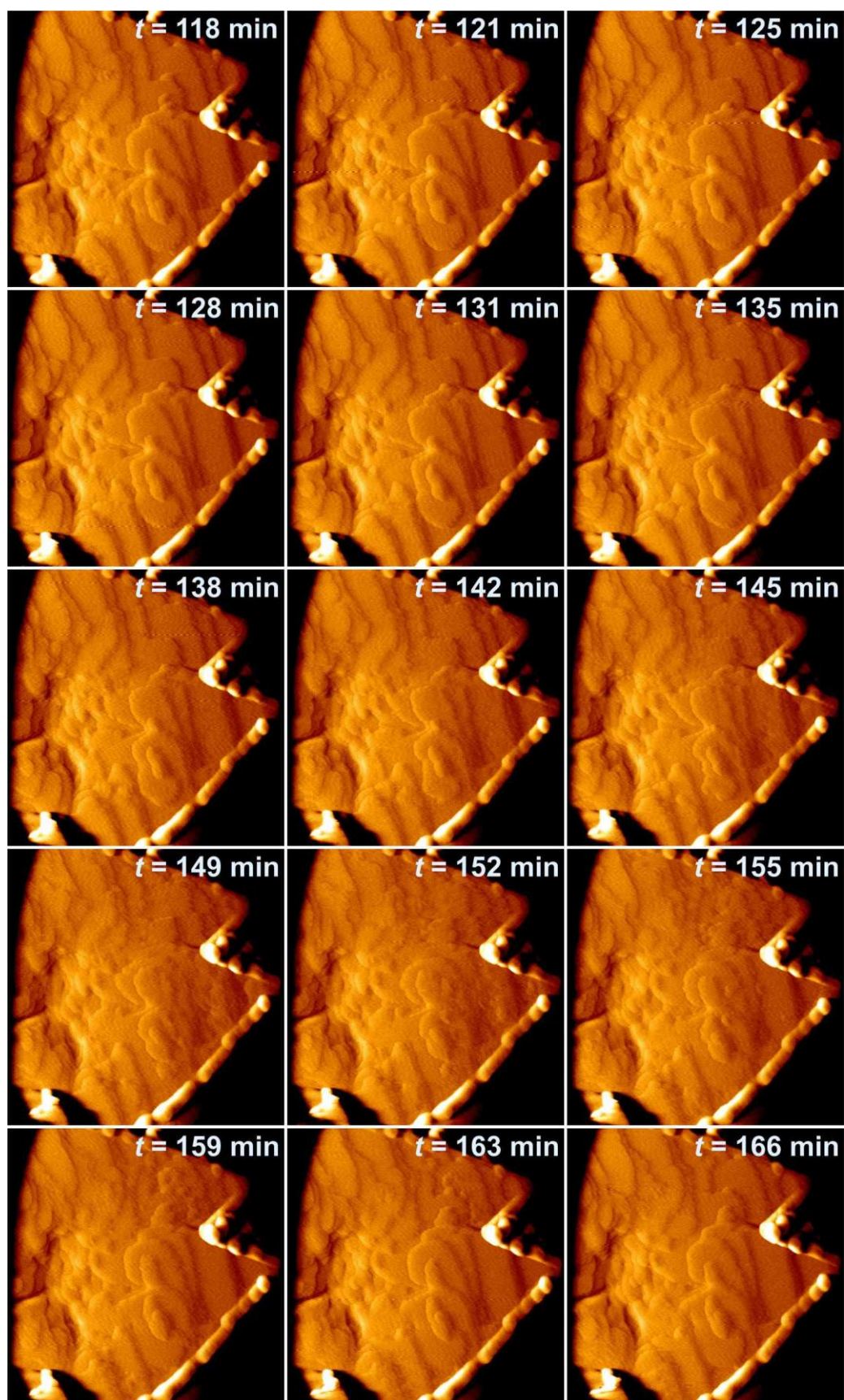


Figure 3.25 (continued). Dissolution process of IM-17 crystal with screw dislocation in 4 M NaOH solution. Scanned area: $1.9\ \mu\text{m} \times 1.9\ \mu\text{m}$ (*to be continued on the next page*).

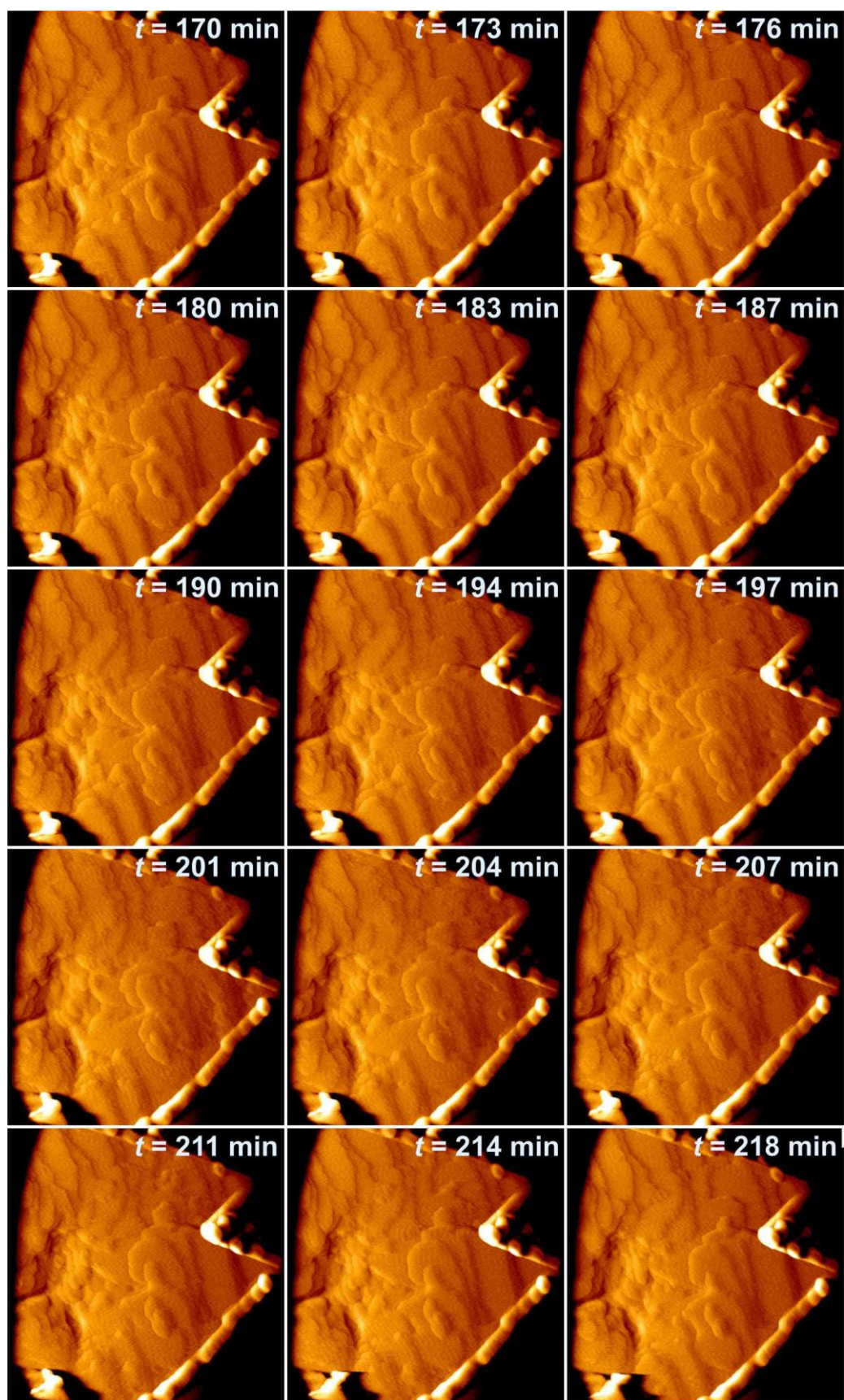


Figure 3.25 (continued). Dissolution process of IM-17 crystal with screw dislocation in 4 M NaOH solution. Scanned area: $1.9\ \mu\text{m} \times 1.9\ \mu\text{m}$ (*to be continued on the next page*).

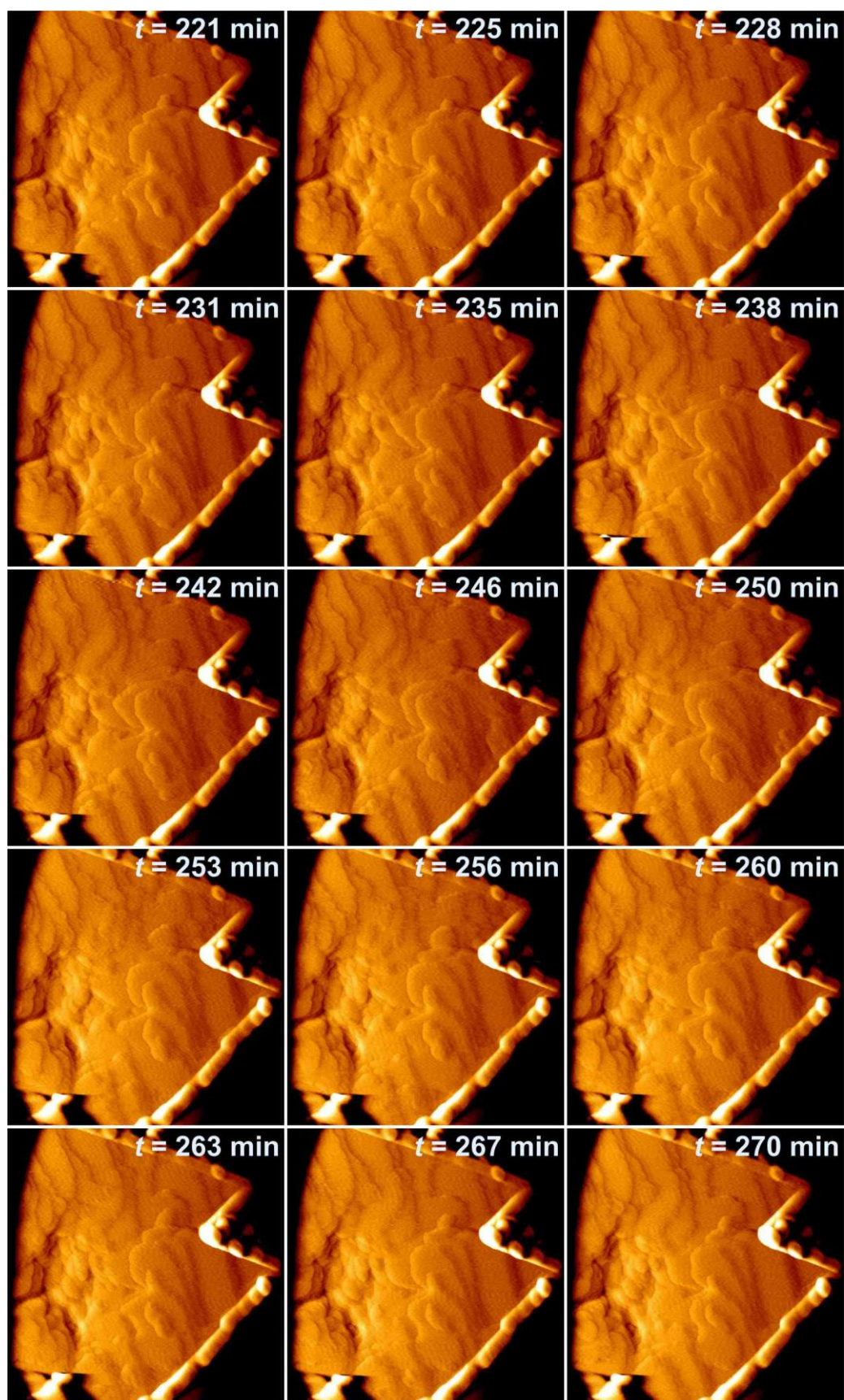


Figure 3.25 (continued). Dissolution process of IM-17 crystal with screw dislocation in 4 M NaOH solution. Scanned area: $1.9\ \mu\text{m} \times 1.9\ \mu\text{m}$.

In addition, on some flat surface of the (100) facet (the area without screw dislocations) depicted in Figure 3.25, the dissolution seems to occur in patches like the dissolution of (100) facet without screw dislocation. Images at $t = 97 - 114$ minutes (enlarged for clarity in Figure 3.26) vividly exhibit how this patches dissolution went on. The solution attacked the crystal leaving pits, marked with yellow arrows, on its even surface. As the dissolution process advanced, the pits were getting larger resulting in the formation of small islands, indicated with cyan arrows, which soon disappeared at $t = 114$ minutes.

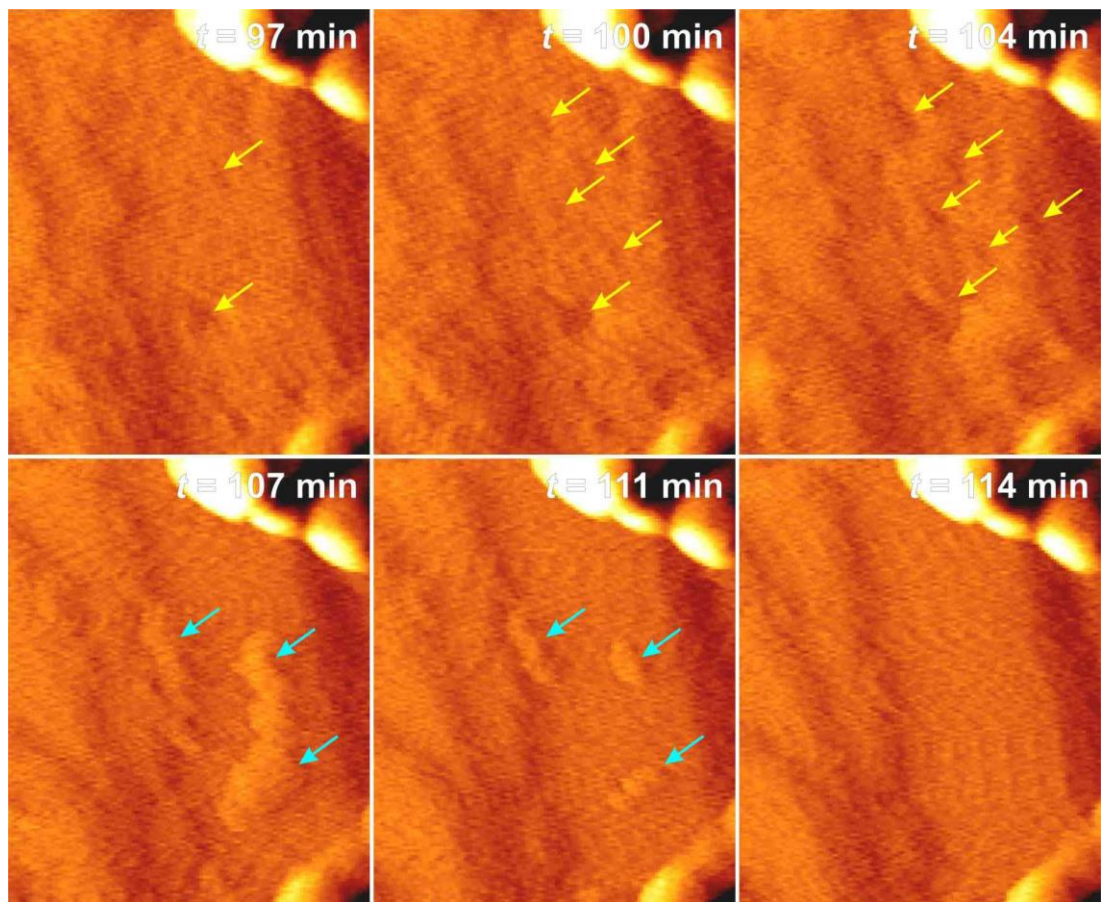


Figure 3.26. A closer look at some images in Figure 3.25 ($t = 97 - 114$ min) revealing how IM-17 particles on (100) surface next to the screw dislocation dissolved in patches. Yellow arrows indicate pits created by the solution attack on the crystal surface, whilst cyan arrows show the crystal particles left on the surface during the dissolution process. AFM image's size: $0.5 \mu\text{m} \times 0.7 \mu\text{m}$.

On the other hand, the area near the screw dislocations on this particular (100) facet in Figure 3.25, seems to be dissolved more consecutively so that the spiral is

maintained during the process. This may be a result of the spiral layer's surface which is not flat because of spiral growth. Owing to this un-flattened position, the double 4-rings on the surface get closer, or even connected, to the particles adjacent to them. As a consequence, the layer dissolution is found to be consecutive.

At $t = 40$ minutes, the end of the spiral started to dissolve by the solution before the other parts of the crystal surface did (see Figure 3.27 for clarity). This is as expected since the end of the spiral is the loosest units which can be easily detached by the solution. However, due to the high concentration of the NaOH solution used in this experiment, soon after the end of the spiral dissolved, the edges of all terraces started to dissolve as well.

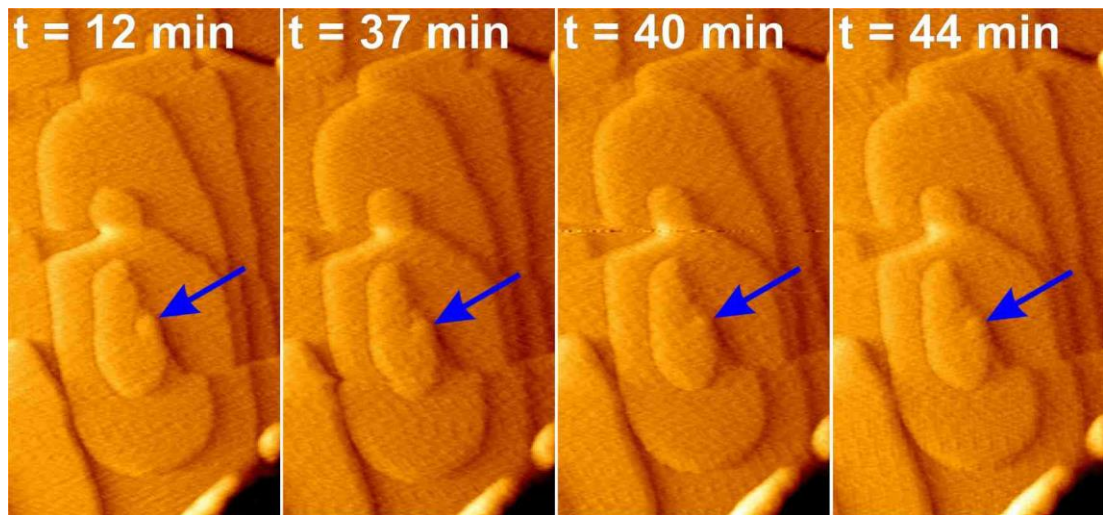


Figure 3.27. Vertical deflection AFM images (sized $0.6 \mu\text{m} \times 1.1 \mu\text{m}$) revealing starting events of dissolution of the spiral's end.

Height measurements performed for this dissolution event are displayed in Figure 3.28 for two consecutive images at $t = 107$ and 111 minutes. The height of the small segments in this event shows a good correlation with that without screw dislocation as we found equal small segment's heights. From around 1.25 nm of full height, the layer was dissolved creating $0.9 \pm 0.1 \text{ nm}$ as observed in the first image along line 3. This segment was then dissolved completely in the second image as the dissolution occurred very fast. Segments with $0.7 \pm 0.1 \text{ nm}$ and $0.75 \pm 0.1 \text{ nm}$ high were also discovered in the first image along line 1 and 2. These patches were eventually

broken down in the second image to 0.45 ± 0.1 nm and 0.3 ± 0.1 nm, respectively. Other small segments with height around 0.3 nm were also found in the first image (line 4, height = 0.35 ± 0.1 nm) and in the second image (line 5, height = 0.33 ± 0.1 nm).

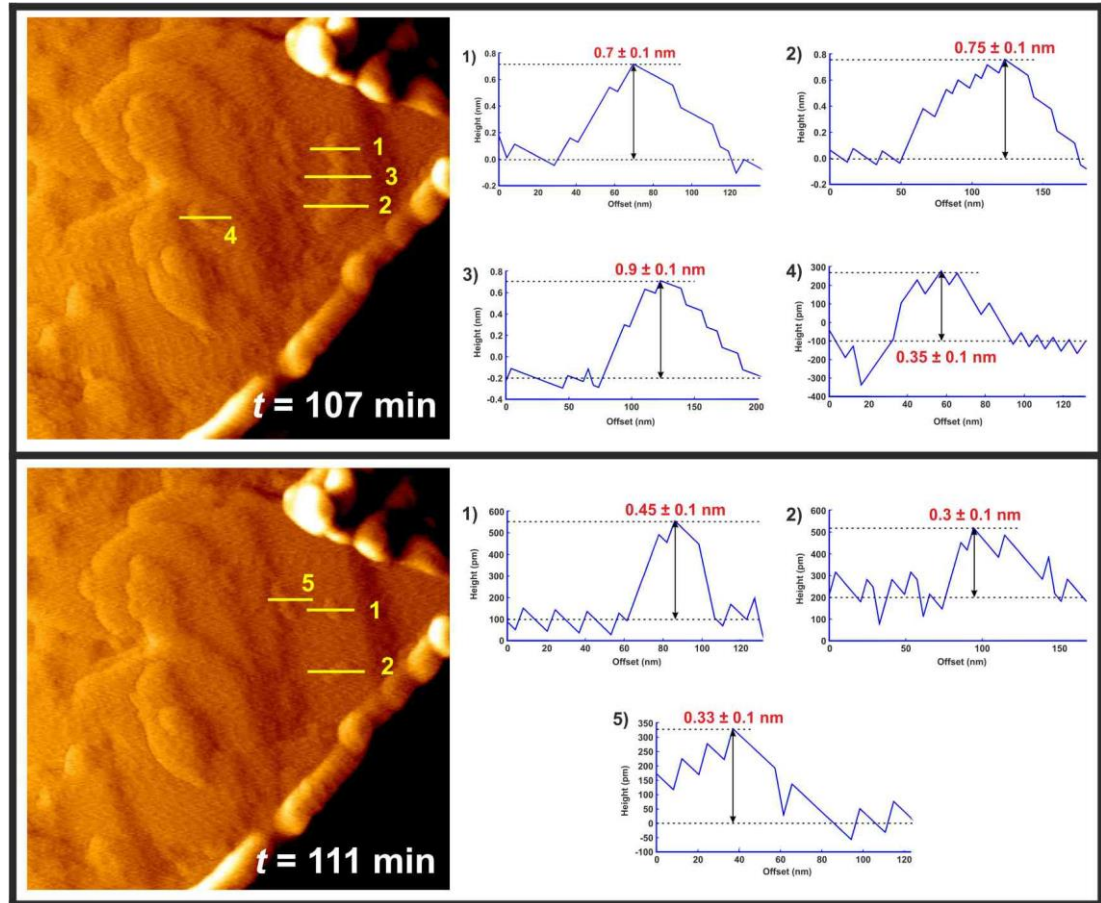


Figure 3.28. Height measurements on small segments of sequential AFM images of IM-17 crystal's (100) facet dissolution.

Not all of the height level in the UOV structure breakdown for this (100) facet was detected in one image sequence at a fixed spot. This is because the high concentration of NaOH solution used in the experiment allowed quick layer dissolution so that the AFM tip did not have a chance to scan every step by step structure breakdown. Or else, it was too difficult for us to measure the height owing to the very small segments' size and the uneven crystal surface.

3.3.4.4. *Dissolution of (013) facet of the IM-17 crystal*

Sodium hydroxide solution having 3 M concentration was used in an experiment to dissolve IM-17 crystal on its (013) facet of which result is presented in Figure 3.29 and Movie 3-4 in Appendix 1. Here, we clearly see that (013) facet of IM-17 crystal, although it is observed to have faults on it, dissolved layer by layer in 3 M NaOH solution. Even though early stages of this dissolution event is not very clear owing to the noise of the AFM scanning, we can still see that the crystal surface started to dissolve at 25 minutes in contact with the solution. This proves that (013) facet of the IM-17 crystal, as well as the (100) facet, is quite resilient in 3 – 4 M NaOH solution.

As seen also in the dissolution of (100) facet of IM-17 crystal, this high concentrated NaOH solution dissolved every crystal surface exposed to it. Anyhow, during the dissolution process, each layer was obviously observed to retreat separately. This indicates that the IM-17 crystal dissolution on (013) surface in NaOH solution occurred following layer by layer mechanism.

In the dissolution event of (013) facet of IM-17 crystal, surface dissolution was started from the terrace's borders (each end of the layers, as shown in Figure 3.29) and moved toward the face centre. Such phenomenon has also been observed by Meza et al [5]. As explained in Kossel model [18], in a growth state, which may be related to the reverse event of the dissolution, the growth unit will be likely to attach to terrace's border (or we call it "step") and kink sites rather than to terrace surface. This is due to step and kink sites offer more stable configuration as the incoming growth unit will form more than one bond at these positions. Hence, for the same reason, we may expect a high probability of the dissolution to start taking place at edge site or terrace's border rather than at the bulk surface because particles in bulk surface form five bonds, more than four and three bonds formed on step and kink sites, respectively. Hence, step and kink sites are more unstable, thus more prone to solution attack.

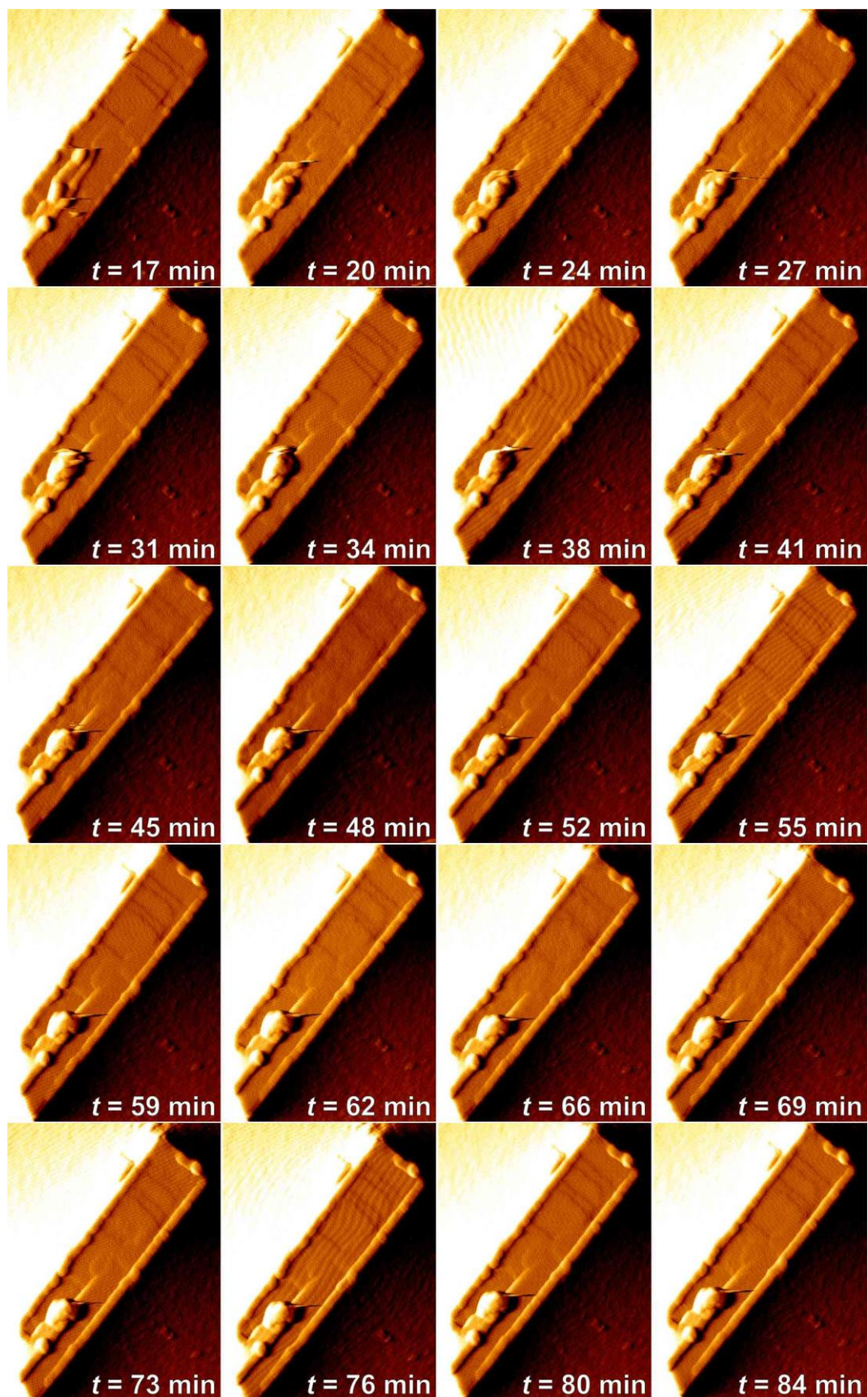


Figure 3.29. Subsequent vertical deflection AFM images showing (013) facet of IM-17 crystal with faults dissolved in 3 M NaOH solution. Scanned area: $0.9\ \mu\text{m} \times 1.2\ \mu\text{m}$ (to be continued on the next page).

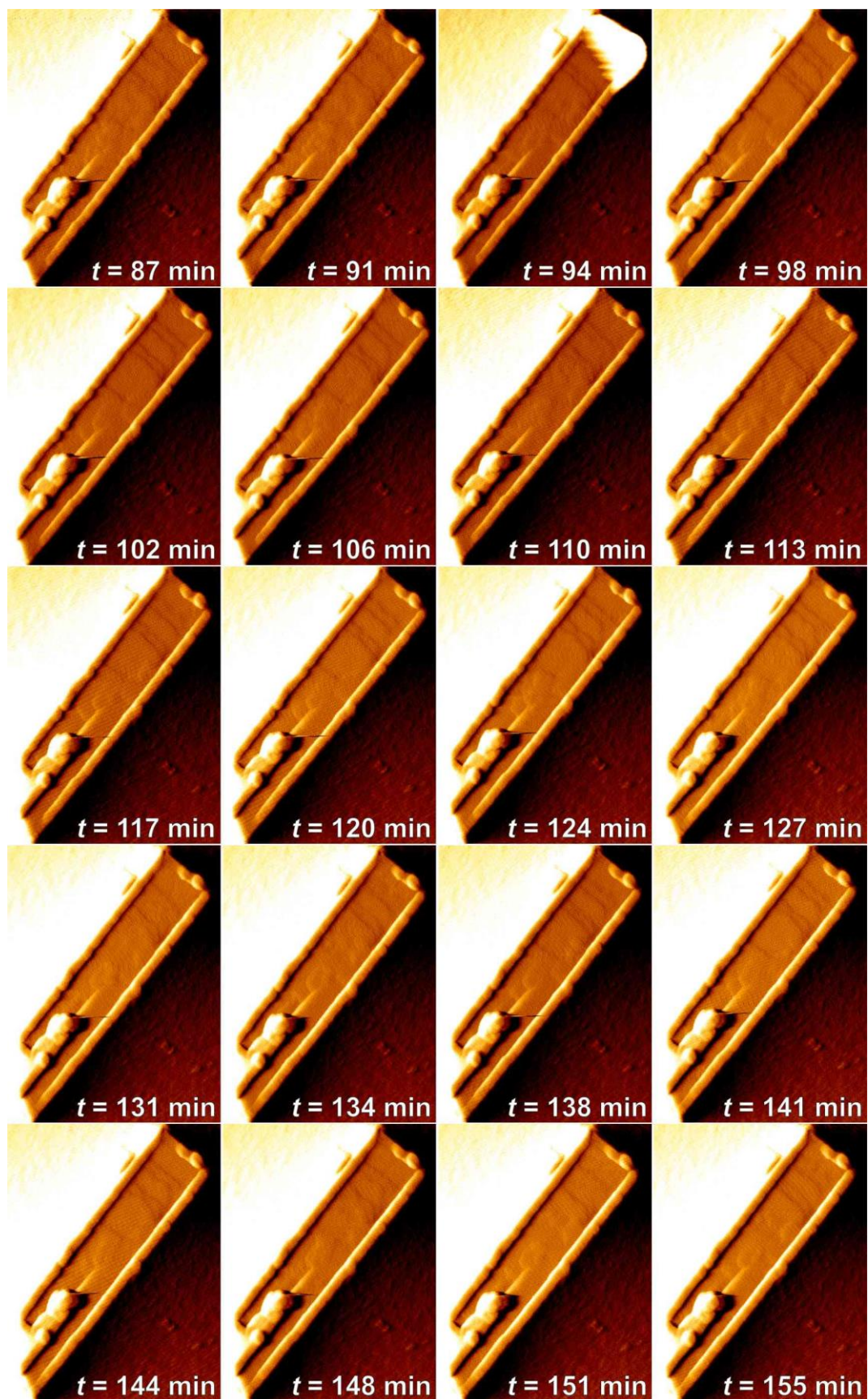


Figure 3.29 (continued). Subsequent vertical deflection AFM images showing (013) facet of IM-17 crystal with faults dissolved in 3 M NaOH solution. Scanned area: $0.9 \mu\text{m} \times 1.2 \mu\text{m}$ (to be continued on the next page).

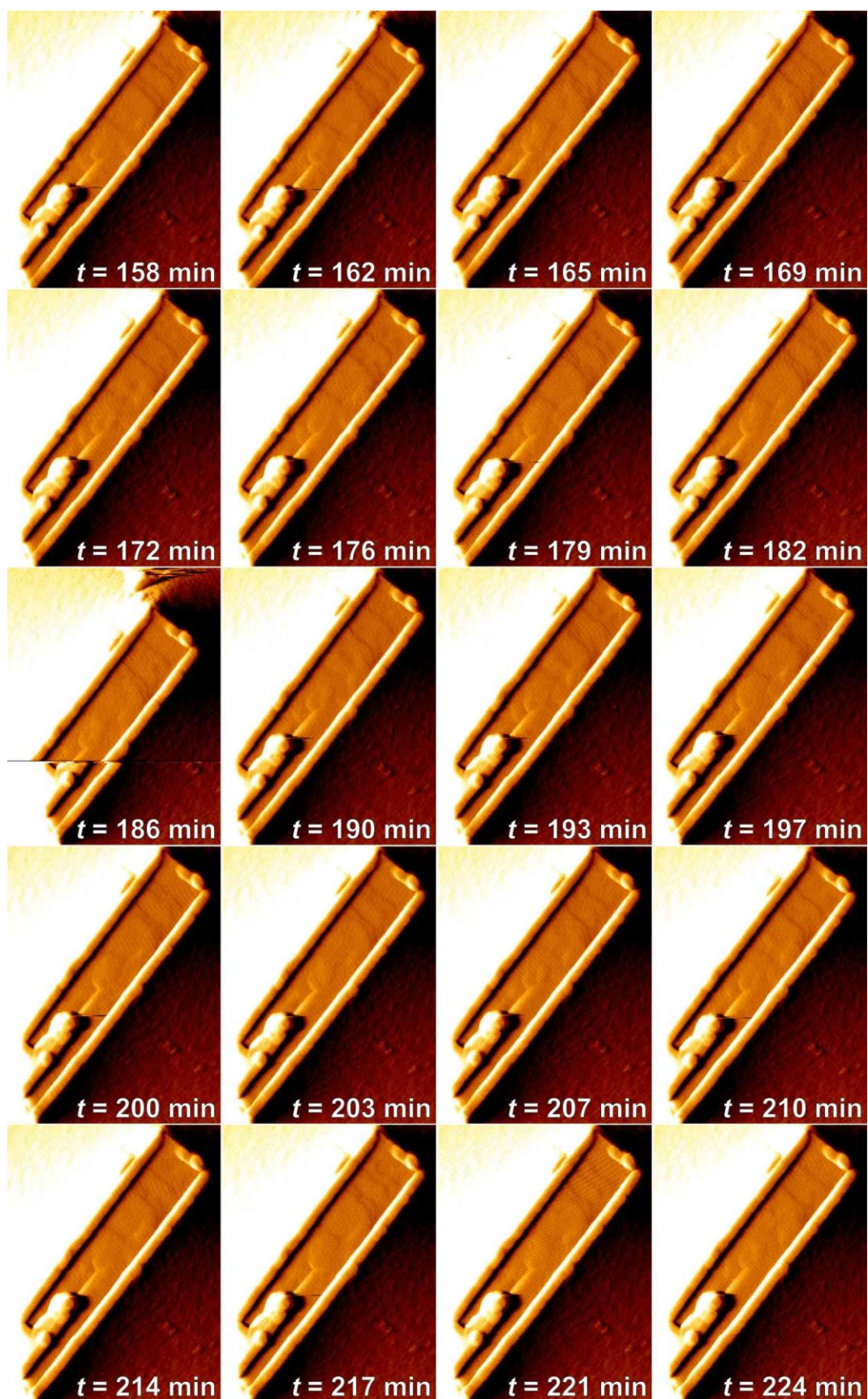


Figure 3.29 (continued). Subsequent vertical deflection AFM images showing (013) facet of IM-17 crystal with faults dissolved in 3 M NaOH solution. Scanned area: $0.9 \mu\text{m} \times 1.2 \mu\text{m}$ (to be continued on the next page).

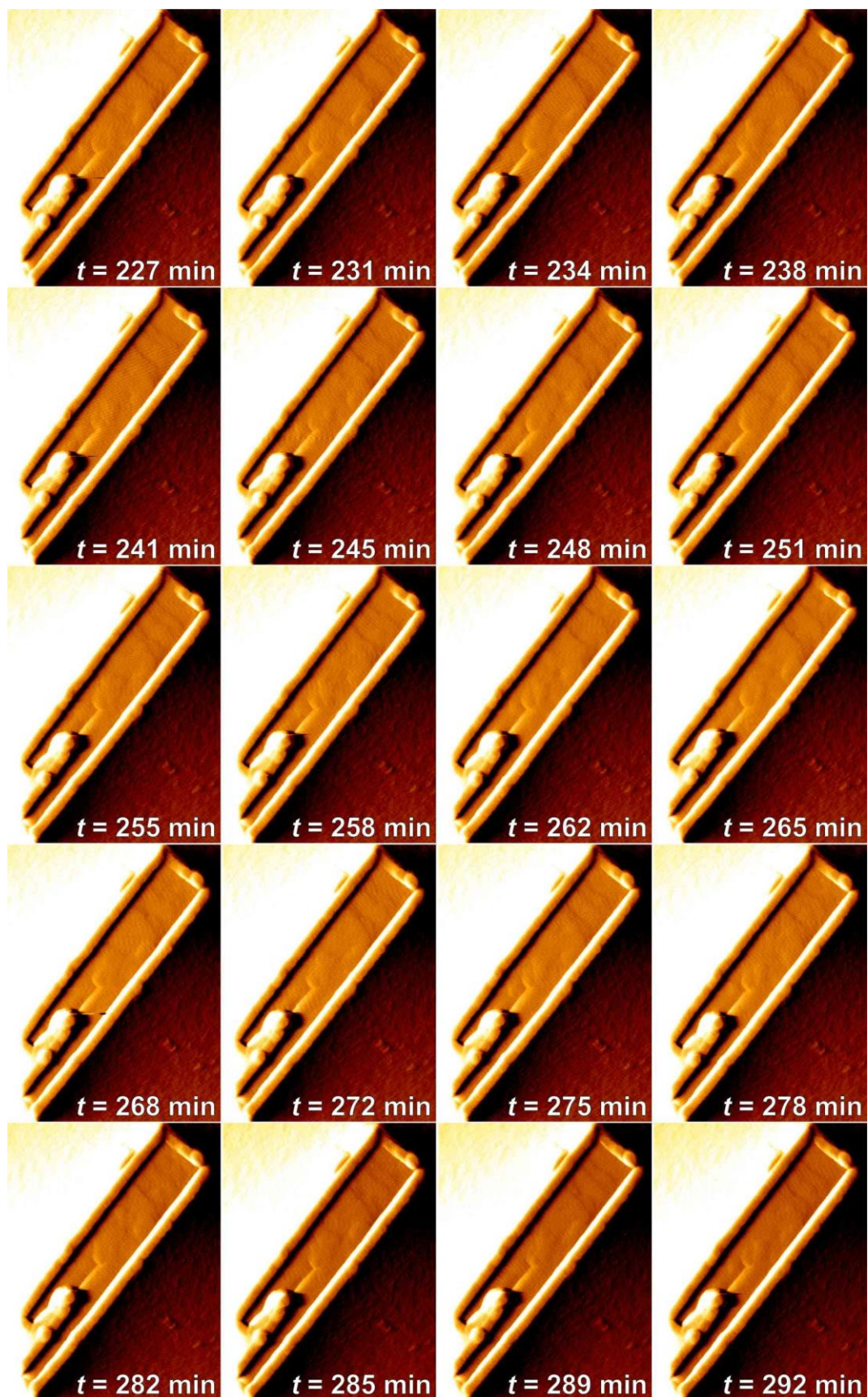


Figure 3.29 (continued). Subsequent vertical deflection AFM images showing (013) facet of IM-17 crystal with faults dissolved in 3 M NaOH solution. Scanned area: $0.9\ \mu\text{m} \times 1.2\ \mu\text{m}$ (*to be continued on the next page*).

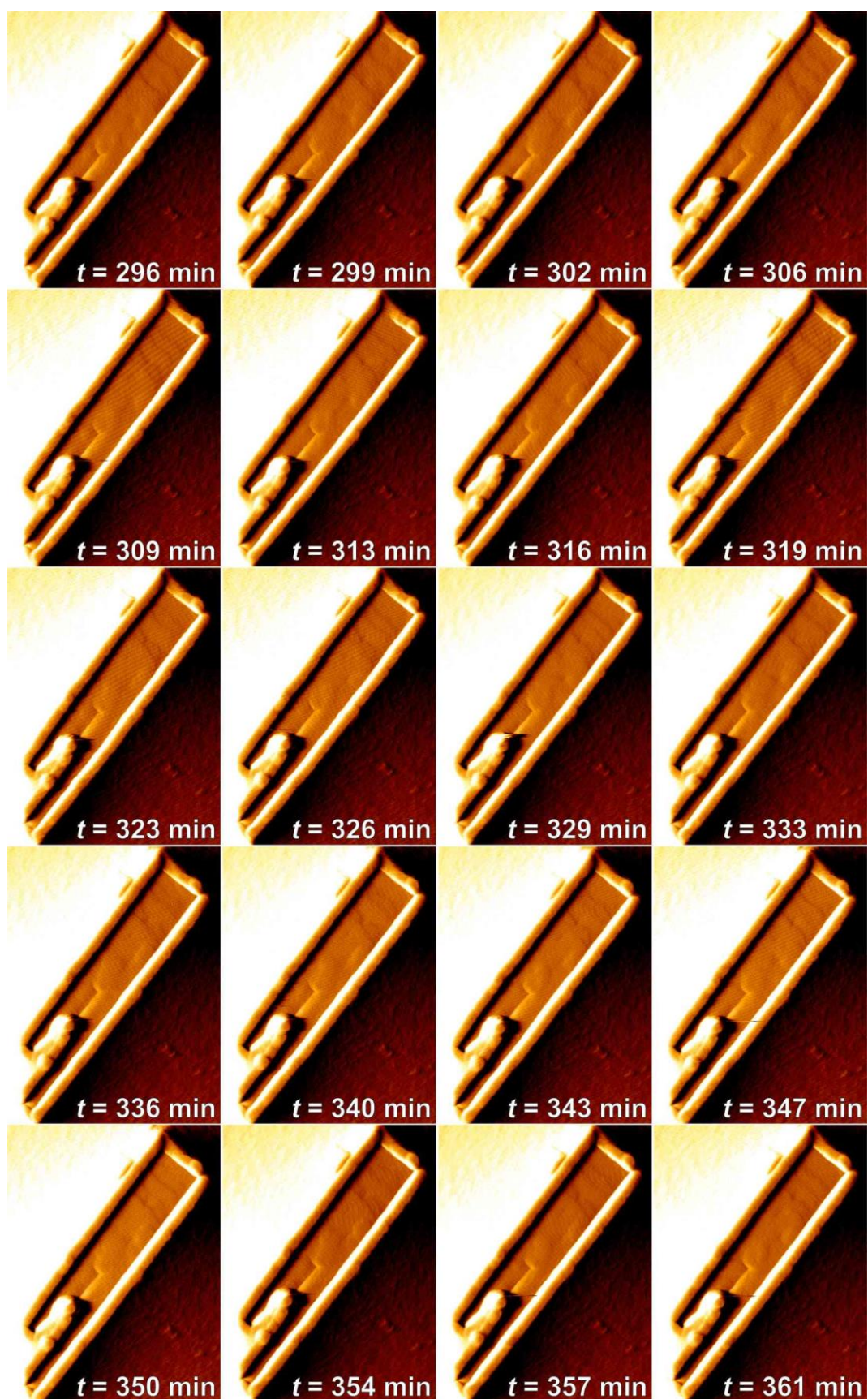


Figure 3.29 (continued). Subsequent vertical deflection AFM images showing (013) facet of IM-17 crystal with faults dissolved in 3 M NaOH solution. Scanned area: $0.9 \mu\text{m} \times 1.2 \mu\text{m}$.

Distinctively from the dissolution event on (100) facet which occurred in patches (uncorrelated dissolution), the dissolution process on this (013) facet followed consecutive dissolution in which the terraces retreated towards the face centre instead of being cut into smaller pieces. The reason why this happened is that the (013) surface terminals are linked together, not separated as the double 4-rings in (100) crystal surface. Thus, the surface particles were withdrawn by the solution from edges and moved toward the centre.

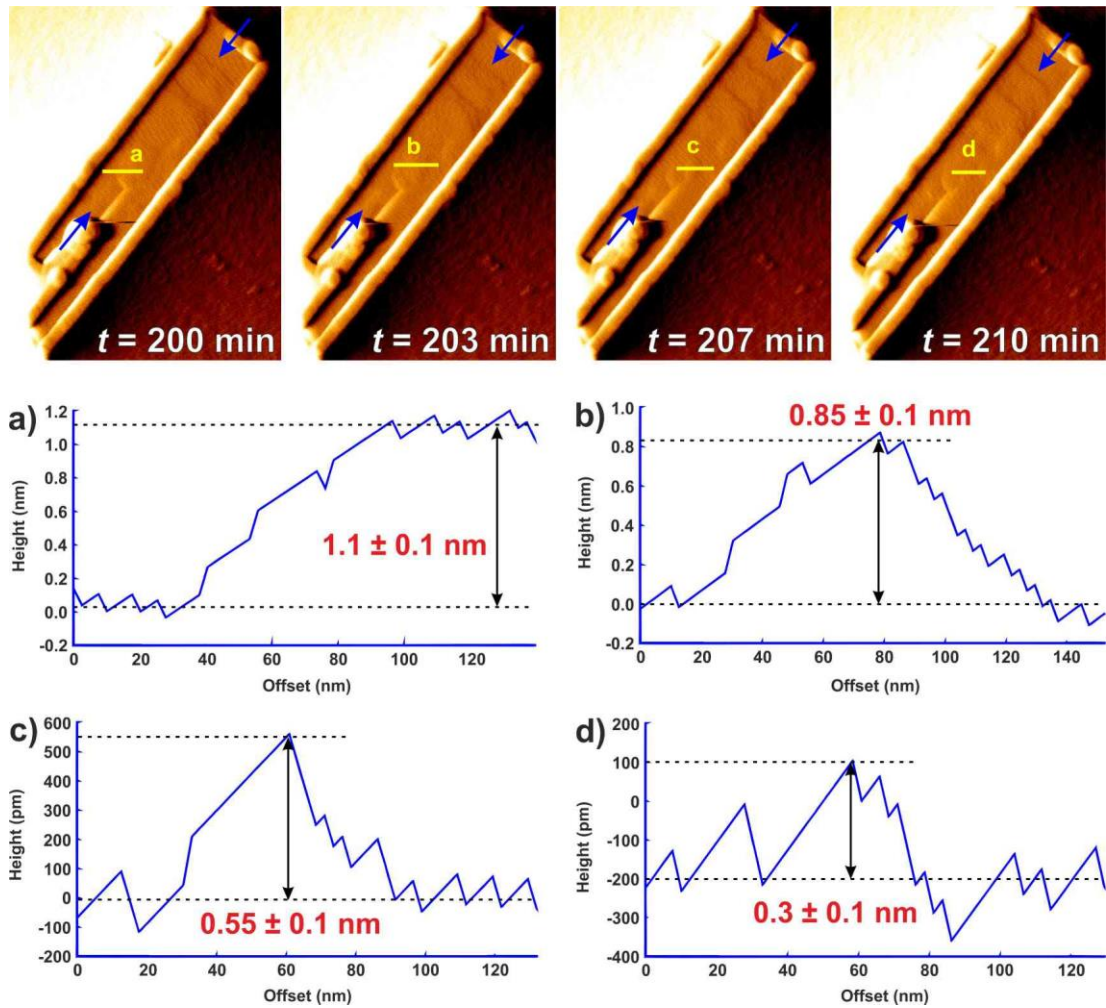


Figure 3.30. Height measurements performed on the same spot of consecutive AFM images of (013) facet of IM-17 crystal.

Dissolution of IM-17 crystal on this facet enables us to investigate structure breakdown during the process. The event started on both terrace ends (shown by blue arrows in Figure 3.30) moved toward the face centre leaving only tiny round

terrace. Similarly to how the (100) facet dissolved, height measurement performed on AFM images of (013) facet also showed gradual surface dissolution, although it is undetectable when early dissolution took place on the terrace's borders. From 1.1 ± 0.1 nm terrace high, the solution dissolved it to be 0.85 ± 0.1 nm. It then further retreated to be 0.55 ± 0.1 nm before it dropped to 0.3 ± 0.1 nm. Finally, the NaOH solution washed out the remaining particles from this terrace to expose the entire terrace below it.

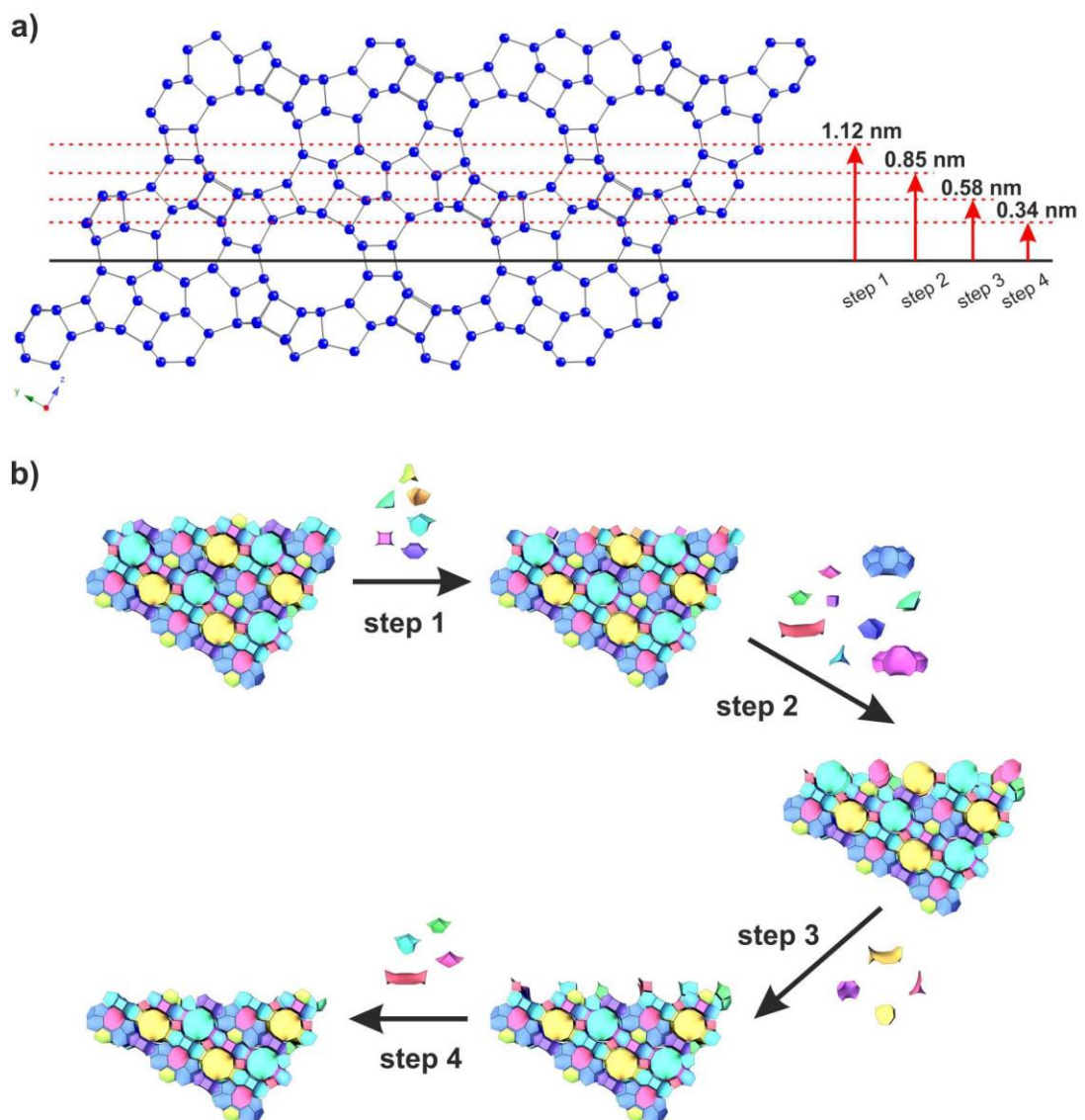


Figure 3.31. a) UOV breakdown for (013) facet viewed along $\langle 100 \rangle$ direction. b) Schematic illustration of the stepwise dissolution of IM-17 crystal on (013) facet.

Terrace's height retreat analysis shows very good correlation between the heights found experimentally on the crystal surface during the dissolution process with the structure breakdown. Figure 3.31 describes this gradual retreat very well both on UOV structure (a) and tiling (b). The schematic illustration of how (013) facet of IM-17 crystal dissolved reveals the tiles etched by the solution to give the formed heights. To cut the full step from 1.1 nm to 0.85 nm (**step 1**), the solution cleared out six tiles on the uppermost step: t-mtw, t-sfg-4, t-tes, t-lau, t-kah, and t-mel. This was followed by dissolution of nine different types of tiles: t-cub (d4r), t-nuh, t-bal, t-bru, t-uov-2, t-kah, t-mel, t-tes and t-iwr to reach 0.55 nm height (**step 2**). Step 2 can actually be divided into several more steps. However, we did not find the height in between 0.85 – 0.55 nm in AFM height measurement. After that, in **step 3**, elimination of t-umx, t-fvw, t-dmp and t-uov-1 left 0.3 nm step height which was due to the presence of t-bal, t-bru, t-sfg-4 and t-nuh. Finally, the solution took away the last four tiles to completely dissolve that particular terrace.

However, unlike the report on dissolution of zeolite A by Meza *et al.* [5], [20] in which alkaline solutions (up to 0.5 M NaOH solutions) slowly retreated the terrace layer by layer (*i.e.* the top layer dissolved almost completely first before the terrace below it followed), all layers (top and below it) on (013) facet of IM-17 crystal dissolved at the same time as exposed to the solution. The quick IM-17 crystal dissolution occurred in this experiment suggests that the higher the concentration of the alkaline solution used to dissolve zeolite material, the faster the dissolution happened.

3.3.4.5. Simulation of IM-17 crystal dissolution on (013) facet

Dissolution on (013) facet of UOV crystal was also modelled. We used the same parameters as that for the simulation of UOV crystal dissolution on (100) facet. The result is displayed in Figure 3.32 and Movie 3-5 in Appendix 1, in which image number 1 is the crystal surface before the dissolution commenced.



Figure 3.32. Subsequent images of IM-17 crystal dissolution simulation on (013) facet with $\Delta\mu_{\text{eq}} = 9.7$ and $\Delta\mu$ for dissolution = 5. The simulation was set with $\Delta U_s = 2 \text{ kcal mol}^{-1}$. The (013) facet of the simulated crystal above is *c.a.* $0.04 \mu\text{m} \times 0.14 \mu\text{m}$. The first image is the crystal before the dissolution started (*to be continued on the next page*).



Figure 3.32 (continued). Subsequent images of IM-17 crystal dissolution simulation on (013) facet with $\Delta\mu_{\text{eq}} = 9.7$ and $\Delta\mu$ for dissolution = 5. The simulation was set with $\Delta U_s = 2 \text{ kcal mol}^{-1}$. The (013) facet of the simulated crystal above is *c.a.* $0.04 \mu\text{m} \times 0.14 \mu\text{m}$. The first image is the crystal before the dissolution started.

The dissolution pattern in this calculation strongly agrees with the experimental outcome. The event tends to retreat the surface layers from its edge (step) towards the centre of the layer suggesting that the building units on this surface terminal are all connected. There is a possibility that the particles in the bulk layer also disappear due to the dissolution as seen from image 13 onward. Yet, this process is not as dominant as the particle retreat from the edge to the centre of the layer.

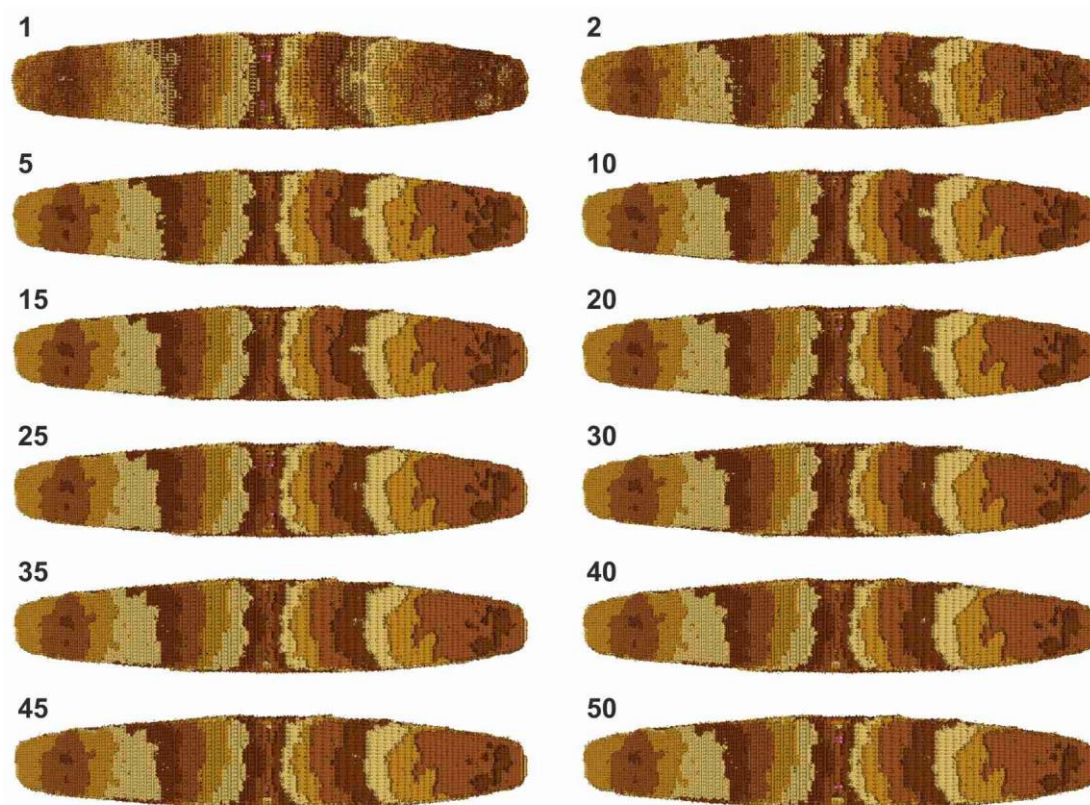


Figure 3.33. Images of IM-17 crystal dissolution simulation on (013) facet with $\Delta\mu_{eq} = 9.7$ and $\Delta\mu$ for dissolution = 7. Images are viewed from a point right between $[013]$ and $[01\bar{3}]$ directions. The simulation was set with $\Delta U_s = 2 \text{ kcal mol}^{-1}$. The simulated crystal has approximately $0.23 \text{ }\mu\text{m}$ longest diagonal and about $0.04 \text{ }\mu\text{m}$ thickness. The first image is the crystal before the dissolution started.

Unlike the patches dissolution on (100) facet, which is related to its unconnected building units constructing the surface, the patches dissolution in the simulation on (013) facet in Figure 3.32 is possibly caused by the large gap between the $\Delta\mu_{eq}$ and the $\Delta\mu$ (9.7 and 5, respectively). The large difference between $\Delta\mu_{eq}$ and $\Delta\mu$ tells the program to set the dissolution in a very under-supersaturated condition. Therefore,

any tiles exposed can be easily detached from the crystal regardless of their positions, whether on kink, step or bulky terrace sites. To show this, we run the same simulation with a smaller gap between $\Delta\mu_{eq}$ and $\Delta\mu$ (9.7 and 7, respectively) with the result shown in Figure 3.33. It is clear from those images that the dissolution process occurs as the layers retreat from the edge towards its centre. The dissolution rate, however, is very slow in this simulation allowing the edge of terraces to fade first.

3.3.5. IM-17 crystal growth studied using X-ray diffraction data

In order to understand the IM-17 crystal growth better, we also investigated the PXRD data of the IM-17 materials synthesized with different hydrothermal reaction times. The IM-17 samples were prepared using the same procedure as that reported in the literature [6], [13] for 4, 7, 11, 12, 13 and 14 days. The PXRD patterns are given in Figure 3.34 along with SEM images of the crystals in Figure 3.35. It is important to note that all UOV materials synthesized were from one synthesis batch except those prepared for 12 and 13 days. Again, all diffractograms of the as-synthesized crystalline IM-17 materials show the presence of two phases as confirmed in Figure 3.5.

It is visible that PXRD pattern for the four-day synthesis time shows amorphous material formed. This amorphous material was still obtained in day 7, but with an indication of some degree of crystallisation for we see early structuring of the crystalline material confirmed by few small peaks in the PXRD pattern and by SEM image in Figure 3.35 (b). Next, PXRD patterns for longer synthesis times (11 to 14 days) evidence fully grown crystalline IM-17 formation. Thus, from this discovery, we can deduce that IM-17 crystallisation started to take place between 4 – 11 days of the hydrothermal reaction.

Furthermore, looking at the PXRD pattern for 7-day synthesis time, the peaks started to form at $2\theta = 21^\circ$ and 22.5° (marked with red asterisks) indicate the initial crystallization of the UOV phase whereas peaks at $2\theta = 23^\circ$ and 24° (marked with black asterisks) demonstrate the new formation of MFI phase. Small peak also arose at $2\theta = 7.9^\circ$ (marked by black and red asterisks) at which both UOV and MFI

structures show intense reflection. Hence, based on this outcome, it is clear that the structuring of both phases competed for each other since the early stage of the crystallisation.

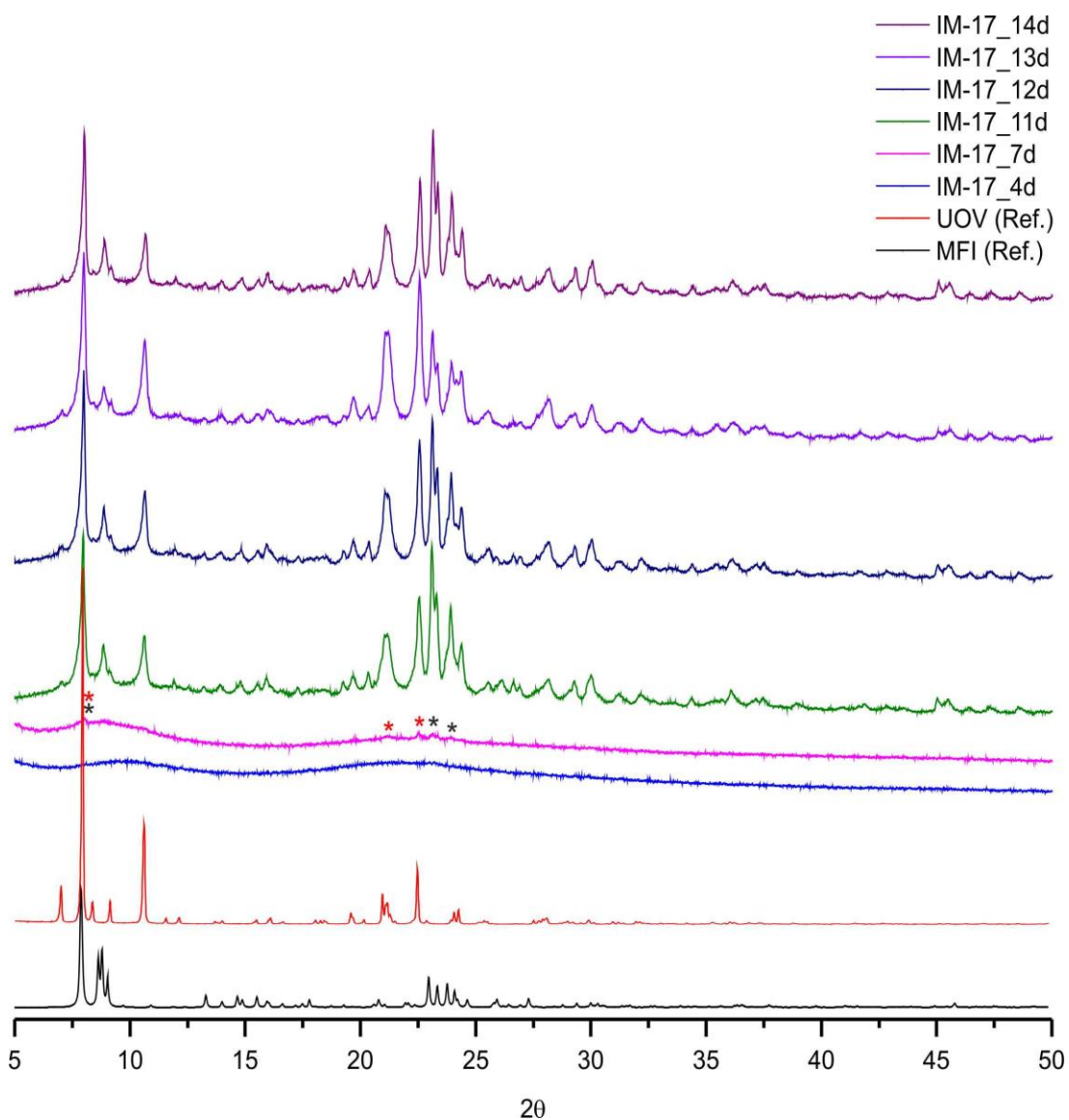


Figure 3.34. PXRD patterns of as-synthesized IM-7 prepared in different crystallization times (in days). UOV and MFI references are XRD patterns for both structures taken from literature [11].

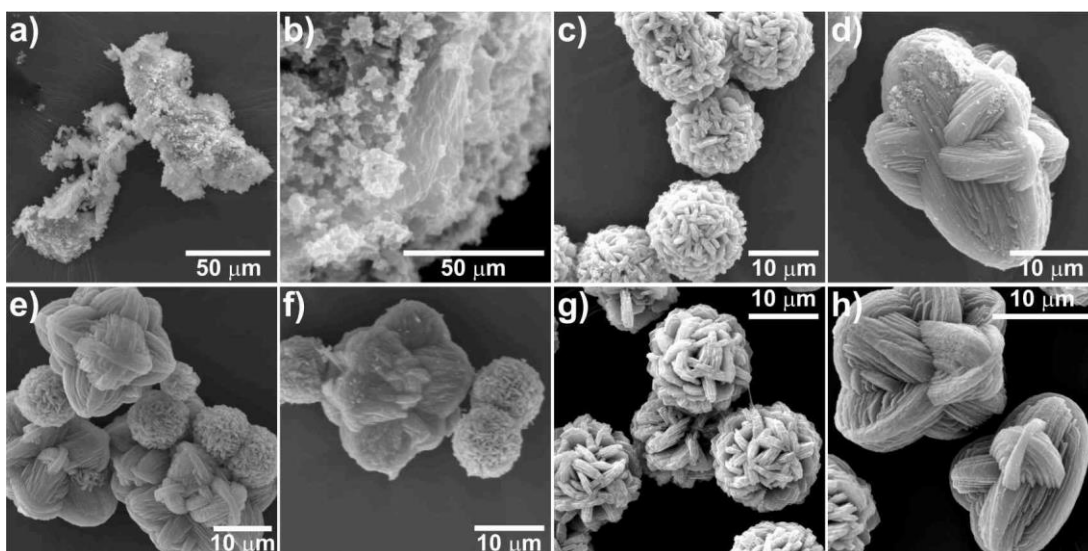


Figure 3.35. SEM images of IM-17 crystals prepared in a) 4 days, b) 7 days, c) 11 days, d) 11 days (showing MFI phase), e) 12 days, f) 13 days, g) 14 days and h) 14 days (showing MFI phase).

The two phases obtained in these syntheses clearly depicted in SEM images of the completely-formed crystalline materials in Figure 3.35 (c – h). Since we know from literature [6] that IM-17 crystal is plate-like rhombus shape, then the crystals synthesized for 11 days shown in Figure 3.35 (c) is definitely the IM-17 crystals. The small intergrowth crystals stick with each other in a ball shape with around 10 μm dimension for a reason that has not been known yet. Therefore, it leaves us with the big chunk of secondary phase in Figure 3.35 (d), which is confirmed in section 3.3.1 as MFI-structured germanosilicate. Equal to this are the materials prepared for 12, 13, and 14 days.

Moreover, crystallisation curve plotting relative crystallinity of crystalline IM-17 as a function of the synthesis time was also produced. To measure relative crystallinity, Peak Height Method described in the literature [21] was chosen over the preferred Integrated Peak Area Method because of the existence of the second crystalline phase of which diffraction peaks will interfere with the measured material's diffraction peaks. On the other hand, the Peak Height Method measures the height of a singlet peak and compare it with the standard peak's height.

To calculate the relative crystallinity of IM-17 using Peak Height Method, we used the formula below:

$$\text{Equation 3.1} \quad \text{Relative crystallinity (\%)} = \frac{H_s}{H_r} \times 100\%$$

where H_s and H_r are the heights (in mm) of the singlet peak at $2\theta = 22.5^\circ$ in PXRD patterns of the sample and reference, respectively. As for the reference, we picked the diffractogram of the IM-17_13d sample since it has the highest peak at that 2θ . The resulting crystallisation curve is presented in Figure 3.36.

The curve gives us an estimation that IM-17 started nucleation from its synthesis gel at some points between 4 and 7 days of the hydrothermal time. The relative crystallinity increases up to 13 days of the crystallization time after which it started to drop while reaching 14 days. This sudden drop may be related to the fact that the IM-17_12d and IM-17_13d samples were obtained from different synthesis batch from the rest of the samples. However, overall we can see that the relative crystallinity of the IM-17 linearly enhanced after half of the synthesis time suggested by literature [6].

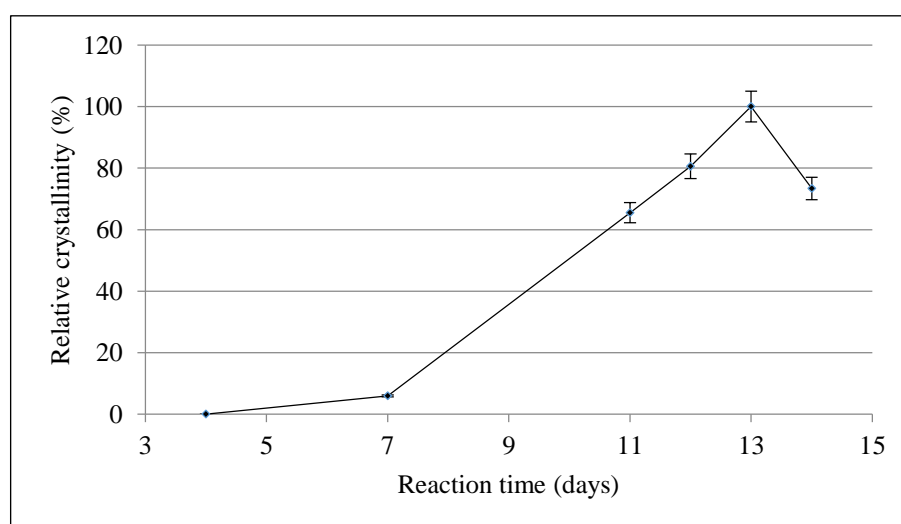


Figure 3.36. Crystallinity curve of the IM-17 crystal.

From a crystal growth point of view, the first half of the synthesis time may be associated with the formation of the growth units from the synthesis gel matrix and the early stages of nucleation. That is why the PXRD patterns indicate dominant

amorphous phase for these times of synthesis. This is then followed by the crystal structuring and ripening in the second half of the hydrothermal reaction demonstrated by the progressive increase of the relative crystallinity in PXRD patterns.

3.4. Conclusions

To conclude, this study successfully observed detailed IM-17 surface features and dissolution of IM-17 crystal on both of its (100) and (013) facets in NaOH solution using AFM as well as simulation employing *CrystalGrower* program. Both surfaces dissolved layer by layer, yet in different ways. The (100) facet dissolved in patches, while (013) facet dissolved consecutively. Those facts are related to the arrangement of the building units on each crystal surfaces. Unconnected building units on the (100) surface led to patches dissolution, yet inter-connected ones on (013) surface gave rise to layer retreat from the terrace edge to its centre. The existence of screw dislocation on (100) facet was also revealed, of which layers interestingly retreated toward the centre of the spiral during the dissolution process rather than dissolved in an uncorrelated way. Additionally, height measurement on the surface particles during the dissolution proved that the layer height dissolved gradually.

In agreement with the experimental result, the *CrystalGrower* simulation informed us that new nucleation on (100) facet is started by the joining of units growth on the surface double 4-rings as if there is t-lau or t-mtw tiles on top of double 4-rings. Meanwhile, new nucleation on (013) facet is initiated by attachment of units of growth on the surface structure so that it looks like either t-bal, t-bru, t-nuh or t-sfg-4 tiles are on those sites.

Meanwhile, the crystallinity curve based on PXRD patterns of IM-17 suggests that during its synthesis, nucleation may be started in synthesis gel at some point between 4 – 7 days of the hydrothermal reaction. All results gained from this work lead us to a better knowledge of how the IM-17 crystal grows and dissolves.

3.5. References

- [1] M. A. Holden, P. Cubillas, M. P. Attfield, J. T. Gebbie, and M. W. Anderson, "Growth Mechanism of Microporous Zincophosphate Sodalite Revealed by In Situ Atomic Force Microscopy," *J. Am. Chem. Soc.*, vol. 134, no. 31, pp. 13066–13073, 2012.
- [2] R. Brent *et al.*, "Unstitching the Nanoscopic Mystery of Zeolite Crystal Formation," *J. Am. Chem. Soc.*, vol. 132, no. 9, pp. 13858–13868, 2010.
- [3] P. Cubillas *et al.*, "Spiral Growth on Nanoporous Silicoaluminophosphate STA-7 as Observed by Atomic Force Microscopy," *Cryst. Growth Des.*, vol. 9, no. 9, pp. 4041–4050, 2009.
- [4] T. Wakihara, Y. Sasaki, H. Kato, Y. Ikumura, and T. Okubo, "Investigation of the surface structure of zeolite A," *Phys. Chem. Chem. Phys.*, vol. 7, no. 19, pp. 3416–3018, 2005.
- [5] L. I. Meza, M. W. Anderson, B. Slater, and J. R. Agger, "In situ atomic force microscopy of zeolite A dissolution," *Phys. Chem. Chem. Phys.*, vol. 10, pp. 5066–5076, 2008.
- [6] Y. Lorgouilloux *et al.*, "IM-17: a new zeolitic material, synthesis and structure elucidation from electron diffraction ADT data and Rietveld analysis," *RSC Adv.*, vol. 4, no. 37, pp. 19440–19449, 2014.
- [7] M. D. Shannon, J. L. Casci, P. A. Cox, and S. J. Andrews, "Structure of the two-dimensional medium-pore high-silica zeolite NU-87," *Nature*, vol. 353, pp. 417–420, 1991.
- [8] J. L. Casci and A. Stewart, "Zeolites," EP 0377291 A1, 1990.
- [9] A. Moini and E. W. Valyocsik, "US 005192521A - Synthesis of Crystalline Silicate ZSM-12," 1993.
- [10] P. A. Wright *et al.*, "Synthesis and structure of a novel large-pore microporous magnesium-containing aluminophosphate (DAF-1)," *J. Chem. Soc. Chem. Commun.*, vol. 104, no. 7, pp. 633–635, 1993.
- [11] "Database of Zeolite Structures." [Online]. Available: <http://www.iza-structure.org/databases/>. [Accessed: 17-Nov-2017].
- [12] M. W. Anderson *et al.*, "Predicting crystal growth via a unified kinetic three-dimensional partition model," *Nature*, vol. 544, no. 7651, pp. 456–459, 2017.

- [13] Y. Lorgouilloux, J.-L. Paillaud, P. Caullet, J. Patarin, and N. Bats, "EP2219997A1 - Crystallised Solid IM-17 and Method for Preparing Same," 2010.
- [14] A. Cizmek, B. Subotic, R. Aiello, F. Crea, A. Nastro, and C. Tuoto, "Dissolution of high-silica zeolites in alkaline solutions I. Dissolution of silicalite-1 and ZSM-5 with different aluminum content," *Microporous Mater.*, vol. 4, pp. 159–168, 1995.
- [15] A. Cizmek *et al.*, "Dissolution of high-silica zeolites in alkaline solutions II . Dissolution of ' activated ' silicalite-1 and ZSM-5 with different aluminum content," *Microporous Mater.*, vol. 8, pp. 159–169, 1997.
- [16] R. L. Hartman and H. S. Fogler, "Understanding the Dissolution of Zeolites," *Langmuir*, no. 23, pp. 5477–5484, 2007.
- [17] J. R. Agger, N. Hanif, and M. W. Anderson, "Fundamental zeolite crystal growth rates from simulation of atomic force micrographs," *Angew. Chemie - Int. Ed.*, vol. 40, no. 21, pp. 4065–4067, 2001.
- [18] P. Cubillas and M. W. Anderson, "Synthesis Mechanism: Crystal Growth and Nucleation," in *Zeolites and Catalysis, Synthesis, Reactions and Applications*, Vol. 1., Weinheim, Germany: Wiley-VCH Verlag GmbH & Co. KGaA, 2010.
- [19] Y. Marui, R. Irie, H. Takiyama, H. Uchida, and M. Matsuoka, "Analysis of nucleation of zeolite A from clear solutions," *J. Cryst. Growth*, vol. 237–239, pp. 2148–2152, 2002.
- [20] L. I. Meza, M. W. Anderson, and J. R. Agger, "Differentiating fundamental structural units during the dissolution of zeolite A," *Chem. Commun.*, pp. 2473–2475, 2007.
- [21] *Standard Test Method for Determination of Relative Crystallinity of Zeolite ZSM-5 by X-Ray Diffraction*. 2015.

Chapter 4

DAF-1 Crystal Dissolution Studied by AFM

4. DAF-1 Crystal Dissolution Studied by AFM

4.1. Introduction

The search for new porous materials to use in a wide range of applications, such as catalysts, ion exchange, sorbents, and many more sectors, has been growing for decades. Potential materials to be applied in these sectors include zeolites, metallophosphates, and MOFs. In 1993, a new metallophosphate material, named DAF-1 having DFO structure type, was invented [1]. This material has proved superior for isobutene cracking [2] and to be preferable as an active and selective catalyst in the isomerisation of but-1-ene to 2-methylpropene at low temperature [3].

DAF-1 is a magnesium-containing aluminophosphate with a large hexagonal unit cell, sized $a = 22.351 \text{ \AA}$ and $c = 43.386 \text{ \AA}$. Aluminium (Al) and phosphorus (P) atoms, along with magnesium (Mg) atom, are tetrahedrally coordinated in the crystal framework. Al and P atom locations are alternating, with the Mg atom substituting some of the Al atoms. However, it is still unclear where each Mg atom is positioned. With chemical formula $(\text{C}_{16}\text{H}_{38}\text{N}_2^{2+})_7 [\text{Mg}_{14}\text{Al}_{52}\text{P}_{66}\text{O}_{264}] \cdot (\text{H}_2\text{O})_{40}$, every three to four Al atoms are alternated by one Mg atom.

The DFO framework structure (see Figure 4.1) possesses two types of channel viewed along the [001] direction: type 1 channel (having 7.5 \AA width 12-ring) and type 2 channel (having 6.1 \AA width 12-ring). One type 1 channel is surrounded by 6 smaller type 2 channels. Double 4-rings connect two type 1 channels and two type 2 channels, as illustrated in Figure 4.1 (a) [1]. The location of the decamethonium dications, used as the structure directing agent in DAF-1 crystal synthesis, has been detected in the type 2 channel [4]. Looking along the [010] direction, there are also two distinct channels: 10-ring and 8-ring channels (see Figure 4.1 (b)).

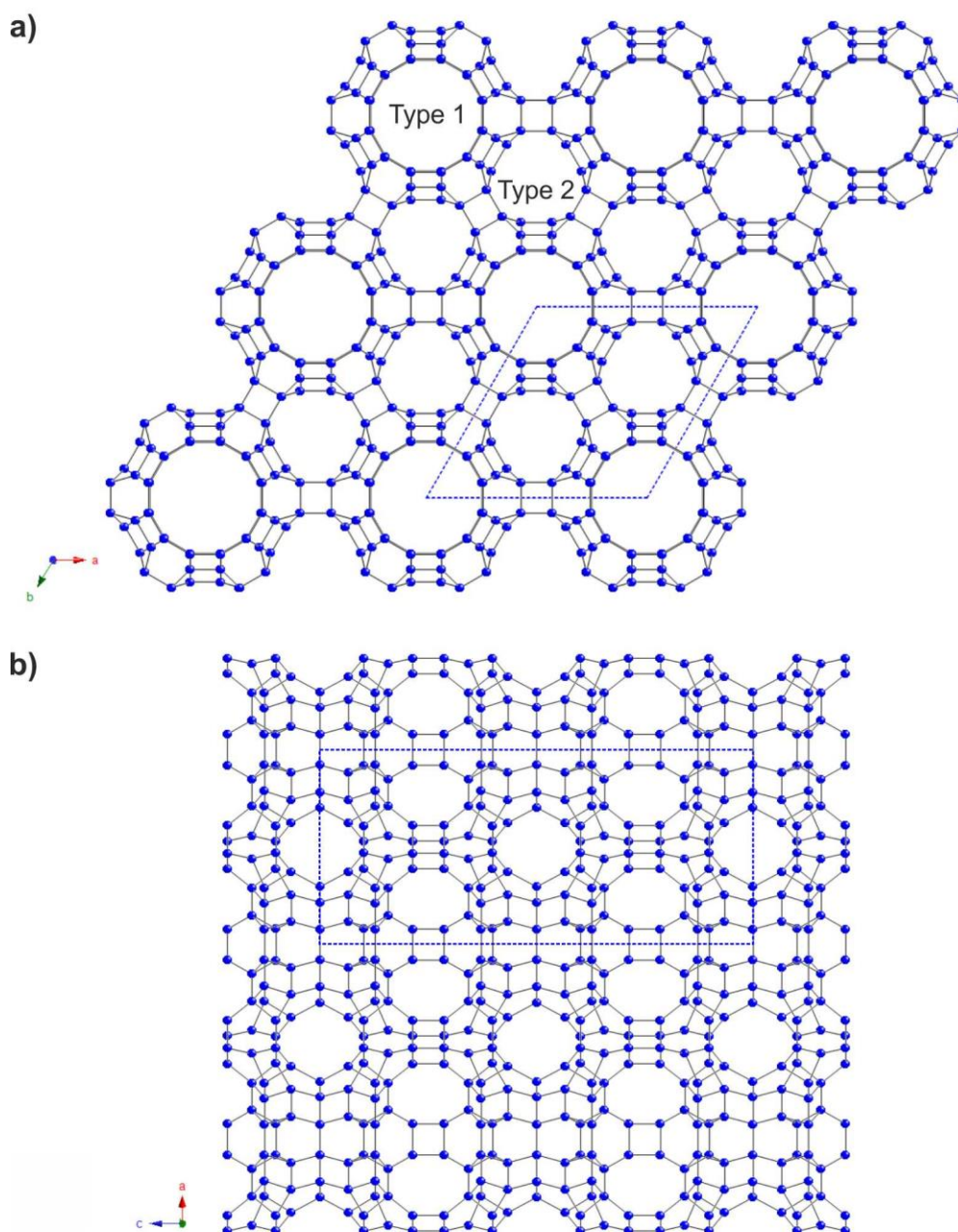


Figure 4.1. DFO framework structure showing a) (001) and b) (010) facets. Blue dashed-lined shapes illustrate one unit cell. The structure is drawn in ball and stick mode. The blue dots represent the Al, P or Mg atoms, whilst the black sticks illustrate the oxygen bridging in between those Al, P or Mg atoms. Oxygen atoms are omitted for clarity.

Nearly as complex as UOV structure described in the previous chapter, the DFO structure framework is constructed by 11 natural tiles. The tiles forming the DFO structure are presented in Figure 4.2 [5]. The last two tiles (t-eni and t-evh) are the two largest tiles in this structure.

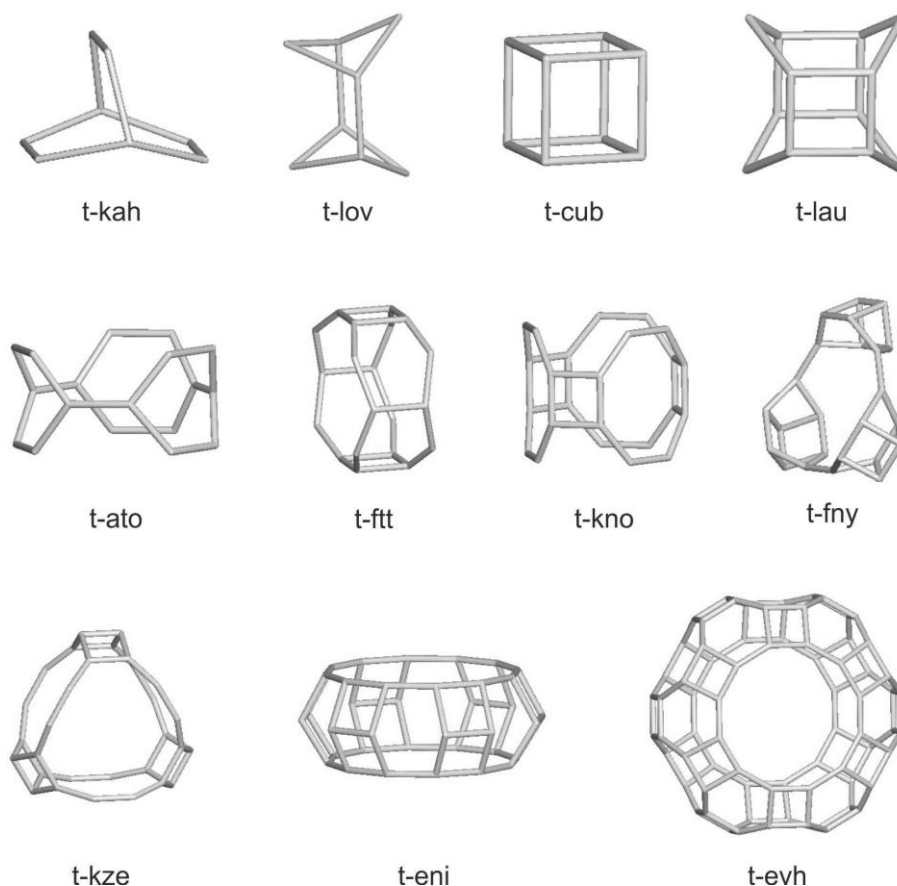


Figure 4.2. Eleven tiles constructing the DFO structure [5].

The large unit cell of DAF-1 crystal and its structure's complexity leave an interesting question in crystal growth, as to how crystal memory is propagated over such a large distance. This is important since most studies in crystal growth and dissolution that have been published reported only mechanisms for inorganic nanoporous materials having a relatively small unit cell. Published examples of this are: a successful in-situ growth observation on crystal with SOD framework, possessing $8.956 \text{ \AA} \times 8.956 \text{ \AA} \times 8.956 \text{ \AA}$ unit cell dimension [6]; very detail growth and dissolution process of zeolite L crystal (LTL structure) with $18.126 \text{ \AA} \times 18.126 \text{ \AA} \times 7.567 \text{ \AA}$ hexagonal unit cell [7]; and spiral growth revealed on STA-7 with tetragonal unit cell having comparable size with zeolite L [8]. Slightly larger than those, zeolite A (LTA structure), having a cubic unit cell with 24.610 \AA side length, has also been studied to reveal its surface structure and dissolution [9], [10]. However, again, these investigations were performed on crystals possessing relatively small unit cell compared to that of DAF-1 crystal.

In order to understand the growth process of the DAF-1 crystal, AFM, which can achieve Ångstrom vertical resolution, is employed to investigate nanoscopic details in these processes. However, due to the working temperature limit, the AFM does not allow an observation at high temperature. As a result, the real-time growth of the DAF-1 crystal at 190 °C [1] is impossible to perform. Thus, the crystal dissolution, which is believed to relate to the reverse version of the growth, was chosen to be studied. Solutions containing decamethonium dihydroxide (Dec(OH)₂) and phosphoric acid were used to dissolve the crystals in this work.

4.2. Experimental and Analytical Techniques

4.2.1. Synthesis of the DAF-1 crystal

DAF-1 was synthesized according to the procedure published by Wright *et al.* (1993) [1]. The chemicals used were Mg-acetate·4H₂O (Sigma-Aldrich, (CH₃COO)₂Mg·4H₂O, 99%), Boehmite Catapal B (Al₂O₃, 72%), phosphoric acid (Sigma-Aldrich, H₃PO₄, 85%), decamethonium bromide (Sigma-Aldrich, DecBr₂, 98%).

First of all, Dec(OH)₂ as template was prepared by stirring DecBr₂ and excess Ag₂O in deionized water for 3 hours. The mixture was then filtered and the resulting greyish filtrate was centrifuged to obtain a clear solution. The Dec(OH)₂ solution was then evaporated using a rotary evaporator to get a concentrated solution.

The next step after the template preparation was adding the Boehmite Catapal B and Mg-acetate·4H₂O into phosphoric acid followed by stirring. Afterwards, the template solution (Dec(OH)₂) was added to the mixture under constant stirring for 15 minutes. The white slurry obtained had the gel composition

$$0.2 \text{ MgO} : 0.4 \text{ HOAc} : 0.9 \text{ Al}_2\text{O}_3 : 1.0 \text{ P}_2\text{O}_5 : c.a. 30 \text{ H}_2\text{O} : 0.9 \text{ Dec(OH)}_2$$

and pH around 8 was then poured into 20 mL internal volume Teflon-lined steel autoclave and reacted at 190 °C for 2 days in a static condition. The solid was recovered by filtration, washed several times with deionized water, and dried overnight at 110 °C. The residue solution from the hydrothermal reaction had pH = 8 – 9.

4.2.2. Material characterizations

4.2.2.1. Powder X-Ray Diffraction (PXRD)

PAN Analytical X'Pert Pro Diffractometer was used to characterize the solid obtained from the synthesis. The X-ray source was $\text{CuK}\alpha$ while the tension and the current were 40 kV and 30 mA, respectively. The sample was placed on a sample holder and scanned with 2θ ranging from 4° – 50° . The data collected were then analysed employing X'Pert Highscore Plus software.

4.2.2.2. Scanning Electron Microscopy (SEM)

To analyse the crystal morphology, FEI Quanta 200 SEM was used. The sample powder was scattered on a sticky carbon attached on a sample holder and then coated with gold to avoid sample charging. The scanning was performed in vacuum with the voltage set at 20.0 kV.

4.2.2.3. Ex-situ Atomic Force Microscopy (AFM)

The surface topography of the crystal was studied using the JPK NanoWizard II AFM instrument. A small piece of thermoplastic was heated to 50°C on a glass slide and pressed flat and clear. A very small amount of sample powder was scattered on top of the flattened thermoplastic and reheated to 50°C so that the crystals stuck on it. Clear crystals were selected to be scanned using a silicon nitride tip with a spring constant of 0.35 Nm^{-1} supplied by Bruker. The scanning was done at room temperature with a set point of 0.3 V and a scan rate of 1 Hz. Terrace height was measured using JPKSPM Data Processing software.

4.2.3. Dissolution of DAF-1 crystal studied with in-situ AFM

The in-situ AFM experiment was performed on JPK instrument and a BioCell to hold the sample slide. To prepare the sample, a small amount of resin was placed on a glass slide. The slide was then heated to 60°C for about four hours. Subsequently, a very small amount of the powdery sample was scattered on top of it followed by heating it again at 60°C overnight.

The next step was putting the slide on the BioCell to which a tube was connected. This BioCell was set under the AFM head with a tip, having the same parameters as

the one used in ex-situ experiment, on top of the chosen crystal. Selected area was scanned ex-situ first to get the surface image before the solution injection ($t = 0$ minute). As soon as 0.25 mL solution was injected slowly through the tube, the same area was scanned continuously to acquire surface images during the dissolution process. The scanning was conducted in contact mode at room temperature with a set point of 0.3 V and a scan rate of 4 Hz. Some solution combinations of decamethonium hydroxide and phosphoric acid (listed later in Table 4.2) were employed in this research to dissolve DAF-1 crystal. Again, JPKSPM Data Processing software was used for height measurement.

4.3. Results and Discussions

4.3.1. Synthesis and characterization of the DAF-1 crystal

The PXRD pattern of the DAF-1 sample is shown in Figure 4.3. All peaks in the reference PXRD pattern (DFO) [5] are also seen in the PXRD pattern of the DAF-1 sample prepared in this experiment with relatively high intensity. The cell parameters of the DAF-1 sample and reference are comparable as evidenced by cell refinement using Celref presented in Table 4.1. An additional peak at $10.8^\circ 2\theta$ having low intensity is also detected in the sample's PXRD pattern. This impurity phase is explained by Wright and co-workers (1995) as a result of the slight difference in the preparation condition [2].

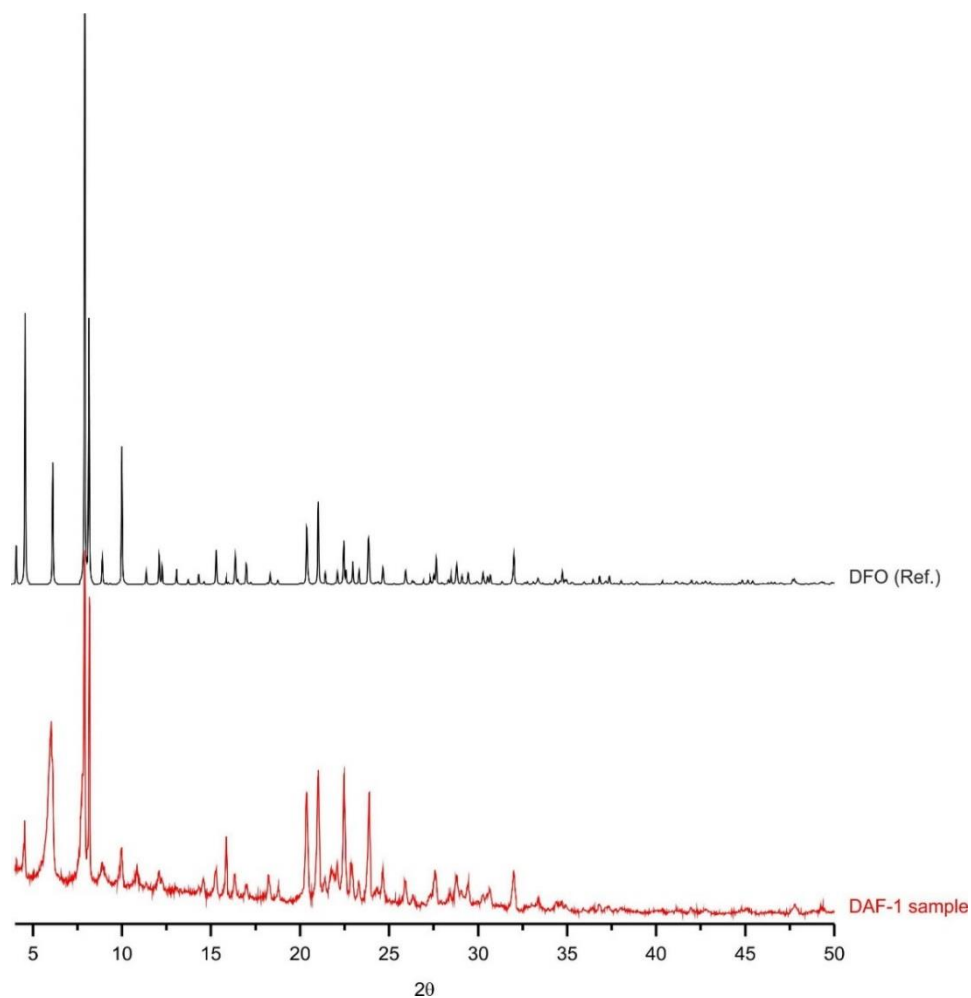


Figure 4.3. PXRD patterns of the as-prepared DAF-1 sample (red line) and DFO reference (black line) [5].

Table 4.1. Cell parameters of DAF-1 crystal

Parameters	Values	
	Reference *	Sample **
a, b (Å)	22.351	22.373
c (Å)	43.278	43.237
d_{002} (nm)	2.16	2.15
d_{010} (nm)	1.94	1.95

* Reference cell parameters [1].

** Measured cell parameters from X-ray reflection of the DAF-1 sample.

The PXRD result is supported by SEM images presented in Figure 4.4. Under an electron microscope, hexagonal single crystals of DAF-1 were observed. The crystals have a wide range of dimensions, from *c.a.* 10 – 100 μm long in diameter and *c.a.* 7 – 70 μm in thickness. The unknown phase, which is detected in the PXRD pattern, with irregular shape is also seen along with the DAF-1 hexagonal prisms. The two characterizations using PXRD and SEM techniques confirm our success in DAF-1 crystal preparation.

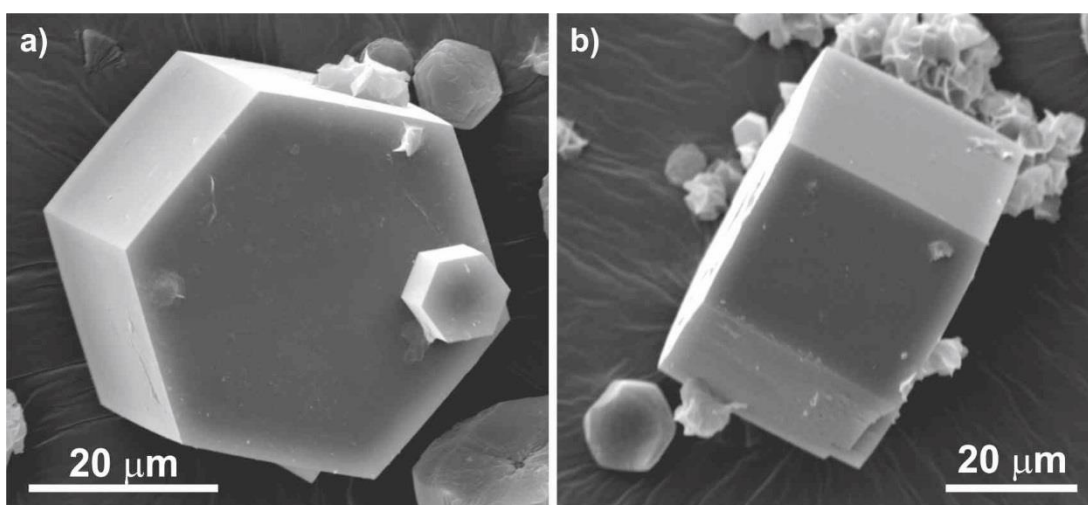


Figure 4.4. Scanning electron micrographs of as-synthesized DAF-1 crystal showing a) (001) and b) (010) facets.

4.3.2. Ex-situ AFM of DAF-1 crystal

4.3.2.1. Crystal surface topography

Ex-situ AFM scanning revealed the surface topography of the DAF-1 crystal as displayed in Figure 4.5. Observed on the (001) facet is the rough surface of the DAF-1 crystal with the presence of small impurity particles. Stacked growth layers are present on this facet leaving a message that the crystal may adopt ‘layer by layer’ mechanism during its growth. The same feature exists on the (010) facet.

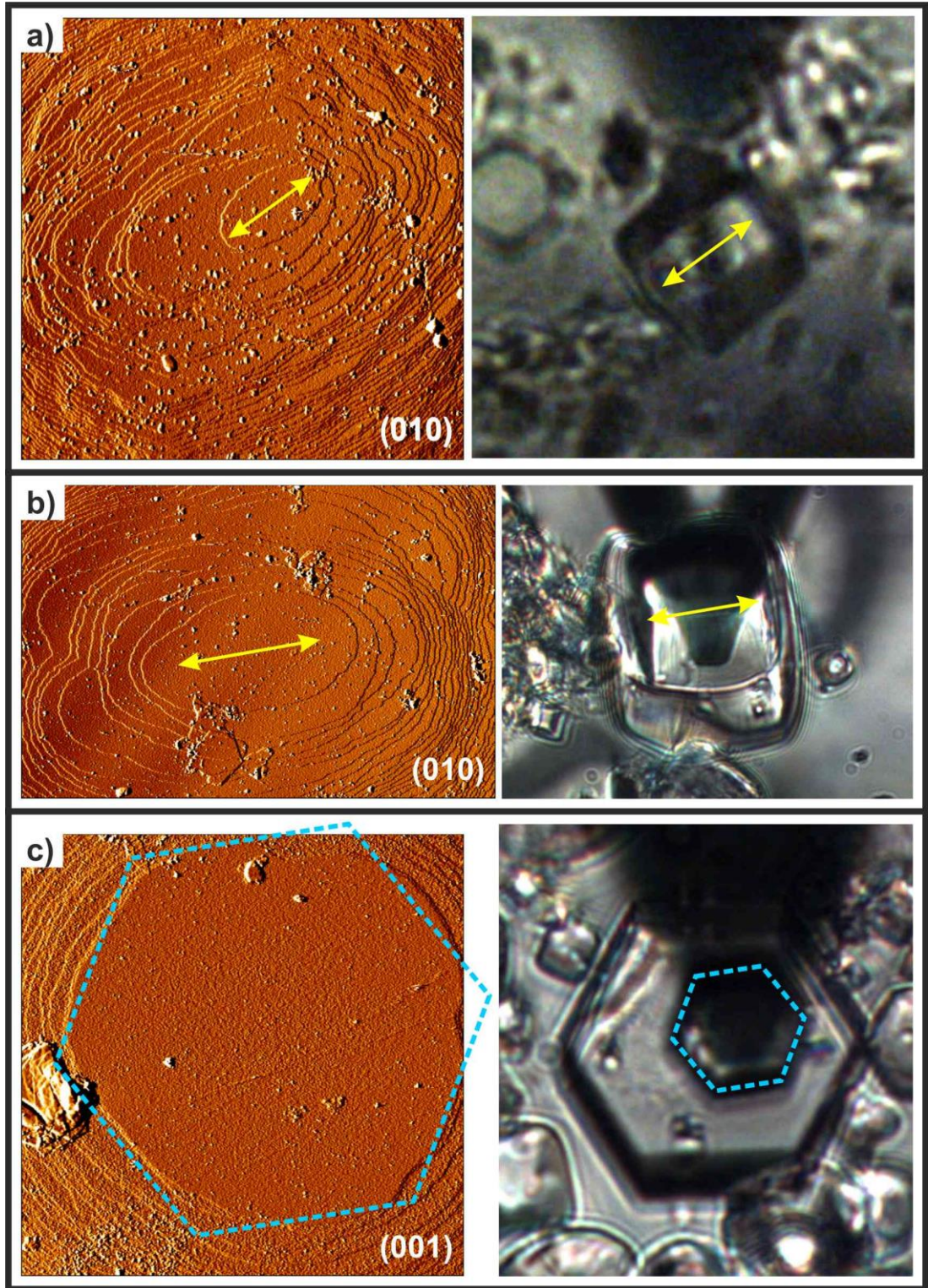


Figure 4.5. AFM vertical deflection images of DAF-1 crystal surface and its orientation under AFM microscope on a) (010) facet sized $6 \times 6 \mu\text{m}^2$, b) (010) facet sized $10 \times 6.62 \mu\text{m}^2$ and c) (001) facet sized $10 \times 10 \mu\text{m}^2$. White irregular dots on the surface are the impurity particles. Yellow double arrows and cyan dashed lines show the matching orientations of the crystal and its layers.

Growth layer orientation on (010) facet tends to mimic the orientation of the crystal, as can be seen in Figure 4.5 (a – b). This is a common behaviour in crystal growth. It is the result of a different growth rate towards distinctive cell directions. In the DAF-1 crystal, the growth rate in the c -direction is faster than that in the a - and b -directions, resulting in a crystal longer in c than the a or b .

The tendency of the layer growth to imitate the crystal orientation is clearly seen on the (010) facet. Yet, although the same phenomenon appears on (001) facet, it is not easily recognized. The rounding of layer edges on the (001) facet is probably generated because of a competition between growth and dissolution [11]. By careful observation, we can draw a hexagon, which has the same orientation as the crystal orientation, on (001) crystal surface following the uppermost layer (see Figure 4.5 (c)).

Another event to be remarked in this DAF-1 crystal that depends on crystal orientation is the defect. This is presented in Figure 4.6. On the (001) facet, the defects tend to form hexagonal shape possessing the same orientation with the crystal, while on (010) facet the defects occur as long lines parallel to the orientation of the unit cell axes.

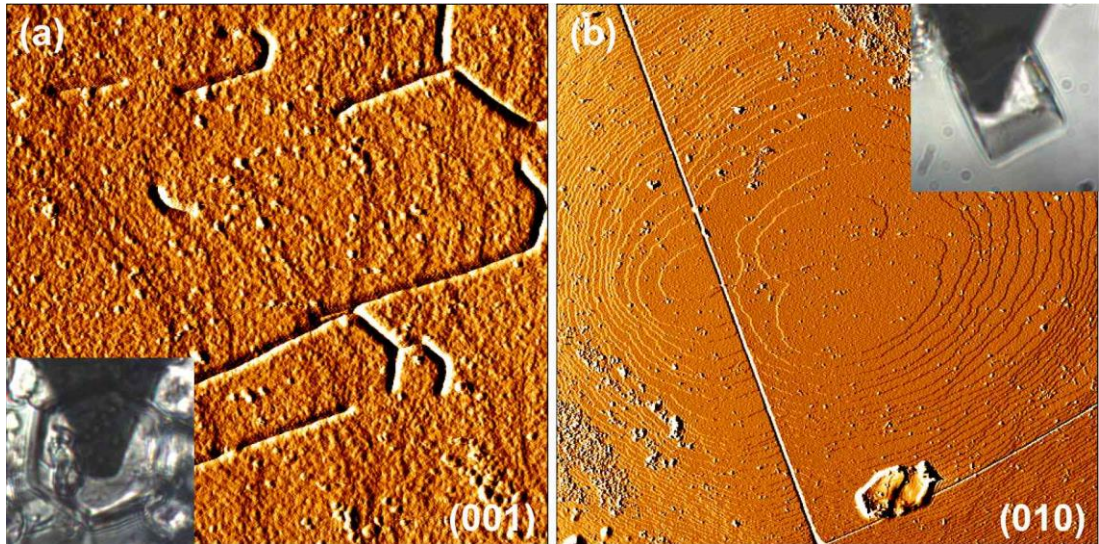


Figure 4.6. AFM vertical deflection images of DAF-1 crystal showing defects on a) (001) facet sized $3 \times 3 \mu\text{m}^2$ and b) (010) facet sized $10 \times 10 \mu\text{m}^2$. Insets depict the crystal orientation.

4.3.2.2. Structure analysis based on AFM result

Both cross-sectional and histogram height measurements were performed on the growth step of the DAF-1 crystal surface for structural analysis. The hexagonal (001) facet of DAF-1 crystal gave 2.0 ± 0.1 nm terrace height (see Figure 4.7), whilst the layers on (010) facet are mostly 2.0 ± 0.1 nm high and some of 1.9 ± 0.1 nm high (see Figure 4.8). The very close fit between cross-sectional and histogram height measurements performed on these crystal surfaces indicate the high accuracy of the measurements. Those measurements show the growth steps on both facets, which are illustrated in Figure 4.7 (d) and Figure 4.8 (d) for (001) and (010) facets, respectively.

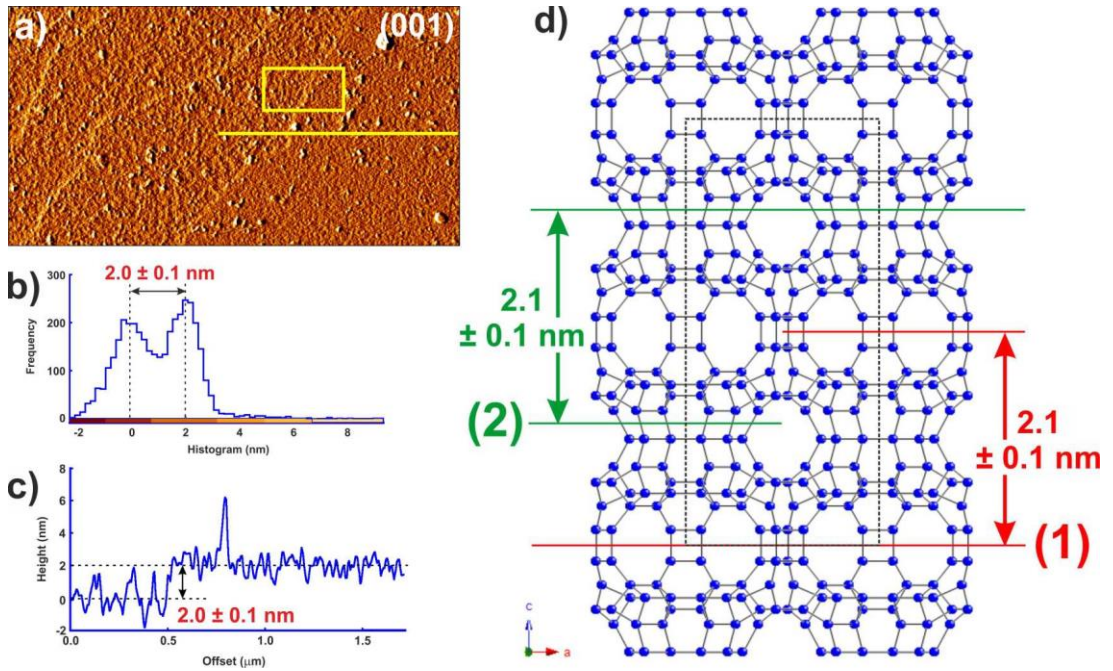


Figure 4.7. a) AFM vertical deflection image of DAF-1 crystal on (001) facet. b) and c) Histogram and cross-sectional terrace height measurements of the yellow rectangle and line, respectively, in the image (a). d) DFO framework structure showing its unit cell (black dashed rectangle) and two possible growth steps illustrated in red and green colours. The blue dots in the structure represent the Al, P or Mg atoms, whilst the black sticks illustrate the oxygen bridging in between those Al, P or Mg atoms. Oxygen atoms are omitted for clarity.

For the (001) facet, half of the length of the c course is responsible for this measured 2.0 ± 0.1 nm height. Two possibilities on how the (001) surface relates to its DFO

structure arose here (see Figure 4.7 (d)). The first possibility (marked as (1) in the image) is that the growth unit cuts the c -axis through one of the double 4-rings to another double 4-rings along the [001] direction. The other likelihood (possibility (2) in the image) is that growth units slice across the 10-membered ring. Theoretically, one growth layer distance based on those two options is 2.1 nm. Considering the error in height measurement undertaken, the two possibilities are in agreement with the AFM result. Hence, in regard to the suitability of the growth layer height, it can be said that both options are possible.

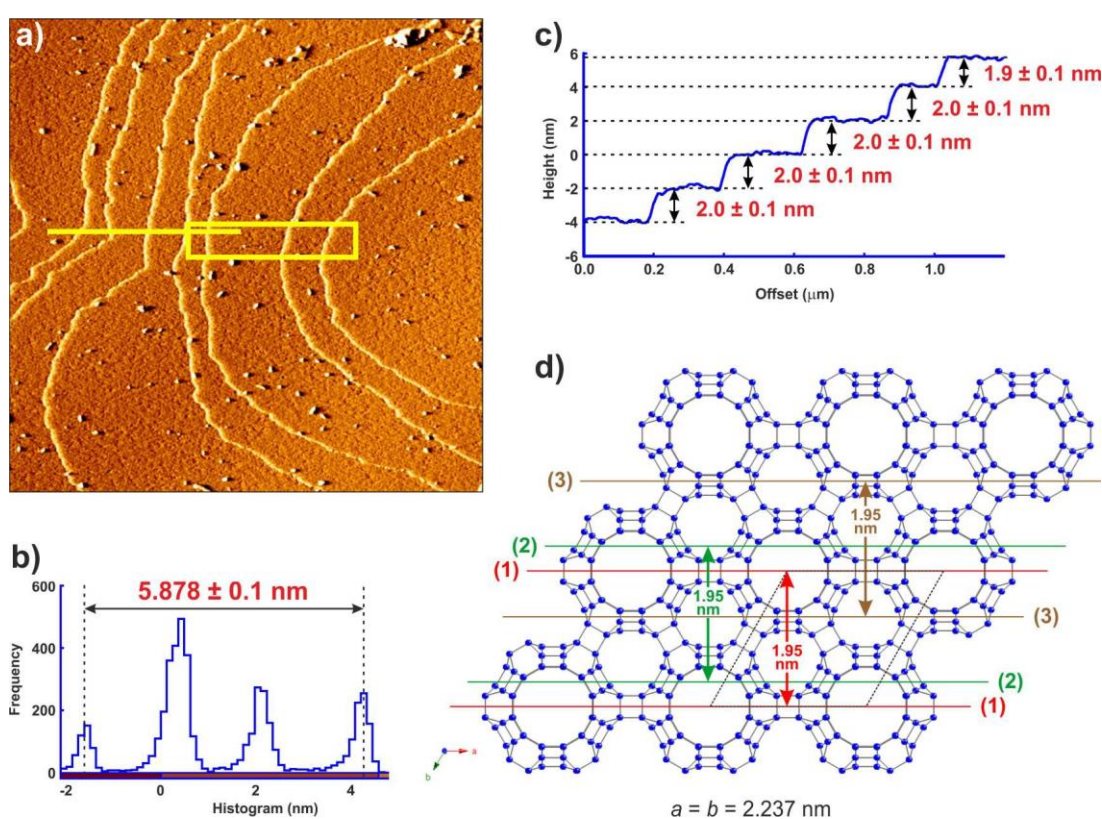


Figure 4.8. a) AFM vertical deflection image of DAF-1 crystal on (010) facet. b) and c) Histogram and cross-sectional terrace height measurements of the yellow rectangle and line, respectively, in the image (a). d) DFO framework structure showing its unit cell (black dashed parallelogram) and three prospective growth steps. The blue dots in the structure represent the Al, P or Mg atoms, whilst the black sticks illustrate the oxygen bridging in between those Al, P or Mg atoms. Oxygen atoms are omitted for clarity.

Looking at the (010) facet, the cross-sectional step height (1.9 ± 0.1 nm to 2.0 ± 0.1 nm) corresponds to the measured d_{010} of DAF-1 sample which is 1.95 nm (Table 4.1)

drawn in Figure 4.8 (d) as double arrows perpendicular to the *a*- or *b*-axes. Histogram measurement results in a more accurate height, which is 1.96 ± 0.1 nm each step (the height 5.878 ± 0.1 nm is for three steps covered in the yellow rectangle in the image (a)). Again, there is more than one possible consequence for the relation between the layer height and its position in DFO structure as illustrated in Figure 4.8 (d). One alternative (possibility 1) is that the growth unit cuts the cell at the red line marked (1), which lies across the double 4-rings and type 1 channel (larger 12-membered ring), to another red line adjacent to it. The second possibility is that the growth unit is from the green line labelled (2) to another green line. This also cuts the type 1 channel but does not half-split the double 4-rings. Possibility 3 for this growth unit is a distance between two nearest brown lines marked (3), which lie across type 2 channel.

From its structure, it is known that possibility 1 cuts through 16 bonds per unit cell on the surface. An equal number of bonds per unit cell in the surface should be broken up by possibility 2 to occur. Whilst for possibility 3, more chemical bonds (24 chemical bonds) needs to be broken up to happen. Thus, based on the minimum number of bonds to be broken up, possibility 1 and 2 seem more likely to take place. More careful height measurement on dissolution result and *CrystalGrower* simulation presented later in this chapter are able to convince which scenario between possibility 1 and 2 is more probable.

The above deduction that possibilities 1 and 2, in which the growth layer's surface cuts across type 1 channel, are more workable than possibility 3 (in which the surface cuts through type 2 channel only) is supported by Muncaster and co-workers' previous study. Muncaster *et al.* (1999) suggested that the decamethonium template molecules were more likely to be located in type 2 channels than in type 1 channel [4]. Therefore, the interactions between template molecules and the atoms in the wall of type 2 channel generate the increase in stability of its wall, making this channel less easily cleaved and left as the growth terminal than the type 1 channel. Thus, it is reasonable to suggest that DAF-1 surface on (010) facet cuts through type 1 channel as illustrated in possibilities 1 and 2.

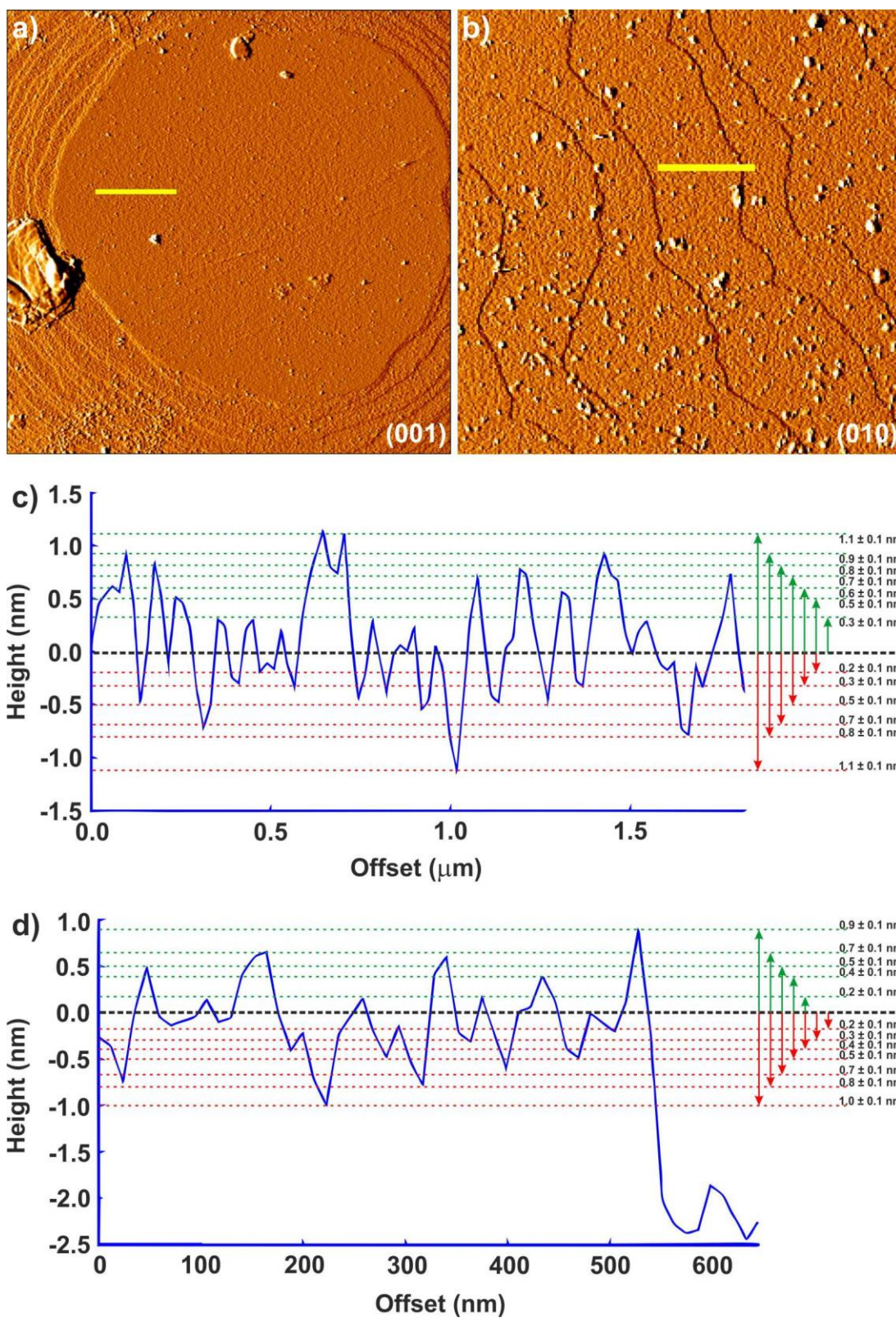


Figure 4.9. a) and b) AFM vertical images of DAF-1 showing (001) and (010) facets, respectively. c) and d) Cross-sectional measurement of surface texture along the yellow lines on (001) and (010) crystal facets, respectively.

Furthermore, the cross-sectional measurement on DAF-1 crystal surface also indicates how rough its texture is. As we can see in Figure 4.9, the (001) facet shows up to 1.1 ± 0.1 nm high spikes and up to 1.1 ± 0.1 nm deep wells. The total height of the surface roughness from the highest spike to the deepest well is 2.2 ± 0.1 nm, which agrees with the terrace height on this facet (2.1 nm in theory). A similar observation is found for (010) facet, which possesses a total of 1.9 ± 0.1 nm distance between the highest peak to the shallowest valley. The distance corresponds to the (010) terrace height. These findings inform us that during the DAF-1 crystal growth, although the growth units were more likely to be attached on the kink sites or step sites, they may as easily be attached on every site of the surface regardless of the position and grew one step upwards. Consequently, there were gaps on the crystal surface creating the valleys and spikes.

4.3.2.3. *Crystal surface impurities*

Under the AFM, it is revealed that DAF-1 crystal is not clean from impurities, which are spread all over the crystal surface. Mostly, the impurities look like white grains in vertical deflection images, which displayed in previous AFM images and in Figure 4.10.

In lateral deflection images, these grains of impurities are shown distinctive colour from other parts of the crystal surface. The contrast colours produced is generated by the different friction the AFM tip experienced, which means that the tip scanned different solid phases. Thus, it tells us that the white grains scattered on the DAF-1 crystal surface possess dissimilar chemical composition to the DAF-1 crystal surface.

The height of these grainy impurities varies in a wide range. Randomly chosen impurity height measurements show they spike up from about 5 nm to more than 40 nm high. However, impurities with height beyond that range may also exist. Depicted in Figure 4.10 are several vertical images showing surface impurities along with their measured impurities' heights and their corresponding lateral images.

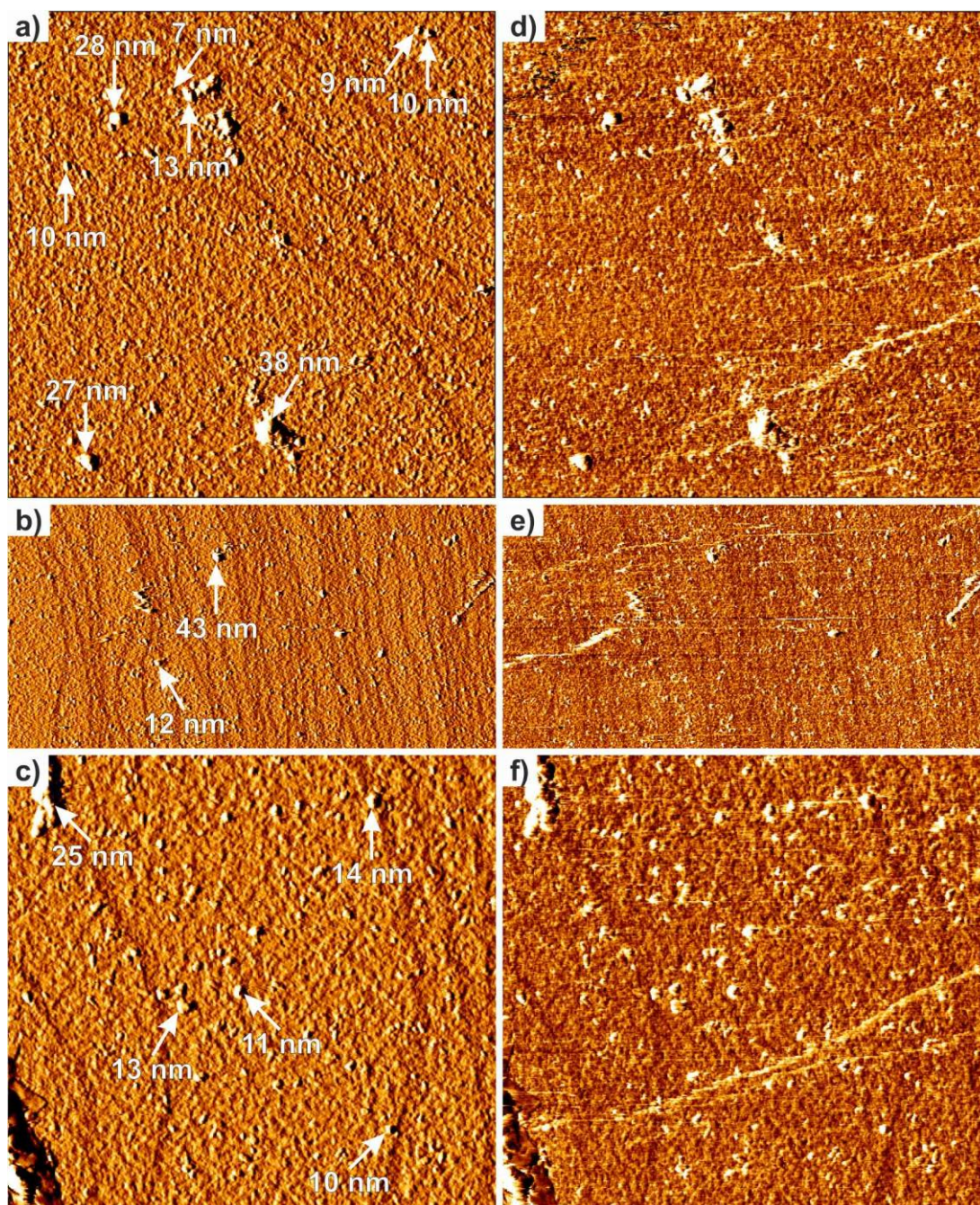


Figure 4.10. AFM vertical deflection (a – c) and its corresponding lateral deflection (d – f) images showing white particles of impurities scattered all over the (001) facet of DAF-1 crystal and random particles' heights.

Other than a rough surface with terraces and impurity particles, the presence of hexagonal sheets on the DAF-1 crystal surface was also observed (see Figure 4.11). The sheets are stacked on both crystal sides, (001) and (010) facets. The stacking sheets' orientations are random, independently from the orientation of the crystal surface where they exist. Furthermore, the orientations of the sheets in one stack are

dissimilar, in which each sheet is slightly tilted from the orientation of the sheet beneath it.

More interestingly, every sheet seems to grow perfectly overlaying the surface topography. As a result, when they grow over a plain surface, they laid flat (see Figure 4.11 (a)). However, when they grow over terraces or impurities, each of the sheets shaped the steps or that particle of the impurity (see Figure 4.11 (e), shown with white arrow). In the image (a), despite the fact that the hexagonal sheets are on a flat crystal surface, one of the sheets overgrows the sheet underneath it (marked with a white arrow). In its corresponding height image (b), the overgrown corner has the same colour, yet the same height (the height level in this kind of image increases as the colour turns lighter), as the lower sheet. This proves that the stacked hexagonal sheets grows on the DAF-1 crystal surface, not only stuck there as are the grainy impurities.

Some of the hexagonal sheets appear to be stacked very high, irregularly in size and orientation, up to hundreds of nanometers. It creates what looks like a hill in Figure 4.11 (f), with height is about 800 nm.

As can be seen in the vertical deflection image in Figure 4.11 (c), the topmost layer displays one large layer. However, the height image in Figure 4.11 (d) shows that the particular layer is not flat as it displays different colours. Smaller and lighter hexagon (marked with double white asterisks) inside the larger and darker hexagon (marked with a single white asterisk) confirms the presence of other smaller sheets, and possibly impurity particles, that are covered below the larger top sheet. Consequently, this irregular position, arrangement and size of the hexagonal sheets on the DAF-1 crystal surface make it very difficult to perform a trustworthy height measurement of a single hexagonal sheet. Nevertheless, 3.0 ± 0.1 nm is the most common sheet height. At present, whether the stacking sheets are intergrown DAF-1 crystals or impurities is not known.

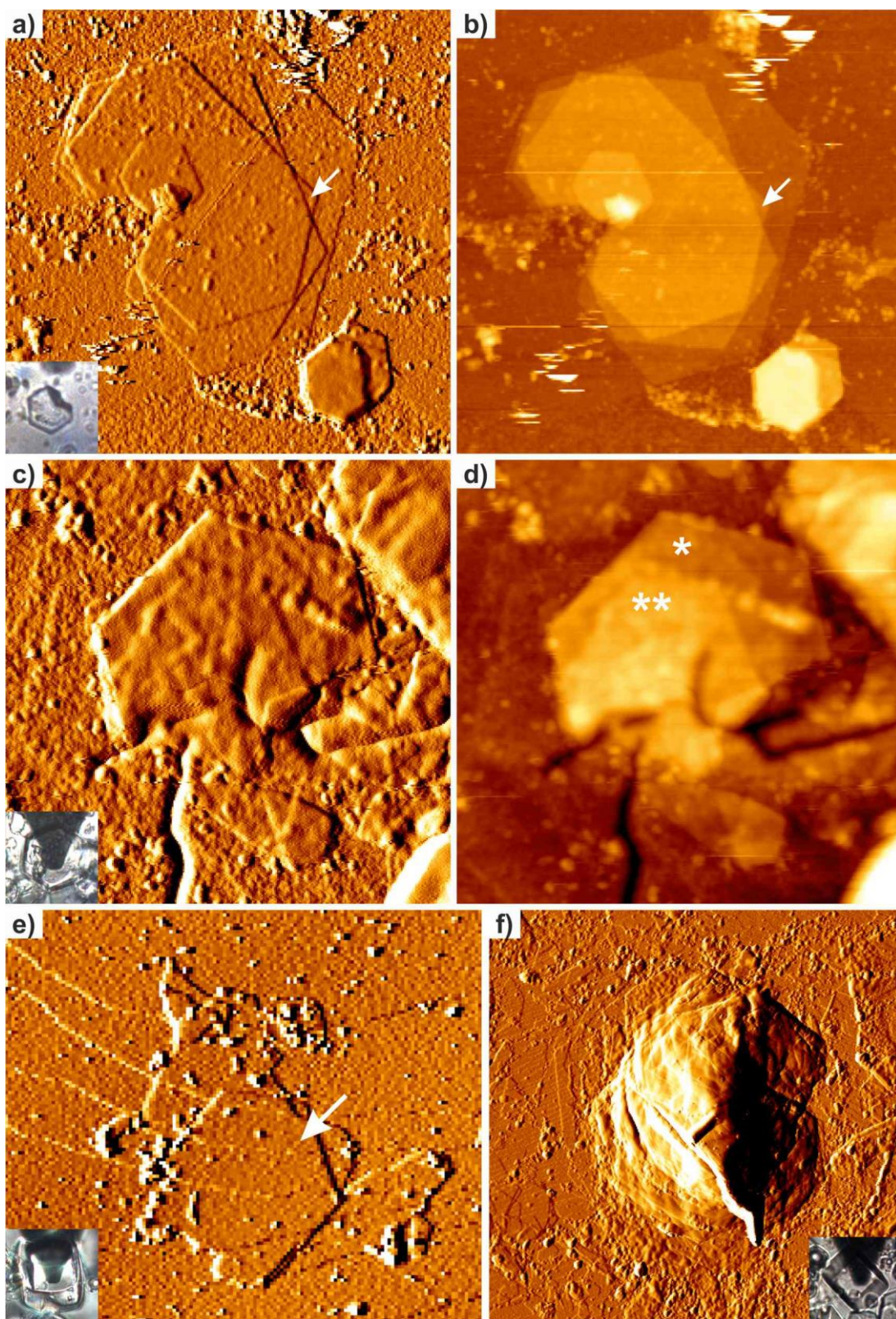


Figure 4.11. AFM images of stacked hexagonal sheets grew on (001) facet (a – d) and (010) facet (e – f) of the DAF-1 crystal surface. The inset shows the face's orientation scanned under the AFM. All images are vertical deflection images, except (b) and (d), which are height images of the corresponding (a) and (c) images, respectively. The dimension of image (a – b) $3.2\ \mu\text{m} \times 3.2\ \mu\text{m}$, (c – d) $1.7\ \mu\text{m} \times 1.7\ \mu\text{m}$, (e) $2.8\ \mu\text{m} \times 2.4\ \mu\text{m}$ and (f) $7.4\ \mu\text{m} \times 7.4\ \mu\text{m}$.

4.3.3. DFO crystal simulation

CrystaGrower was used to simulate the DFO structured crystal and the results are shown in Figure 4.12. The simulation resulted in a hexagonal prism with layer by layer terraces on the crystal surface. Different colours in the crystal surface show different layers. Several new nuclei are seen on the crystal surface and start a new layer although the top layer does not fully cover the facet.

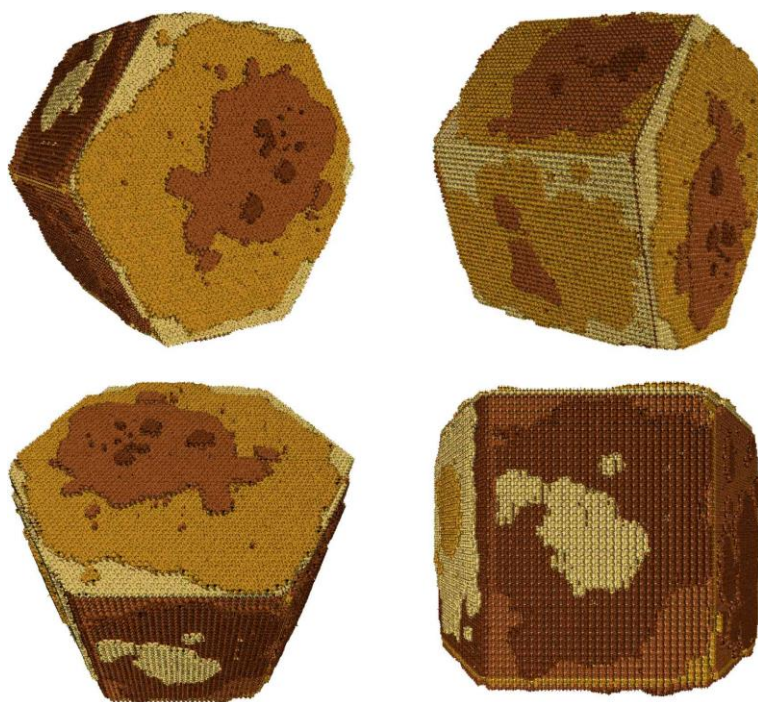


Figure 4.12. Simulation of DFO crystal using *CrystalGrower* with $\Delta U_s = 0.875$ kcal mol⁻¹ and viewed with *CG Visualiser*. The simulated crystal has approximately 0.13 μm long of the (001) facet's diameter and 0.10 μm of the hexagonal thickness.

Figure 4.13 presents a closer look on the tile configuration for (001) facet of the crystal surface. One terrace height is started from the 10-membered ring channel to the next 10-membered ring channel above it as marked by yellow dashed lines in the image (a), which cut through tiles t-ftt (pink) and t-kze (yellow) as more clearly shown in the DFO's tiling image (c). The two tiles actually form the 10-membered ring channel in the structure. The t-eni (blue) and t-kah (light green) tiles terminate the terrace. This calculation agrees with the possibility 2 in our early structural

analysis based on the AFM result regarding where the DAF-1 crystal (001) surface terminates (see Figure 4.7).

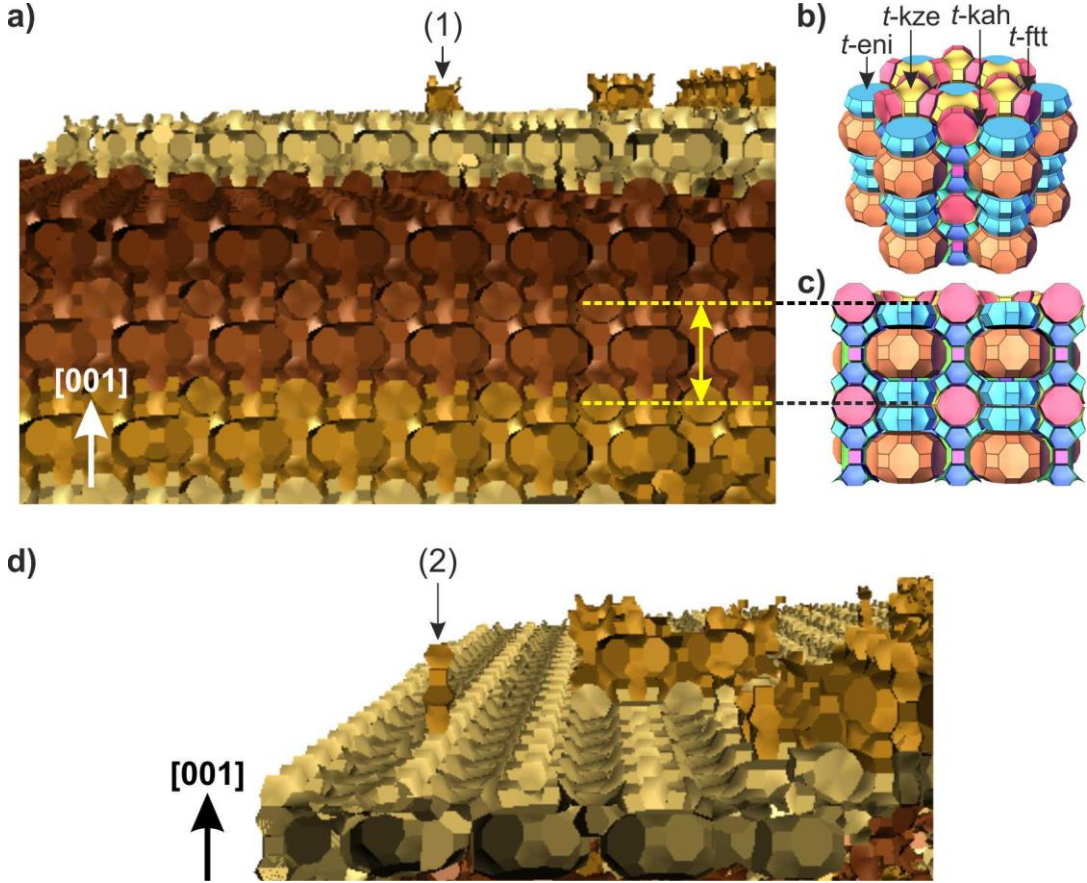


Figure 4.13. a) Cross-sectional of the (001) facet of simulated DFO crystal. Yellow double arrows show one growth layer. b) and c) DFO structure tilings drawn with *Gavrog 3dt* having the same orientation as the crystal model in (a), although the orientation of the image (b) is a little tilted to show the tiles on (001) surface termination. d) Simulated (001) surface of the DFO crystal model.

The presence of lower steps on the model crystal (marked (1) in Figure 4.13 (a)) indicates that the layers are built step by step by gradual attachment of units of growth to the crystal surface. New nucleation is also found on the surface of the model crystal (marked (2) in Figure 4.13 (d)). The nucleation seems to start with an attachment of units growth to construct surface structure as if the small tiles, *e.g.* t-kah, t-lov, t-cub and t-lau, are on top of a bulky terrace.

In terms of the (010) facet of the simulated crystal, of which a closer examination is presented in Figure 4.14, one growth layer is shown as cyan double arrows. Each

growth layer is illustrated in different colour as can be observed in the image (d). The layer growth is terminated by t-lau, t-kah, t-lov, t-cub and t-fft tiles. Meanwhile, the crystal surface cuts across the two largest DFO tiles (t-evh and t-eni), which in reality construct 12-membered ring type 1 channel along the [001] direction. Therefore, open half-cages build the structure on the (010) surface terminal. This simulation supports the possibility 2 of the previous structure analysis according to the laboratory experiment result (see Figure 4.8).

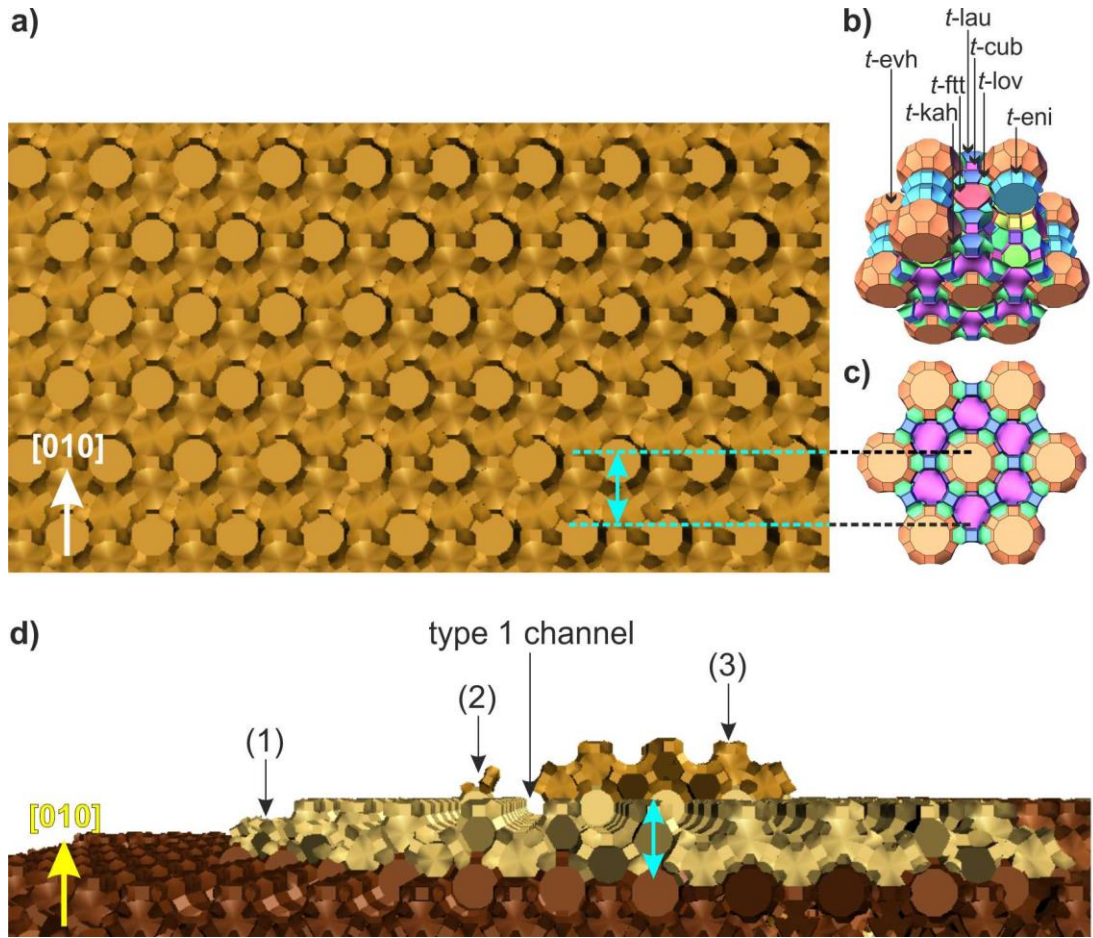


Figure 4.14. a) Cross-sectional of the (010) facet of simulated DFO crystal. b) and c) DFO structure tilings drawn using *Gavrog 3dt* having the same orientation as the crystal model in (a), although the orientation of the image (b) is a little tilted to show the tiles on (010) surface termination. d) Simulated (010) surface of the DFO crystal model. Cyan double arrows show one growth layer.

The modelling also gave lower steps on the crystal surface (indicated as (1) in Figure 4.14). It tells us that during the growth, the layers on the (010) facet are built in

gradations by the incorporation of units of growth. So far, this phenomenon is adopted by the complex structures of DFO and UOV to grow the layers on the crystal surface. New nucleation (marked as (2) in the image) is another phenomenon that always exists in both facets of DAF-1 crystal. When it grows, the new nucleation creates a new layer (marked as (3)) on the crystal surface although the layer below it is incomplete. This leads to the formation of a crystal surface with terraces as evidenced in this work.

4.3.4. In-situ AFM of DAF-1 crystal dissolution

An in-situ AFM experiment of DAF-1 crystal dissolution was performed using the solutions listed in Table 4.2. All solutions in the list dissolved the crystal. However, not all of them dissolved it slowly enough to be followed by the AFM scanning. The effect of each solution on the DAF-1 crystal surface is presented and discussed in this section.

Table 4.2. Solutions used in in-situ AFM experiment to dissolve the DAF-1 crystal

Solution	Molar ratio	pH
1	1 Dec(OH) ₂ : 0 H ₃ PO ₄	~11
2	0 Dec(OH) ₂ : 1 H ₃ PO ₄	~3
3	1 Dec(OH) ₂ : 1.3 H ₃ PO ₄	9 – 10
4	1 Dec(OH) ₂ : 2.4 H ₃ PO ₄	8 – 9
5	1 Dec(OH) ₂ : 2.7 H ₃ PO ₄	6 – 7

4.3.4.1. Dissolution of DAF-1 crystal in solution 1

Decamethonium hydroxide 1×10^{-3} M (pH \approx 11) was one of the solutions used in this in-situ AFM experiment. The basic solution injection resulted in DAF-1 crystal dissolution as displayed in the forthcoming images in Figure 4.15.

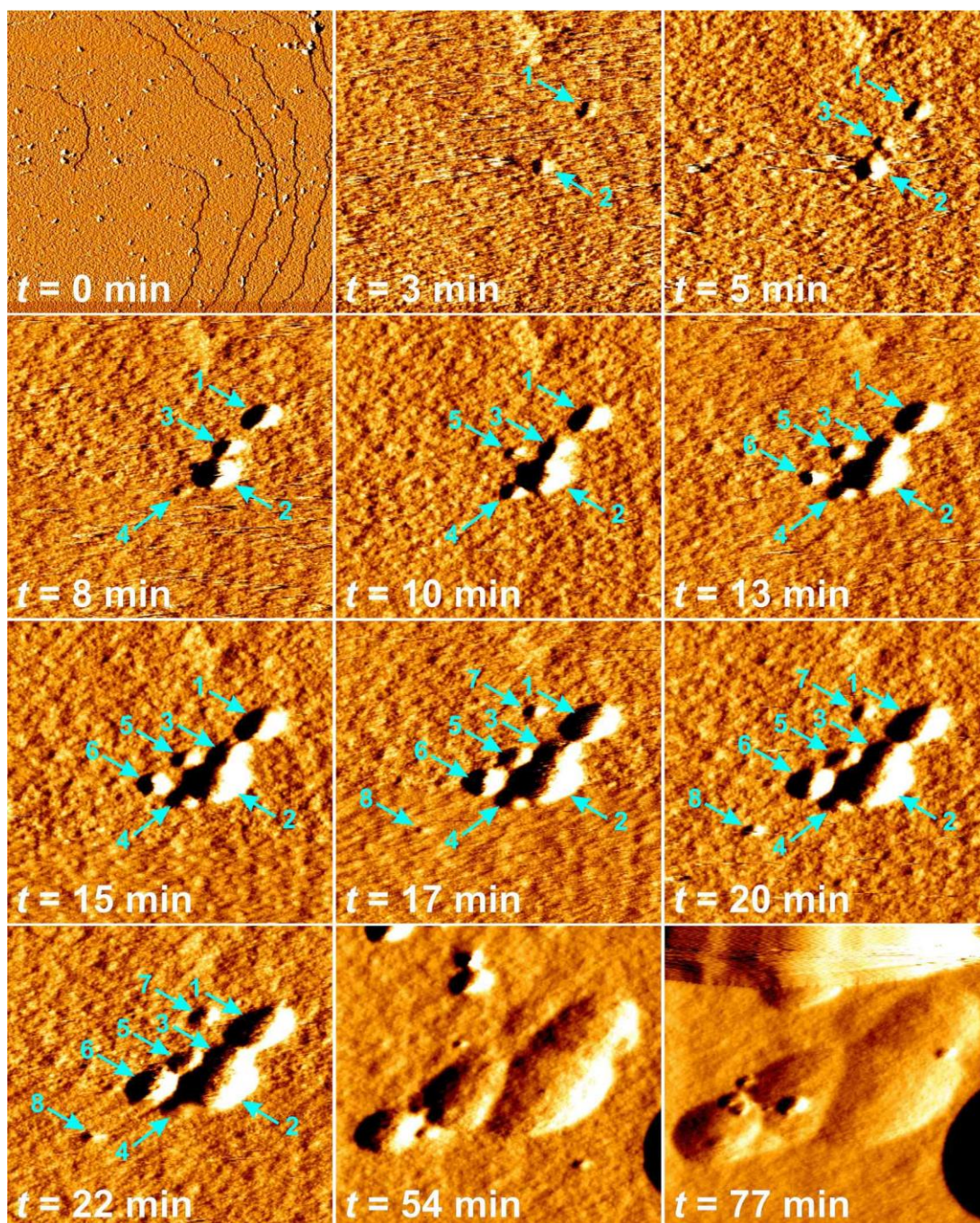


Figure 4.15. Sequential AFM vertical deflection images sized $3.0\ \mu\text{m} \times 2.8\ \mu\text{m}$ of DAF-1 crystal dissolution in Dec(OH)_2 with $\text{pH} \approx 11$ on (010) facet. Pit formation is shown, indicated by cyan arrows.

As we can see in Figure 4.15, the solution attacked the (010) surface of the DAF-1 crystal very aggressively. Pits (indicated by cyan arrows) were already formed in 3 minutes after the crystal surface was in contact with the solution. The pits grew very quickly in size, as well as in the number of new pits created. The terraces, which

existed before the solution injection ($t = 0$ min), is vaguely seen afterwards. Most of the pits at $t = 54$ and 77 minutes have grown larger, thus they merged with each other. At $t = 77$ minutes, many areas on the DAF-1 crystal surface have been dissolved as observed by AFM, as well as seen under the optical microscope in Figure 4.16. Subsequently, the crystal dissolved more after about 3.5 hours immersed in the solution.

In regard to the (001) facet of the DAF-1 crystal, the same basic solution gave similar rapid crystal dissolution as the side facet. Pits were formed on the hexagonal side once the solution was injected. The pits grew larger very quickly as the dissolution time was getting longer.

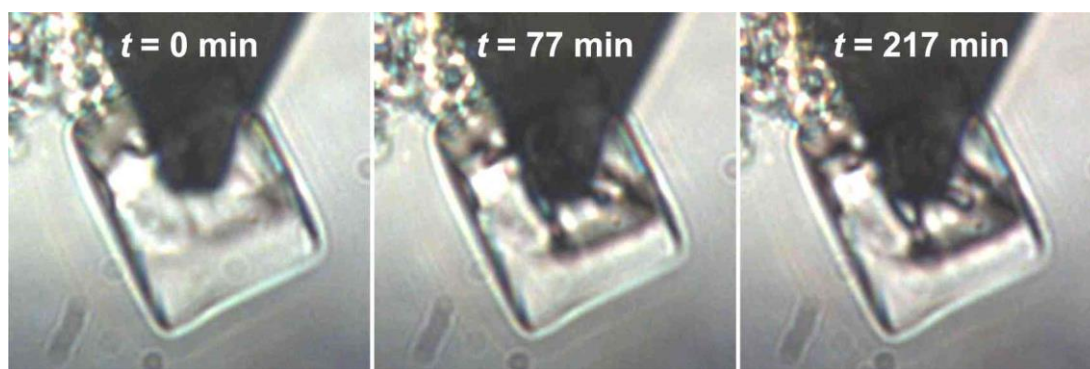


Figure 4.16. DAF-1 crystal showing (010) facet under the optical microscope during in-situ AFM scanning in Dec(OH)₂ solution (pH \approx 11).

Since the DAF-1 crystal dissolution in this pH 11 Dec(OH)₂ solution took place rapidly, the dissolution mechanism becomes unclear. Such rapid pits formation on zeolite crystal surface in high pH solution has also been reported by Yamamoto and co-workers (1996) [12]. They also stated that the pits formed during the dissolution increased in size with time.

4.3.4.2. Dissolution of DAF-1 crystal in solution 2

The use of phosphoric acid solution having pH around 3 to dissolve DAF-1 crystal in this work did not demonstrate an observable sequence of layer dissolution for over 3 hours. However, from the AFM images, we can observe gradual pit formation on the

DAF-1 crystal surface during its dissolution in the H_3PO_4 solution. The images are presented in Figure 4.17 and Figure 4.18 for (010) and (001) facets, respectively.

For the (010) facet (see Figure 4.17), one phenomenon noticed is that the pit formation was initiated by a very small particle which appeared on the DAF-1 surface, as pointed by the white arrow in the image at $t = 53$ minutes. Prior to this, at $t = 50$ minutes, this small particle did not exist on the particular location. Thus, we call this very small particle as an unknown nano-dot. Subsequently, this unknown nano-dot was removed or dissolved by the H_3PO_4 solution (image at $t = 55$ minutes) leaving a very small hole on the surface under where it sat ($t = 58$ minutes). The small hole gave room for the solution to penetrate into, get in contact with and dissolve the side wall of the hole. As a consequence, this opening was getting larger since the DAF-1 particles inside it were gradually etched before finally created an extensive pit.

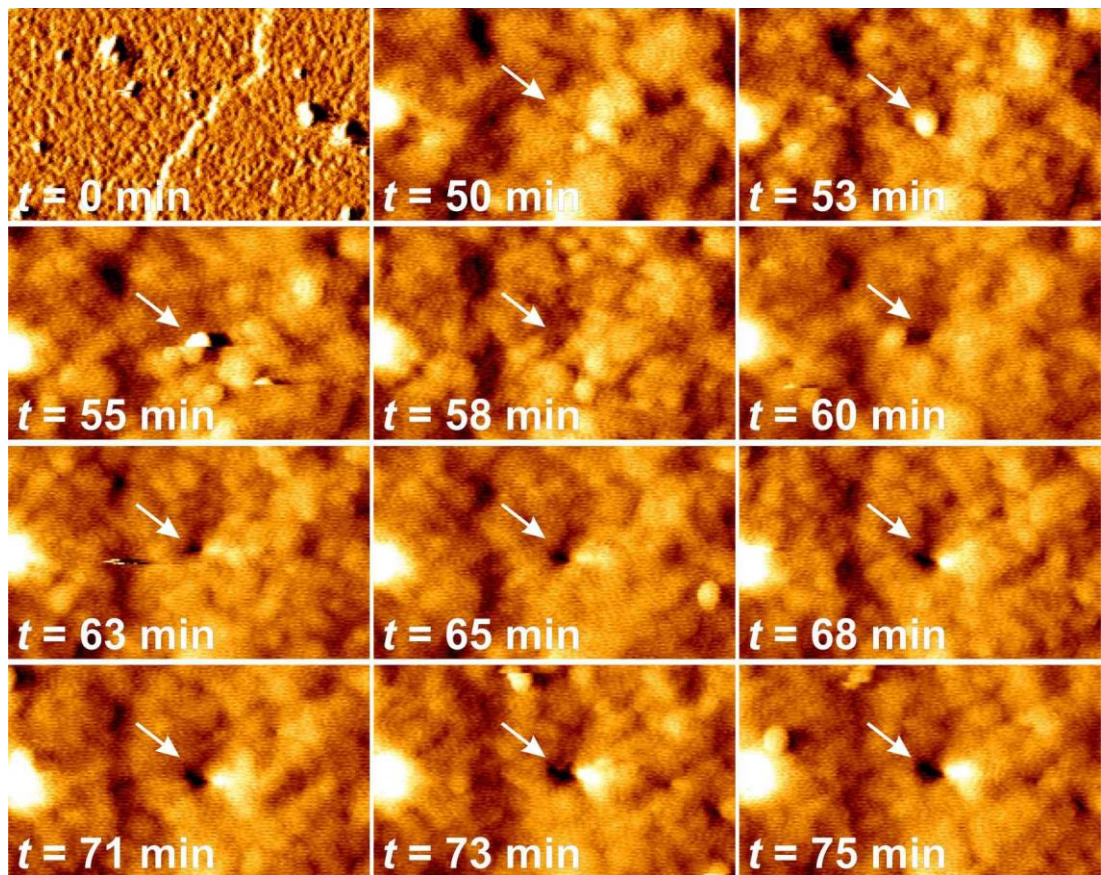


Figure 4.17. AFM vertical deflection images of DAF-1 crystal on (010) facet sized $1.0\ \mu\text{m} \times 0.6\ \mu\text{m}$ dissolved in an H_3PO_4 solution having $\text{pH} \approx 3$. White arrows point to pit formation sequence.

The hexagonal (001) facet of DAF-1 crystal (see Figure 4.18) seems to experience a similar pit formation mechanism in this solution 2. An unknown nano-dot emerged on DAF-1 crystal surface for several seconds followed by the removal of this dot, leaving an opening on the crystal surface. The opening was then getting bigger as the solution reached the particles on its wall and dissolved it.

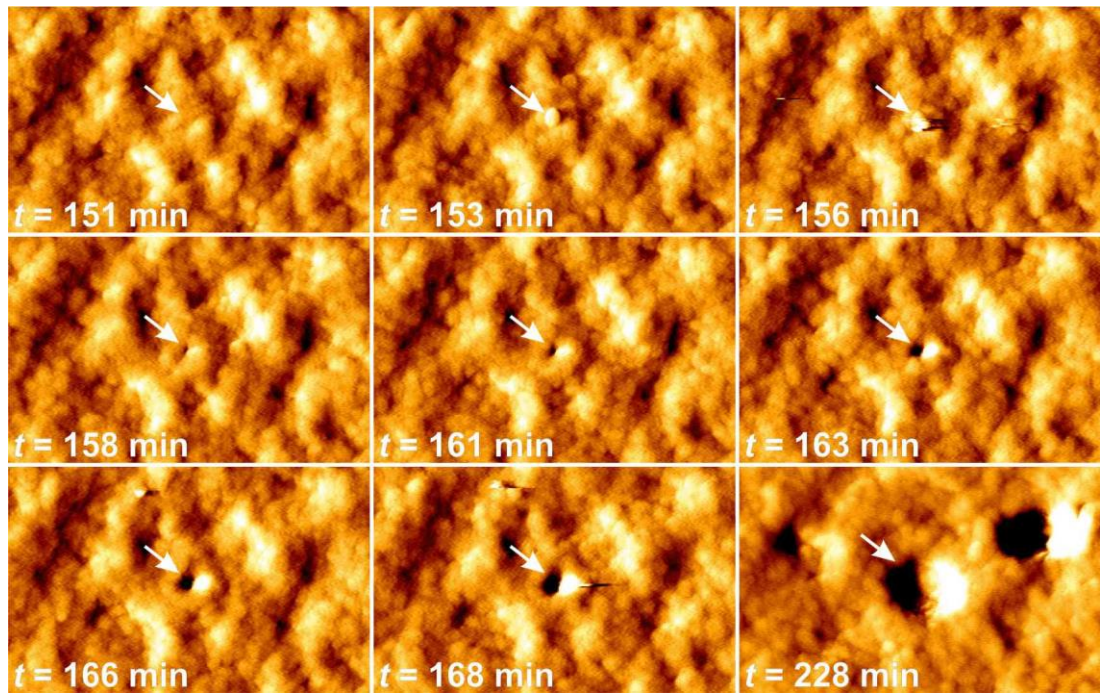


Figure 4.18. AFM vertical deflection images of DAF-1 crystal on (001) facet sized $1.4 \mu\text{m} \times 0.9 \mu\text{m}$ dissolved in H_3PO_4 having $\text{pH} \approx 3$. White arrows point to pit formation sequence.

4.3.4.3. Dissolution of DAF-1 crystal in solution 3

Clear solution 3 prepared from $\text{Dec}(\text{OH})_2$ and H_3PO_4 solutions with molar ratio 1 : 1.3 used in this experiment had pH around 9 – 10. Figure 4.19 exhibits the orientation of the DAF-1 crystal scanned in-situ in solution 3 in this work.

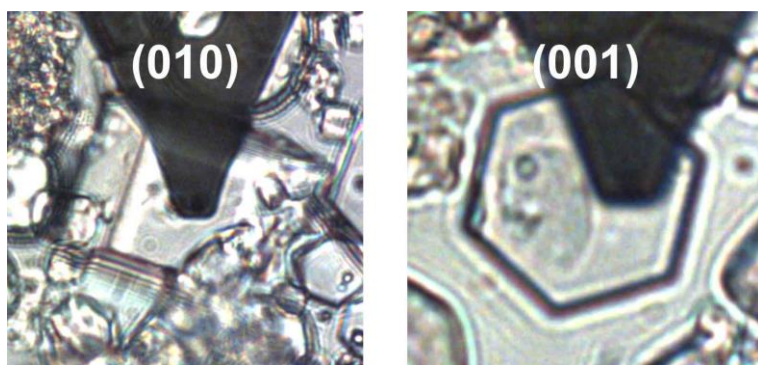


Figure 4.19. DAF-1 crystal orientation during in-situ AFM experiment in solution 3.

The result of the (010) facet dissolution is displayed as consecutive images in Figure 4.20 and as Movie 4-1 in Appendix 1. The in-situ AFM scanning was performed for about 2.5 hours. Before the solution was injected ($t = 0$ minute), the presence of other grainy phases on top of the DAF-1 crystal surface was clearly seen. Five minutes after the solution 3 was introduced, the impurity grains became more obvious. During the in-situ experiment, these surface impurities slowly dissolved in solution.

Solution 3 dissolved the crystal in a way of ‘surface thinning’, as we can see through the whole images. It seems that the solution attacked any particles exposed to it regardless of their position in terraces’ layers. However, interestingly, DAF-1 crystal maintained the terraces’ positions on the surface during this 2.5-hour dissolution process. The average step height was also preserved to be around 2.0 ± 0.1 nm as evidenced by cross-sectional height measurements conducted before solution injection ($t = 0$ min) and during the dissolution process (shown here only for $t = 13$ min and 26 min).

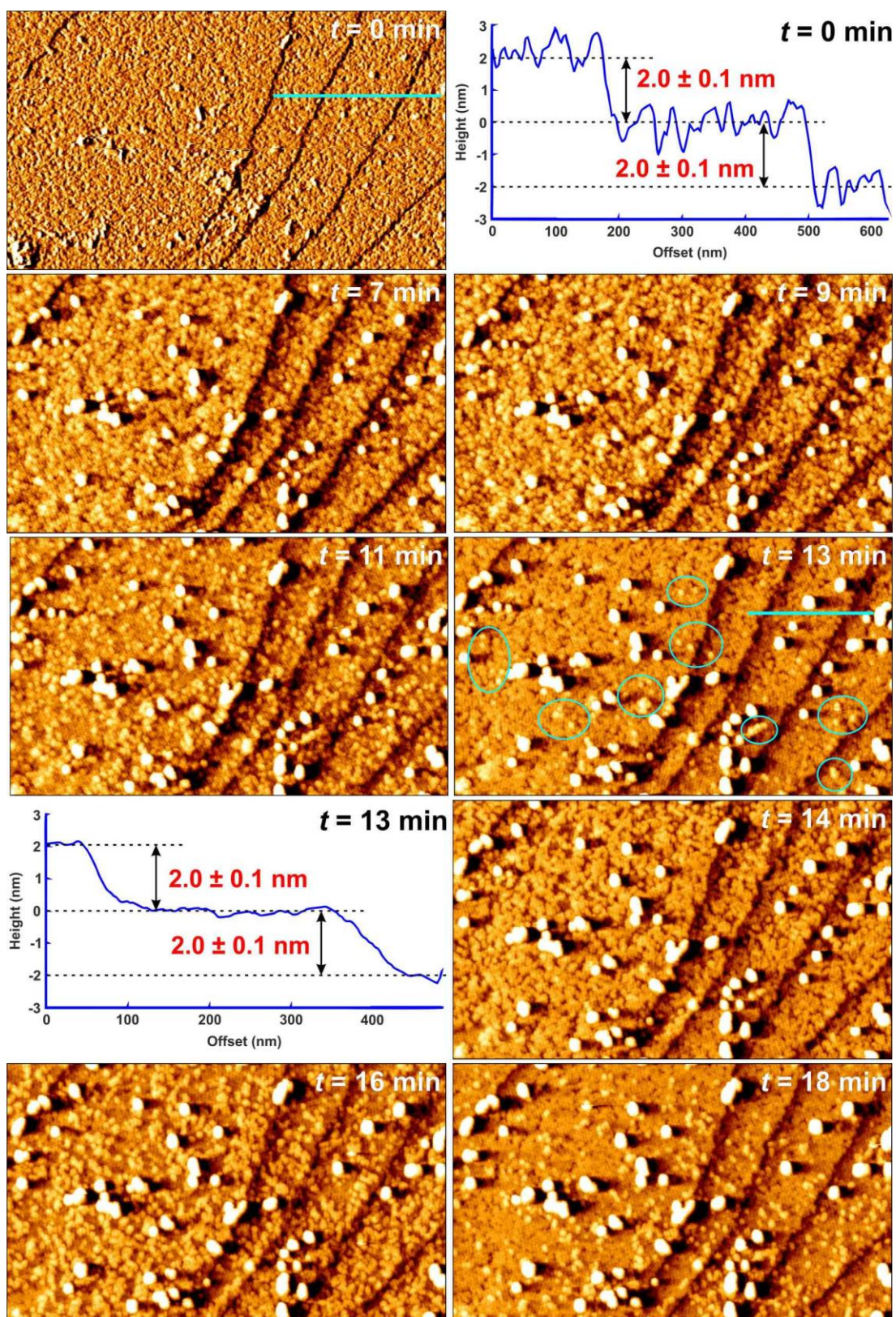


Figure 4.20. AFM vertical deflection images of DAF-1 crystal dissolution in solution 3 displaying $1.7 \mu\text{m} \times 1.0 \mu\text{m}$ area of (010) facet and height measurements along the cyan lines drawn on several images (*to be continued on the next page*).

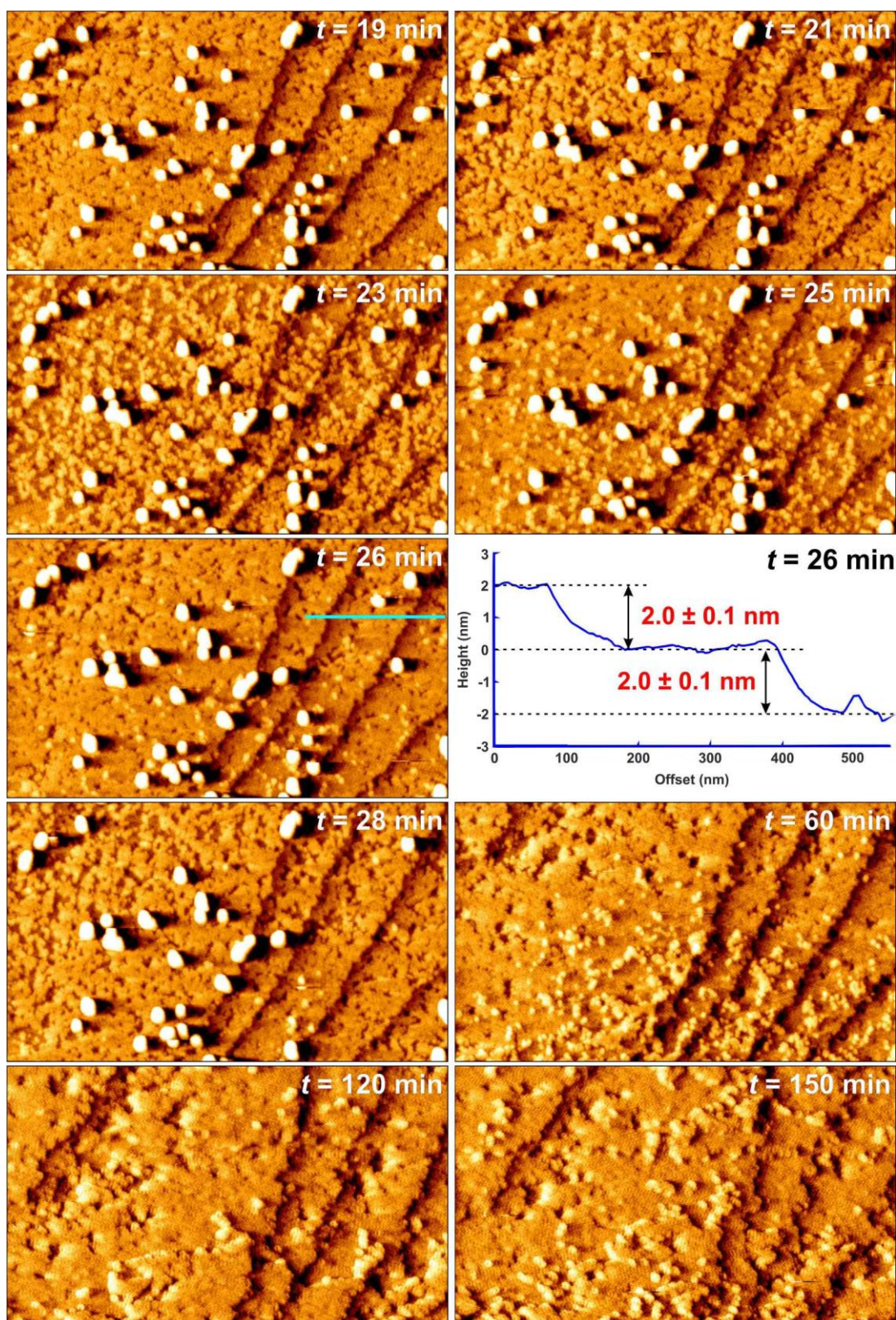


Figure 4.20 (continued). AFM vertical deflection images of DAF-1 crystal dissolution in solution 3 displaying $1.7 \mu\text{m} \times 1.0 \mu\text{m}$ area of (010) facet and height measurements along the cyan lines drawn on several images.

Advantageously, the unchanged layer position can be used to work out the dissolution rate, although only by a rough determination. The observation was made on the images from $t = 14$ minutes to $t = 21$ minutes. It is apparent that in the image at $t = 13$ minutes, there were still a few small dots. Those small dots represent DAF-1 particles from the just-dissolved layer during the dissolution process for 13 minutes (circled cyan in the image to be clearly seen). At $t = 14$ minutes, these small dots disappeared completely, entirely exposing the layer just beneath them. From this point, we started to count the dissolution time for one growth step (approximately 2 nm high). Following the removal stages of particles in this particular layer, until all of them no longer exist on the surface (which means that the surface appearance is similar to that of the image at $t = 14$ minutes), we noted that the described condition occurred in the image at $t = 21$ minutes.

Further observation on the consecutive images in Figure 4.20 to follow the disappearance of the topmost growth step at $t = 21$ minutes gave the same result that one layer was dissolved totally in 7 minutes, started from $t = 21$ to $t = 28$ minutes. By making a rough observation on the dissolution process as explained above, it is reasonable to say that the time needed for each surface layer (approximately 2 nm high) on (010) facet to be dissolved completely was 7 minutes.

From images obtained during the in-situ experiment in Figure 4.20, height measurements were performed to follow the height breakdown of the nano-dot (DAF-1 particle on crystal surface) during the dissolution process. This was carried out to understand the full story of this particular dissolution process. Figure 4.21 displays the measurements of a nano-dot height (the nano-dot is indicated by cyan arrows) in several subsequent images at $t = 16$, 18 and 19 minutes. A series of height: (ii) 1.0 ± 0.1 nm, (iii) 0.5 ± 0.1 nm and (iv) 0.3 ± 0.1 nm were recorded before the dot was dissolved completely.

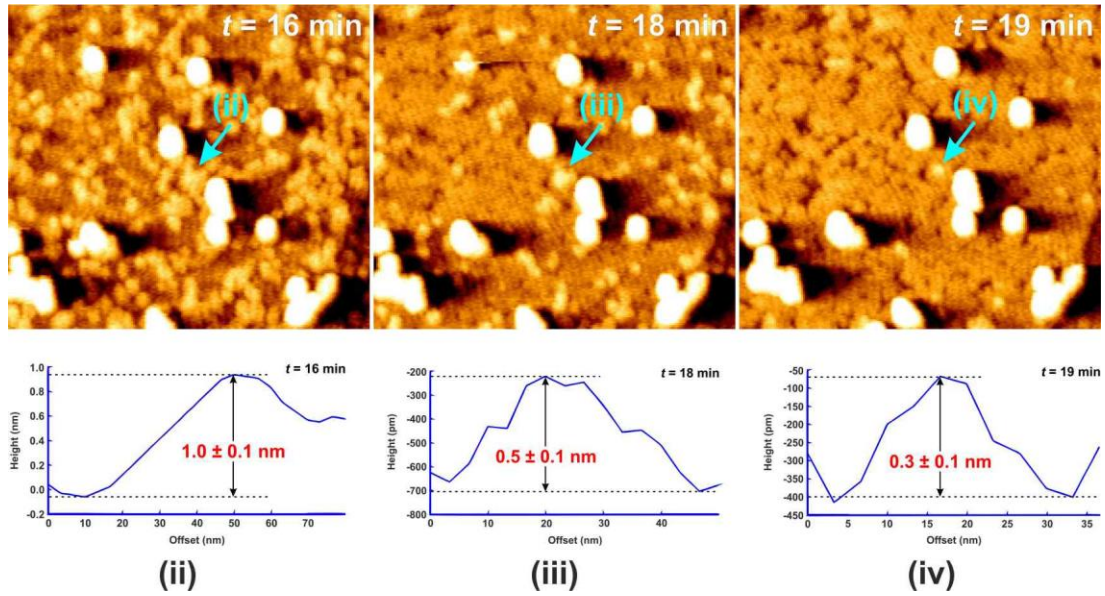


Figure 4.21. A series of height measurements performed on the same nano-dot (very small DAF-1 particle) on (010) DAF-1 crystal surface at three consecutive dissolution times.

Two possibilities where the surface cuts through the structure, as explained in the previous section (section 4.3.2), can also be tested here with a more detailed measurement. Both possibility 1, with growth layer surface cut across the double 4-rings in the middle of the type 1 channel (see Figure 4.22 (a)), and possibility 2, of which growth layer surface cuts just above the bridge connecting two type 1 channels (see Figure 4.22 (b)), show reasonable structure break-down which fits the nano-dot height measurement obtained. The two possibilities contain sensible structure break-downs resulted in 1.0 ± 0.1 nm, 0.5 ± 0.1 nm and 0.3 ± 0.1 nm high as the nano-dot heights found in this experiment. In spite of the sensible structure break-downs from our analysis, it cannot be denied that, during the scanning, the AFM might miss observing other nano-dots' heights in between those three detected heights.

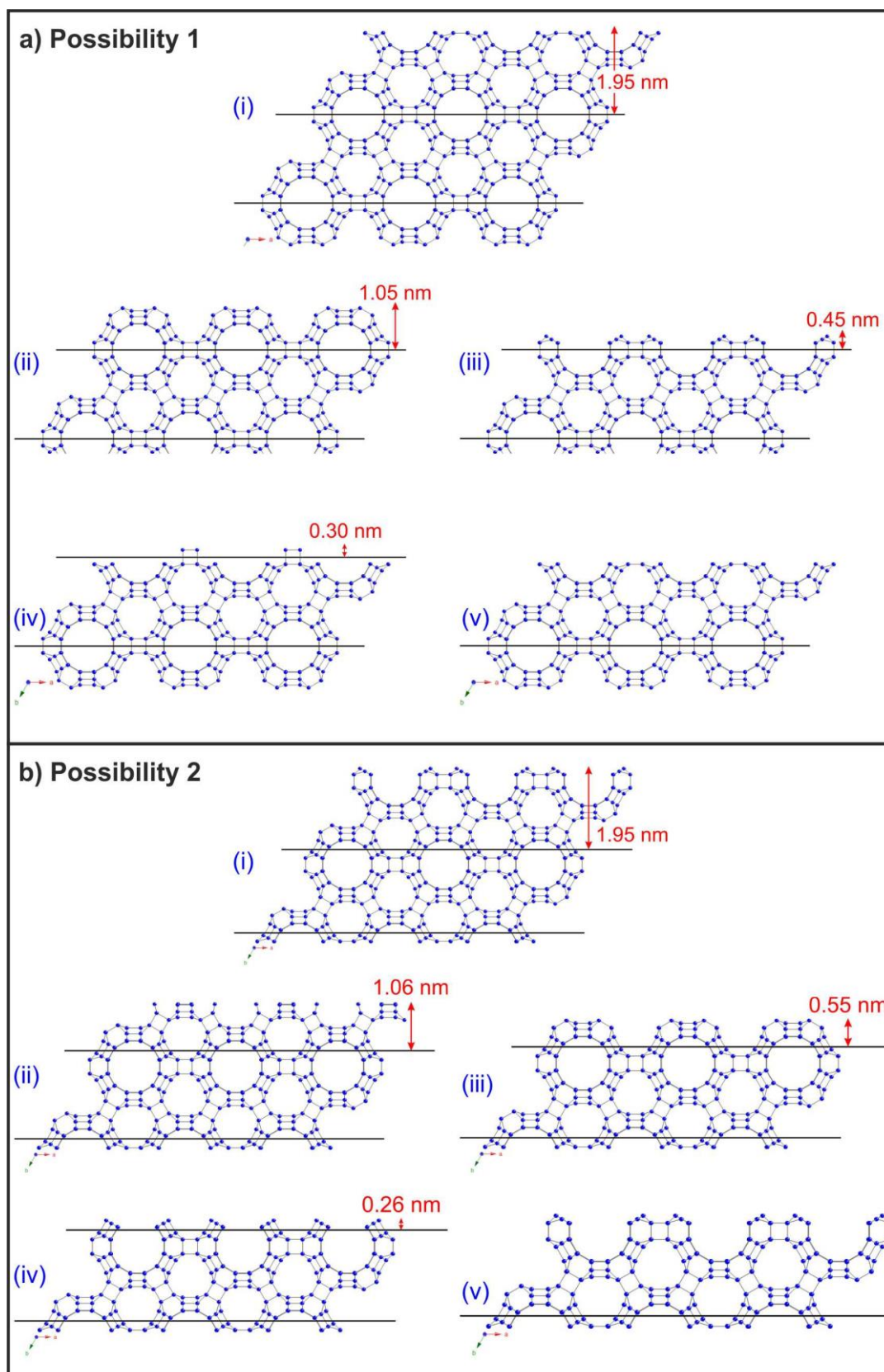


Figure 4.22. a) Possibility 1 and b) possibility 2 of the DFO structure breakdown viewed along the [001] direction. The blue dots in the structure represent the Al, P or Mg atoms, whilst the black sticks illustrate the oxygen bridging in between those Al, P or Mg atoms. Oxygen atoms are omitted for clarity.

In terms of DAF-1 crystal dissolution on (001) facet in solution 3, the dissolution pattern is not very clearly observed. Nevertheless, looking carefully at the images in Figure 4.23, we can see the same dissolution pattern as the one that occurred on the (010) facet. Magnified images at $t = 135 - 140$ minutes (see Figure 4.24) clarify this conclusion. The circled areas in Figure 4.24 clearly show some particles of the crystal surface were wiped away during the process. Anyhow, very uneven surface texture in this facet causes the difficulty to perform reliable height measurement of the nano-dots in these images. As a result, a detailed structure breakdown along the dissolution process on this facet cannot be performed. Movie 4-2 in Appendix 1 presents a movie on this dissolution.

Here, in Figure 4.23, we can see that the (001) facet also maintained its terraces position and height during the dissolution process. Before the solution was injected, the growth step was 2.1 ± 0.1 nm high, which agrees with the theoretical height (2.162 nm) stated in Figure 4.7 (d). Evidenced from the height measurement, the steps kept preserving the height for 31 and 142 minutes in contact with solution 3. They gave 2.1 and 2.0 ± 0.1 nm respectively. Because of the small height distinction, we may say that the results are indifferent.

The image at $t = 142$ minutes in Figure 4.23 proves that DAF-1 surface thinning was the result of the dissolution process rather than being caused by the cantilever tip interference, as the area outside the scanned zone experienced the same thinning process and showed the same height level as the scanned one (marked with white rectangle in the image). Growth step height measurements inside and outside the scanning area also show the same height, which is 2.0 ± 0.1 nm.

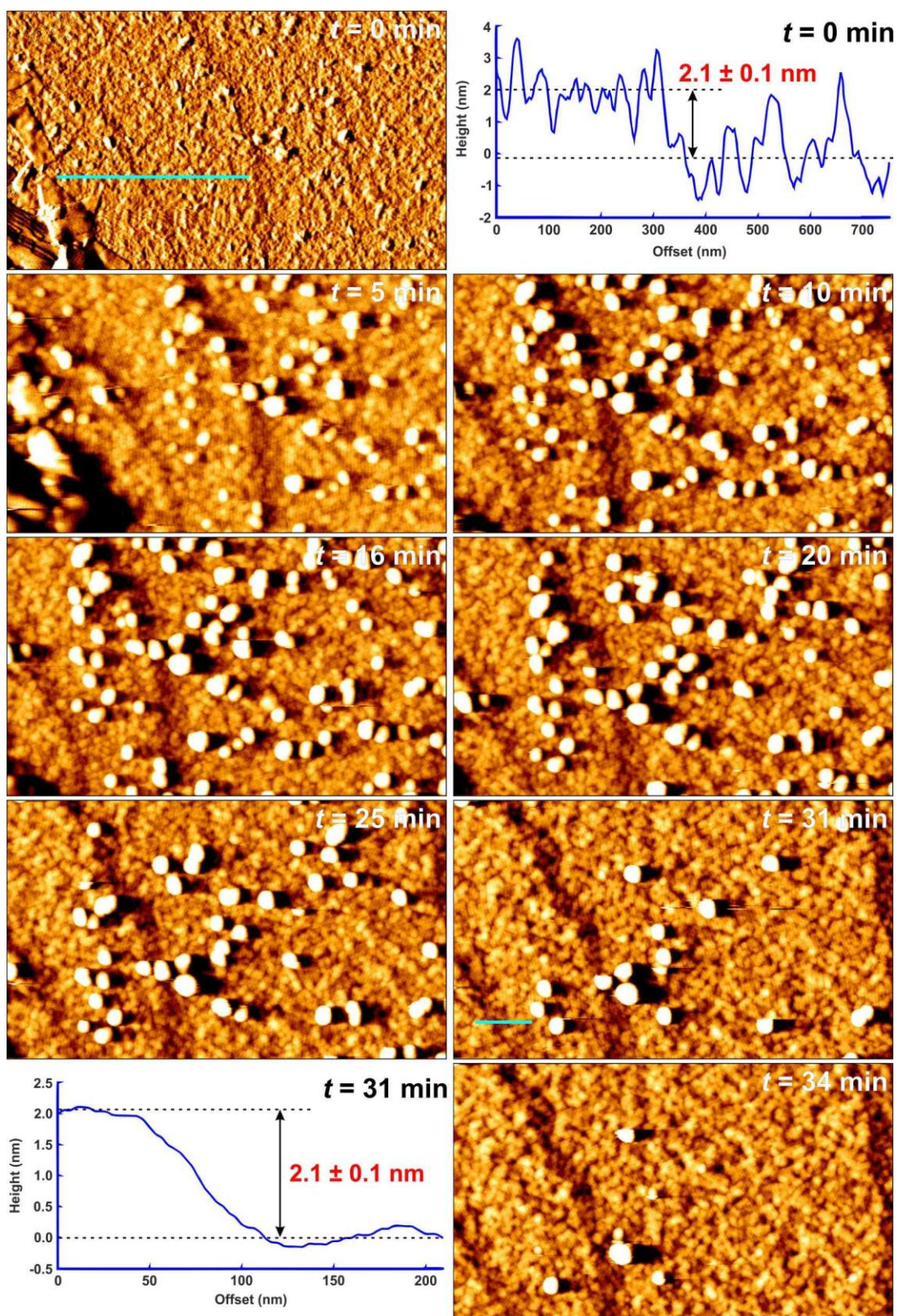


Figure 4.23. Successive AFM vertical deflection images on (001) facet of DAF-1 crystal dissolution in solution 3, with cross-sectional height measurements performed on cyan lines. Scanned area: $1.7 \mu\text{m} \times 1.0 \mu\text{m}$ ($t = 0 - 100$ min) and $5.2 \mu\text{m} \times 3.0 \mu\text{m}$ ($t = 142$ min). White rectangle in the image at $t = 142$ minutes is the area scanned previously (*to be continued on the next page*).

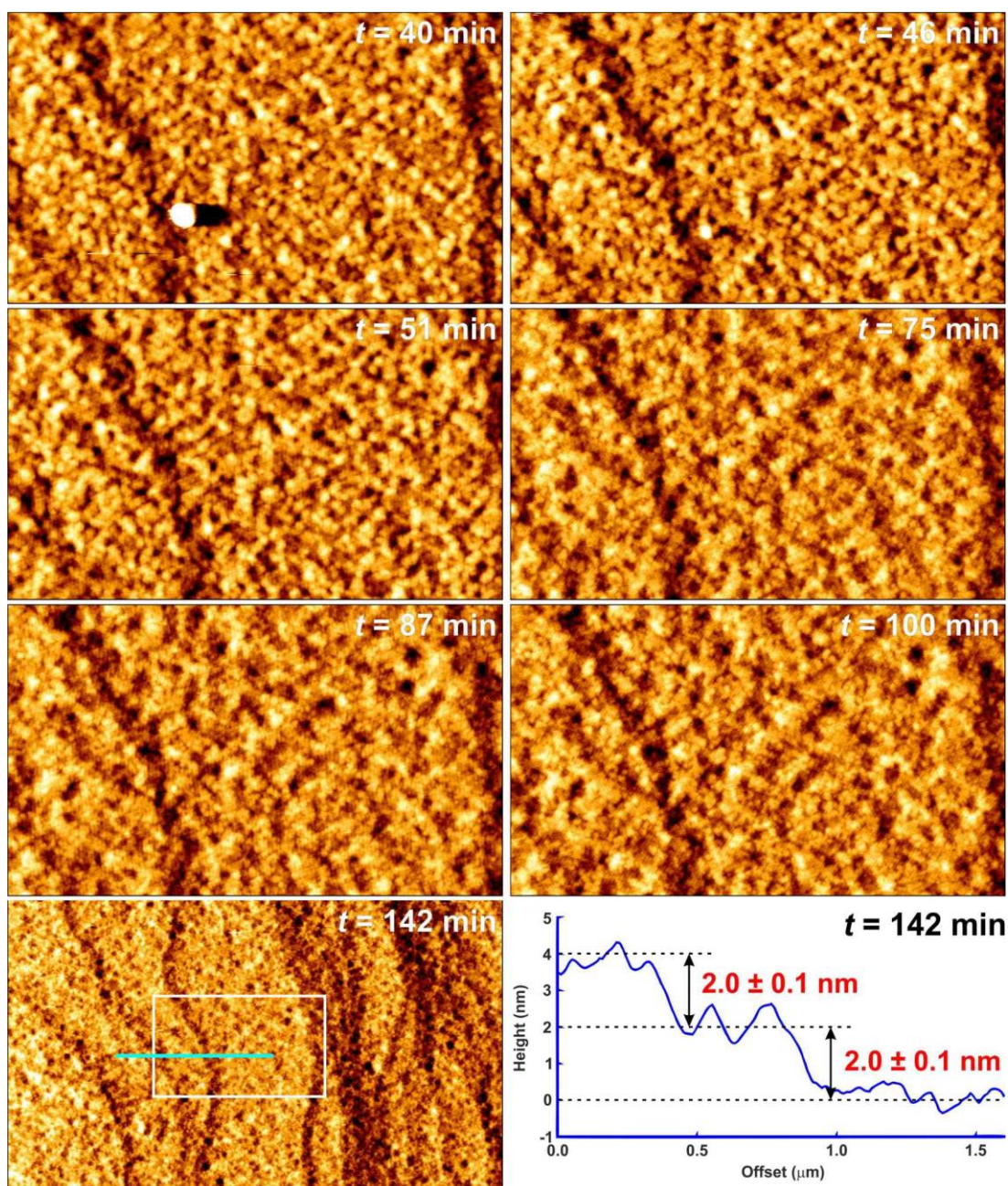


Figure 4.23 (continued). Successive AFM vertical deflection images on (001) facet of DAF-1 crystal dissolution in solution 3, with cross-sectional height measurements performed on cyan lines. Scanned area: $1.7 \mu\text{m} \times 1.0 \mu\text{m}$ ($t = 0 - 100$ min) and $5.2 \mu\text{m} \times 3.0 \mu\text{m}$ ($t = 142$ min). White rectangle in the image at $t = 142$ minutes is the area scanned previously.

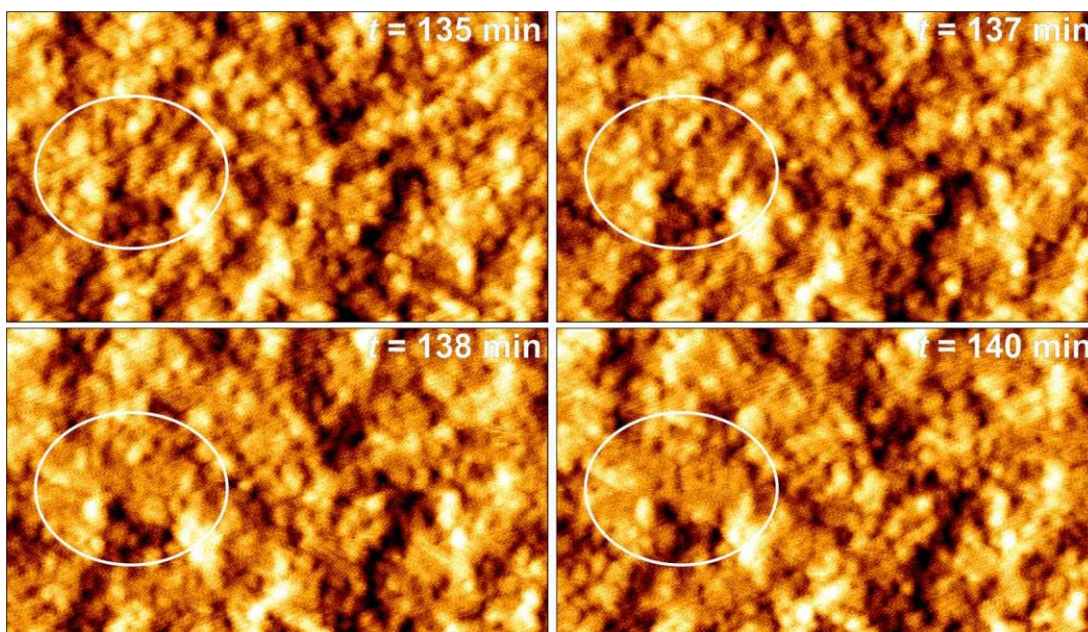


Figure 4.24. AFM vertical deflection images of DAF-1 crystal on (001) facet during dissolution in solution 3 showing a closer look (the scanned area is $0.7 \mu\text{m} \times 0.4 \mu\text{m}$) of the scanned area in *Figure 4.23*.

4.3.4.4. Dissolution of DAF-1 crystal in solution 4

Reducing the solution pH to 8 – 9 (solution 4) by adding more H_3PO_4 resulted in DAF-1 crystal dissolution process as presented in *Figure 4.25* and *Figure 4.28* for (010) and (001) facets, respectively.

Similarly to the dissolution in solution 3, the dissolution profile of the (010) facet of DAF-1 crystal in solution 4 adopted the ‘surface thinning’ process as observed in *Figure 4.25* and *Movie 4-3* in Appendix 1. Once particles in the crystal surface were in contact with the solution, they eventually dissolved without any special preference. The crystal also maintained the terrace position as, in the last image, the terraces were found to be where they were before the dissolution process. Beside the terrace position, its height was also preserved at *c.a.* 2 nm (see height measurements in *Figure 4.25* which gave 1.9 and 2.0 ± 0.1 nm). Considering ± 0.1 nm error the measurement may make, it is safe to say that the measured heights match the calculated one, which is 1.95 nm.

The crystal dissolution rate in solution 4, with a lower pH, is somewhat higher than that in solution 3 for the same facet, (010) facet. Here, in solution 4, we learned that

one layer or growth step, approximately 2 nm thick, dissolved completely in 6 minutes. This rough observation was made from Figure 4.25 at $t = 18 - 24$ minutes and $t = 24 - 30$ minutes using the same approach as the determination of the dissolution rate in solution 3 explained previously.

Furthermore, after about one hour being immersed in this solution having pH 8 – 9, we started to notice the development of holes on (010) facet. The holes were getting larger as the crystal was soaked longer in the solution. Unlike the solution 3 (pH 9 – 10), which has not created any pits on DAF-1 crystal surface in its first hour of the dissolution process, solution 4 started the pit formation more quickly. This is one of the indications that in less basic solution, DAF-1 crystal dissolves faster, either layer by layer dissolution or the vertical attack through the formation of pits.

The DAF-1 crystal was immersed in solution 4 for about 5.5 hours in this experiment, but again, there is no sign of dissolution caused by tip interference on the (010) facet as can be seen in the last image in Figure 4.25. It means that the dissolution that happened was a pure product of the reaction between solution 4 and DAF-1 crystal.

Zooming in on the scanning area makes it easier to perform more careful measurement of nano particle height in the images. There is a lot of missing information as the AFM did not record every change in nano particle height owing to its fast dissolution rate in this solution 4. Therefore, we cannot follow the height of a single nano particle as we did for the dissolution in solution 3. However, since the AFM tip scanned the nano-dots in their different dissolution states during the dissolution process, we decided to measure many nano-dot heights to get many distinctive heights, which gave information on, hopefully, every height breakdown a growth step experienced. Shown in Figure 4.26 are the majority of the nano dot heights found all along the dissolution process. Those heights are 1.2, 1.0, 0.8, 0.5 and 0.3 ± 0.1 nm.

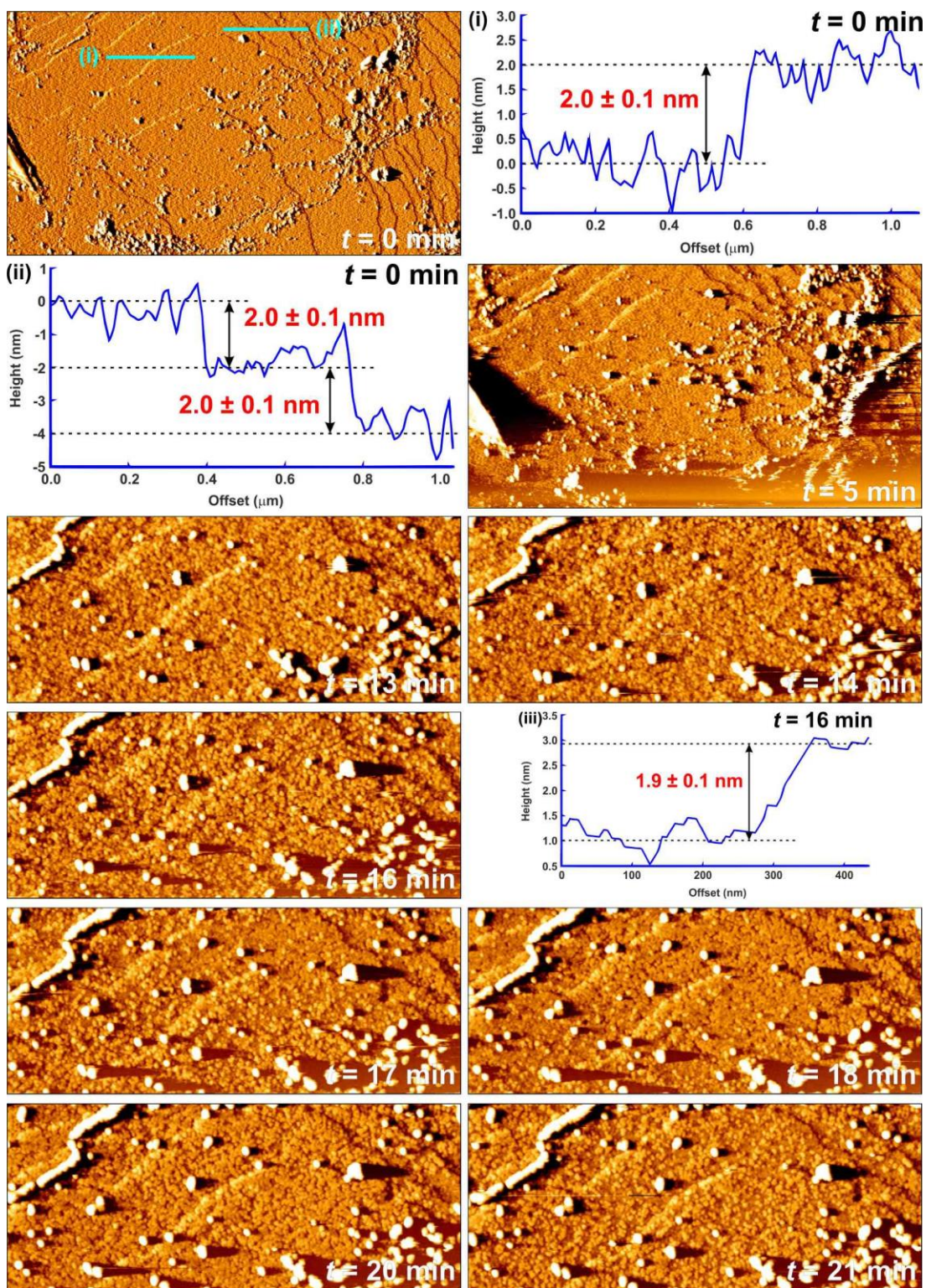


Figure 4.25. Subsequent AFM vertical deflection images displaying the dissolution of (010) facet of DAF-1 crystal in solution 4. Scanned areas are $5.5 \mu\text{m} \times 3.0 \mu\text{m}$ ($t = 0 - 5$ min), $3.0 \mu\text{m} \times 1.3 \mu\text{m}$ ($t = 13 - 119$ min), $1.3 \mu\text{m} \times 1.3 \mu\text{m}$ ($t = 141 - 168$ min) and $5.0 \mu\text{m} \times 5.0 \mu\text{m}$ ($t = 324$ min). Blue squares in images at $t = 119$ and 324 mins show the scanning areas for $t = 141 - 168$ min, whilst white rectangle in image at $t = 324$ min is the scanning region for $t = 13 - 119$ min (to be continued on the next page).

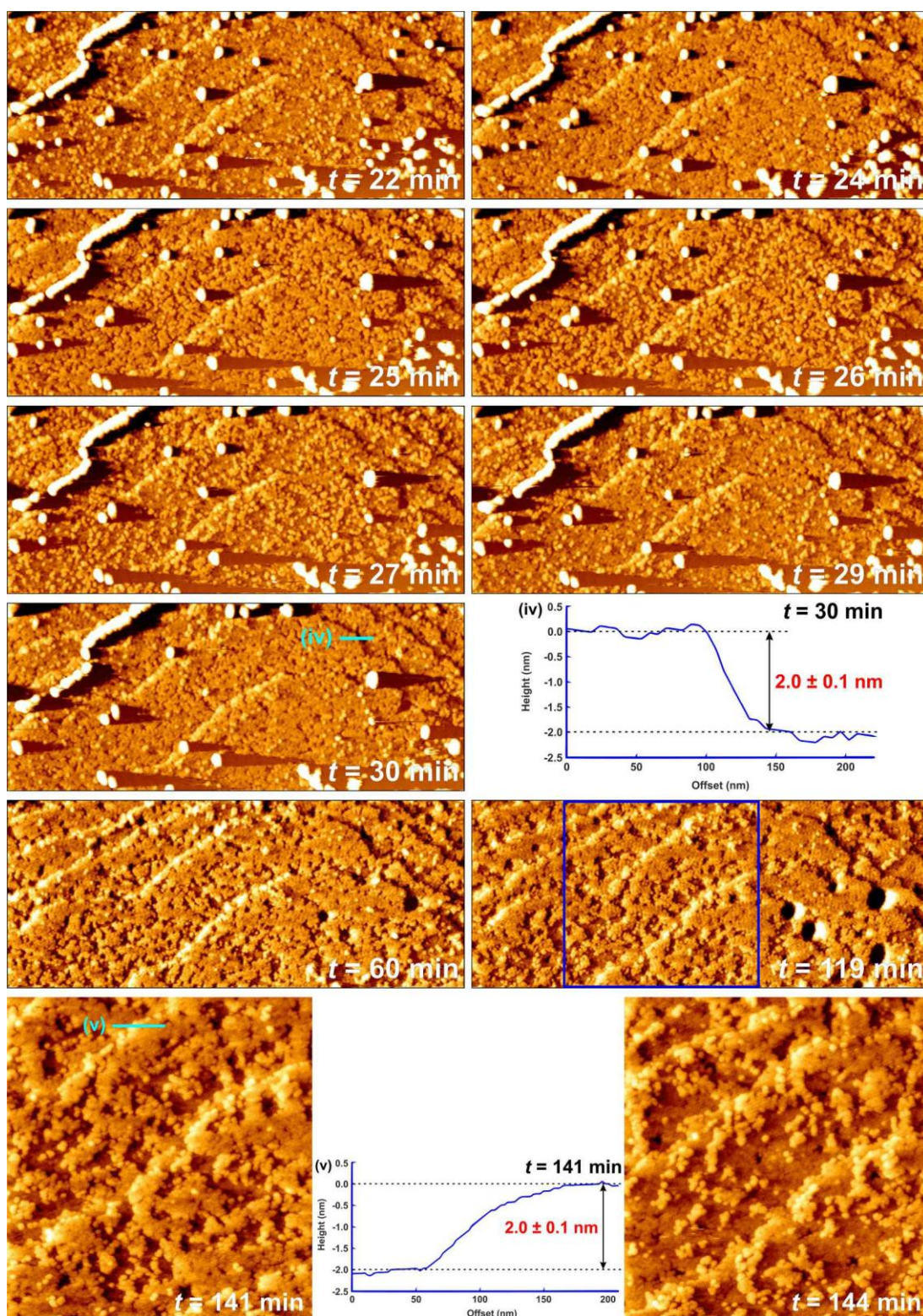


Figure 4.25 (continued). Subsequent AFM vertical deflection images displaying the dissolution of (010) facet of DAF-1 crystal in solution 4. Scanned areas are $5.5 \mu\text{m} \times 3.0 \mu\text{m}$ ($t = 0 - 5$ min), $3.0 \mu\text{m} \times 1.3 \mu\text{m}$ ($t = 13 - 119$ min), $1.3 \mu\text{m} \times 1.3 \mu\text{m}$ ($t = 141 - 168$ min) and $5.0 \mu\text{m} \times 5.0 \mu\text{m}$ ($t = 324$ min). Blue squares in images at $t = 119$ and 324 mins show the scanning areas for $t = 141 - 168$ min, whilst white rectangle in image at $t = 324$ min is the scanning region for $t = 13 - 119$ min (*to be continued on the next page*).

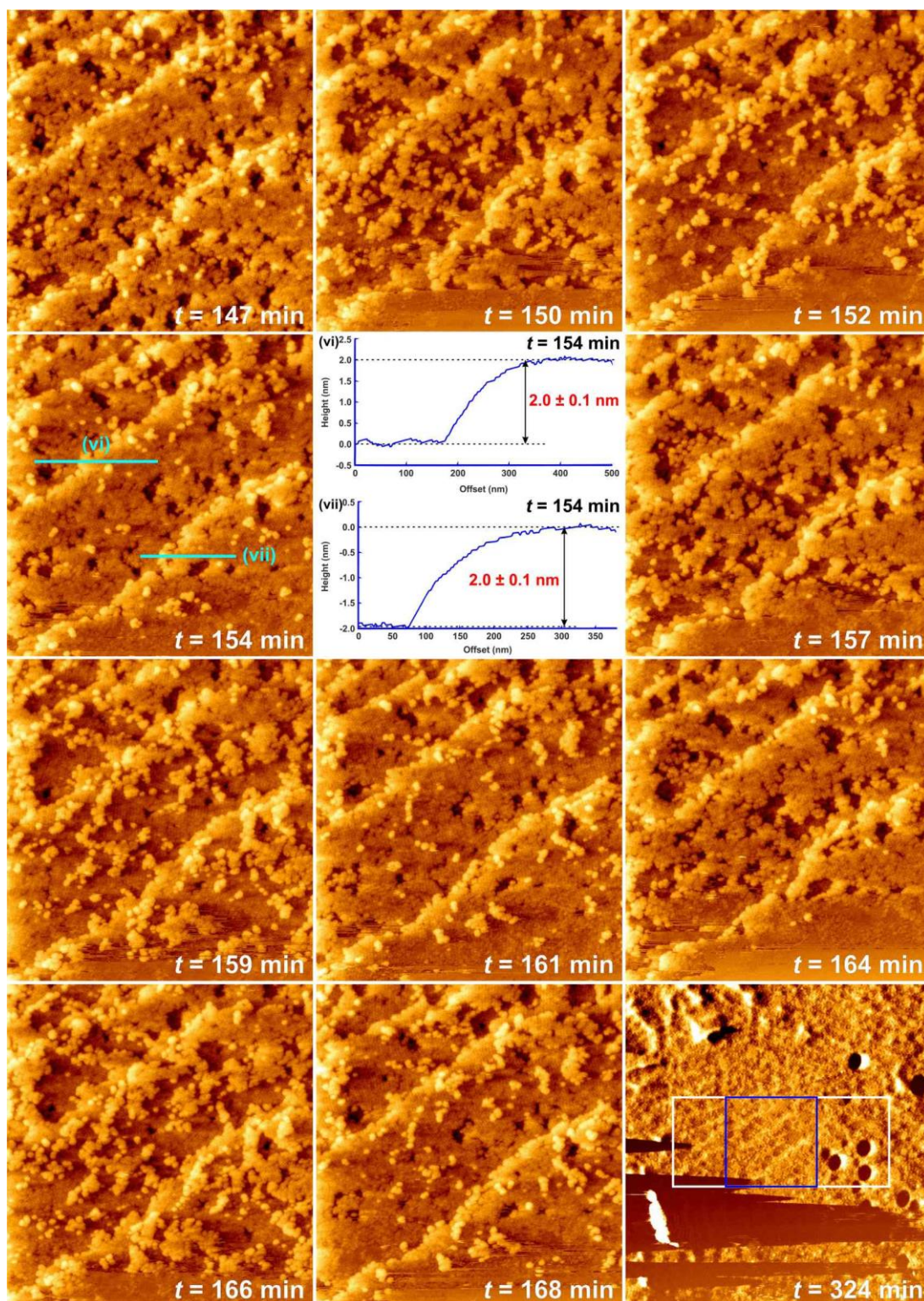


Figure 4.25 (continued). Subsequent AFM vertical deflection images displaying the dissolution of (010) facet of DAF-1 crystal in solution 4. Scanned areas are $5.5 \mu\text{m} \times 3.0 \mu\text{m}$ ($t = 0 - 5$ min), $3.0 \mu\text{m} \times 1.3 \mu\text{m}$ ($t = 13 - 119$ min), $1.3 \mu\text{m} \times 1.3 \mu\text{m}$ ($t = 141 - 168$ min) and $5.0 \mu\text{m} \times 5.0 \mu\text{m}$ ($t = 324$ min). Blue squares in images at $t = 119$ and 324 mins show the scanning areas for $t = 141 - 168$ min, whilst white rectangle in image at $t = 324$ min is the scanning region for $t = 13 - 119$ min.

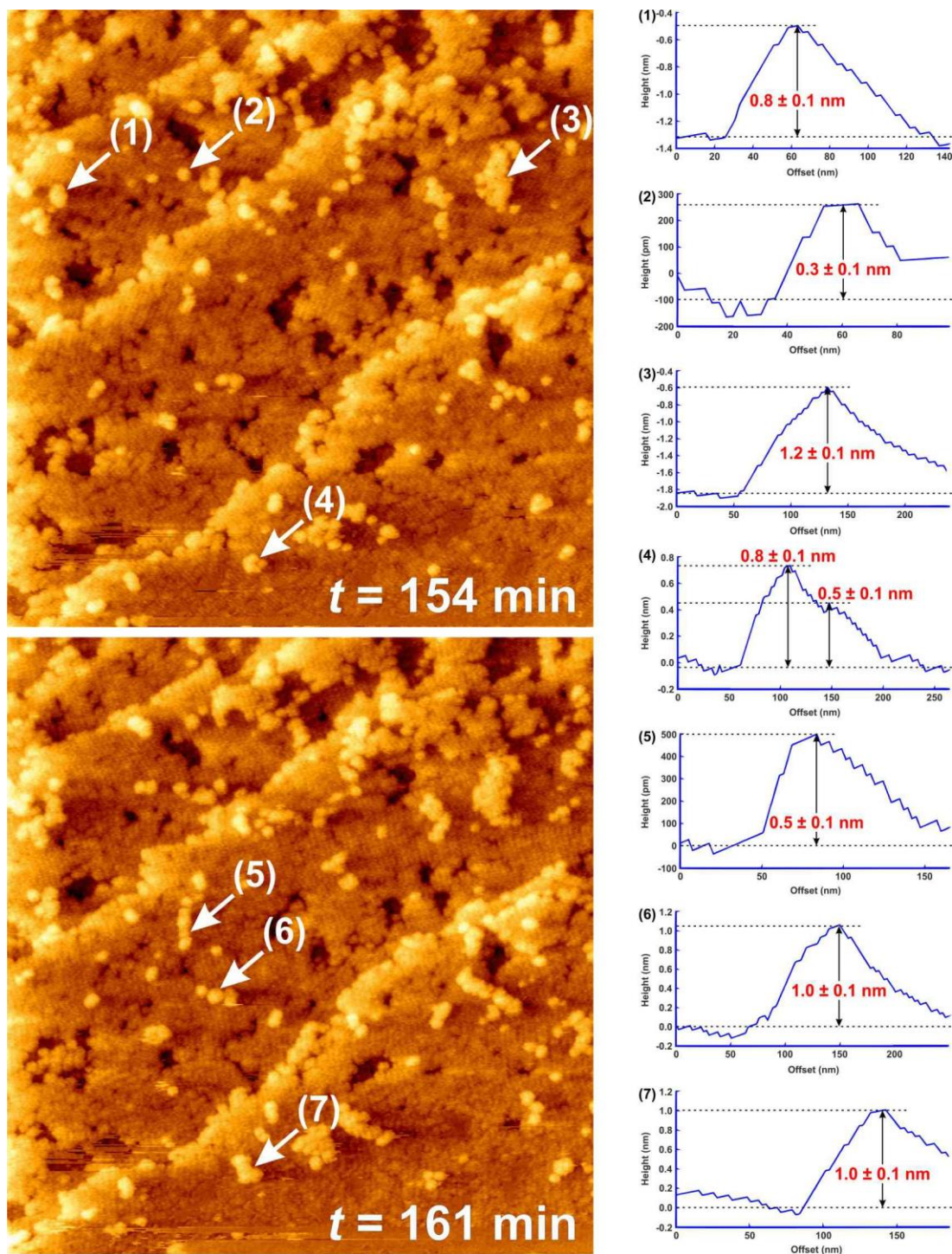


Figure 4.26. Cross-sectional height measurements of random dots on (010) facet of DAF-1 crystal dissolution in solution 4.

As previously proved in section 4.3.4.3 that both possibilities 1 and 2's structure break-downs met the nano-dot heights in solution 3, they also match the nano-dot

heights found due to dissolution in this solution 4. The structure break-downs for both likelihoods are illustrated in Figure 4.27.

Taking the possibility 1 as the growth terminal, the nano-dot heights detected can be explained as follows (see the DFO structure breakdown in Figure 4.27 (a)). If a 12-membered ring type 2 channel is on top of a layer surface during the dissolution process, it leaves 1.2 nm high particles. Whilst, as it is detected in dissolution using solution 3, dots with *c.a* 1.0 ± 0.1 nm high correspond to the height of half of a completed-wall 12-membered ring type 1 channel, which is 1.05 nm in theory. Removal of this type 1 channel top wall, but still leaving the channel ring, gives a 0.7 nm high dot. Further dissolution of this state results in 0.5 nm high dot. Moreover, only the double 4-rings on the surface gives rise to a 0.3 nm high dot.

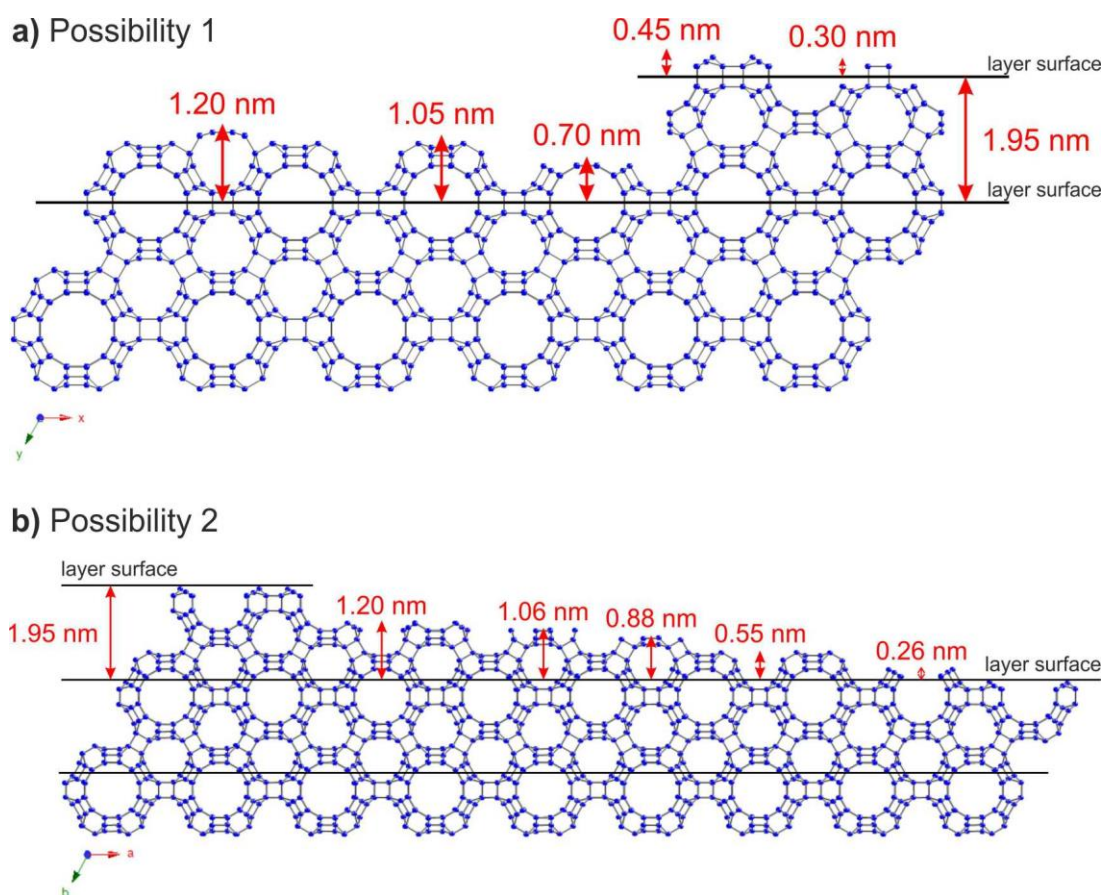


Figure 4.27. Two possibilities of DFO structure break-down corresponding to the height measurements of nano-dots on (010) DAF-1 facet in Figure 4.26. The blue dots in the structure represent the Al, P or Mg atoms, whilst the black sticks illustrate the oxygen bridging in between those Al, P or Mg atoms. Oxygen atoms are omitted for clarity.

Meanwhile, assuming the possibility 2 as the layer surface, all of the nanoparticle heights also match a sensible structure break-down. Removing the bridging between two type 1 channels results in 1.20 nm high particle, and so on as can be seen in Figure 4.27 (b). It is acceptable to say that those heights in the structure break-down match the AFM height measurement since the difference is within the allowed ± 0.1 nm measurement error.

Since both possibilities 1 and 2 related to how the growth layer terminates on (010) facet are so far reasonable after being confirmed with the laboratory evidence from dissolution in solution 3 and 4, the crystal simulation described in section 3.3.3 is very helpful to determine the right growth layer termination. It is clear from Figure 4.14 that the connector between type 1 channels, of which double 4-rings is one of the tiles constructing, ends the growth layer on (010) facet. This agrees with a study published by Slater *et al.* (2001), which concluded that having double 4-rings on zeolite LTA termination is the most thermodynamically stable configuration [13]. Hence, we are confident to note here that the second probability is the most preferred growth layer termination of (010) facet.

In terms of the (001) facet of DAF-1 crystal, solution 4 dissolved the crystal surface in the same way as that of solution 3, although the process cannot be seen very clearly. This may be associated with the fact that the two types of large channels (a uniform one with 6.1 Å channel opening and the wider one having 7.5 Å channel diameter) are located on (001) facet stretching along the [001] direction. Moreover, the larger channel has super-cages in it, which will make the crystal surface more uneven due to larger pits created when they open up during the dissolution. The sequence AFM images of the dissolution for this facet are presented in Figure 4.28 and clarified in Figure 4.29. Meanwhile, the missing AFM images between $t = 61 - 97$ minutes in Figure 4.28 are presented as Movie 4-4 in Appendix 1.

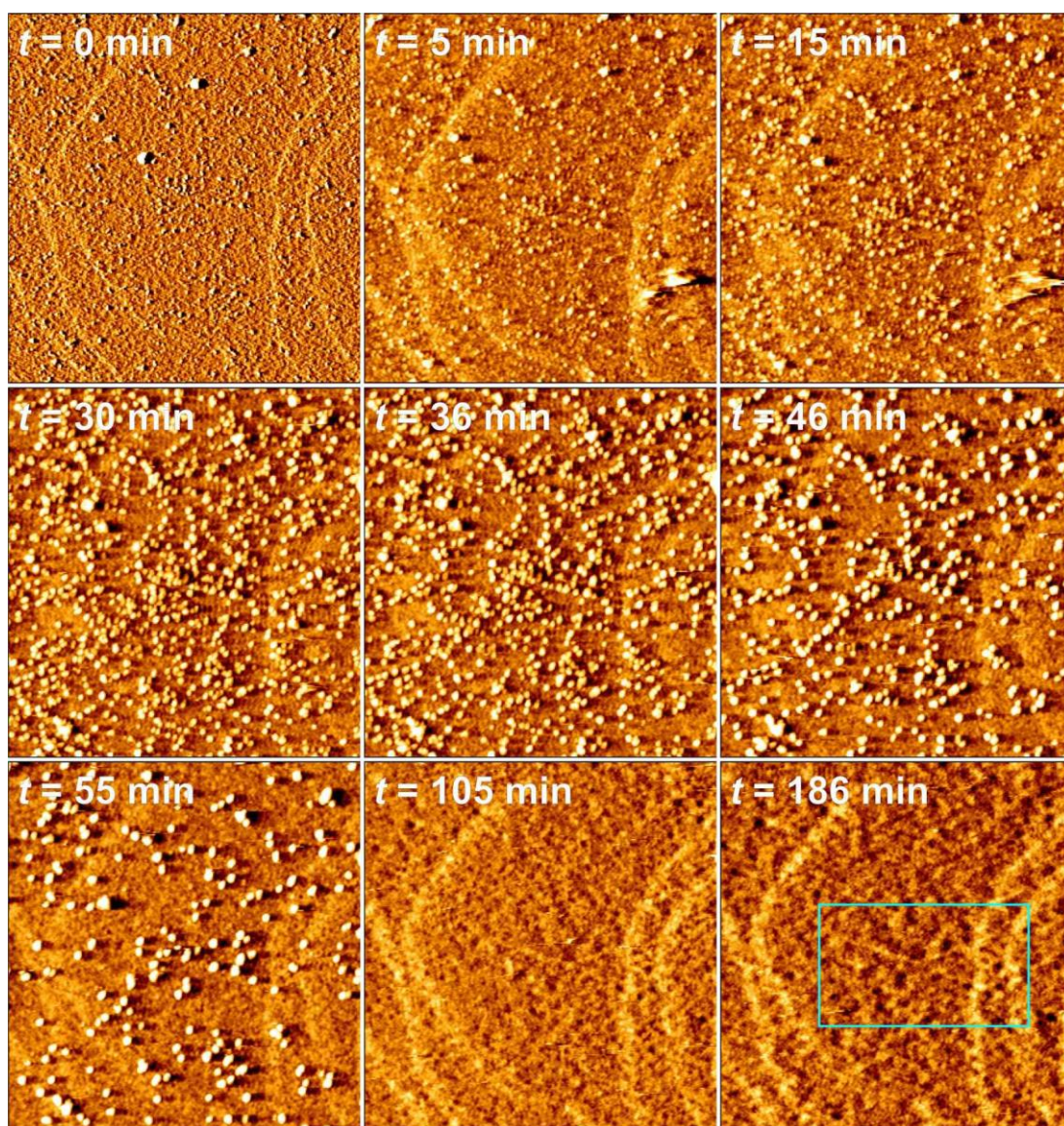


Figure 4.28. Consecutive AFM vertical deflection images of (001) facet of DAF-1 crystal dissolution in solution 4. Each area's width is $2.8 \mu\text{m} \times 3.0 \mu\text{m}$. Cyan rectangle represents the zoomed area scanned in Figure 4.29.

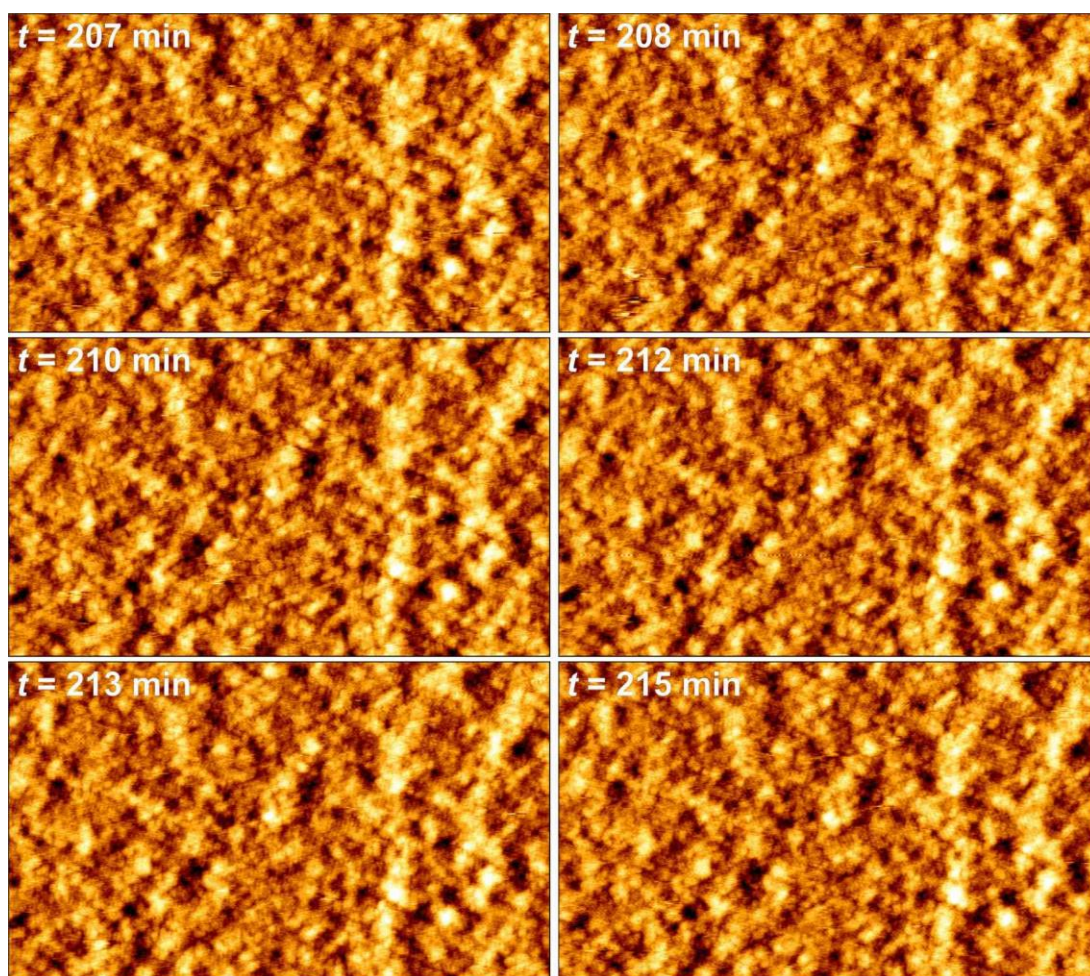


Figure 4.29. A closer look at the cyan rectangle in Figure 4.28 of consecutive AFM vertical deflection images of (001) surface of DAF-1 crystal dissolution in solution 4 with each area's width is $1.7 \mu\text{m} \times 1.0 \mu\text{m}$.

Figure 4.30 compares the AFM vertical and lateral deflection images when the dissolution reached 38 minutes. White impurity grains scattered all over crystal surface in vertical deflection image look black in lateral deflection image, while the crystal surface is in orange colour. In the lateral deflection image, having distinctive colours from the surface means that these lumps gave different friction from the other area when the AFM tip scanned them. Again, this is another fact indicating that the lumps are a distinctive phase (impurity) from the surface of the DAF-1 crystal.

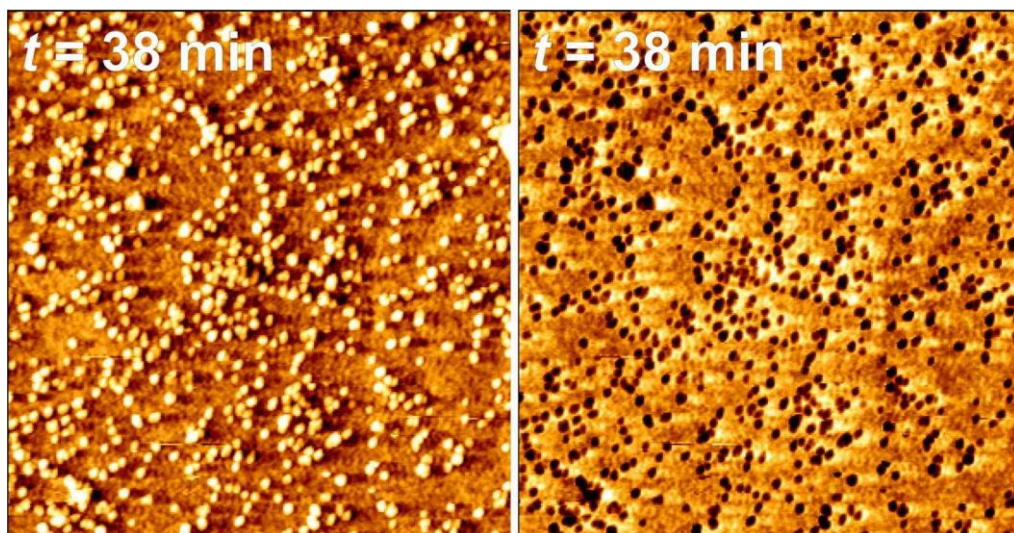


Figure 4.30. Corresponding AFM vertical deflection (left) and lateral deflection (right) images of (001) surface of DAF-1 crystal in solution 4.

4.3.4.5. Dissolution of DAF-1 crystal in solution 5

Solution 5 gave similar DAF-1 dissolution process to the former outcomes. The results, which are displayed in the following subsequent images (see Figure 4.31), are comparable to the dissolution in solution 3 and 4 regarding the dissolution mechanism, terraces' position, growth step's height before and along the dissolution, even the corresponding DFO crystal structure responsible for the nano-dots' heights measured. The outcomes of this dissolution is also given in Movie 4-5 in Appendix 1.

Nevertheless, comparing to those with higher pH values, setting the solution pH close to neutral (pH 6 – 7) in solution 5 seems to raise the rate of DAF-1 crystal dissolution. It is observable in Figure 4.31 that the bottom layer (marked with a white asterisk) in the image at $t = 10$ minutes remained half of it at $t = 12$ minutes. However, at $t = 13$ minutes, this layer has disappeared completely. Again, this particular layer showed most of its layer at $t = 13$ minutes and still retained a little part of the layer at $t = 15$ minutes. Even so, the layer was totally wiped away at $t = 17$ minutes, and so on. The findings drive to a qualitative conclusion that complete dissolution of one layer or growth step, about 2 nm high, in this solution 5 took place for only about 2 minutes, which is much faster than the same events in higher pH solutions described previously.

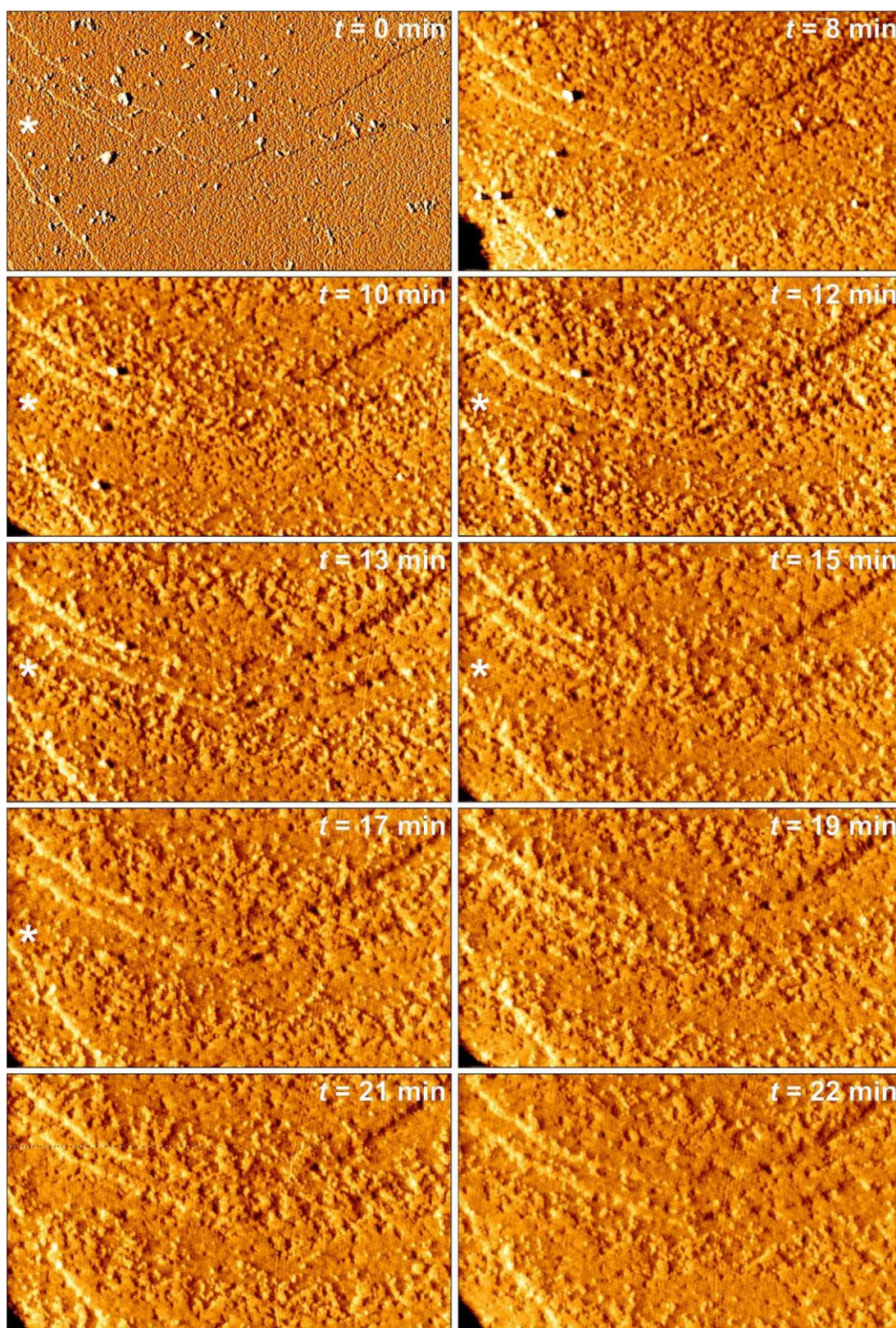


Figure 4.31. Subsequent AFM vertical deflection images of (010) facet of DAF-1 crystal dissolution in solution 5. Each image width is $3.0\ \mu\text{m} \times 1.8\ \mu\text{m}$. Cyan arrows point at step by step pit formation (*to be continued on the next page*).

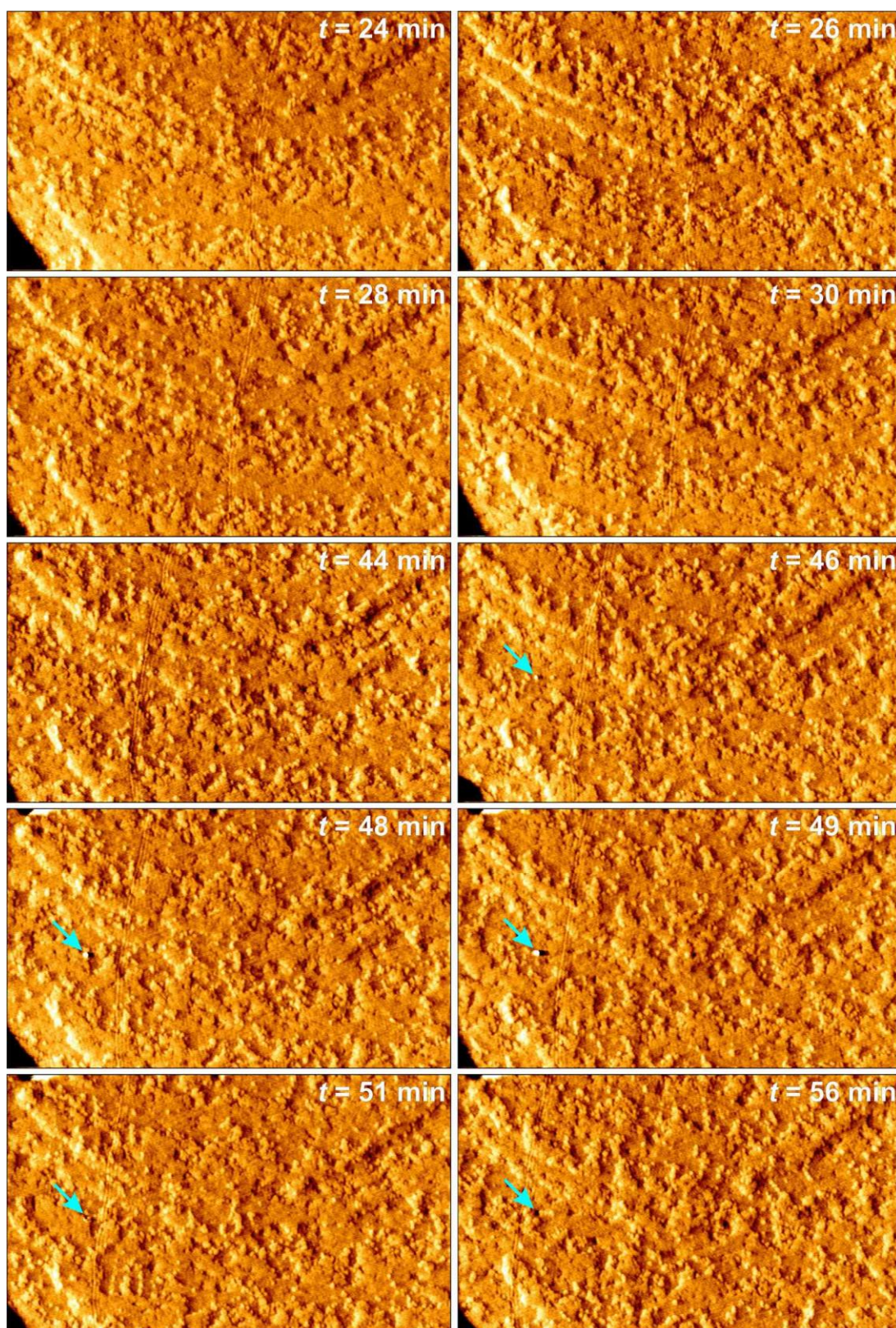


Figure 4.31 (continued). Subsequent AFM vertical deflection images of (010) facet of DAF-1 crystal dissolution in solution 5. Each image width is $3.0 \mu\text{m} \times 1.8 \mu\text{m}$. Cyan arrows point at step by step pit formation (*to be continued on the next page*).

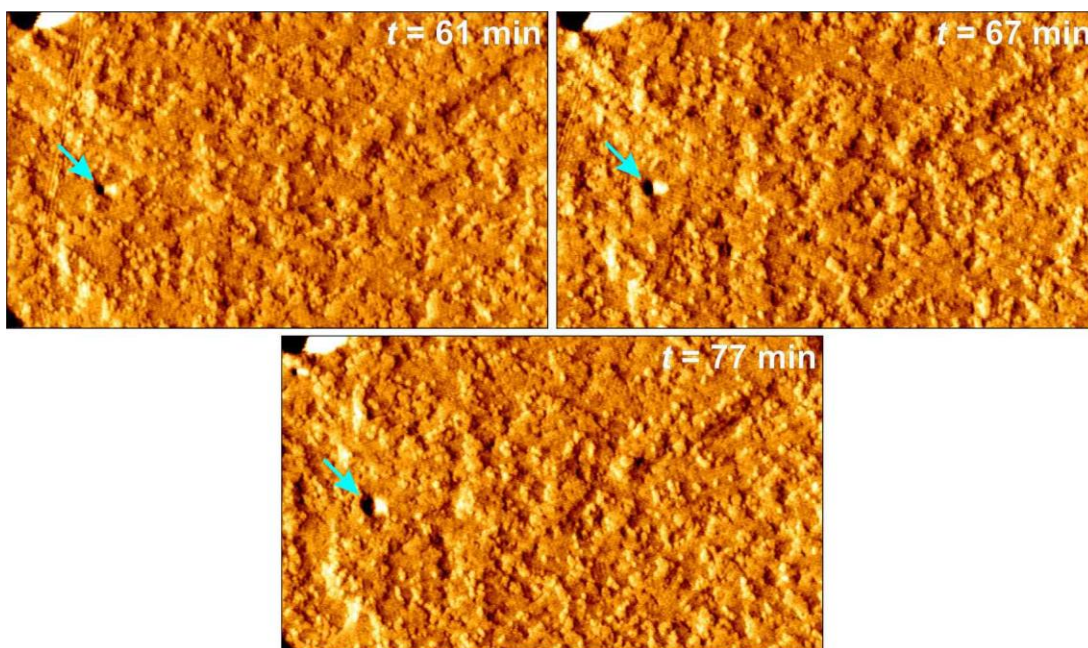


Figure 4.31 (continued). Subsequent AFM vertical deflection images of (010) facet of DAF-1 crystal dissolution in solution 5. Each image width is $3.0\ \mu\text{m} \times 1.8\ \mu\text{m}$. Cyan arrows point at step by step pit formation.

Moreover, the impurity particles on the crystal surface also seem to dissolve much more quickly in solution 5 rather than in the more basic solutions displayed previously. Contact with solution 5 for just around 17 minutes has successfully cleaned the surface from those additional phases. Whilst in solution 3 and 4, those impurities still lingered for over an hour being immersed in the solution. This phenomenon is another proof that those grainy particles on the surface are different phase from the DAF-1 crystal.

In regards to the (001) facet of the DAF-1 crystal, Figure 4.32 reveals that its dissolution pattern in solution 5 appears to be similar to the dissolution in other solutions explained previously. Full images of this result are also presented in Movie 4-6 in Appendix 1. Here, the solution attack to the crystal surface caused the surface to become very rough. As explained in the previous section, this rough surface during the dissolution is considered to be related with the two large channels along the [001] direction and large cages, which opened up as the crystal structure around them dissolved very quickly.

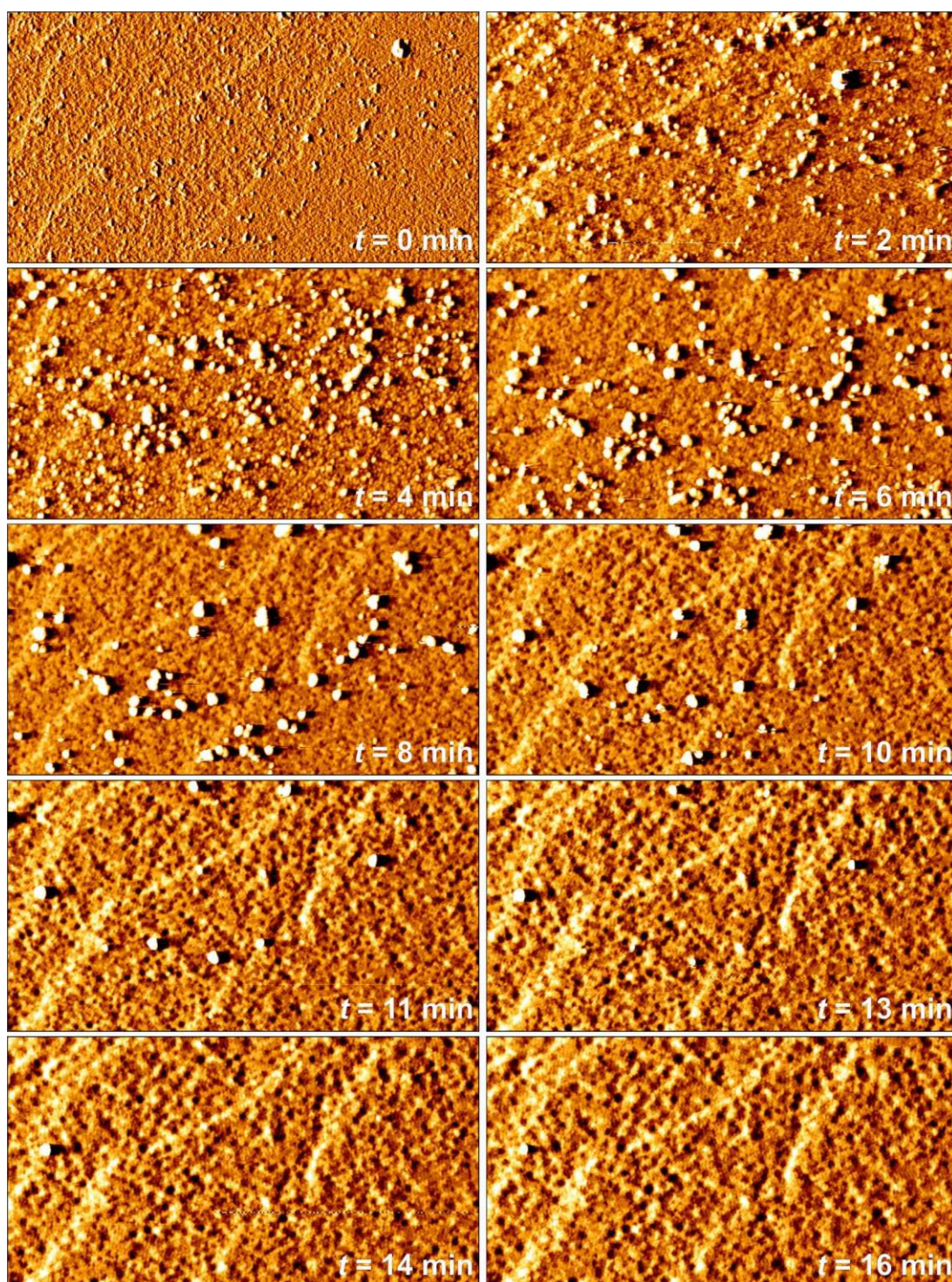


Figure 4.32. Consecutive AFM vertical deflection images of (001) facet of DAF-1 crystal dissolution in solution 5. Each image width is $1.7\ \mu\text{m} \times 1.0\ \mu\text{m}$, except the last image which is $20\ \mu\text{m} \times 20\ \mu\text{m}$. Cyan rectangle in the last image shows the area scanned prior to it (*to be continued on the next page*).

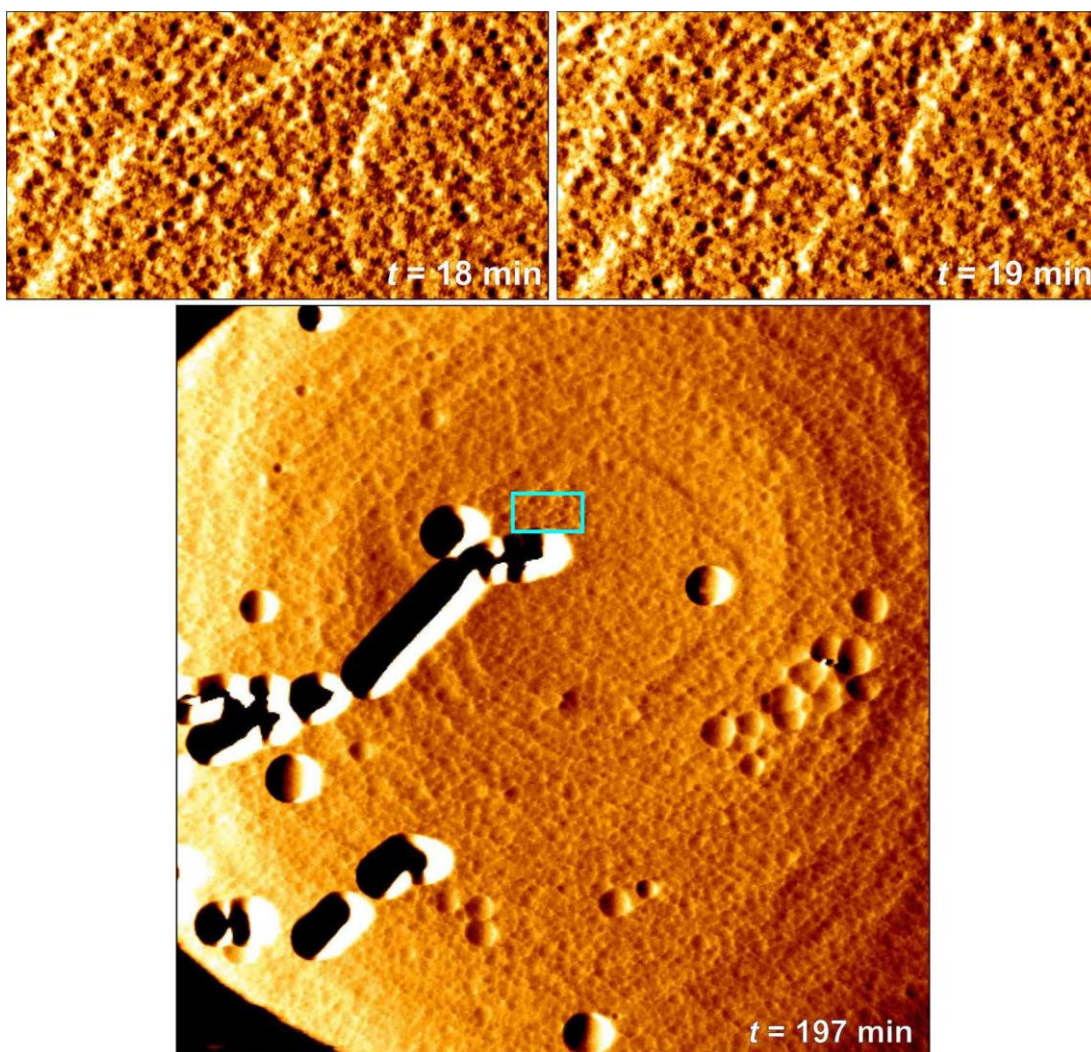


Figure 4.32 (continued). Consecutive AFM vertical deflection images of (001) facet of DAF-1 crystal dissolution in solution 5. Each image width is $1.7\ \mu\text{m} \times 1.0\ \mu\text{m}$, except the last image which is $20\ \mu\text{m} \times 20\ \mu\text{m}$. Cyan rectangle in the last image shows the area scanned prior to it.

The fact that the rate of dissolution is more rapid with the decrease of pH gives the idea that the dissolution rate of DAF-1 in H_3PO_4 and $\text{Dec}(\text{OH})_2$ mixture is an $[\text{H}^+]$ dependent reaction. The more H_3O^+ in solution, the faster the reaction between the solution and the species on the DAF-1 crystal surface.

Pits were also formed in both facets of this DAF-1 crystal during the dissolution process in solution 5. For the (010) facet in Figure 4.31, the process was caught as shown by the cyan arrows. Meanwhile, the last image in Figure 4.32 displays the (001) facet with large pits and craters created all along the dissolution. Further analysis of the pits formation is explained in the following section.

4.3.4.6. Pits formation on the DAF-1 crystal surface

Formation of large holes or pits on the crystal surface during the DAF-1 dissolution process was observed in all solutions used in this experiment. The effect of the solution pH on how fast the large pits formed cannot be determined as the AFM tip only scans a narrow region on the crystal surface. This means that it is very probable that the surface area monitored by the AFM does not show any big holes formation, yet a high number of large holes is manifested beyond the scanning area. All AFM images of DAF-1 crystal dissolution presented in this chapter demonstrate large pits formation on the crystal surface, except the dissolution in solution 3. Nonetheless, the large pits were actually formed outside the scanning area. This was noticed, in this experiment using solution 3, as we scanned larger area as well as observing the crystal's appearance, which was no longer clear, via AFM microscope.

The large pit formation mechanisms for different solutions in this work are the same. Figure 4.17 and Figure 4.18 show progressive hole formation during the dissolution of DAF-1 crystal in solution 2. Clearer step-by-step big hole generation events are found in the crystal dissolution using solution 5, from which the pits formation mechanism can be described in detail in this section.

As explained previously (in section 4.3.4.2), the hole formation was initiated by the appearance of an unknown nano-dot on the DAF-1 crystal surface, which eventually after around 4 to 6 minutes (in this solution 5) dissolved in solution, leaving a small hole after it (see Figure 4.33). The small hole then became larger over time to allow a pit to form. Further etching on the pit wall created a large crater, just like the one shown next to the unknown nanoparticle in the images. The sequence images of the pit formation are also displayed in Movie 4-7 in Appendix 1.

By further investigation on the AFM images in this work, it is believed that the unknown nano-dot, which initiated the pit formation, is not part of the surface impurities since it appeared after all of the surface impurity particles dissolved. However, knowing its different properties from the nano-dots created when the crystal dissolved, we also cannot say that the unknown nano-dot is part of DAF-1 crystal particle. The best explanation is that this unknown nano-dot is an 'extrinsic defect', an impurity which was included in the DAF-1 crystal framework during its

growth, occupying the lattice or interstitial sites in the framework as explained in the literature [14].

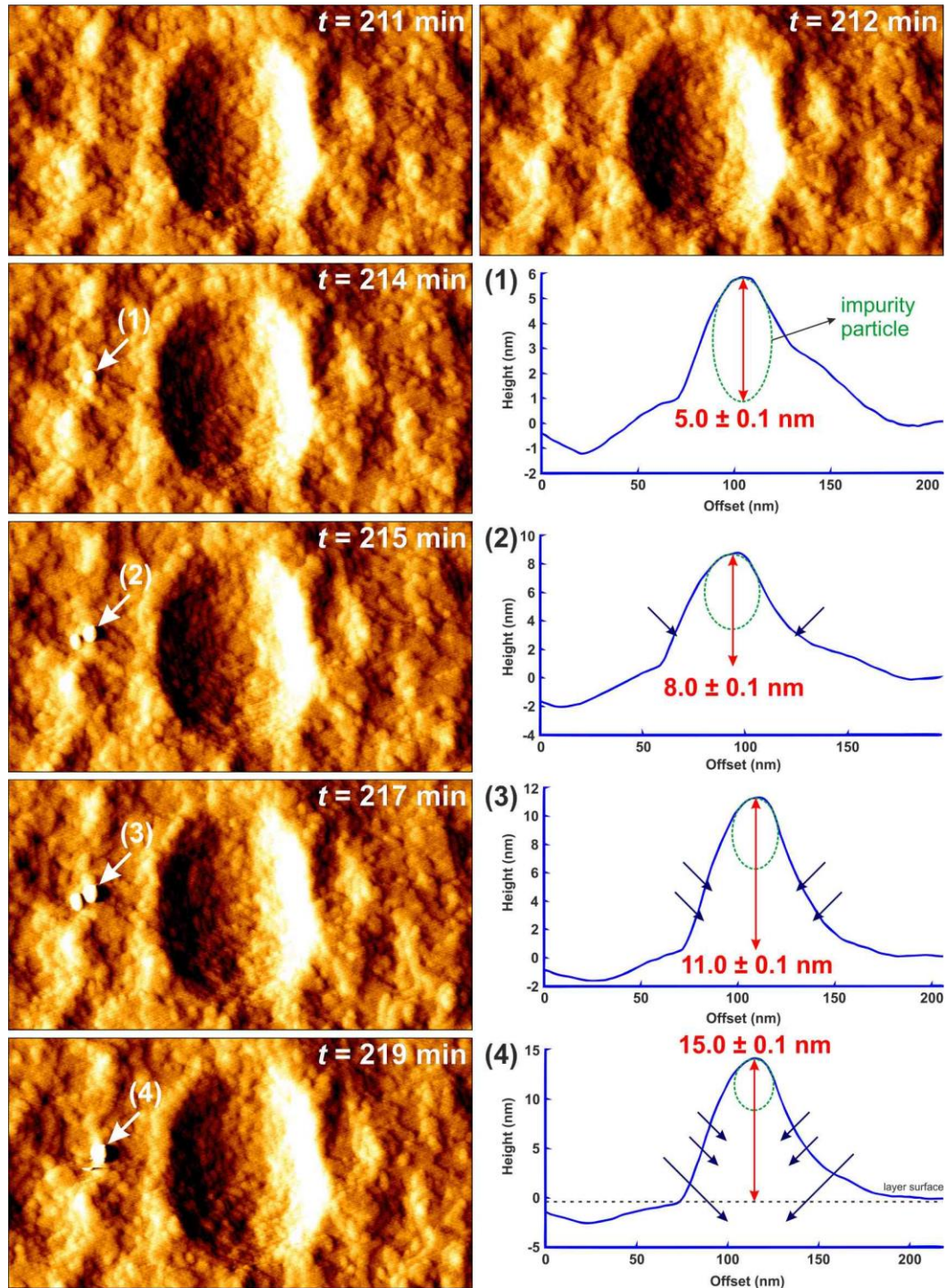


Figure 4.33. AFM vertical deflection images sized $1.3 \mu\text{m} \times 0.7 \mu\text{m}$ of (010) facet of DAF-1 crystal exhibiting a pit formation in solution 5 and cross-sectional height measurements on the extrinsic impurity particle. The last image at $t = 228$ min (on the right) is a lateral deflection image corresponding to the image on its left (*to be continued on the next page*).

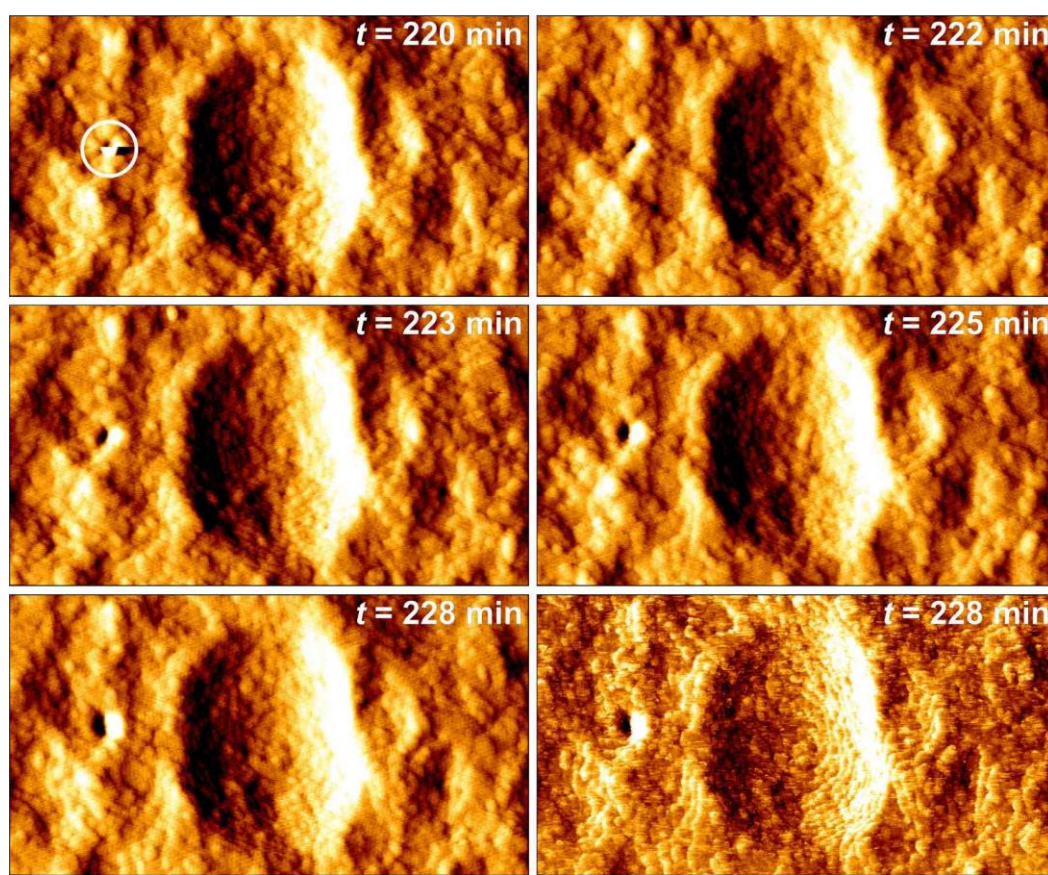


Figure 4.33 (continued). AFM vertical deflection images sized $1.3 \mu\text{m} \times 0.7 \mu\text{m}$ of (010) facet of DAF-1 crystal exhibiting a pit formation in solution 5 and cross-sectional height measurements on the extrinsic impurity particle. The last image at $t = 228 \text{ min}$ (on the right) is a lateral deflection image corresponding to the image on its left.

Although very difficult, owing to its bumpy surrounding, height measurement of the extrinsic imperfection particle (illustrated in Figure 4.33 as a green circular shape) was performed, giving $5.0 \pm 0.1 \text{ nm}$ high when it was detected for the first time perching on the crystal surface (at $t = 214 \text{ min}$). The height of this extrinsic particle then increased to $8.0 \pm 0.1 \text{ nm}$, $11.0 \pm 0.1 \text{ nm}$ and $15.0 \pm 0.1 \text{ nm}$ high during its existence, which was about 5 seconds on the crystal surface before it dissolved in solution. The height increase was not generated by the impurity growth, but due to gradual dissolution of the surface around it, which made its height seem to rise.

The removal of this extrinsic particle itself is presumably more about the dissolution of crystal particles beneath it so that there was none to attach the particle with the crystal surface, rather than because of the impurity particle's gradual dissolution.

This can be proved in the image at $t = 220$ minutes in Figure 4.33 when the AFM caught only half of the impurity particle during scanning (shown within the white circle). This indicates that the extrinsic particle was removed, not gradually dissolved, during scanning (the scanning itself went up in this image).

Considering the assumption above, the formation of the hole on the DAF-1 surface can be explained as proposed here. When the surface around the extrinsic defect particle dissolved, DAF-1 crystal particles just beneath the impurity stayed in place, supporting the extrinsic particle. The arrangement like this was not detected by the AFM owing to the tip's limitation to scan lateral position. As a consequence, when performing a height measurement, this seems as if the foreign particle height increased.

The presence of an extrinsic imperfection particle in the lattice or interstitial sites of the DAF-1 crystal framework may weaken the Al–O and P–O bonds. Therefore, when the solution was in contact with the edge of the supporting particles (represented as dark blue arrows in Figure 4.33), it attacked this position severely. This allowed the solution to reach atoms or particles underneath the layer surface, thus created a hole, which was then observed by the AFM after the extrinsic particle was removed. As the solution could reach the molecules composed the wall of this hole, it dissolved them gradually. Eventually, a big crater was created.

4.3.4.7. *Dissolution mechanism of DAF-1 crystal*

It is said that the most likely location for crystal surface dissolution to start is on the step site. In this step site, according to Kossel model for crystal surface [11], the species is attached to three or four sides, while species on the bulky surface, which is bound to five other sides, is more resistant to dissolution. Energetically, it is more advantageous to break three or four chemical bonds on the step rather than more bonds possessed by the species on the terrace. Dissolving the species on the step site bit by bit eventually makes the terrace gets narrower, followed by the disappearance of that particular terrace completely. This is what is called ‘layer-by-layer’ dissolution mechanism.

Many scientists have reported the observation of the above-mentioned dissolution mechanism on zeolite crystals. Brent *et al.* (2010) found that the cancrinite column

in zeolite L dissolved in NaOH solution from its edges towards the middle of it until full-length of the column is etched [7]. Meza *et al.* also witnessed regular retreat of zeolite A's square terraces from edge to the centre under diluted mother liquor, although the layer dissolved in two ways: layer dissolution and terrace retreat due to the unconnected and connected building units constructing the structure [10], [15].

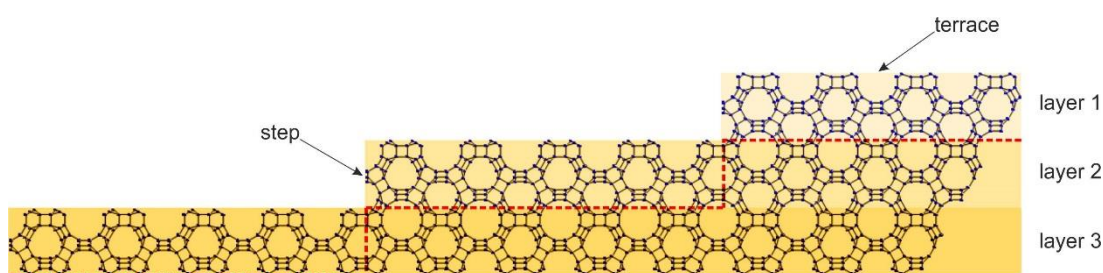


Figure 4.34. Schematic illustration of the DFO crystal structure showing cross section for (010) crystal surface. The blue dots in the structure represent the Al, P or Mg atoms, whilst the black sticks illustrate the oxygen bridging in between those Al, P or Mg atoms. Oxygen atoms are omitted for clarity.

DAF-1 crystal, both (010) and (001) facets, showed comparable dissolution mechanism in a solution containing phosphoric acid and decamethonium dihydroxide as the ‘layer-by-layer’ dissolution mechanism. However, interestingly, the distinctive result was observed in DAF-1 crystal dissolution, that the crystal surface retained its layer step positions. The solution attacked and dissolved any species in contact with it without selectively choosing particular sites to dissolve first. As illustrated in Figure 4.34, the solution etched the exposed terrace on layer 1 (upper-most layer) to layer 3 at the same time regardless of the site position. As the particles in those layers retreated, the layers just underneath them were exposed to the solution, also at the same time. Thereby, the new crystal surface had terraces and steps (represented by red dashed line in Figure 4.34) at exactly the same location as that before the above layer retreatment. This is what was observed as the retained terrace position in the AFM images. Subsequently, once the solution reached the newly exposed layers, they started to dissolve in the same way as the layers on top of them. This explains how DAF-1 crystal reserved its terrace position during the dissolution process.

A similar mechanism of edge conservation as described above was also observed previously for a heulandite crystal surface during dissolution in low concentration sodium hydroxide or sulfuric acid solution [12]. This phenomenon is possible to take place only if the environment is in a very under-saturated condition so that it allows the breaking of any chemical bonds independently of the bond strength.

All AFM images of the DAF-1 crystal dissolution displayed in this chapter show the formation of patches, as nanodots, during the crystal surface retreat. This behaviour is similar to that of the IM-17 crystal described in the previous chapter. Moreover, dissolution process by creating patches was also observed in zeolite A dissolution previously reported by Meza *et al.* [10], [15].

The course of the event is possible when the surface terminal's framework is discontinued structured. As presented here, the (010) facet of the DAF-1 crystal is terminated by open type 1 channel, while its (001) facet also exposes open 10-membered channel. This configuration creates a discontinued surface structure that is required for the solution to easily attack the bulk surface. Consequently, the crystal surface dissolved in patches.

4.3.4.8. Suggested DAF-1 crystal growth

It is known that the crystal dissolution process may be related to the reverse process of its growth. Given that fact, the information on DAF-1 crystal dissolution in this chapter can be used to suggest its growth as follows.

Based on the dissolution process explained in this chapter, DAF-1 crystal growth on its (010) surface may be initiated by incorporation of units of growth on the type 1 channel bridge to form completed type 1 channel. By completing this step, part of the type 2 channel wall is also built. Type 1 channel bridge itself is structured one of it by double 4-rings. Step-by-step units of growth installation, including attachment of type 1 channel bridge into the framework, will then make up complete type 2 channel as well as the type 1 channel walls.

Meanwhile, the (001) facet may grow as the units of growth assemble to form a structure marked (2) in Figure 4.13 (d). This is the same structure as the type 1 channel's bridge mentioned above. After the structure (2) is attached on (001)

surface, incorporation of other units of growth into it will then form completed framework.

4.3.5. Simulations of DAF-1 crystal dissolution

The large data collected from the laboratory regarding the dissolution of the DAF-1 crystal in under-saturated solutions, as presented previously, is also compared to the calculation data. Again, the *CrystalGrower* program was used for this purpose. All simulations were set to grow a DAF-1 crystal in a high supersaturation ($\Delta\mu = 100$), then to drop the supersaturation ($\Delta\mu$) to 5 for the dissolution to proceed. The new $\Delta\mu$ was lower than the supersaturation at the equilibrium ($\Delta\mu_{eq} = 7.2$), making the simulation condition under-saturated to mimic the dissolution condition in the laboratory.

During the dissolution, some of the tiles detached from the crystal are still lingering above the crystal surface, which are expected in this work to be noise. Having knowledge about the potential noise to appear in the simulation benefits us to make careful analyses on the result. Another thing to note here is that the dissolution progress was recorded as frames, which were taken once per 200,000 iterations. The number of iterations each frame was captured is not the finest one but is good to show significant changes.

4.3.5.1. Simulation of DAF-1 crystal dissolution on (010) facet

The dissolution simulation of the (010) facet of the DAF-1 crystal is displayed in sequence in Figure 4.35 and Movie 4-8 in Appendix 1. The layer dissolution was demonstrated in the images. As anticipated, the uppermost layer (small terraces in dark brown colour pointed with white arrows in the first frame) dissolved immediately due to the smallest areas these terraces had. Dissolution worked on any exposed tiles similarly to the experiment result described in the previous section (section 4.3.4).

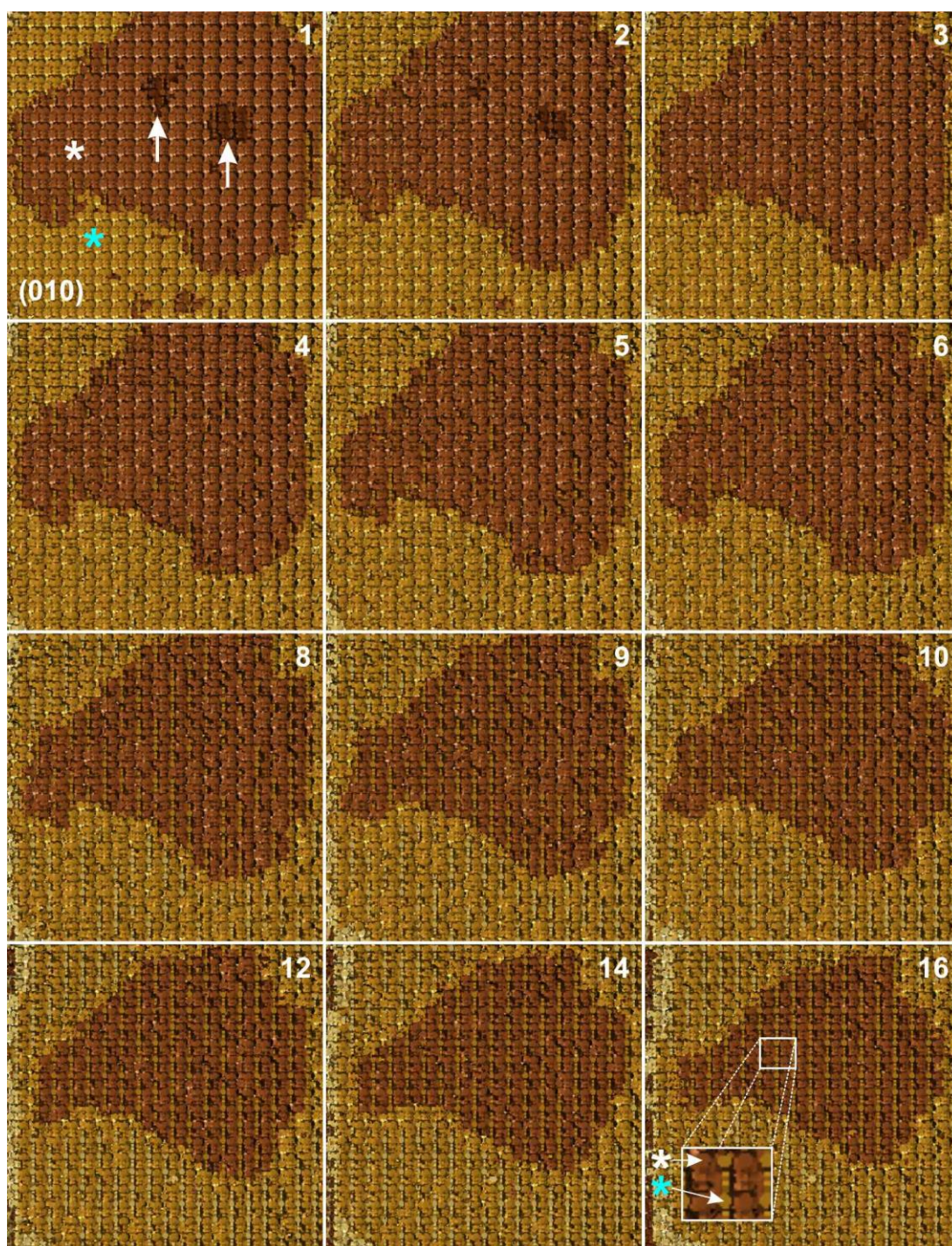


Figure 4.35. Subsequent images of DAF-1 crystal dissolution simulation on (010) facet using *CrystalGrower* with $\Delta\mu_{\text{eq}} = 7.2$ and $\Delta\mu$ for dissolution = 5. The simulation was set with $\Delta U_s = 0.875 \text{ kcal mol}^{-1}$. The simulated hexagonal crystal's diameter is about 110 nm and its thickness is up to 85 nm. The first image is the crystal before the dissolution is started. The number on the top right-hand corner of each image is the frame's number, in which the frame was taken in every 200,000 iterations.

In general, the second layer (the brown layer marked with a white asterisk in frame 1) in Figure 4.35 retreated very fast from the edge towards the terrace centre. The size of this layer became smaller as the dissolution progressed. This is as expected since the structure in the step position is very prone to detachment. However, we can also observe that during the dissolution some tiles on the bulky terraces were dissolving too, creating gaps in between the surface structure. As a result, the layer beneath it (the layer marked with a cyan asterisk) appeared to be like what we can see more clearly in the inset in the last image. This is a phenomenon that was also noticed under the AFM as the patches dissolution as presented in the previous sections.

Interestingly, looking carefully at the inset in the frame in Figure 4.35, we can note that there is a difference in how the terrace structure broke up into patches in this simulation from the lab result. The patches from the experiment are small, round-shaped and separated individually, whilst the *CrystalGrower* calculated that the patches tend to form long columns along the [001] direction. The process is displayed more obviously in Figure 4.36 and illustrated in Figure 4.37 for clearer understanding. Moreover, it is also presented in Movie 4-9 in Appendix 1.

Each layer on (010) facet comprises the structures around the type 2 channels (see image 1 in Figure 4.37 (a)), which can be distinguished into two based on their positions: the upper and lower type 2 channels. Both structures create columns that extend in the [001] direction. During the dissolution, the upper type 2 channels and the structure on top of them (red rectangle in image 1) dissolved first due to its more open location. Of course, the dissolution occurred step by step, starting from the removal of double 4-rings and so on, as proved from the height measurement of AFM images described in section 4.3.4.4. Following the rule that the parts at the edge are more weakly attached than those in the bulk, upper type 2 channels retreated from the edge to the centre of the column as demonstrated in Figure 4.36 (see the cyan arrows).

As a result from the removal of the type 2 channels, on the crystal surface was left the lower type 2 channels and the structures around them (black rectangle in image 2 in Figure 4.37 (a)). These are shown in the dissolution simulation as the columns left during the dissolution of one layer (indicated by the red arrows in Figure 4.36). Full height of this lower column is about 1.2 nm in regard to the structure break down in

possibility 2 given in Figure 4.27 in the previous section. Then, these lower columns also retreated as the upper ones. Again, the lower type 2 channels must dissolve step by step as the AFM imaging has proven although it is not presented here.

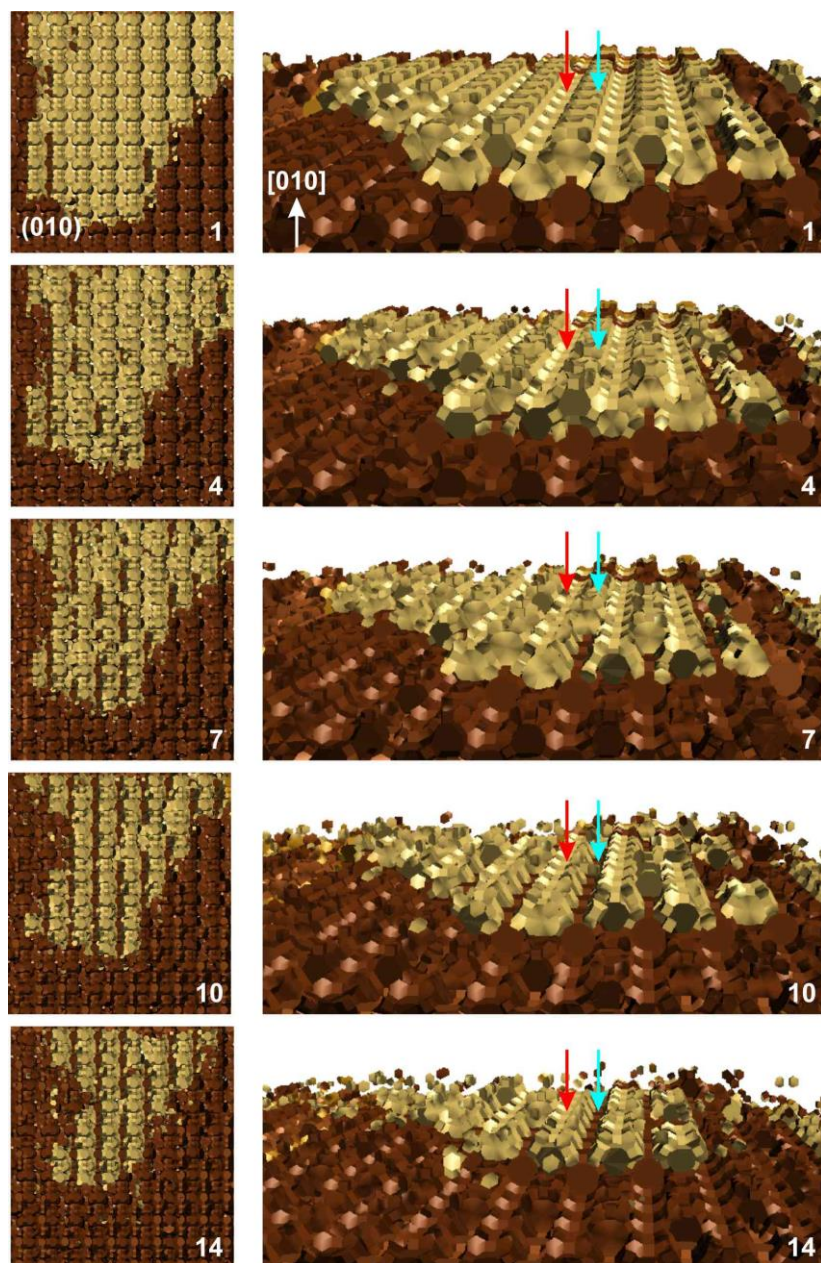


Figure 4.36. DAF-1 crystal dissolution simulation on (010) facet using *CrystalGrower* with $\Delta\mu_{\text{eq}} = 7.2$ and $\Delta\mu$ for dissolution = 5. The simulation was set with $\Delta U_s = 0.875 \text{ kcal mol}^{-1}$. The first image is the crystal before the dissolution is started. The number on the bottom right-hand corner of each image is the frame's number, in which the frame was taken in every 200,000 iterations. The left images are viewed closely in the right images along the [001] direction.

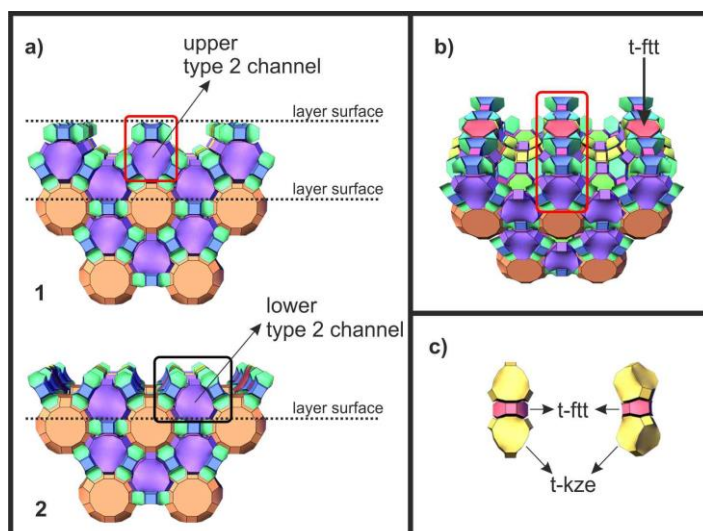


Figure 4.37. Diagrams of DFO structure tiling drawn using *Gavrog 3dt*. a) The dissolution on (010) facet seen along [001] direction. b) Tilted image 1 in (a) to clearly display the (010) facet's tiles. c) The arrangement of t-ftt tile in the DFO structure with its two closest tiles above and below it parallel to [010] axis.

The fact that in this simulation the dissolution process created columns instead of patches like the AFM has scanned is probably due to the presence of t-ftt tiles, which build the layer surface of the (010) facet. In reality, the t-ftt forms a structure with a large void inside it but is considered as a rigid tile in the simulation. The t-ftt tile is sandwiched between two t-kze tiles parallel to [010] axis. The t-kze tile itself, in its real material, constructs a framework with a big void in the middle. As a consequence, the (010) surface has channels that allow solution particles to interact with the structure in the bulky (010) layer. This leads to the patches dissolution as observed under the AFM. Meanwhile, in *CrystalGrower* t-ftt is seen as a rigid tile composing rigid column. Thus, the dissolution does not break the columns from the middle but retreats it from the edge.

4.3.5.2. Simulation of DAF-1 crystal dissolution on (001) facet

Before the dissolution of the (001) facet of the DAF-1 crystal is presented, it is important to understand Figure 4.38. On the left image, the cyan arrows point at a number of new nucleations on the (001) crystal surface. The new nucleation always starts with an attachment of tiles or growth units on the (001) surface so that

structure 4 (or part of it) in the right image is formed. The structure 4 extends towards [001] direction to form structure 2, which lies at the top part of the upper column that dissolved first during the layer dissolution on (010) crystal surface in section 4.3.5.1. In reality, the t-ftt constructs a channel along [010] direction so that structure 2 in the right image looks like structure 3.

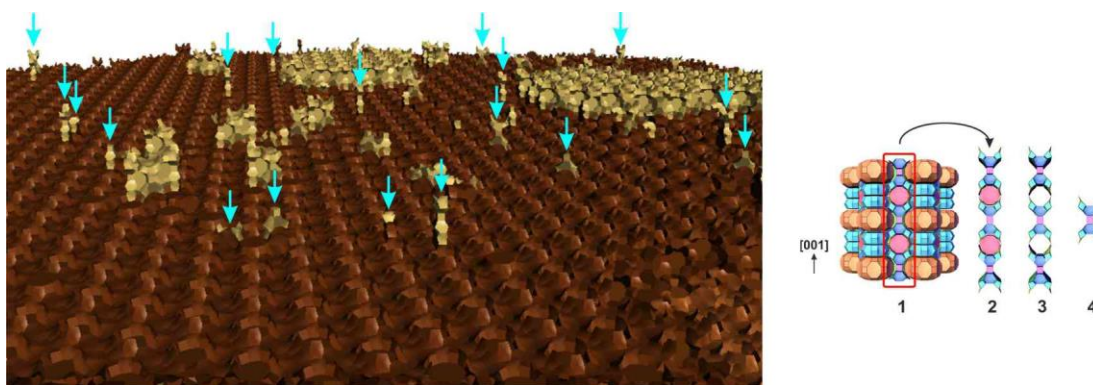


Figure 4.38. The left image shows nucleation on the (001) facet of DFO crystal simulated using *CrystalGrower* with $\Delta U_s = 0.875$ kcal mol⁻¹. The modelled hexagonal crystal's diameter is about 110 nm and its thickness is up to 85 nm. The right image is the DFO structure tiling drawn with *Gavrog 3dt* and arrangement of some tiles constructing it.

CrystalGrower simulation of DAF-1 crystal dissolution on (001) facet is shown in Figure 4.39 and Movie 4-10 in Appendix 1. The uppermost layer (dark brown colour) retreated from the layer edge, which represents the structure on the terrace's step, to the centre of the layer. The tiles on the terrace step bind more weakly to the surface than that on the bulky terrace.

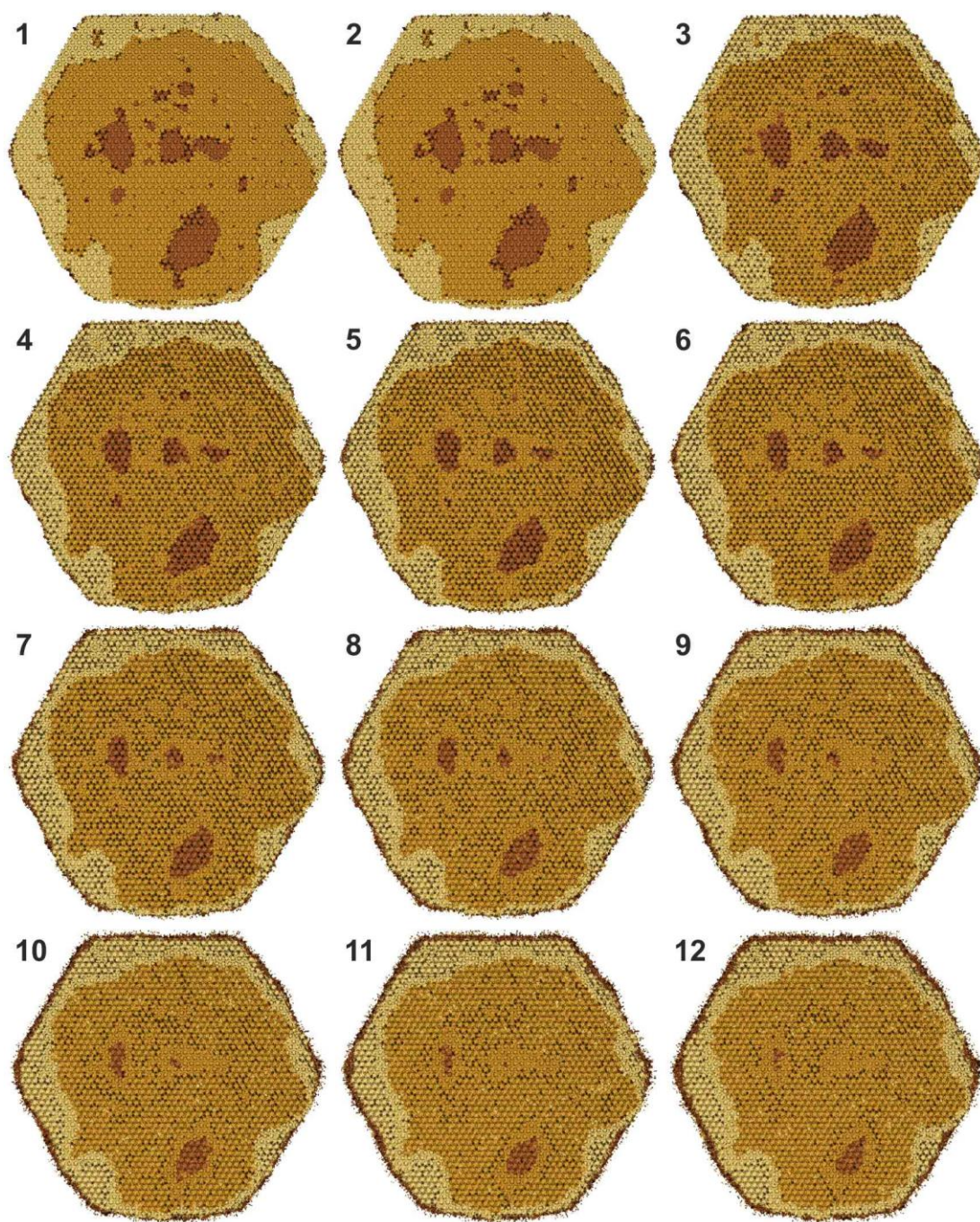


Figure 4.39. A series of DAF-1 crystal dissolution simulation images on (001) facet with $\Delta\mu_{\text{eq}} = 7.2$ and $\Delta\mu$ for dissolution = 5. The simulation was performed using *CrystalGrower* with ΔU_s set to $0.875 \text{ kcal mol}^{-1}$. The simulated hexagonal crystal's diameter is about 110 nm and its thickness is up to 85 nm. The first image is the crystal before the dissolution is started. The number on the top right-hand corner of each image is the frame's number, in which the frame was taken in every 200,000 iterations.

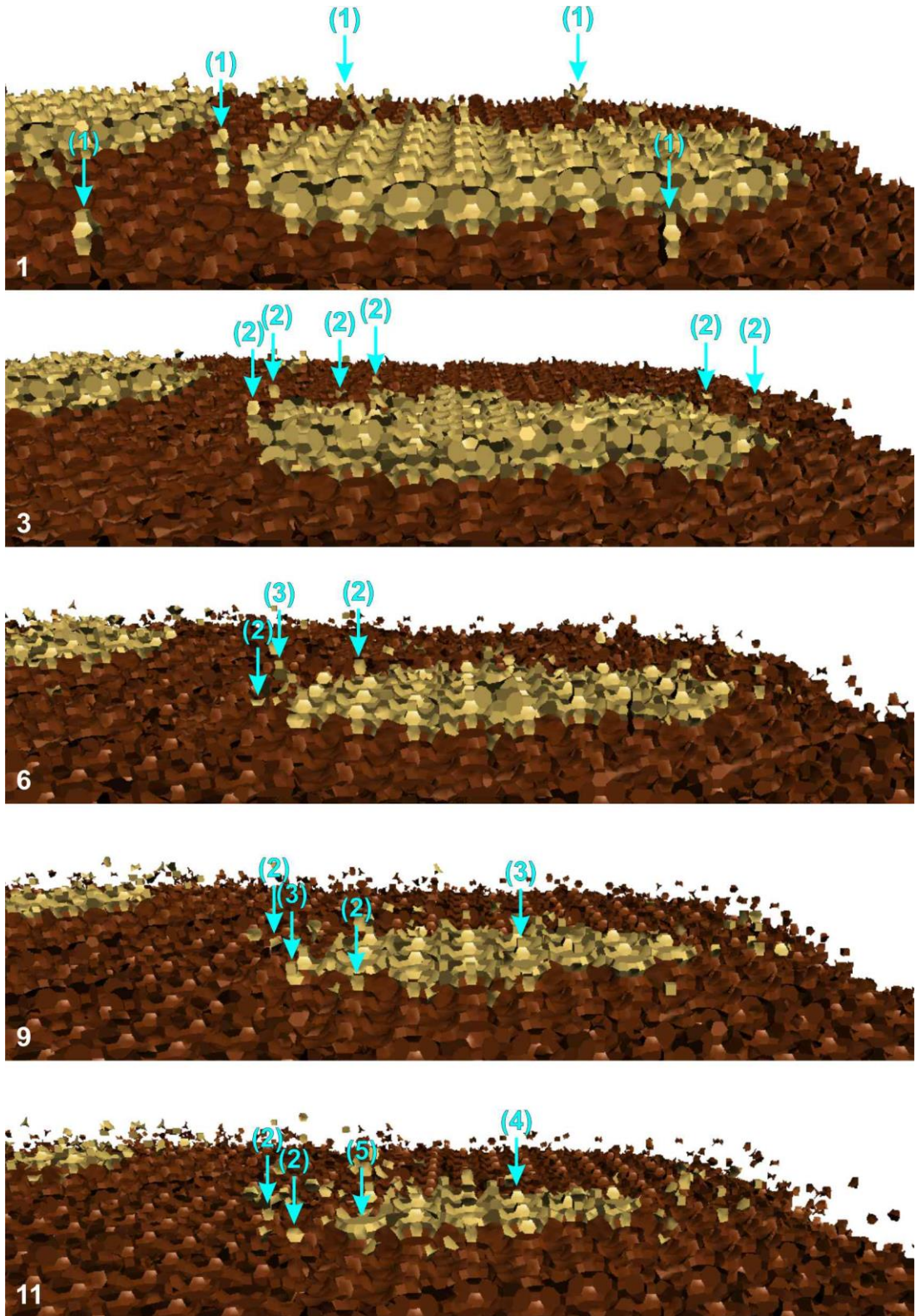


Figure 4.40. DAF-1 crystal dissolution simulation on (001) facet using *CrystalGrower* with $\Delta\mu_{\text{eq}} = 7.2$ and $\Delta\mu$ for dissolution = 5. The simulation was set with $\Delta U_s = 0.875 \text{ kcal mol}^{-1}$. The first image is the crystal before the dissolution is started. The number on the bottom right-hand corner of each image is the frame's number, in which the frame was taken in every 200,000 iterations.

Since the frames in this simulation captured in every 200,000 iterations, the images taken do not show each step of the dissolution. However, the frames in Figure 4.40 still prove that the layers on this (001) facet also dissolved step by step as the layers on the (010) crystal surface. New nuclei marked as (1) in frame 1 disappeared very quickly as expected. Although we cannot follow a consecutive breakdown of the layer, the next frames show different fragments (marked with (2) – (5)) from the breakdown of a full layer structure. The structures labelled (3) are terminated with double 4-rings. They are like half of the structure 4 in Figure 4.38 (an arrangement from the bottom to the double 4-rings). Further breakage to the double 4-rings of these structures resulted in the structures labelled (4) in frame 11. A lower structure on the crystal surface in t-eni tile arrangement, which is marked (5) in frame 11, were also found as a result of a full layer breakdown during the dissolution along with other small structures labelled (2). This is a proof that dissolution of the layer at (001) crystal surface also occurs step by step.

4.4. Conclusions

To conclude, very interesting DAF-1 crystals possessing a large unit cell with hexagonal crystal shape have been successfully synthesized in this experiment. The crystal has layers on both of its facets showing traces of ‘layer-by-layer’ growth mechanism. Despite its extremely rough crystal surface, height measurement on the terraces was accomplished. The measured growth steps are mostly 2.0 ± 0.1 nm on both (001) and (010) facets, which agree very well with the calculated ones.

AFM proved to be superior to study dissolution processes that took place on both (010) and (001) facets of the DAF-1 crystal in the H_3PO_4 and $\text{Dec}(\text{OH})_2$ solution combinations having different pH values. It was found that the crystal dissolved via surface thinning mechanism, while interestingly the surface maintained its layer positions and height. The results also suggest that the layers on DAF-1 crystal surface dissolved as patches due to the unconnected surface structure configuration.

Another finding to note in the present work is that the rate of DAF-1 crystal dissolution process (dissolution of about 2 nm high layer) using particular solutions depends on the concentration of H_3O^+ in solution. High concentration of H_3O^+

provides a high rate of dissolution and vice versa. The extrinsic defect also took place during the dissolution process, producing the formation of holes in the crystal surface.

CrystalGrower was used to simulate the DAF-1 crystal and its dissolution. The results from this simulation agree very well with the experimental outcomes although finer dissolution process could be observed if more frames were taken during the dissolution.

4.5. References

- [1] P. A. Wright *et al.*, “Synthesis and structure of a novel large-pore microporous magnesium-containing aluminophosphate (DAF-1),” *J. Chem. Soc. Chem. Commun.*, vol. 104, no. 7, pp. 633–635, 1993.
- [2] P. A. Wright *et al.*, “Synthesis, characterisation and catalytic performance of the solid acid DAF-1,” *J. Chem. Soc. Faraday Trans.*, vol. 91, no. 19, pp. 3537–3547, 1995.
- [3] S. Natarajan, P. A. Wright, and J. M. Thomas, “Catalytic isomerization of but-1-ene to 2-methylpropene over solid acids: comparison between DAF-1 and other shape-selective magnesium-containing aluminophosphates and aluminosilicates,” *J. Chem. Soc. Chem. Commun.*, vol. 256, no. 24, pp. 1861–1863, 1993.
- [4] G. Muncaster *et al.*, “An in Situ Microcrystal X-ray Diffraction Study of the Synthetic Aluminophosphate Zeotypes DAF-1 and CoAPSO-44,” *Chem. Mater.*, vol. 11, no. 1, pp. 158–163, 1999.
- [5] “Database of Zeolite Structures.” [Online]. Available: <http://www.iza-structure.org/databases/>. [Accessed: 17-Nov-2017].
- [6] M. A. Holden, P. Cubillas, M. P. Attfield, J. T. Gebbie, and M. W. Anderson, “Growth Mechanism of Microporous Zincophosphate Sodalite Revealed by In Situ Atomic Force Microscopy,” *J. Am. Chem. Soc.*, vol. 134, no. 31, pp. 13066–13073, Aug. 2012.
- [7] R. Brent *et al.*, “Unstitching the Nanoscopic Mystery of Zeolite Crystal Formation,” *J. Am. Chem. Soc.*, vol. 132, no. 9, pp. 13858–13868, 2010.
- [8] P. Cubillas *et al.*, “Spiral Growth on Nanoporous Silicoaluminophosphate STA-7 as Observed by Atomic Force Microscopy,” *Cryst. Growth Des.*, vol. 9, no. 9, pp. 4041–4050, Sep. 2009.
- [9] T. Wakihara, Y. Sasaki, H. Kato, Y. Ikuhara, and T. Okubo, “Investigation of the surface structure of zeolite A,” *Phys. Chem. Chem. Phys.*, vol. 7, no. 19, pp. 3416–3018, Sep. 2005.
- [10] L. I. Meza, M. W. Anderson, B. Slater, and J. R. Agger, “In situ atomic force microscopy of zeolite A dissolution,” *Phys. Chem. Chem. Phys.*, vol. 10, pp. 5066–5076, 2008.

- [11] P. Cubillas and M. W. Anderson, "Synthesis Mechanism: Crystal Growth and Nucleation," in *Zeolites and Catalysis, Synthesis, Reactions and Applications*, Vol. 1., Weinheim, Germany: Wiley-VCH Verlag GmbH & Co. KGaA, 2010.
- [12] S. Yamamoto *et al.*, "Dissolution of zeolite in acidic and alkaline aqueous solutions as revealed by AFM imaging," *J. Phys. Chem.*, vol. 100, no. 47, pp. 18474–18482, 1996.
- [13] B. Slater, J. O. Titiloye, F. M. Higgins, and S. C. Parker, "Atomistic simulation of zeolite surfaces," *Curr. Opin. Solid State Mater. Sci.*, vol. 5, no. 5, pp. 417–424, 2001.
- [14] J. W. Morris Jr., "Defects in Crystals," in *Materials Science and Engineering: An Introduction*, Wiley, 2013, pp. 76–107.
- [15] L. I. Meza, M. W. Anderson, and J. R. Agger, "Differentiating fundamental structural units during the dissolution of zeolite A," *Chem. Commun.*, pp. 2473–2475, 2007.

Chapter 5

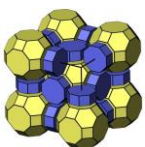
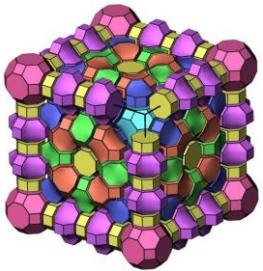
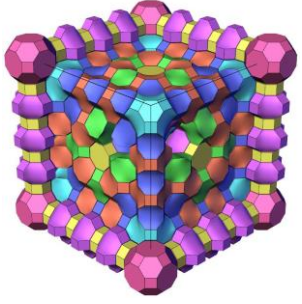





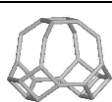



Zeolite Rho Crystal Dissolution Studied by AFM

5. Zeolite Rho Crystal Dissolution Studied by AFM

5.1. Introduction

Zeolite Rho's framework structure (RHO) is formed by two tiles: t-opr (double 8-rings) and t-grc (α -cage). It has a very simple structure arranged as body centred cubic with the α -cages connected via the double 8-rings. The zeolite Rho also has a small unit cell, with $a = b = c = 15.031 \text{ \AA}$ [1], [2]. The investigation of zeolite Rho crystal in this work was meant to study the crystal growth and dissolution of the larger and more complex structures of Rho-family zeolites, *i.e.* ECR-18 (PAU framework), ZSM-25 and PST-20 (MWF framework). The PAU and MWF are extended structures of the RHO framework structure [3]. The comparison of the three structures is given in Table 5.1.

Table 5.1. A comparison of RHO, PAU and MWF structures [2].

Structure	RHO	PAU	MWF
Material	Zeolite Rho	ECR-18	ZSM-25 and PST-20
Framework tiling			
Constructing tiles	 t-opr  t-grc	 t-oto  t-opr  t-gsm  t-phi  t-plg  t-pau  t-grc	
Cell parameters	$a = b = c = 15.031 \text{ \AA}$ $\alpha = \beta = \gamma = 90^\circ$	$a = b = c = 35.093 \text{ \AA}$ $\alpha = \beta = \gamma = 90^\circ$	$a = b = c = 45.071 \text{ \AA}$ $\alpha = \beta = \gamma = 90^\circ$

The main difference among the three framework structures is the distance between two adjacent α -cages. In zeolite Rho, α -cages (t-grc tiles) are separated by one double 8-rings (t-opr tiles). Meanwhile, in PAU and MWF the α -cages are connected by three and four double 8-rings, respectively, along with t-pau tiles in between the double 8-rings. This makes the unit cells of the PAU and MWF structures extended and, of course, more complex.

Nevertheless, the ECR-18, ZSM-25 and PST-20 crystals synthesized are very small (about or less than 1 μm) with a roundish shape. In addition, the round crystal surface is segmented (see the images in Appendix 1). Such crystal surface topography is not beneficial for the AFM technique, either ex-situ or in-situ. Therefore, we cannot work with these three materials having PAU and MWF structures in this project.

Although zeolite Rho crystals prepared for this study are also very small in size, they have flat surfaces large enough to keep the crystal unmoved during the in-situ AFM scanning. This makes zeolite Rho more favourable to work on. Furthermore, since RHO structure is related to the PAU and MWF, a study on the dissolution of zeolite Rho in alkaline solution, which is the purpose of this work, will add valuable insights into the understanding of the growth and dissolution of the complex PAU and MWF structures. However, owing to its high synthesis temperature, which is above the AFM working temperature limit, only the zeolite Rho crystal dissolution observation can be conducted.

Zeolite Rho itself is an aluminosilicate first discovered by Robson (1973) [4], after which many reports on the investigation, modification and application of the material were published [1], [5]–[9]. The material crystallized with the chemical formula $(\text{Na}^+, \text{Cs}^+)_{12} [\text{Al}_{12}\text{Si}_{36}\text{O}_{96}] \cdot (\text{H}_2\text{O})_{44}$. Zeolite Rho has proved to be a good catalyst, hydrogen storage, gas adsorbent and so on [7], [10]–[14].

5.2. Experimental and Analytical Techniques

5.2.1. Synthesis of the zeolite Rho crystal

Zeolite Rho material used in this work was synthesized by Suk Bong Hong' research group in POSTECH, South Korea. The synthesis procedure followed a method by Chatelain *et al.* (1995) [15] using 18-crown-6 ether (18C6) as the structure directing agent. The chemicals were mixed to get a synthesis having a composition as follows:



The hydrothermal reaction in a Teflon-lined autoclave was carried out at 110 °C for 72 hours. After filtration, the solid obtained was then washed and dried.

5.2.2. Material characterizations

PXRD technique to characterize the solids obtained from the synthesis was conducted using PAN Analytical X'Pert Pro Diffractometer with $CuK\alpha$ as the X-ray source. The tension was set 40 kV, while the current is 30 mA. The solids were crushed and placed on a sample holder. The scanning was done with 2θ ranging from $5^\circ - 50^\circ$. The data produced were analyzed using X'Pert HighScore Plus software.

FEI Quanta 200 SEM was used to analyse the crystal morphology. After being scattered on a sticky carbon attached on a sample holder, the samples were coated with gold to avoid sample charging. The scanning was performed in vacuum with a high voltage set at 20.0 kV.

To study the surface topography of the crystal, ex-situ AFM scanning was done using an AFM instrument from JPK. A small piece of thermoplastic was heated at 50 °C on a glass slide until it was warm. The warm thermoplastic was pressed flat and clear, on to which very small amount of powdery sample was scattered. This was then reheated at 50 °C so that the crystals stuck on it. The crystals were then scanned using a non-conductive silicon nitride tip from Bruker and a set point of 0.5 V. Terrace height measurements were performed employing the JPKSPM Data Processing software.

5.2.3. Dissolution of zeolite Rho crystal studied with in-situ AFM

The dissolution of the zeolite Rho crystals was monitored in-situ using the AFM instrument from JPK. The crystals were sprinkled on a very small amount of resin on a glass slide. Previously, the resin was warmed at 60 °C for about four hours. After the crystals were sprinkled on it, the resin was cured at 60 °C overnight. The glass slide was then placed in a BioCell and put under the AFM head for scanning. A tube was connected the BioCell with the solution used to dissolve the crystals.

After a nice crystal surface was found, the solution was injected into the BioCell and the scanning was continued. The in-situ scanning was performed in contact mode using a non-conductive silicon nitride tip from Bruker. The set point and scan rate were set to 0.3 V and 4Hz, respectively. Different concentrations of NaOH and KOH solutions were used in the attempts to dissolve the zeolite Rho crystals in this in-situ AFM experiment.

5.3. Results and Discussions

5.3.1. Characterization of the zeolite Rho crystal

PXRD pattern of the as-synthesized zeolite Rho is presented in Figure 5.1. High crystalline RHO phase was produced from the synthesis. Peak positions of the zeolite Rho sample match those from the reference, although there is an additional peak at 2θ of about 9.5° in the sample's PXRD pattern, which indicates the presence of impurity phase. This peak is associated with a peak of chabazite (CHA) as reported by Araki *et al.* (2012) in their zeolite Rho synthesis using 18-crown-6 ether as the organic template [14]. In addition, chabazite was also found as one of the impurity phases in zeolite Rho preparations published by Robson (1975) [4] and Park *et al.* (1996) [6]. In the PXRD pattern of the zeolite Rho sample, the peak at $2\theta = 8.3^\circ$ is very low. This possibly relates to the higher baseline at 2θ less than 10. *CelRef* analysis on the sample's PXRD pattern shows cell units, $a = b = c = 14.933$ Å, which are equivalent to the reference [2]. Additionally, the d_{110} of the sample crystal is 10.48 Å based on this *CelRef* analysis. This value is comparable to the calculated d_{110} , which is 10.63 Å.

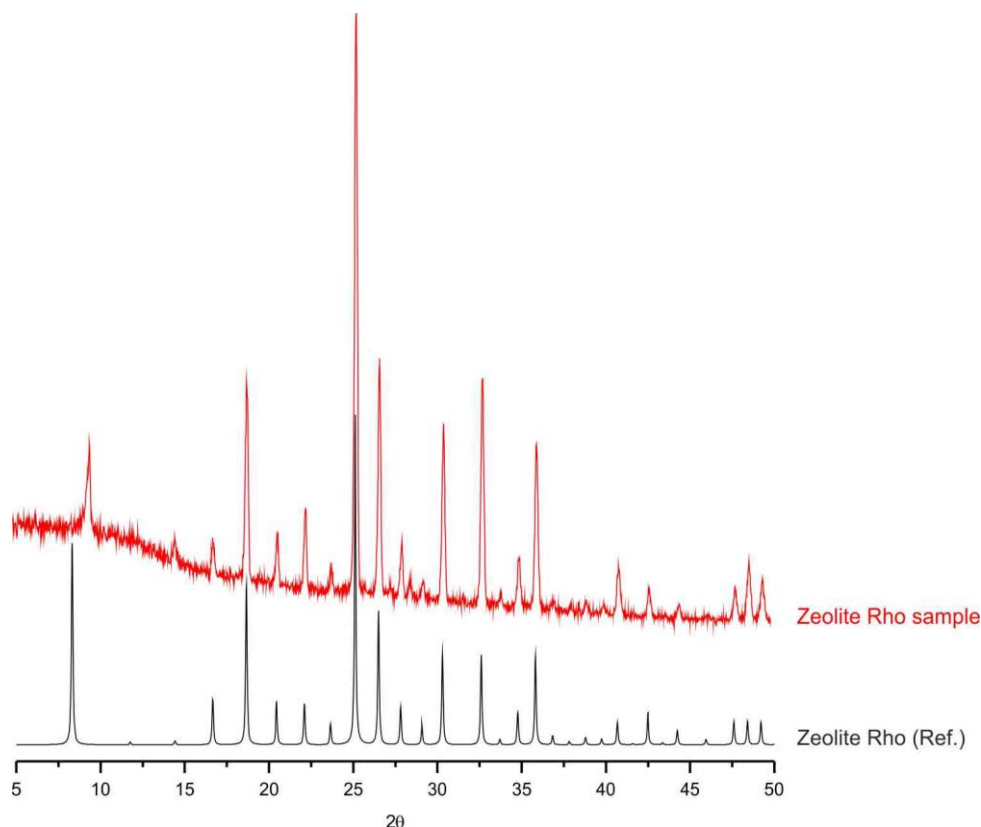


Figure 5.1. PXRD patterns of the as-prepared zeolite Rho sample (red line) compared to the reference (black line) [2].

The SEM image of the as-synthesized zeolite Rho in Figure 5.2 shows the formation of single crystals in rhombic dodecahedral shape having twelve $\{110\}$ facets. The crystals are very small, less than $2\ \mu\text{m}$, with a quite uniform crystal size distribution. Different crystal morphologies of zeolite Rho have been reported. Using the same SDA as used in this work, Chatelain *et al.* (1995) prepared sphere-like shaped zeolite Rho [15], while Araki and co-workers (2012) reported a synthesis resulting in small angular particles of zeolite Rho [8], [14]. The same angular particles of zeolite Rho were also made by Palomino *et al.* (2012) [7]. Nevertheless, in 1996 Park *et al.* reported the formation of 12-faced hedron zeolite Rho [6], just like we found here. Zeolite Rho crystal size tends to be small, about $2\ \mu\text{m}$ or less, as published in the literature. The crystal size increase was achieved as a result of no synthesis gel ageing [15] or an increase in the ageing temperature [6].

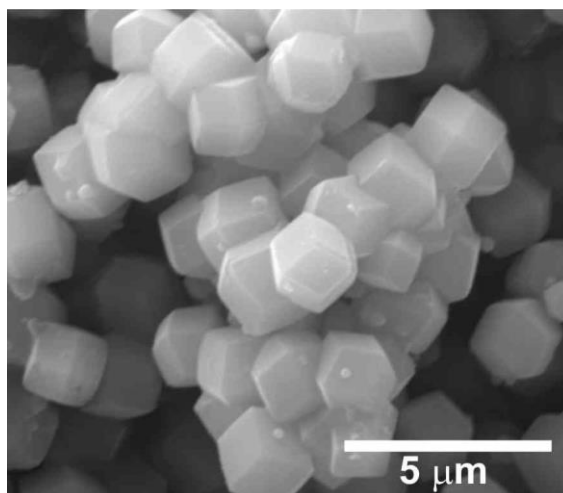


Figure 5.2. SEM image of the as-synthesized zeolite Rho crystals.

5.3.2. Ex-situ AFM of zeolite Rho crystal

The ex-situ AFM displayed in Figure 5.3 (a–b) reveals not only the morphology of the zeolite Rho crystal but also its surface topography. The presence of small terraces on the crystal surface indicates that the crystal grows via layer growth mechanism. The terraces on the (110) facet show similar shape and orientation as the facet. The same phenomenon was also observed on the crystal surface of RHO structured MOF [16].

Cross-sectional height measurements on the zeolite Rho surface given in Figure 5.3 (c–d) show that the zeolite Rho's layers are 1.1 ± 0.1 nm high. Considering the errors in this measurement, the heights agree with the d_{110} of the crystal. This height corresponds to the distance between the black dashed line in Figure 5.4, which represents the growth step of zeolite Rho.

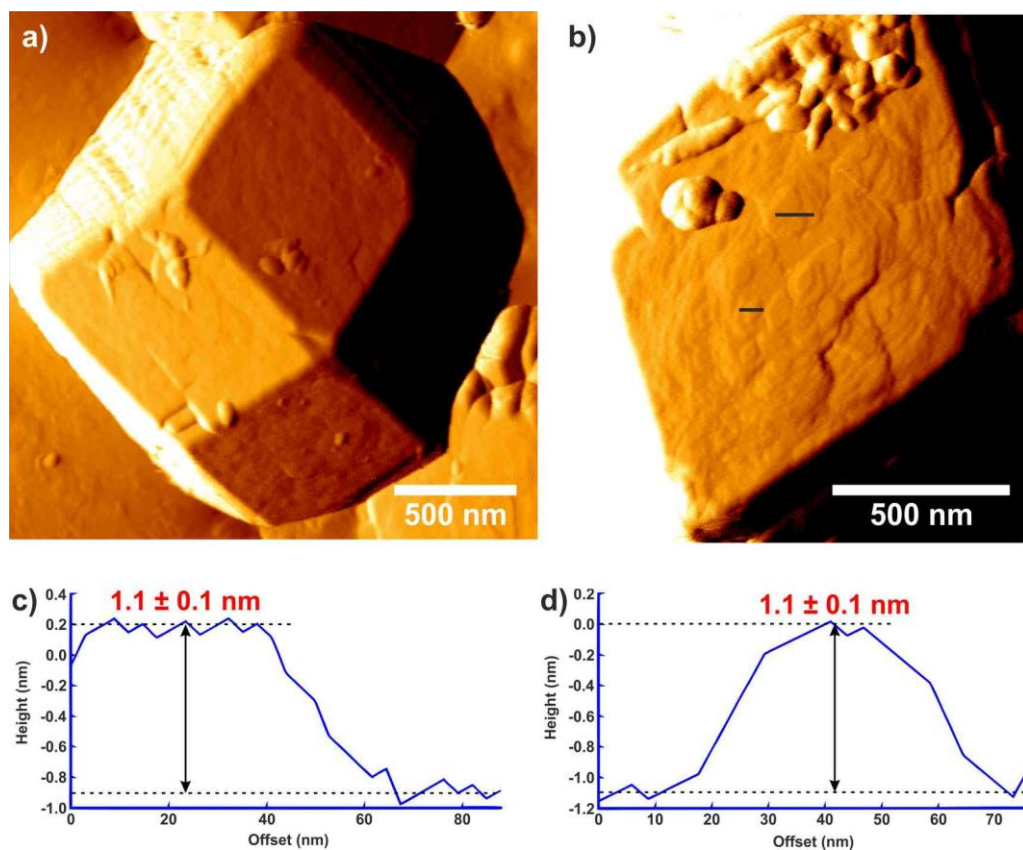


Figure 5.3. a–b) Vertical deflection AFM images of zeolite Rho crystals with the image (b) shows the (110) facet. c–d) Cross-sectional height measurements along the top and bottom horizontal black lines, respectively, in the image (b).

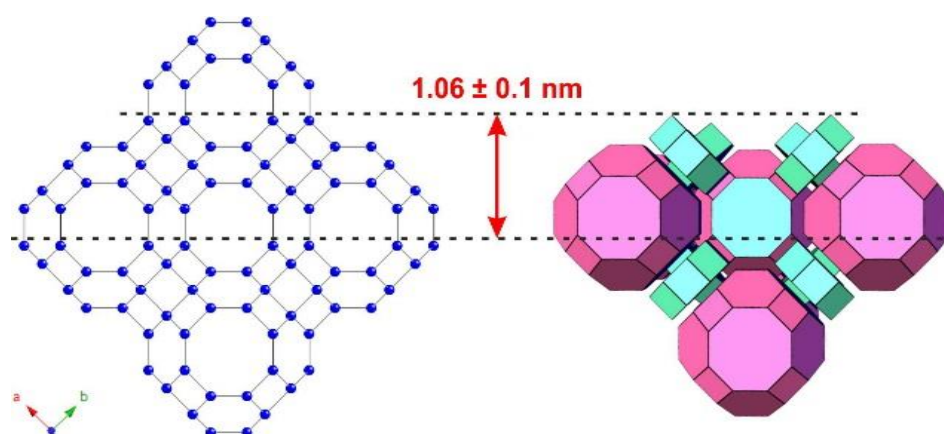


Figure 5.4. RHO structure framework viewed along c direction illustrated in ball and stick mode (left) and tiling drawn using Gavrog 3dt (right). The blue balls represent the Si or Al atoms, while the black sticks are the oxygen bridging in between the Si and Al. The oxygen atoms are omitted for clarity. The pink tiles on the right are the α -cages and the green ones are the double 8-rings. The growth step height is based on the calculation.

5.3.3. RHO crystal simulation

Simulation of the zeolite Rho crystal was performed using the *CrystalGrower* program and the result is viewed using *CG Visualiser*. The result is presented in Figure 5.5. The model crystal demonstrates rhombic dodecahedral shape, which matches with the crystal morphology of the zeolite Rho studied in this work. Each of the $\{110\}$ facets shows the presence of terraces that also have the same shape and orientation as the facet on which they grow as shown the images (a–b).

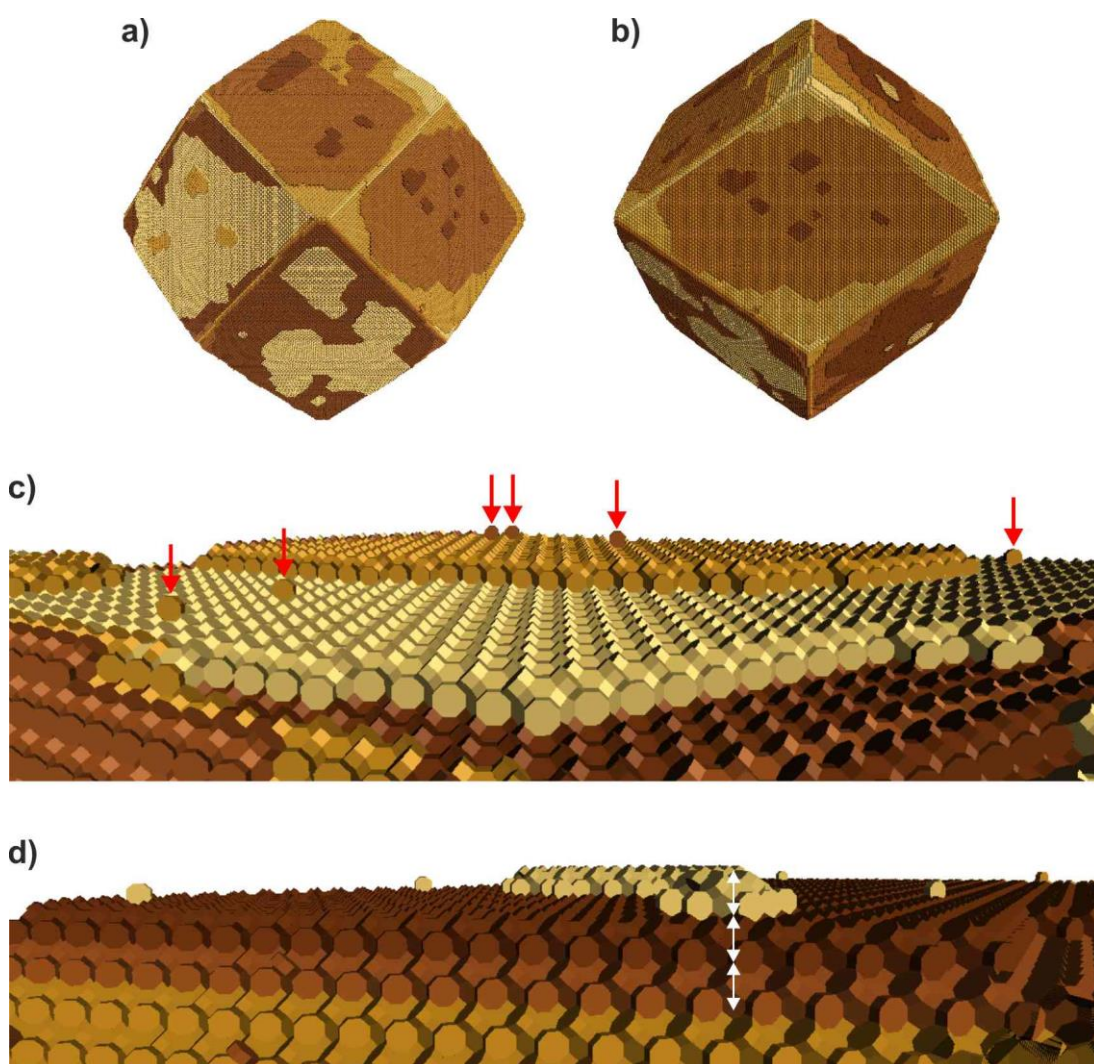


Figure 5.5. Simulation of RHO crystal using *CrystalGrower* with $\Delta U_s = 2 \text{ kcal mol}^{-1}$ and viewed with *CG Visualiser*. a–b) Full look of the simulated crystals sized approximately $0.16 \text{ }\mu\text{m}$. c–d) Closer looks at the $\{110\}$ surface of the simulated RHO crystal.

Looking closely at the crystal surface (images c–d), we can see the double 8-rings at the surface terminal. Small nucleations (pointed by red arrows in the image (c)) also exist on the surface. These will further grow into new terraces. Each white double arrows in the image (d) marks the distance of one surface layer, which is from a double 8-rings to another double 8-rings on top of them. This arrangement in the simulated crystal agrees very well with the analysis in Figure 5.4.

5.3.4. In-situ AFM of zeolite Rho crystal dissolution

In-situ AFM on the dissolution of zeolite Rho crystal was very difficult to perform owing to its very small crystal size. The alkaline solutions used to dissolve the crystal softened the resin that held the crystal. As a result, the crystal was wobbling and easily removed by the AFM tip during the scanning. Among the in-situ AFM experiments that we conducted to dissolve zeolite Rho crystal in NaOH and KOH solutions with different concentrations, good results were obtained from the dissolutions of the crystal in 0.2 M – 0.5 M KOH solutions. The sequence AFM images from the dissolution in 0.2 M KOH solution are displayed in Figure 5.6 and can be watched in Movie 5-1 in Appendix 1.

Overall, the zeolite Rho crystal was very tough in this low concentrated KOH solution. For about four hours, the solution was able to retreat only small terraces and the edge of the large terraces. The two small terraces, of which dissolution process are followed, are shown with cyan and white arrows. The heights of these small terraces are given in the images.

In the first sixty minutes in contact with the solution, height measurement performed on the small terrace pointed by the cyan arrows gave 1.1 and 1.0 ± 0.1 nm high. However, during this time, the width of this terrace decreased as the dissolution time increased. This is because the solution retreated the structure at the step sites since this position. After an hour immersing the zeolite Rho crystal in this solution, the terrace height started to drop from 1.0 to 0.8 ± 0.1 nm at $t = 61$ minutes and continued to decrease to 0.5, 0.3 and 0.25 ± 0.1 nm before completely gone at $t = 82$ minutes. This height decrease relates to the vertical dissolution of the growth step.

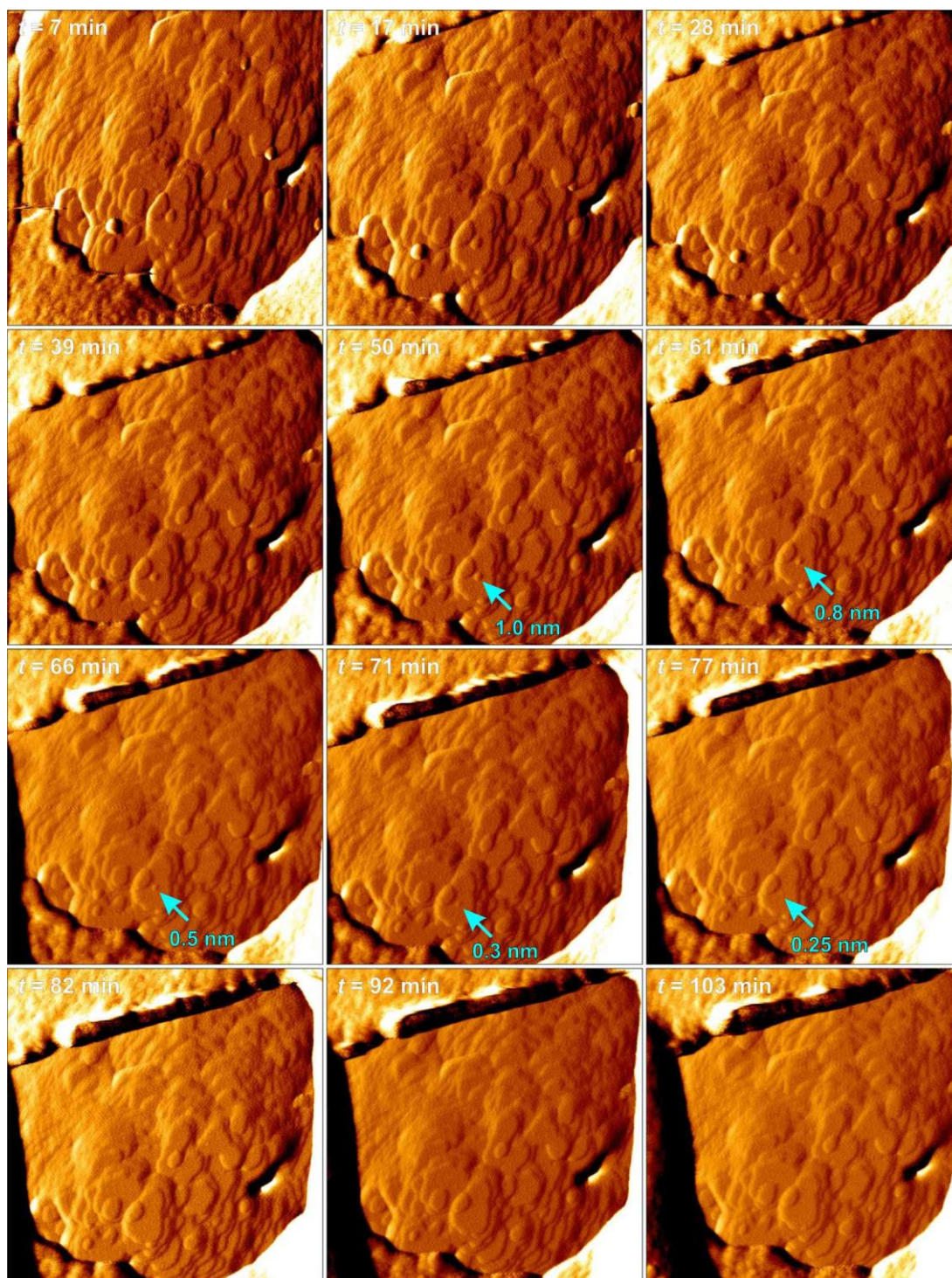


Figure 5.6. Successive AFM vertical deflection images on the (110) facet of zeolite Rho crystal dissolution in 0.2 M KOH solution. The scanned area is $1.0\ \mu\text{m} \times 1.0\ \mu\text{m}$. Cyan and white arrows point at the dissolution of two different small terraces and their heights during the process. All heights given here have $\pm 0.1\ \text{nm}$ measurement error (*to be continued on the next page*).

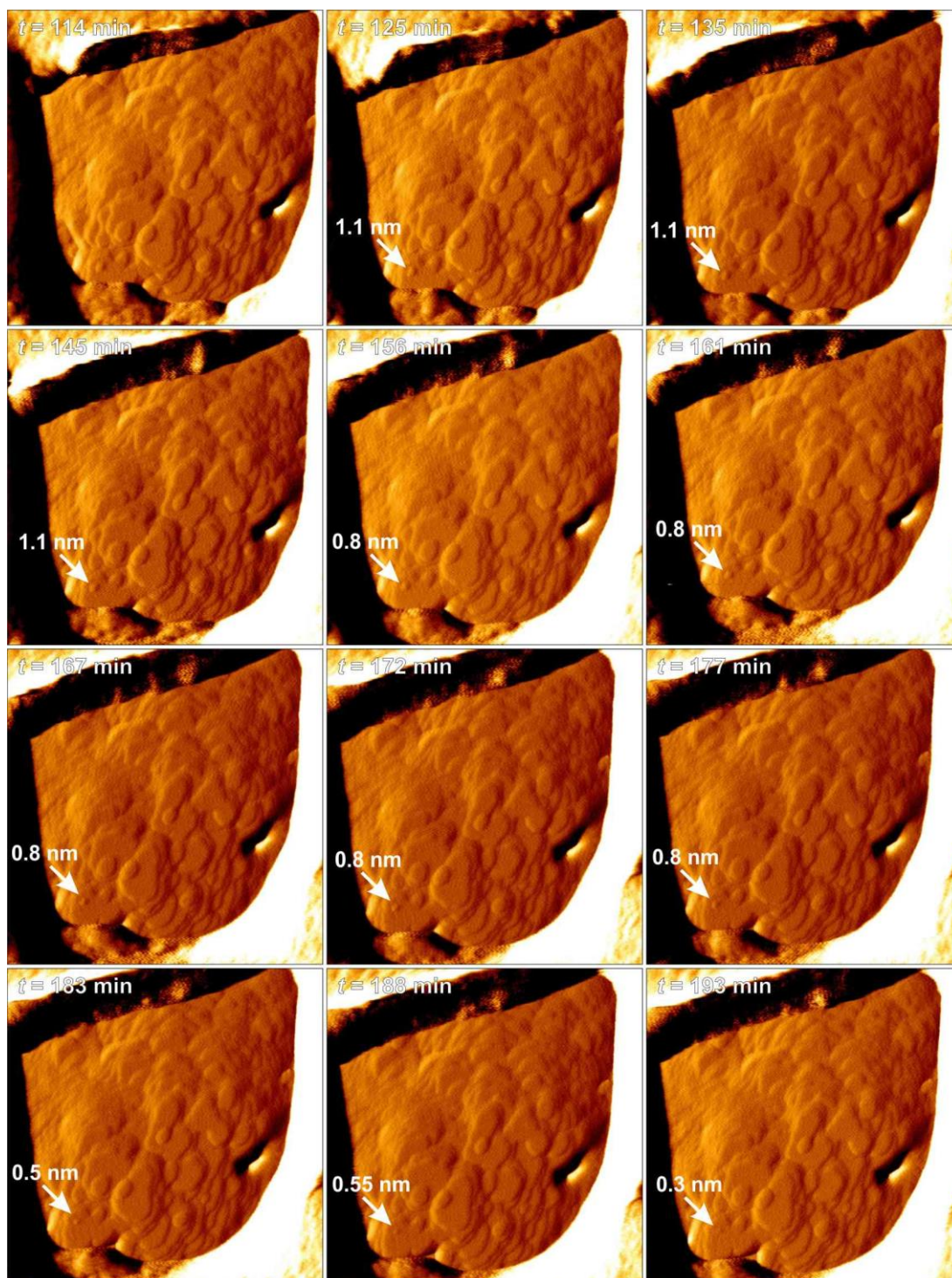


Figure 5.6 (continued). Successive AFM vertical deflection images on the (110) facet of zeolite Rho crystal dissolution in 0.2 M KOH solution. The scanned area is $1.0 \mu\text{m} \times 1.0 \mu\text{m}$. Cyan and white arrows point at the dissolution of two different small terraces and their heights during the process. All heights given here have ± 0.1 nm measurement error (*to be continued on the next page*).

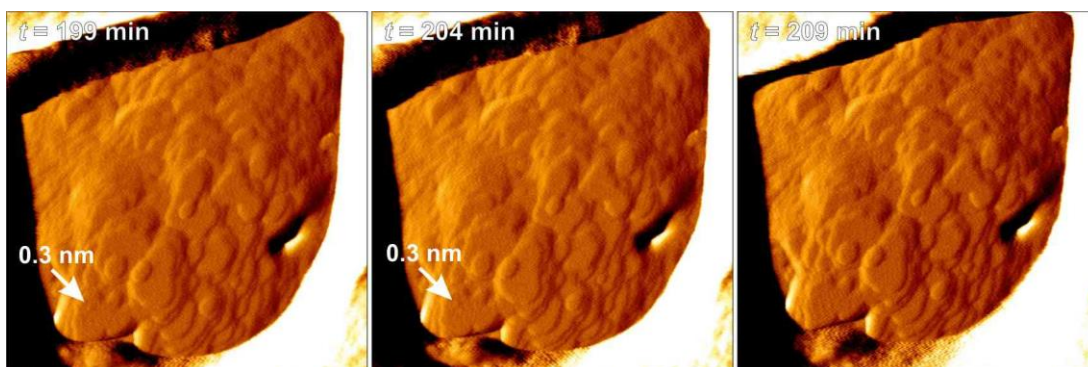


Figure 5.6 (continued). Successive AFM vertical deflection images on the (110) facet of zeolite Rho crystal dissolution in 0.2 M KOH solution. The scanned area is $1.0 \mu\text{m} \times 1.0 \mu\text{m}$. Cyan and white arrows point at the dissolution of two different small terraces and their heights during the process. All heights given here have ± 0.1 nm measurement error.

The same phenomenon was observed on the second small terrace aimed by the white arrows. The terrace height started to decline from 1.1 nm to 0.8 ± 0.1 nm at $t = 156$ minutes after the solution injection, after which the height decreased to 0.8, 0.5 and 0.3 ± 0.1 nm. At $t = 209$ minutes, the terrace did not exist on the crystal surface anymore.

From this result, we understand that in low concentrated KOH solution the layers on zeolite Rho crystal surface favour to retreat from terrace edge as the crystal structures at the step sites are easily detached than those in the bulk terrace. Furthermore, the inter-connected structure at the growth terminal of this framework is also a contributing factor that mostly defines how the growth steps on the zeolite Rho crystal surface retreat during the dissolution process. This layer retreat continues until the dimension of the terraces is small enough to hold the structure in the bulk terrace from solution attack. Thus, the structure break down starts vertically, reducing the growth step height. The full height of the growth step of the second small terrace in Figure 5.6 lasted longer in the solution than that of the first small terrace. This is because the area of the second terrace was larger than the first one so that it took longer for the solution to retreat the terrace from the step sites until it reached the critical size for the vertical dissolution to begin.

Both small terraces of which dissolutions were followed in Figure 5.6 showed the same height decrease. Figure 5.7 compares those observed heights with the RHO structure break down, which we found matching each other. A full growth step of

this framework structure dissolves step by step, which is common in nanoporous crystal dissolution. Height decrease from 1.0 nm or 1.1 nm to 0.8 nm was due to the removal of the topmost atoms until the height is at the same level as the α -cage. Reducing this height to 0.5 nm means dissolving the top parts of the structure, leaving it at the same height as the double 8-rings facing the [001] direction, and so on as illustrated in Figure 5.7 (a).

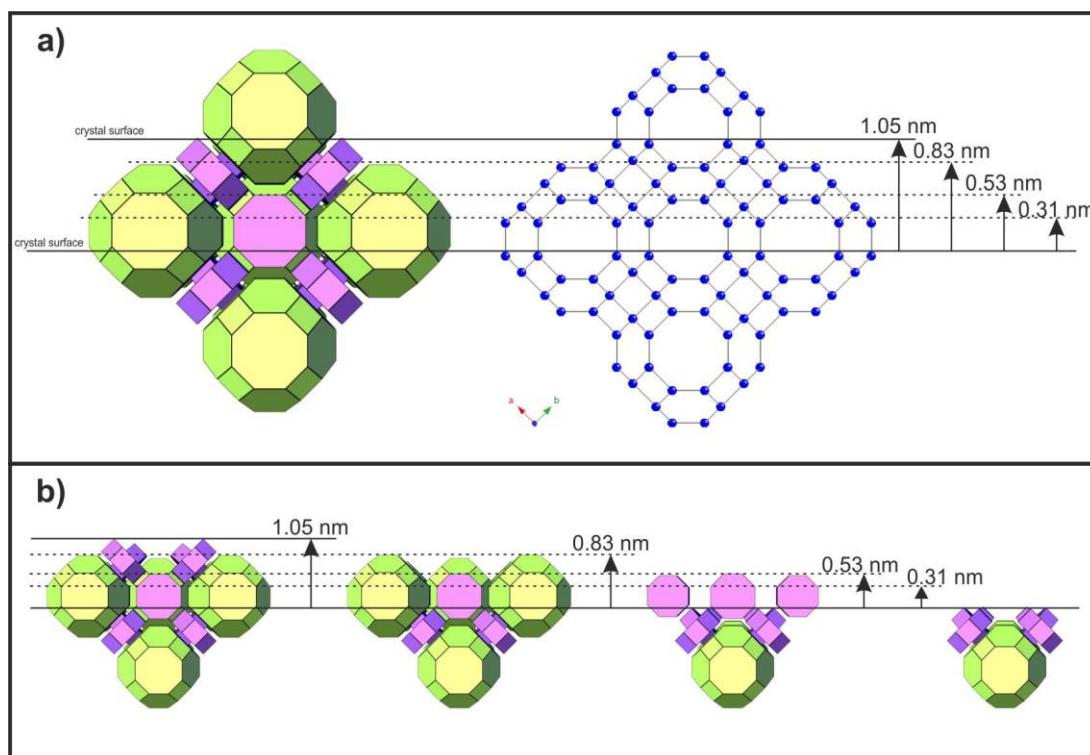


Figure 5.7. a) RHO structure breakdown of the (110) facet expressed in tiling (left) and ball and stick mode (right). The blue balls represent the Si or Al atoms, while the black sticks are the oxygen bridging in between the Si and Al. The oxygen atoms are omitted for clarity. b) Illustration of step by step RHO tiling breakdown.

In relation to the crystal growth, as it is believed that the dissolution may be associated to the reverse process of the growth, zeolite Rho crystal may also grow gradually by attachment of its small units of growth. This was observed too in the growth of RHO type MOF crystal, CdIF_4 , by Wagia *et al.* (2016) [16]. In addition, correlating this result to the more complex structure of Rho-family zeolites, PAU and MWF, we expect their growth and dissolution processes to also occur in gradation, although further study is required to prove it.

5.4. Conclusions

AFM proved to be very reliable to investigate the nanoscopic event on the crystal surface. Terraces on the {110} facet of zeolite Rho crystal were detected using the technique. Height measurement on the terraces shows that the growth step on {110} facet is 1.1 ± 0.1 nm high. Observed using in-situ AFM, the 0.2 M KOH solution dissolved the layer on zeolite Rho crystal surface from its step sites towards the centre of the layer owing to the inter-connected structure on the surface terminal. This layer retreat continued until the layer is small enough to hold the structure pack together. After that, the layer's height started to decrease to 0.8, 0.5 and 0.3 nm high. These heights perfectly fit the calculated framework structure breakdown. The experimental results have been confirmed to exactly matches the RHO model crystal simulated using the *CrystalGrower*.

5.5. References

- [1] L. B. McCusker, "Crystal structures of the ammonium and hydrogen forms of zeolite rho," *Zeolites*, vol. 4, no. 1, pp. 51–55, 1984.
- [2] "Database of Zeolite Structures." [Online]. Available: <http://www.iza-structure.org/databases/>. [Accessed: 17-Nov-2017].
- [3] P. Guo *et al.*, "A zeolite family with expanding structural complexity and embedded isorecticular structures," *Nature*, vol. 524, no. 7563, pp. 74–78, 2015.
- [4] H. E. Robson, "Zeolite Rho," US 3 904 738, 1975.
- [5] J. B. Parise, T. E. Gier, D. R. Corbin, and D. E. Cox, "Structural Changes Occurring upon Dehydration of Zeolite Rho. A Study Using Neutron Powder Diffraction and Distance-Least-Squares Structural Modeling," *J. Phys. Chem.*, vol. 88, no. 8, pp. 1635–1640, 1984.
- [6] M. Park, S. H. Kim, N. H. Heo, and S. Komarneni, "Synthesis of Zeolite Rho: Aging Temperature Effect," *J. Porous Mater.*, vol. 3, no. 3, pp. 151–155, 1996.
- [7] M. Palomino, A. Corma, J. L. Jorda, F. Rey, and S. Valencia, "Zeolite Rho: a highly selective adsorbent for CO₂/CH₄ separation induced by a structural phase modification," *Chem. Commun.*, vol. 48, no. 2, pp. 215–217, 2012.

- [8] S. Araki, Y. Kiyohara, S. Tanaka, and Y. Miyake, "Crystallization process of zeolite rho prepared by hydrothermal synthesis using 18-crown-6 ether as organic template," *J. Colloid Interface Sci.*, vol. 376, no. 1, pp. 28–33, 2012.
- [9] L. Abrams and D. R. Corbin, "Sorption Properties of Zeolite Rho," *J. Catal.*, vol. 127, no. 1, pp. 9–21, 1991.
- [10] L. Abrams, D. R. Corbin, and M. Keane, Jr., "Synthesis of dimethylamine by zeolite Rho: A rational basis for selectivity," *J. Catal.*, vol. 126, no. 2, pp. 610–618, 1990.
- [11] D. R. Corbin, S. Schwarz, and G. C. Sonnichsen, "Methylamines synthesis: A review," *Catal. Today*, vol. 37, no. 2, pp. 71–102, 1997.
- [12] H. W. Langmi *et al.*, "Hydrogen storage in ion-exchanged zeolites," *J. Alloys Compd.*, vol. 406, pp. 637–642, 2005.
- [13] V. V. Krishnan, S. L. Suib, D. R. Corbin, S. Schwarz, and G. E. Jones, "Encapsulation studies of hydrogen on cadmium exchanged zeolite rho at atmospheric pressure," *Catal. Today*, vol. 31, no. 3–4, pp. 199–205, 1996.
- [14] S. Araki, Y. Kiyohara, S. Tanaka, and Y. Miyake, "Adsorption of carbon dioxide and nitrogen on zeolite rho prepared by hydrothermal synthesis using 18-crown-6 ether," *J. Colloid Interface Sci.*, vol. 388, no. 1, pp. 185–190, 2012.
- [15] T. Chatelain, J. Patarin, E. Fousson, M. Soulard, J. L. Guth, and P. Schulz, "Synthesis and characterization of high-silica zeolite RHO prepared in the presence of 18-crown-6 ether as organic template," *Microporous Mater.*, vol. 4, no. 2–3, pp. 231–238, 1995.
- [16] R. Wagia, I. Strashnov, M. W. Anderson, and M. P. Attfield, "Determination of the Preassembled Nucleating Units That Are Critical for the Crystal Growth of the Metal–Organic Framework CdIF-4," *Angew. Chemie - Int. Ed.*, vol. 128, no. 31, pp. 9221–9225, 2016.

Chapter 6

NU-87 Crystal Dissolution Studied by AFM

6. NU-87 Crystal Dissolution Studied by AFM

6.1. Introduction

The interesting IM-17 and DAF-1 crystals with their large unit cells and complex structures discussed in the previous chapters are both hydrothermally synthesized using decamethonium dications as the structure directing agent. The decamethonium dications are organic substances with a chain of 10 carbons between trimethylammonium cations (see Figure 6.1). This substance was also reported to direct the formation of NU-87, an aluminosilicate possessing NES structure [1], [2].

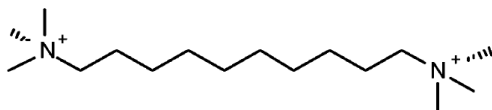


Figure 6.1. Decamethonium dications structure.

Distinctively from the orthorhombic NES unit cell with $\alpha = \gamma = \beta = 90^\circ$, the crystal system of the NU-87 is monoclinic, which has lattice parameters as follows: $a = 14.324 \text{ \AA}$, $b = 22.376 \text{ \AA}$ and $c = 25.092 \text{ \AA}$, with $\alpha = \gamma = 90^\circ$ and $\beta = 151.51^\circ$. The structure framework has 2-dimensional 10-ring channels sized $4.8 \times 5.7 \text{ \AA}$ [3] (see Figure 6.2).

Even though having smaller unit cell than those of the UOV and DFO, the NES tiling structure is built by very large t-nes tiles combined with three other small tiles. The largest tile leads to a complication and difficulty for the *CrystalGrower* to grow the NES crystal. Thus, this large t-nes tile needs to be divided into three smaller tiles in order to grow the crystal [4]. With its unique structure framework and tiling, it is very interesting to investigate how this complex structure of the NU-87 grows. Again, owing to the temperature limit in operating the AFM, the NU-87 crystal dissolution is more sensible to observe than its growth at 180°C [1]. AFM is used to study the surface events while *CrystalGrower* program is employed to simulate the crystal in order to produce a crystal model.

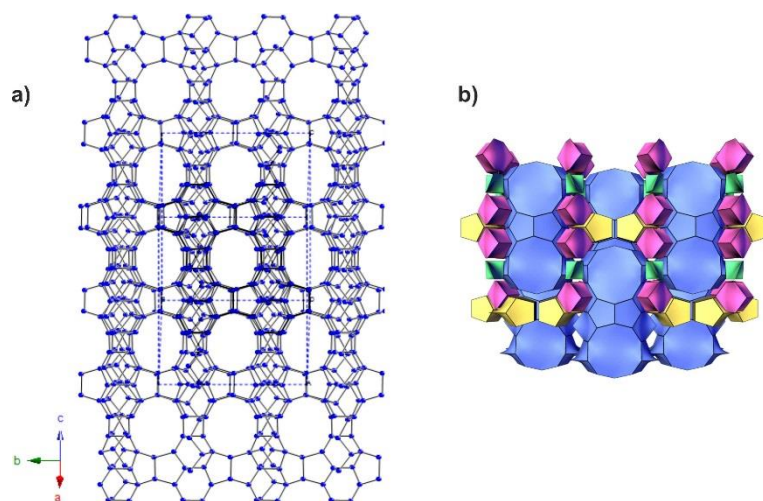


Figure 6.2. a) Framework structure of NU-87 crystal viewed at (201) facet drawn in ball and stick mode. The blue balls represent the Si or Al atoms, while the black sticks are the oxygen bridging in between the Si and Al. The oxygen atoms in this framework are omitted for clarity. One unit cell is displayed by the blue dashed lines. b) NU-87 tiling drawn using *Gavrog 3dt* (large blue tiles: t-nes, yellow tiles: t-non, pink tiles: t-pes and green tiles: t-euo).

Possessing a unique pore structure, NU-87 has a great capacity to be applied as catalysts. The use of this aluminosilicate to catalyze 1,2,4-trimethylbenzene disproportionation to generate xylene and tetramethyl benzene was reported to take over H-beta and H-mordenite's performances [5]. Park and Rhee also employed NU-87 crystal to disproportionate toluene in order to yield benzene and xylene. The result showed a very promising catalytic activity and the slowest catalyst deactivation of this aluminosilicate compared to other catalysts tested (MCM-22, mordenite, zeolite beta, and ZSM-5) [6]. In addition, this NU-87 material has been utilized in the production of cumene via alkylation of benzene with propene [7], conversion methylnaphthalene [8] as well as ammoxidation of ethane to get acetonitrile [9]. They all proved that NU-87 is a zeolite less prone to deactivation due to coke formation during the catalysis process.

Casci and Stewart (1990), the inventors of the NU-87, advised the usage of decamethonium bromide as the directing agent, 30 % silica solution or fumed silica as the silicon source, sodium aluminate as an aluminium source and NaOH to enhance the pH of the prepared synthesis gel. Addition of NaBr is also recommended in order to make the NU-87 crystallization from the reaction gel

faster. The $\text{SiO}_2/\text{Al}_2\text{O}_3$ molar ratio is best between 20 and 250 to get high purity of the crystal. The use of stirring during the crystallization process is meant to decrease the reaction time as well as to raise the product's degree of purity [1].

This procedure has been cited for other successful NU-87 syntheses. Shannon *et al.* (1991) reported the same process of making this zeolite [2]. From the molar composition information, apparently, they followed example 8 of the parent patent [1] to produce a high degree crystallinity of the targeted solids confirmed by the PXRD pattern peak positions that match the reference. Based on the electron microscopy study, Shannon and co-workers (1991) announced that NU-87 crystal synthesized with decamethonium bromide as the template had a rod or lath-like morphology with the predominant dimension of the crystals is less than 1 μm long [2].

The PXRD pattern and crystal shape of the NU-87 crystals from the work by Shannon *et al.* (1991) [2] are supported by Glaser *et al.* (1998) [8] and Zhang *et al.* (2013) [10], who have prepared NU-87 crystals with the same directing agent although the latter modified the procedure. NU-87 crystals made by both research groups showed rectangular lath with their size bigger than that previously reported (see Figure 6.3).

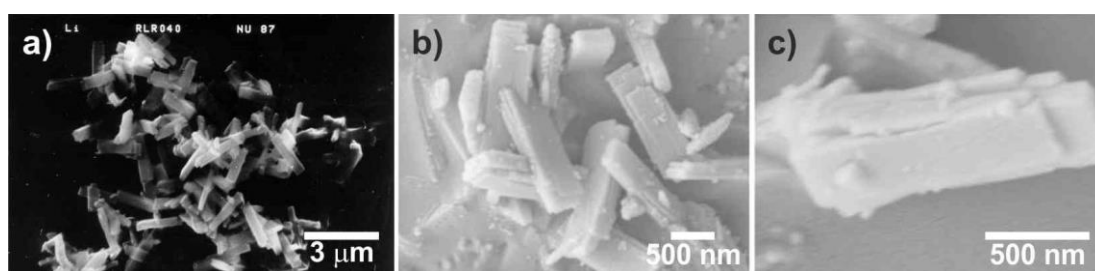


Figure 6.3. SEM images of NU-87 synthesized using decamethonium bromide as SDA reported by (a) Glaser *et al.* (1998) [8] and (b–c) Zhang *et al.* (2013) [10].

Using the same procedure to synthesize NU-87 crystals [1], Corma and co-workers (1999) got a relatively small crystal size, which is 0.3 – 0.4 μm [11]. In spite of that, the catalytic accomplishment of the material is still superior in cracking of gasoline,

especially its constituent *n*-heptane. Park and Rhee (2003) [6] used the same procedure to crystallize NU-87. They mentioned that the result was in a good agreement with the reference [2]. In addition, the material was successfully employed as a catalyst in organic reaction.

A different approach to the synthesis of NU-87 crystal was published by Adair *et al.* in 1996 [12]. They prepared the aluminosilicate without the addition of sodium bromide. It is stated in the paper that the peak positions in the PXRD pattern coincided with regard to the reference [1] and showed single phase formation of NU-87 with larger crystal size, 3 – 4 μm .

Only recently was there a publication by Burton, Jr. about alternative SDAs to synthesize NU-87. The SDAs he used were 1,4-bis(N,N-dimethylcyclohexylammonium)butane dications and 1,5-bis(N,N-dimethylcyclohexylammonium)pentane dications [13]. The SEM study showed a fine crystal size with dissimilar morphology to the previous citation [1]. Another dissimilar directing agent, which was 1,8-diquinuclidiniumoctane $\text{C}_8\text{H}_{16}-(\text{C}_7\text{H}_{13}\text{N}^+)_2$, was also reported to crystallize NU-87 in a fluoride medium. This method resulted in a large crystal size [14]. However, these publications seem to be not as popular as the original invention.

Nevertheless, pure NU-87 is very difficult to be crystallized. It has been observed that some impurities, such as mordenite, analcime, quartz, and cristobalite, are commonly found co-existed in a low amount [1], [10].

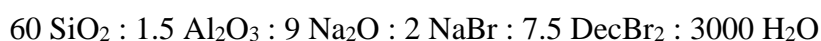
6.2. Experimental and Analytical Techniques

6.2.1. Synthesis of the NU-87 crystal

NU-87 was prepared using decamethonium bromide as the template following the example 8 in a patent published by Casci and Stewart (1990) [1]. First of all, solution A, B and C were made. Solution A consisted of sodium aluminate anhydrous (Sigma-Aldrich), sodium hydroxide (Fisher Scientific, NaOH, 98.4 %), sodium bromide (Sigma, NaBr, 99.5 %) and a part of deionized water. Those chemicals were

stirred using a magnetic stirrer to be a clear solution A. Solution B was prepared by dissolving decamethonium bromide (Sigma-Aldrich, DecBr₂) in deionized water. Meanwhile, solution C is the rest of the deionized water required in this synthesis.

The next step is pouring solution A into colloidal silica solution (Sigma-Aldrich, LUDOX AS-30, 30 %) as the silica source with stirring. This was done slowly for about 30 seconds. After all the solution A was mixed with the silica sol, the stirring was continued for 5 minutes before solution B was added. The addition of this solution B was also done slowly for the period of approximately 30 seconds with stirring to let the solutions mixed well. Lastly, after an additional 5 minutes stirring, solution C was introduced under stirring for 30 seconds. Then, this synthesis mixture was aged with stirring for the next 5 minutes. This prepared gel having a molar ratio as follows:



was poured into a 40 mL Teflon liner, which was then put into the autoclave. The hydrothermal reaction was conducted at 180 °C in a rotary oven for 451 hours.

The solid was recovered from the mixture after the hydrothermal reaction was finished by filtration and continued with washing it using deionized water. After that, the solid was dried overnight at 70 °C.

6.2.2. Material characterizations

The solids produced underwent characterizations using the PXRD and SEM techniques. PAN Analytical X'Pert Pro Diffractometer was used to analyze the phase obtained with Cu_{Kα} as the source of the X-ray. The tension was set 40 kV, while the current was 30 mA. After being crushed, the solid was placed on a sample holder and scanned with 2θ ranging from 5° – 50°. The data obtained were analyzed using X'Pert HighScore Plus software.

The crystal morphology analysis was conducted using FEI Quanta 200 SEM. The crystals were scattered on a sticky carbon attached on a sample holder. Then, the

samples were coated with gold to avoid sample charging. The electron scanning was performed in vacuum with the high voltage set at 20.0 kV.

A study on the crystal surface topography was conducted under the JPK NanoWizard II AFM instruments. A small piece of thermoplastic was heated at 50 °C on a glass slide until it was warm and can be pressed flat and clear. A very small amount of sample was then scattered on the flat thermoplastic and reheated so that the crystals stuck on it. The crystals were scanned with a set point of 0.5 V using a non-conductive silicon nitride tip from Bruker. The terrace heights were measured employing the JPKSPM Data Processing software.

6.2.3. Dissolution of NU-87 crystal studied with in-situ AFM

The in-situ AFM experiment was conducted to observe the dissolution process of the NU-87 crystals. The crystals were first scattered on a small amount of resin on a glass slide that was heated at 60 °C for about four hours. It was then heated again at 60 °C overnight to cure the resin. After that, the glass slide was placed in a BioCell and put under the AFM head. A tube has been attached to the BioCell to inject the solution into it.

Once a nice crystal was found, a solution was injected into the BioCell so that the crystal was immersed in the solution. The crystal surface was then scanned again for a period of time using a scan rate at 4 Hz and contact forces set to 0.3 V in ambient temperature. Several basic solutions and acid solution were used in this in-situ AFM experiment.

There were two kinds of resin used in this experiment. Resin 1 was the Embed 812 Kit from Electron Microscopy Sciences. This was used in low concentrations of a basic solution (1 M and lower) and acid solution. Meanwhile, resin 2 was the EP41S-5 from MasterBond, which was believed to have better performance in the higher concentration of basic solutions. This resin was employed in the dissolutions in basic solutions with concentration of more than 1 M.

6.3. Results and Discussions

6.3.1. Synthesis and characterization of the NU-87 crystal

The synthesis of NU-87 crystals has been performed successfully following the procedure reported by Casci and Stewart (1990) [1]. PXRD diffractogram of the as-made NU-87 crystals is given in Figure 6.4. The PXRD pattern clearly indicates that highly crystalline NU-87 phase has been formed from the synthesis. All peak positions are in a good match to those from the literature [1]–[3] suggesting that pure phase of NU-87 was obtained. From *Celref* analysis on this PXRD pattern, the as-prepared NU-87 crystals have lattice parameters as follows: $a = 14.335 \text{ \AA}$, $b = 22.366 \text{ \AA}$ and $c = 25.102 \text{ \AA}$. These values are equivalent to the cell parameters of the reference NU-87 mentioned previously in section 6.1 [3].

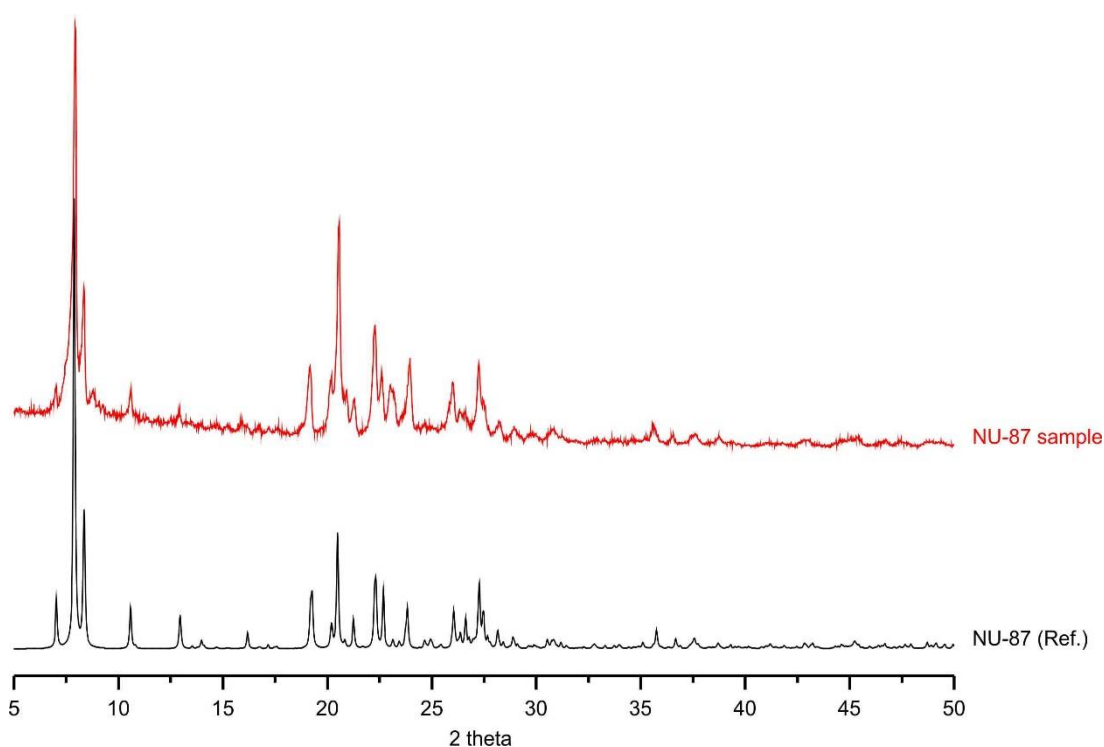


Figure 6.4. PXRD patterns of the as-prepared NU-87 sample (red line) compared to the reference (black line) [3].

SEM images of the as-synthesized NU-87 crystals are presented in Figure 6.5. The sample crystals show the same rod-like crystal morphology, indicating that the

synthesis produced one crystalline phase. The as-prepared NU-87 crystal shape agrees with the crystal shape of NU-87 crystal reported in the literature, which is given in Figure 6.3 [2], [8], [10]. The crystal size distribution of the sample is uniform with the crystal length of about 2 – 3 μm . The crystals are very thin with less than 0.5 μm of the thickness. The SEM images of the NU-87 sample support the PXRD result, which deduced that pure crystalline NU-87 was formed in this work.

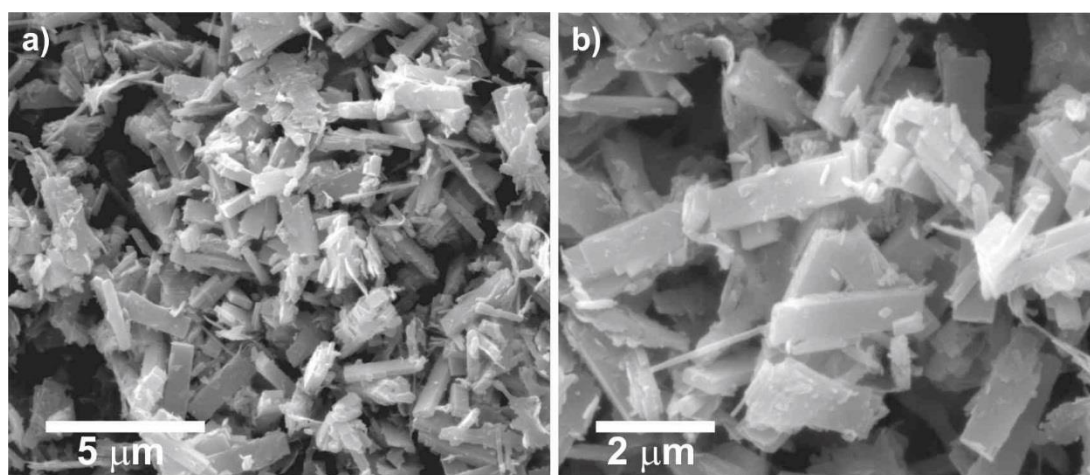


Figure 6.5. SEM images of the as-synthesized NU-87 crystals.

6.3.2. Ex-situ AFM of NU-87 crystal

AFM scanning was performed ex-situ to observe the NU-87 crystal surface topography. The AFM micrographs are presented in Figure 6.6. The largest surface area of the crystal shows layer by layer terraces (see the image a–b). These curved terraces (traced with the yellow dashed lines) indicate that they result from several nucleations on the crystal surface, which grew larger in any directions until they merged together. The same phenomenon was also observed on the NU-87 crystal simulation using *CrystalGrower* as reported previously [4]. Cross-sectional height measurement on the terraces gave an average of about 1.3 ± 0.1 nm high. The images (d–e) depict the side facets of the crystal, of which width is only about 0.2 μm .

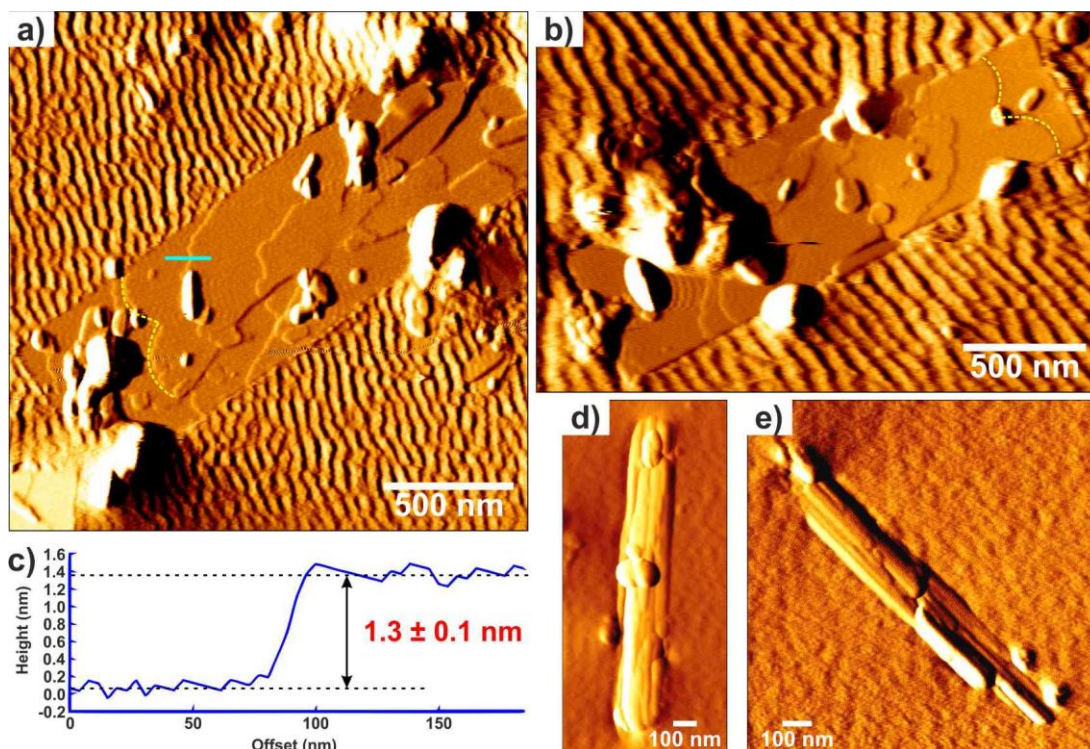


Figure 6.6. a–b) Vertical deflection AFM images of NU-87 crystals showing the surface having the largest area. c) Cross-sectional height measurement along the cyan line in the image (a). d–e) Vertical deflection AFM images of NU-87 crystals showing the side facet.

In our previous publication, *CrystalGrower* simulation of the NU-87 crystal yielded a lath-like crystal with the (001) facet as the largest surface area [4]. Using this calculation, the growth step measurement of *c.a.* 1.3 ± 0.1 nm in Figure 6.6 (c) can be correlated with half of its d_{001} (1.255 nm) based on the *CelRef* analysis. Hence, the growth step on this framework is the height of the red arrow in Figure 6.7 (a–b), cutting across the middle of the 2-dimensional 10-ring channel. This growth step is also displayed is the corresponding tiling in the image (b). Meanwhile, image (d) in Figure 6.7 displays the tiling in the image (b) that has been tilted forward to see the (001) facet. The calculated NU-87 crystal given in the image (c) supports this analysis that the (001) crystal surface is terminated by t-pes tiles.

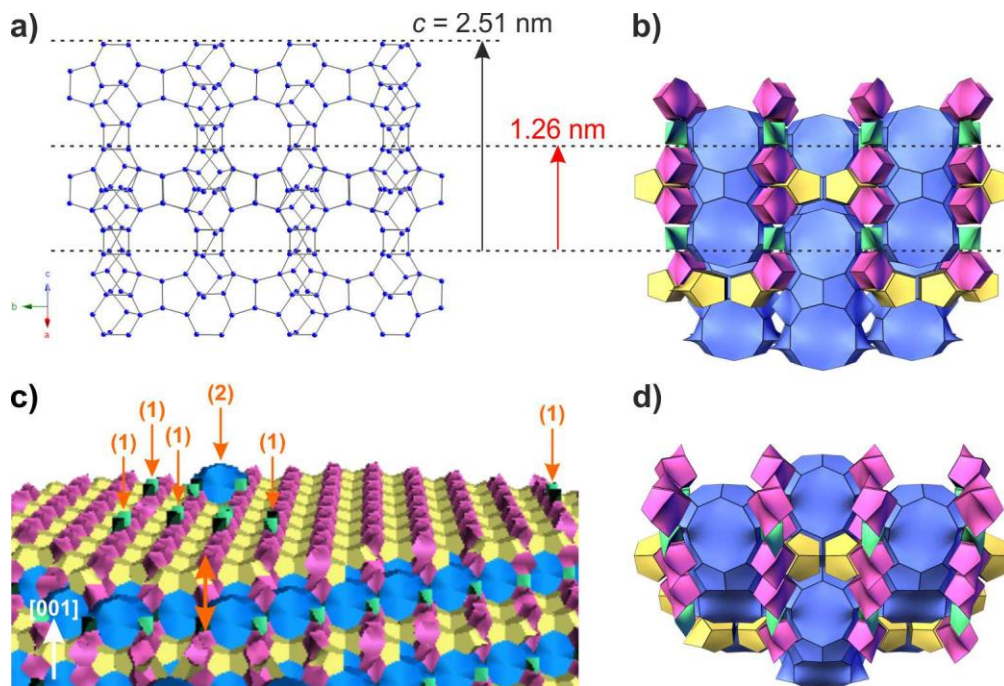


Figure 6.7. a) NU-87 structure framework illustrated in ball and stick mode. The blue balls represent the Si or Al atoms, while the black sticks are the oxygen bridging in between the Si and Al. The oxygen atoms in this framework are omitted for clarity. b) NU-87 tiling drawn using *Gavrog 3dt* (large blue tiles: t-nes, yellow tiles: t-non, pink tiles: t-pes and green tiles: t-euo). The growth step height of the framework in the image (a) and its corresponding tiling in the image (b) is shown with the red arrow. c) (001) surface of the simulated NU-87 crystal resulted from *CrystalGrower* calculation and viewed with *CG Visualiser* in ‘tyle type’ colouring. The colours of the tiles correspond to that of the tiling in the image (b). d) Tilted NU-87 tiling in the image (b) to show the (001) facet.

6.3.3. NES crystal simulation

The NU-87 crystal model simulated using *CrystalGrower* program has a very thin lath or rod-like shape crystal as previously reported [4]. This crystal shape is in agreement with the crystals produced experimentally in the laboratory. In addition, the surface topology of both simulated and practically observed crystals correspond with each other.

Detailed (001) crystal surface, which is the largest facet of the NU-87, is presented in Figure 6.7 (c). As we can see, the orange double arrows in the image represent the height of the growth step on this (001) surface, which is terminated by t-pes tiles. This matches very well with the structural analysis of the AFM result. Several new

nucleations can also be observed landed on the (001) crystal surface. These are pointed by the orange arrows labelled (1) for units of growth structuring a shape like the small t-euo tiles. The new structures then grow to build the 10-ring cage as marked (2) in the image. Thus, the simulation suggests step by step growth of the (001) facet of the NU-87 crystal until a full layer height is achieved.

6.3.4. In-situ AFM of NU-87 crystal dissolution

The in-situ AFM experiments were conducted in various solutions, both acidic and alkaline solutions on the (001) facet of the NU-87 crystal. However, no satisfying results were achieved from these attempts.

In very low concentrations of NaOH solution (0.05 to 0.1 M), the NU-87 crystal experienced no dissolution even until more than 3 hours immersed in the solution. Doubling the solution concentration to 0.2 M made the terraces retreat from their edges. Some of the AFM images from this dissolution were presented in Figure 6.8. As we can see, the curly terrace edges on the crystal surface in the first image turned to be smoothly round with smaller surface area in the last image. However, the height measurements performed on these terraces do not show any vertical structural breakdown on the surface layer's height. The height of the terrace was maintained while its area was reduced. The retreat occurred very slowly. It took almost 8 hours for the terraces to retreat to be like those in the last image. From its pattern, this might happen from tip assisted retreat when the AFM tip moved back and forth scanning the surface in contact mode.

The same results were observed for the dissolution of the crystal in 0.3 and 0.4 M NaOH solutions. Nevertheless, after 3.5 hours and less than 2 hours of immersion, respectively, the crystals popped out of the resin as it got softer and failed to hold them longer. Resin 1 was used in the dissolutions using NaOH solution with the concentration of 0.5 M and lower.

Increasing the solution concentration to 0.5 M and 2 M resulted in quicker crystal removal from the resin. The higher the concentration of the alkaline solution injected, the quicker the cured resin became softer. Consequently, the quicker was

the crystal removed from the resin. The crystals did not show any dissolution during the period of the scanning performed.

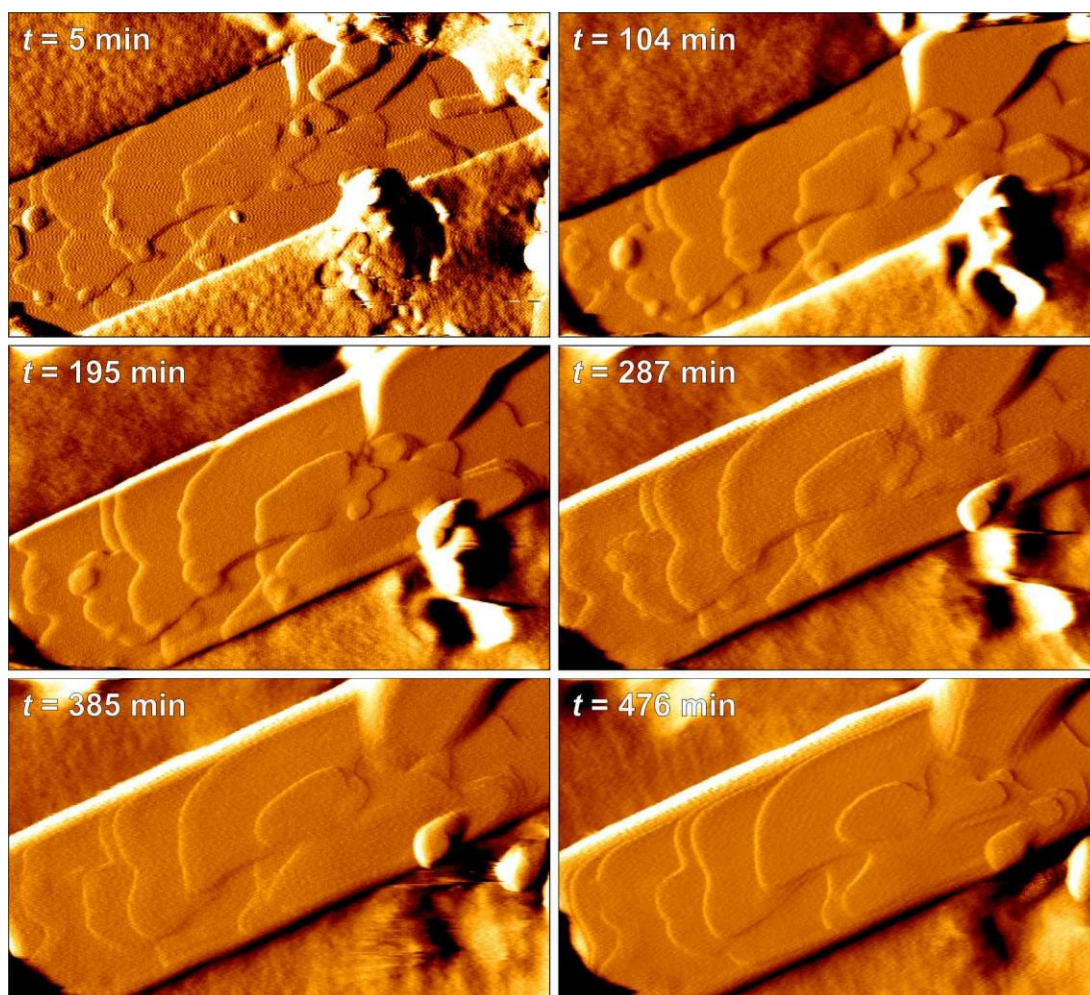


Figure 6.8. AFM vertical deflection images on the (001) facet of NU-87 crystal dissolution in 0.2 M NaOH solution. The scanned area is $2.0\ \mu\text{m} \times 1.2\ \mu\text{m}$.

Clear AFM images of the NU-87 crystal surface were obtained when the crystal was immersed in NaOH solutions with a concentration of 2 M and lower. However, the solutions have no effect of height breakdown on the growth step. The crystal structure proved to be very tough in this low concentrated NaOH solution attack. Increasing the solution concentration to 4 M and 5 M did not give clear images of the crystal surfaces as the highly concentrated alkaline solutions softened the cured resin. As a result, the AFM tip dragged the softened resin over the crystal surface causing the surface topology fully covered in about one hour in contact with the

solution. Therefore, the crystal dissolution could not be observed. Higher concentration of NaOH solution (6 M) softened the resin even quicker so that in less than an hour of solution injection the resin could not hold this very thin NU-87 crystal anymore. The crystal wobbled and then popped out of the resin.

Attempts were also conducted to dissolve the NU-87 crystal in other basic solutions and acid solutions. However, again, the results were not good. These dissolution results were summarized in Table 6.1.

Table 6.1. A summary of the NU-87 crystal dissolutions performed using solutions other than NaOH solution.

Solution	Conc. (M)	Dissolution time (hours)	Observations
KOH	0.2	> 5	No change observed on the crystal surface.
	0.5	7	No change observed on the crystal surface.
	0.75	2	The crystal popped out of the resin very quickly.
	1	2	Wobbled crystal during the dissolution time. No change observed.
	4	3.5	Resin covered the crystal surface was covered.
Dec(OH) ₂	0.1	2	No change observed on the crystal surface (see Figure 6.9). The crystal was then popped out of the resin.
	0.6	0.25	The crystal popped out of the resin very quickly.
HCl	2	3	No change observed on the crystal surface.

To get the best dissolution condition for NU-87 crystal to investigate is a challenge in this work. It has to be assured that the solution is strong enough to break the bonds of the species at the crystal surface (Si–OH, Si–O–Si or Si–O–Al), but not too strong so that the dissolution cannot be followed. The resin also plays an important part for this purpose as the NU-87 has a very thin crystal. Softened resin due to its interaction with the solution cannot hold the thin crystal long enough for the

dissolution to start. There is a possibility that the crystal removal is because of the AFM tip that sweeps the crystal away during the scanning in contact mode. Nonetheless, AFM scanning in tapping mode has also been performed in this project, but the NU-87 crystal still popped out of the resin. This means that the type of resin used for such an experiment is crucial.

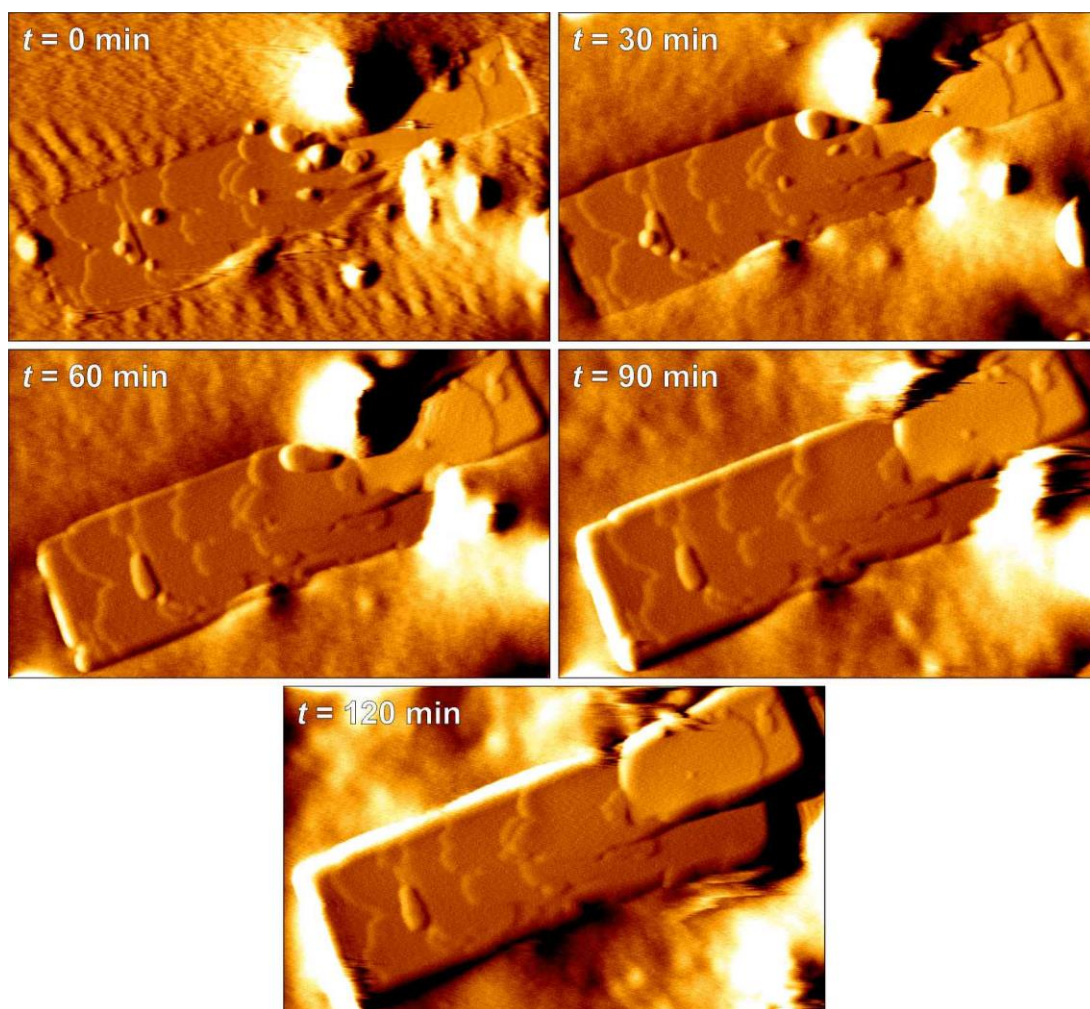


Figure 6.9. A series of AFM vertical deflection images on the (001) facet of NU-87 crystal dissolution in 0.1 M Dec(OH)₂ solution. The scanned area is 2.2 μm \times 1.3 μm .

6.4. Conclusions

PXRD and SEM techniques confirmed the success in the preparation of crystalline NU-87 material using decamethonium bromide as the template. The AFM revealed

layer-by-layer terraces on the (001) crystal surface. The terrace height is approximately 1.3 nm, which corresponds to half of the d_{001} value. Analysis of this growth step height on NU-87 structure framework matches with the simulated NU-87 crystal using *CrystalGrower*, which clearly shows the tiles at the particular surface terminal. Other features possess by the simulated crystal also agree with those of the experimental result. However, the NU-87 crystal dissolution was unsuccessful in this work owing to its very thin crystal and the resin that lost hold of the crystal when the basic solution was intact. Nonetheless, the crystal simulation suggests the step by step attachment of the units of growth on the (001) crystal facet during its growth.

6.5. References

- [1] J. L. Casci and A. Stewart, "Zeolites," EP 0377291 A1, 1990.
- [2] M. D. Shannon, J. L. Casci, P. A. Cox, and S. J. Andrews, "Structure of the two-dimensional medium-pore high-silica zeolite NU-87," *Nature*, vol. 353, pp. 417–420, 1991.
- [3] "Database of Zeolite Structures." [Online]. Available: <http://www.iza-structure.org/databases/>. [Accessed: 17-Nov-2017].
- [4] M. W. Anderson *et al.*, "Predicting crystal growth via a unified kinetic three-dimensional partition model," *Nature*, vol. 544, 2017.
- [5] S.-H. Park, J.-H. Lee, and H.-K. Rhee, "Disproportionation of 1,2,4-Trimethylbenzene over Zeolite NU-87," *Korean J. Chem. Eng.*, vol. 17, no. 2, pp. 198–204, 2000.
- [6] S.-H. Park and H.-K. Rhee, "Catalytic properties of zeolites MCM-22 and NU-87 in disproportionation of toluene," *React. Kinet. Catal. Lett.*, vol. 78, no. 1, pp. 81–89, 2003.
- [7] R. Glaser, S. Gomm, and J. Weitkamp, "In situ investigation of cumene synthesis over dealuminated zeolite catalysts by means of a tapered element oscillating microbalance," *Stud. Surf. Sci. Catal.*, vol. 154, pp. 2125–2132, 2004.

- [8] R. Glaser, R. Li, M. Hunger, S. Ernst, and J. Weitkamp, "Zeolite HNU-87: synthesis, characterization and catalytic properties in the shape-selective conversion of methylnaphthalenes," *Catal. Letters*, vol. 50, no. 3–4, pp. 141–148, 1998.
- [9] Y. Li and J. N. Armor, "Ammoxidation of Ethane to Acetonitrile over Metal-Zeolite Catalysts," *J. Catal.*, vol. 173, no. 2, pp. 511–518, 1998.
- [10] Z. Zhang, B. Qin, X. Zhang, F. Ling, W. Sun, and X. Fang, "The seeds effect on zeolite NU-87: Synthesis parameters and structural properties," *J. Porous Mater.*, vol. 20, no. 3, pp. 515–521, Jun. 2013.
- [11] A. Corma, V. González-Alfaro, and A. V. Orchillés, "The role of pore topology on the behaviour of FCC zeolite additives," *Appl. Catal. A Gen.*, vol. 187, no. 2, pp. 245–254, 1999.
- [12] B. Adair, C.-Y. Chen, K.-T. Wan, and M. E. Davis, "Reactions of meta-xylene on zeolites with intersecting medium and large pores. I. Basic studies," *Microporous Mater.*, vol. 7, no. 5, pp. 261–270, 1996.
- [13] A. W. Burton, Jr., "Method for preparing NES-type zeolites using novel structure directing agents," US 7 682 599 B2, 2010.
- [14] M. J. Díaz-Cabañas, M. A. Camblor, Z. Liu, T. Ohsuna, and O. Terasaki, "Zeolite syntheses using linear diquats of varying length in fluoride media. The synthesis of ITQ-8, ITQ-10, ITQ-14 and high silica Nu-87," *J. Mater. Chem.*, vol. 12, no. 2, pp. 249–257, 2002.

Chapter 7

Conclusions and Future Work

7. Conclusions and Future Work

7.1. Conclusions

This project was aimed to study the dissolution of inorganic nanoporous crystals having complex structures using AFM. The complexly structured crystals under study are IM-17 (UOV), DAF-1 (DFO), zeolite Rho (RHO) and NU-87 (NES). The results are expected to add valuable insights into the crystal growth study. The crystal dissolution process is chosen to be observed in this work as it may be related to the reverse process of crystal growth. In addition, owing to the working temperature limit of the AFM, this instrument cannot be used to scan the nanoporous crystals in-situ during their growth at very high temperature (100 – 190 °C) [1]–[4]. The dissolution experiments were conducted in alkaline solutions. As for DAF-1, combinations of decamethonium dihydroxide and phosphoric acid in different pH values were used to dissolve crystals.

The material syntheses in this work are successful as confirmed by the PXRD and SEM results. Except for the DAF-1 crystal, all crystals obtained in very small crystal sizes. Additional phases may co-exist alongside the main targeted products. Nevertheless, this does not hinder the investigation under the AFM since their morphologies are different. Thus, using a microscope we can easily pick the crystal to scan.

The AFM revealed the surface topography of the crystals. All crystals showed terraces on their surfaces as a result of layer-by-layer growth mechanism during their hydrothermal processes. In this work, we found spiral growth only on the (100) facet of the IM-17 crystal. The in-situ AFM scanning during the dissolution process uncovered gradual growth step breakdown of the complex-structured crystals under study. This outcome also suggests that the growth of these crystals may be a result of small growth unit attachment on the crystal surface to construct the framework.

Furthermore, the dissolution gave evidence that the structure at the surface terminal determines how the layers on the surface dissolve. Interconnected structure framework allows a terrace to retreat from its edge to its centre during the dissolution. This is as explained that, energetically, it is easier to detach the surface layer structure from the step sites than from the bulky terrace [5]. This behaviour

was observed in this work during the dissolution of the (013) facet of the IM-17 crystal and {110} facet of zeolite Rho. Interestingly, the previous study on crystal dissolution of nanoporous materials with small unit cells and simpler structures than IM-17 also gave a similar mechanism of crystal dissolution. This phenomenon was reported in the dissolution of the cancrinite cage in zeolite L [6], [7].

Meanwhile, the unconnected structure framework at the surface terminal enables the solution to attack the bulky terrace, creating patches. Hence, this dissolution mechanism is called patches dissolution. In this project, we found such mechanism during the dissolution of the (100) facet of the IM-17 crystal and both sides of the DAF-1 crystal. A similar phenomenon was also observed by Meza *et al.* [8] during the dissolution of zeolite A in which uncorrelated structure of the material's surface led to patches dissolution.

Interestingly, the spiral layer on the (100) facet of IM-17 crystal showed terrace retreat instead of patches dissolution. This is possible as the spiral causes the unconnected structure to tilt (not parallel) resulting in inter-connected structure. In addition, the dissolution of the DAF-1 crystal demonstrated a new phenomenon called as 'surface thinning', in which the surface layers dissolved while keeping their edge positions unmoved. This occurs due to the very under-saturated solution used in the process.

In general, from the dissolution of the three nanoporous materials in this study, we can conclude that the way the surface layer dissolves in solution is regardless of the complexity or the size of the repeating unit of the structure framework, but depends on the structure of the building units at the structure terminal. Terrace retreat from layer edge to the centre is a consequence of interconnected building units, whilst patches dissolution is a result of uncorrelated building units at the surface terminal.

Nonetheless, the in-situ AFM scanning on the NU-87 crystal dissolution in this work was unsuccessful. Very thin NU-87 crystal was removed quickly from the resin holding it as the alkaline solution softened the resin. The crystal removal was too soon for the solution to start dissolving the crystal structure. AFM scanning in tapping mode has also been tried, but this did not solve the problem. As a consequence, no data on this particular crystal dissolution was obtained.

The experimental results in this project are also confirmed with the crystal simulation using *CrystalGrower* [9]. The modelling also includes the simulation of the crystal dissolution. It is found that all features of the crystal observed in the lab, *i.e.* morphology, surface topology, nucleation, growth and dissolution behaviours, can be seen as well in the model crystal. The simulated UOV, DFO, RHO and NES crystals are perfect matches of those crystallized in the laboratory. Thus, this program is very useful in predicting crystal growth and dissolution.

7.2. Future Work

In-situ AFM scanning on the dissolutions of the four crystals in this study was performed. Despite the success, more work could be done to get optimum result to understand the dissolution process of the complex structures.

The small crystal sizes of the materials, except for the DAF-1 crystal, in this project is a hard challenge to work with in-situ AFM observation. The resin must be very tough to hold the tiny crystals, especially very thin crystal like NU-87, in highly concentrated solutions. The performance of the two-part epoxy system of adhesive from Master Bond in this study was tough enough in the dissolution of small crystals of IM-17 and zeolite Rho, but not for the very thin and resilient crystal of NU-87. The use of tougher and harder resin than the one used in this project is worth trying in the dissolution of small crystal, especially in a high concentration of alkaline solutions.

Besides changing the resin or the solution for the dissolution, working with larger crystal size may be one of the answers. Thus, it is necessary to synthesize a larger and thicker crystal of the NU-87 for this purpose.

The use of the solutions mentioned in this work was effective to dissolve the crystals. However, the analysis suggests that some of the dissolution steps might not be observed. Reducing the solution concentration while ensuring that the dissolution keeps progressing is worth trying to get more complete data. Moreover, in order to enhance the understanding in the DAF-1 crystal dissolution process, enlarging the pH range of the phosphoric acid and decamethonium hydroxide solution combinations used to dissolve the crystal could be done. Other than that, defining the

impurity particles started the pit formation in DAF-1 crystal surface will also be very useful to collect more information to explain the whole story of the extrinsic defect mechanism.

7.3. References

- [1] Y. Lorgouilloux *et al.*, “IM-17: a new zeolitic material, synthesis and structure elucidation from electron diffraction ADT data and Rietveld analysis,” *RSC Adv.*, vol. 4, no. 37, pp. 19440–19449, 2014.
- [2] P. A. Wright *et al.*, “Synthesis and structure of a novel large-pore microporous magnesium-containing aluminophosphate (DAF-1),” *J. Chem. Soc. Chem. Commun.*, vol. 104, no. 7, pp. 633–635, 1993.
- [3] T. Chatelain, J. Patarin, E. Fousson, M. Soulard, J. L. Guth, and P. Schulz, “Synthesis and characterization of high-silica zeolite RHO prepared in the presence of 18-crown-6 ether as organic template,” *Microporous Mater.*, vol. 4, no. 2–3, pp. 231–238, 1995.
- [4] M. D. Shannon, J. L. Casci, P. A. Cox, and S. J. Andrews, “Structure of the two-dimensional medium-pore high-silica zeolite NU-87,” *Nature*, vol. 353, pp. 417–420, 1991.
- [5] P. Cubillas and M. W. Anderson, “Synthesis Mechanism: Crystal Growth and Nucleation,” in *Zeolites and Catalysis, Synthesis, Reactions and Applications*, Vol. 1., Weinheim, Germany: Wiley-VCH Verlag GmbH & Co. KGaA, 2010.
- [6] R. Brent and M. W. Anderson, “Fundamental crystal growth mechanism in zeolite L revealed by atomic force microscopy,” *Angew. Chemie - Int. Ed.*, vol. 47, no. 29, pp. 5327–5330, 2008.
- [7] R. Brent *et al.*, “Unstitching the Nanoscopic Mystery of Zeolite Crystal Formation,” *J. Am. Chem. Soc.*, vol. 132, no. 9, pp. 13858–13868, 2010.
- [8] L. I. Meza, M. W. Anderson, B. Slater, and J. R. Agger, “In situ atomic force microscopy of zeolite A dissolution,” *Phys. Chem. Chem. Phys.*, vol. 10, pp. 5066–5076, 2008.
- [9] M. W. Anderson *et al.*, “Predicting crystal growth via a unified kinetic three-dimensional partition model,” *Nature*, vol. 544, no. 7651, pp. 456–459, 2017.

Appendices

Appendices

Appendix 1

1-1 Dissolution Movie Link:

<https://data.mendeley.com/datasets/7k7mkpnyt3/draft?a=2b759b4b-08fc-42f9-ac8d-e09fe946436d>

The link above comprises of:

Chapter 3

Movie 3-1 Dissolution of IM-17 crystal on (100) facet in NaOH solution

Movie 3-2 Simulation of IM-17 crystal dissolution on (100) facet

Movie 3-3 Dissolution of IM-17 crystal on (100) facet with screw dislocation in NaOH solution

Movie 3-4 Dissolution of IM-17 crystal on (013) facet in NaOH solution

Movie 3-5 Simulation of IM-17 crystal dissolution on (013) facet

Chapter 4

Movie 4-1 Dissolution of DAF-1 crystal on (010) facet in solution 3

Movie 4-2 Dissolution of DAF-1 crystal on (001) facet in solution 3

Movie 4-3 Dissolution of DAF-1 crystal on (010) facet in solution 4

Movie 4-4 Dissolution of DAF-1 crystal on (001) facet in solution 4

Movie 4-5 Dissolution of DAF-1 crystal on (010) facet in solution 5

Movie 4-6 Dissolution of DAF-1 crystal on (001) facet in solution 5

Movie 4-7 Pit formation on (010) facet of DAF-1 crystal in solution 5

Movie 4-8 Simulation of DAF-1 crystal dissolution on (010) facet

Movie 4-9 Simulation of DAF-1 crystal dissolution on (010) facet showing column formation

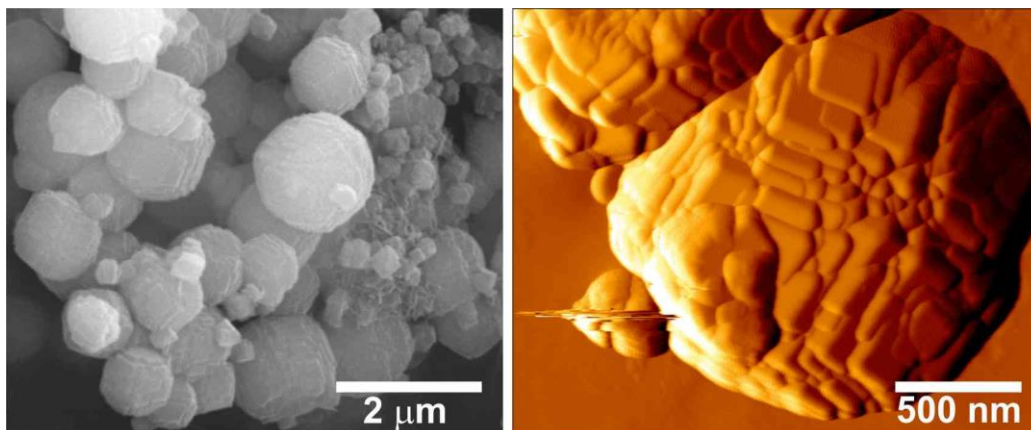
Movie 4-10 Simulation of DAF-1 crystal dissolution on (001) facet

Chapter 5

Movie 5-1 Dissolution of Zeolite Rho crystal on (110) facet in KOH solution

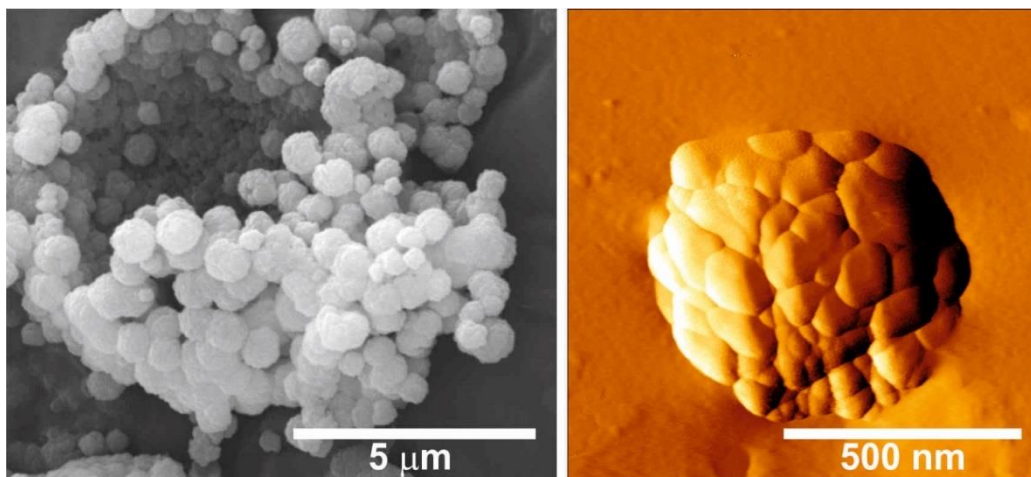
1-2 CHAPTER 5

ECR-18



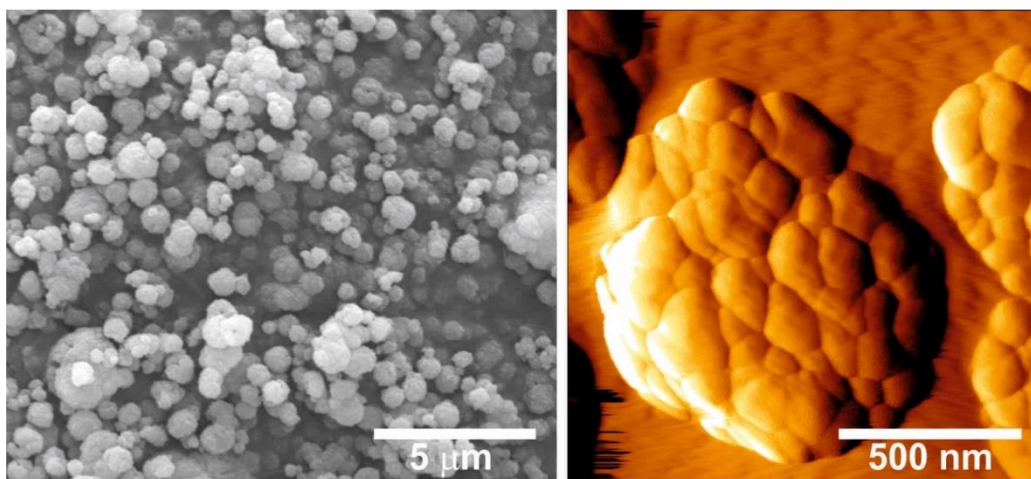
SEM image of the as-synthesized ECR-18 crystals (left) and vertical deflection AFM image of the ECR-18 crystals (right).

ZSM-25



SEM image of the as-synthesized ZSM-25 crystals (left) and vertical deflection AFM image of the ZSM-25 crystals (right).

PST-20



SEM image of the as-synthesized PST-20 crystals (left) and vertical deflection AFM image of the PST-20 crystals (right).

Appendix 2

Publication from collaboration

- “Predicting crystal growth via a unified kinetic three-dimensional partition model”. M. W. Anderson, J. T. Gebbie-Rayet, A. R. Hill, N. Farida, M. P. Attfield, Pablo Cubillas, V. A. Blatov, D. M. Proserpio, D. Akporiaye, B. Arstad and J. D. Gale. *Nature*, vol. 544, **2017**.

Presentations

- “Atomic Force Microscopy of Template Interactions on Nanoporous Materials”. N. Farida, M. P. Attfield and M. W. Anderson. *39th Annual Meeting of the British Zeolite Association*, **2016**. [Poster]
 - “Crystal Growth on Complex Framework Structures”. N. Farida. *Postgraduate Conference University of Manchester*, **2017**. [Talk]
 - “Dissolution of Nanoporous Magnesium-aluminophosphate DAF-1 Studied by Atomic Force Microscopy”. N. Farida, M. P. Attfield and M. W. Anderson. *British Association for Crystal Growth Annual Conference*, **2017**. [Poster]
-